

# Conditioning, Reduction, and Disturbance Analysis of Large Order Integrated Models for Space-Based Telescopes

by

Scott Alan Uebelhart

S.B. Aeronautics and Astronautics  
Massachusetts Institute of Technology, 1998

Submitted to the Department of Aeronautics and Astronautics  
in partial fulfillment of the requirements for the degree of

Master of Science in Aeronautics and Astronautics

at the

MASSACHUSETTS INSTITUTE OF TECHNOLOGY

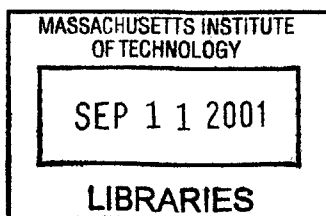
February 2001

© Massachusetts Institute of Technology 2001. All rights reserved.

Author .....  
Department of Aeronautics and Astronautics  
February 1, 2001

Certified by .....  
David W. Miller  
Associate Professor  
Thesis Supervisor

Accepted by .....  
Wallace E. Vander Velde  
Professor of Aeronautics and Astronautics  
Chair, Committee on Graduate Students



AERO ..



# Conditioning, Reduction, and Disturbance Analysis of Large Order Integrated Models for Space-Based Telescopes

by

Scott Alan Uebelhart

Submitted to the Department of Aeronautics and Astronautics  
on February 1, 2001, in partial fulfillment of the  
requirements for the degree of  
Master of Science in Aeronautics and Astronautics

## Abstract

A new fleet of flexible space observatories is being prepared to follow up on the success of the Hubble Space Telescope. The Next Generation Space Telescope (NGST) and the Space Interferometry Mission (SIM) are being designed at NASA centers for launch within the decade. In addition, the on-orbit testbed Nexus was planned as a precursor mission to NGST. Because of their stringent optical requirements, detailed integrated models of these spacecraft are being assembled to simulate their performance in the presence of disturbance forces and optical control loops. The **D**ynamics, **O**ptics, **C**ontrols, and **S**tructures (DOCS) toolbox is used to model and assemble the individual components of the integrated system, and to run dynamical analyses of the spacecraft for the purpose of design iterations.

These integrated models, cast in state-space form, have grown beyond the small “stick” models used for initial disturbance studies, and may now have upwards of thousands of states. To lower the computational burden of the DOCS analyses, and to improve the numerical quality of the models as they are manipulated, this thesis concentrates on model quality management for large systems. This includes steps that can be taken to improve the numerical conditioning of large matrices, and methods to balance and reduce the state vectors in large systems. The linear algebra routines required for balancing are reviewed, and a faster method of solving the Lyapunov equation is introduced. A variation of the typical gramian balancing technique is used to successfully balance models that could not be balanced using traditional MATLAB tools. These models are then reduced to as little as one sixth of their original size.

A review of reaction wheel disturbances includes both broadband and discrete wheel speed models using power spectral density (PSD) curves and white noise shaping filters. Using these disturbances along with the reduced models, disturbance analyses are run that compare the open loop dynamics of NGST and Nexus, and examine the closed loop behavior of the latest and most complete SIM model. Prominent dynamical features are pointed out, and modes requiring further study are identified. A final comparison between multiple versions of the SIM model is included to judge the ability of smaller stick models to capture important spacecraft dynamics.

Thesis Supervisor: David W. Miller  
Title: Associate Professor





## Acknowledgments

This research was supported by the NASA Goddard Space Flight Center, under contract NAG 5-7839 (Structural Dynamics and Controls Analysis and Simulation for NASA's NGST), with Gary Mosier as Technical/Scientific Officer, and by JPL Contract #961123 (Modeling and Optimization of Dynamics and Control for the NASA Space Interferometry Mission and the Micro-Precision Interferometer Testbed), with Robert Grogan as Technical/Scientific Officer and Dr. Sanjay Joshi as Contract Monitor.

I would like to thank Professor Dave Miller for his assistance and support, and for his perseverance in showing me the path for this thesis. Many people in the Space Systems Lab deserve thanks for helping me along the way. Homero Gutierrez, Greg Mallory, and Jeremy Yung all provided their time and insights to help me understand linear systems theory. I wish to particularly thank Oli de Weck for providing guidance and suggestions, and for proof-reading this entire document. Gary Mosier at NASA Goddard provided a desk for the summer and the opportunity to let me watch the actual spacecraft design process.

Becky Masterson provided waterfall plots, generous amounts of MATLAB and L<sup>A</sup>T<sub>E</sub>X advice, and a guest room by the beach. Alice Liu was a kind listener who was there for all of my controls questions. Special thanks go to Laila Elias, who walked side-by-side with me through writing a thesis and earning a pilot's license. Alvar Saenz Otero was there with a patient ear and candy.

SharonLeah Brown and Peggy Edwards both keep the lab running smoothly. Marie Stuppard has provided immeasurable amounts of assistance ever since I arrived at MIT many years ago, and continues to have the warmest smile in the department.

A thanks goes to all of my friends who would talk about things other than research, including my office mates Seung Chung and Elisabeth Lamassoure, my housemate Shawn Kelly, Patrick Trapa and Tim Glenn, Alissa Clawson, and especially to Nate and Zohra Rawling, for putting up with me for so long.

And the final and warmest thanks to Granny, Lori, and Mom and Dad, for helping me get to this point in the first place, and for supporting me, together as a family.



# Contents

<b>1</b>	<b>Introduction</b>	<b>21</b>
1.1	Motivation . . . . .	21
1.2	Dynamics, Optics, Controls, Structures (DOCS)	
	Framework . . . . .	23
1.3	State Space Balancing and Reduction Routines . . . . .	24
1.4	Thesis Overview . . . . .	26
<b>2</b>	<b>Space Telescope Descriptions</b>	<b>29</b>
2.1	Next Generation Space Telescope (NGST) . . . . .	30
	2.1.1 NGST Mission Architecture . . . . .	32
	2.1.2 NGST Structural Finite Element Model . . . . .	33
	2.1.3 NGST Optical Performance . . . . .	35
2.2	Nexus . . . . .	36
	2.2.1 Nexus Mission Architecture . . . . .	37
	2.2.2 Nexus Structural Finite Element Model . . . . .	38
	2.2.3 Nexus Optical Performance Metrics . . . . .	40
2.3	Space Interferometry Mission (SIM) . . . . .	41
	2.3.1 SIM Mission Architecture . . . . .	42
	2.3.2 SIM State-Space Model . . . . .	45
2.4	Summary . . . . .	49
<b>3</b>	<b>Numerical Tools</b>	<b>51</b>
3.1	Eigenvalues . . . . .	52
3.2	Singular Value Decomposition . . . . .	53
	3.2.1 Properties of SVD matrices . . . . .	54

3.2.2	Condition Number of Matrices . . . . .	56
3.3	Lyapunov Equation . . . . .	58
3.3.1	Controllability and Observability Gramians . . . . .	58
3.3.2	Analytical Solution . . . . .	60
3.3.3	Fast Lyapunov Solvers . . . . .	61
3.4	Summary . . . . .	67
<b>4</b>	<b>Methods for Maintaining Model Quality</b>	<b>69</b>
4.1	Model Preparation . . . . .	69
4.1.1	Rigid Body Modes . . . . .	71
4.1.2	Low- and High- Frequency Modes . . . . .	72
4.1.3	Input/Output Selection . . . . .	73
4.2	Tracking Numerical Quality . . . . .	76
4.3	Summary . . . . .	78
<b>5</b>	<b>Balancing and Model Reduction</b>	<b>81</b>
5.1	Methods of Model Reduction . . . . .	81
5.2	Balancing Routines . . . . .	83
5.2.1	Gramian Transformations . . . . .	84
5.2.2	Eigenvalue Approach . . . . .	87
5.2.3	SVD Approach . . . . .	87
5.3	Balancing Routines on Large Models . . . . .	89
5.3.1	Difficulties . . . . .	89
5.3.2	Balanced Truncation Method . . . . .	91
5.4	Reducing the Model . . . . .	94
5.5	Spacecraft Examples . . . . .	100
5.5.1	NGST . . . . .	100
5.5.2	SIM . . . . .	105
5.6	Summary . . . . .	116
<b>6</b>	<b>Disturbance Sources</b>	<b>119</b>
6.1	Reaction Wheel Disturbances . . . . .	119
6.2	Reaction Wheel Assemblies . . . . .	123

6.3	Broadband Wheel Speed Model . . . . .	126
6.4	Discrete Wheel Speed Model . . . . .	128
6.5	Summary . . . . .	133
<b>7</b>	<b>Disturbance Analysis</b>	<b>135</b>
7.1	Integrated Modeling . . . . .	135
7.1.1	Structural, Optical, and Disturbance models . . . . .	136
7.1.2	ACS and Optical Controllers . . . . .	137
7.2	Disturbance Analysis Methodology . . . . .	140
7.3	PSD Analysis on Nexus & NGST . . . . .	143
7.3.1	Broadband wheel speeds . . . . .	143
7.3.2	Discrete wheel speeds . . . . .	148
7.3.3	Nexus/NGST Analysis Summary . . . . .	151
7.4	Lyapunov and PSD Analysis on SIM . . . . .	151
7.4.1	Lyapunov Analysis . . . . .	152
7.4.2	Reaction Wheel Comparison . . . . .	156
7.4.3	Frequency-based PSD Analysis . . . . .	159
7.4.4	State-Space versus Tonal Comparison . . . . .	165
7.4.5	SIM Analysis Summary . . . . .	167
7.5	Summary . . . . .	168
<b>8</b>	<b>Model Evolution</b>	<b>169</b>
8.1	SIM Classic Version 1.0 . . . . .	170
8.2	Model Comparison . . . . .	171
8.3	Summary . . . . .	176
<b>9</b>	<b>Conclusions</b>	<b>177</b>
9.1	Overview . . . . .	177
9.2	Recommendations for Future Work . . . . .	181
<b>A</b>	<b>Nexus/NGST Disturbance Analysis Results Comparison</b>	<b>185</b>
<b>B</b>	<b>SIM Lyapunov Disturbance Analysis Results</b>	<b>195</b>
<b>C</b>	<b>SIM PSD Disturbance Analysis Results</b>	<b>201</b>



# List of Figures

1-1	Overview of the DOCS framework. . . . .	24
1-2	Structure of the SIM state-space $A$ matrices . . . . .	25
1-3	Thesis Outline . . . . .	28
2-1	Earth-Sun Lagrangian points. . . . .	30
2-2	NGST designs proposed by the contractor candidates and GSFC [5] . . . .	31
2-3	ngst603ss FE Model . . . . .	34
2-4	Original Nexus/Horizon spacecraft . . . . .	37
2-5	Current Nexus design . . . . .	38
2-6	Nexus stowed configuration in a Delta II fairing. . . . .	39
2-7	Nexus/Horizon Finite Element Model . . . . .	40
2-8	Primary Mirror of the Reduced Nexus/Horizon FEM . . . . .	41
2-9	Comparison of modal frequencies between high- and low-fidelity Nexus/Horizon models . . . . .	42
2-10	An artist's drawing of the Space Interferometry Mission [6] . . . . .	43
2-11	Basic elements of the SIM interferometer . . . . .	44
2-12	SIM Finite Element Model . . . . .	45
2-13	Devices used in SIM's optical train . . . . .	46
3-1	Complex conjugate poles on the complex plane . . . . .	52
3-2	CPU Time in minutes to solve a Lyapunov equation of size $n$ using blocks of size $m$ . . . . .	64
3-3	Number of flops for the sample problem, along with curves showing the flop count approximation . . . . .	66
4-1	Block diagram outlining the model preparation steps. . . . .	70

4-2	Structure of the system $A$ matrix after appending RBMs. . . . .	72
4-3	Distribution of modal frequencies in SIM Version 2.0 . . . . .	73
4-4	Sample transfer functions show the effect of units on the relative importance of modes. . . . .	74
4-5	SIM Version 2.0 controllability gramian singular values, comparing reaction wheel inputs alone to reaction wheel and PZT and voice coil actuators. . . .	76
4-6	Transfer function of RWA $F_x$ to Star OPD #1 for SIM model v2.2 . . . . .	77
4-7	Singular values of SIM model v2.2 $A$ matrices. . . . .	79
5-1	Hankel Singular Values for ngst603ss 200-state model . . . . .	90
5-2	RWA force X to centroid X transfer function for ngst603ss 200-state model	90
5-3	Outline of the balanced truncation routine. . . . .	92
5-4	Structure of $A$ matrices through balancing . . . . .	94
5-5	Modal Frequencies of the ngst603ss 600-state and reduced 100-state models.	100
5-6	Singular Values of the NGST gramians . . . . .	102
5-7	Original and balanced $A$ -matrix singular values for ngst603ss. . . . .	103
5-8	Full order versus Balanced Transfer Function: RWA $F_x$ to Centroid X . . . .	103
5-9	Transfer Function between RWA force X and centroid X, NGST 100-state reduced model. . . . .	106
5-10	Transfer Function between RWA torque X and centroid X, NGST 100-state reduced model. . . . .	106
5-11	Transfer Function between RWA force Y and centroid Y, NGST 100-state reduced model. . . . .	107
5-12	Transfer Function between RWA force Y and the first ray's WFE, NGST 100-state reduced model. . . . .	107
5-13	A comparison of reduction methods: brutal truncation versus static condensation. . . . .	108
5-14	Comparison of original and reduced frequencies for SIM v2.0. . . . .	109
5-15	Controllability and augmented observability singular values and Hankel Singular Values for SIM v2.0 . . . . .	110
5-16	Singular values of the system $A$ matrices. . . . .	110



5-17	Balanced and Reduced transfer functions of RWA Force X to Star OPD #1, SIM v2.0 . . . . .	113
5-18	Balanced and Reduced transfer Functions of RWA Force X to Star X WF1 Tilt #1, SIM v2.0 . . . . .	114
5-19	Balanced and Reduced transfer Functions of RWA Torque X to Internal Metrology Opd #1, SIM v2.0 . . . . .	115
5-20	1063 state TF of RWA Force X to Star Opd #1 for SIM model v2.2 . . . .	117
5-21	608 state TF of RWA Force X to Star Opd #1 for SIM model v2.2 . . . .	117
5-22	316 state TF of RWA Force X to Star Opd #1 for SIM model v2.2 . . . .	118
6-1	Ithaco Type E reaction wheel [2] . . . . .	120
6-2	Ithaco B-wheel waterfall plot . . . . .	122
6-3	Reaction wheel frame $x_w$ , $y_w$ , $z_w$ within the spacecraft frame $X_{s/c}$ , $Y_{s/c}$ , $Z_{s/c}$	125
6-4	Sample broadband wheel speed PSD . . . . .	127
6-5	Ithaco E-wheel axial disturbance force amplitude spectra . . . . .	129
6-6	Ithaco E-wheel axial disturbance force amplitude spectra: tones and state space model at 1000 RPM . . . . .	132
6-7	Ithaco E-wheel axial disturbance force PSD below, and RMS above: tones and state space model at 1000 RPM . . . . .	133
7-1	Effect of ACS “pseudo-controller” on Nexus/Horizon plant . . . . .	138
7-2	Effect of simple ACS controller on SIM plant . . . . .	139
7-3	Wave Front Error PSD and cumulative RMS plots for NGST and Nexus; broadband wheel speeds . . . . .	145
7-4	Normalized Cumulative RMS WFE curves . . . . .	146
7-5	Disturbance contributions to Critical WFE Frequencies . . . . .	147
7-6	WFE performance PSD for Nexus/Horizon using a tonal RWA model at 1000 RPM . . . . .	149
7-7	WFE performance versus wheel speed . . . . .	150
7-8	Wheel harmonic numbers $h_i$ versus wheel harmonic coefficients $C_i$ . . . . .	153
7-9	Open and Closed Loop performance RMS versus RPM for Star OPD #1. .	154
7-10	Open and Closed Loop performance RMS versus RPM for Star OPD #2. .	155
7-11	Open and Closed Loop performance RMS versus RPM for Star X WFT #1.	156

7-12	Closed Loop performance RMS versus RPM for Star OPD #3 for the Ithaco E- and B-wheels and the HST wheels. . . . .	157
7-13	Star OPD #1 open loop at 11 RPS; PSD and cumulative RMS plot. . . . .	161
7-14	Star OPD #1 closed loop at 36 RPS; PSD and cumulative RMS plot. . . . .	162
7-15	Star OPD #1 closed loop at 58 RPS; PSD and cumulative RMS plot. . . . .	163
7-16	Star OPD #1 closed loop at 66 RPS; PSD and cumulative RMS plot. . . . .	164
7-17	Critical frequencies of Star OPD #1 at 66 RPS. . . . .	166
7-18	Comparison of tonal and shaping filter PSD and RMS results for Star OPD #3 at 60 RPS . . . . .	166
8-1	SIM Version 1.0 FE model. . . . .	170
8-2	Cumulative RMS curves and PSDs for the broadband RWA disturbances . . . . .	171
8-3	Sample original and reduced transfer functions for SIM Versions 1.0 and 2.2. . . . .	172
8-4	SIM Version 1.0 cumulative RMS curve, performance PSD, and disturbance contributions for Total OPD . . . . .	174
8-5	Normalized cumulative RMS curve for SIM Version 1.0, Total OPD . . . . .	175
8-6	Contributions of critical frequencies and disturbance inputs to the Total OPD RMS for SIM Version 1.0. . . . .	175
A-1	Centroid X performance PSD given a broadband wheel speed disturbance. . . . .	186
A-2	Centroid Y performance PSD given a broadband wheel speed disturbance. . . . .	187
A-3	Disturbance contribution at the critical frequencies for Centroid X. . . . .	188
A-4	Disturbance contribution at the critical frequencies for Centroid Y. . . . .	189
A-5	Normalized cumulative RMS performance curve for Centroid X . . . . .	190
A-6	Normalized cumulative RMS performance curve for Centroid Y . . . . .	191
A-7	Centroid X performance PSD given a discrete wheel speed disturbance at 1000 RPM. . . . .	192
A-8	Centroid Y performance PSD given a discrete wheel speed disturbance at 1000 RPM. . . . .	193
A-9	Centroid X and Y performance RMS versus Reaction Wheel Speed. . . . .	194
B-1	Star OPD open and closed loop performances. . . . .	196
B-2	Internal Metrology OPD open and closed loop performances. . . . .	197

B-3	Star WFT open and closed loop performances. . . . .	198
B-4	FEC and External Metrology open loop performances. . . . .	199
C-1	PSD and cumulative RMS plots of Star OPD around 11 RPS . . . . .	202
C-2	PSD and cumulative RMS plots of Star OPD at 19.8 RPS . . . . .	203
C-3	PSD and cumulative RMS plots of Star WFT at 28.2 RPS . . . . .	204
C-4	PSD and cumulative RMS plots of Star OPD and WFT at 36.0 RPS . . . .	205
C-5	PSD and cumulative RMS plots of Star OPD at 36.2 RPS . . . . .	206
C-6	PSD and cumulative RMS plots of Star OPD at 58.0 RPS . . . . .	207
C-7	PSD and cumulative RMS plots of Star OPD at 58.6 RPS . . . . .	208
C-8	PSD and cumulative RMS plots of Star OPD at 66.0 RPS . . . . .	209



# List of Tables

2.1	Comparison of telescopes . . . . .	33
2.2	SIM v2.0 inputs for analysis . . . . .	47
2.3	SIM v2.0 outputs for analysis . . . . .	48
3.1	Time improvements using fast Lyapunov method . . . . .	63
3.2	Improvements in flop counts using fast Lyapunov method . . . . .	66
5.1	Effects of number of kept states for the NGST 600-state model . . . . .	104
5.2	Effects of number of kept states on the SIM Version 2.0, 2148-state flexible model. . . . .	111
6.1	Reaction Wheel Specifications [2, 14] . . . . .	121
6.2	Variables to produce broadband wheel disturbance PSDs . . . . .	127
7.1	Critical Frequencies in Hz . . . . .	148
7.2	Summary of RMS Performances from SIM Lyapunov Analysis . . . . .	158
7.3	Selection of SIM Critical RWA Speeds . . . . .	160
7.4	SIM v2.2 Critical Frequencies . . . . .	165
8.1	SIM closed loop OPD critical frequencies [Hz] . . . . .	176



# Abbreviations

ACS	Attitude Control System
asec	arcseconds
COBE	Cosmic Background Explorer
CCA	Component Cost Analysis
DOF	Degree of Freedom
EO3	Earth Observer 3
FE	Finite Element
FEC	Wave Front Tilt, Front End Camera (SIM)
FEM	Finite Element Model (or Method)
FSM	Fast Steering Mirrors
GEO	Geosynchronous Orbit
GSFC	Goddard Space Flight Center
HPF	High Pass Filter
HST	Hubble Space Telescope
HSV	Hankel Singular Values
IMOS	Integrated Modeling of Optical Systems (software package)
ISIM	Integrated Science Instrument Module (NGST)
JPL	Jet Propulsion Laboratory
LEO	Low Earth Orbit
LOS	Line-of-sight
LPF	Low pass filter
MACOS	Modeling and Analysis for Controlled Optical Systems (software package)
mas	Milli-arcseconds
$\mu$ as	Micro-arcseconds

MCA	Modal Cost Analysis
MSC	MacNeal-Schwendler (Nastran)
MIR	Mid Infrared
NGST	Next Generation Space Telescope
NIR	Near Infrared
ODL	Optical Delay Line
OPD	Optical Pathlength Difference
OTA	Optical Telescope Assembly
PM	Primary Mirror
PSD	Power Spectral Density
PSS	Precision Support Structure (SIM)
PZT	Piezoelectric Translator (SIM)
RBM	Rigid Body Modes
RMS	Root mean square
RPM	Revolutions per Minute
RPS	Revolutions per Second
RSS	Root Sum Squared
RWA	Reaction Wheel Assembly
SIM	Space Interferometry Mission
SIMTAC	SIM Technical Advisory Committee
SM	Secondary Mirror
SSM	Spacecraft Support Module (NGST)
SVD	Singular Value Decomposition
TF	Transfer Function
WFE	Wave Front Error
WFSC	Wave Front Sensing and Control
WFT	Wave Front Tilt



# Chapter 1

## Introduction

### 1.1 Motivation

A decade after the launch of the Hubble Space Telescope, a new fleet of space-based observatories is being prepared to look even further into the cosmos. The successors to Hubble are being designed as part of NASA's Origins Program [4], an attempt to answer the basic questions of where do we come from, and are we alone in the universe? Two of the key missions in the program are the Next Generation Space Telescope (NGST), being designed at NASA Goddard Space Flight Center, and the Space Interferometry Mission (SIM), being designed at the Jet Propulsion Laboratory. These flexible observatories will push the limits in space-based optical control. Telescope resolutions are on the order of milli-arcseconds; optical pathlengths must be controlled to within nanometers, or to within the diameters of tens of hydrogen atoms. A complete understanding of the structural dynamics of these telescopes is necessary, where even the slightest disturbance vibration could ruin science observations.

Years before any metal will be cut or mirrors polished for these instruments, their behavior is being studied through the use of integrated computer models. All aspects of the spacecraft are examined using empirical or analytical models to simulate the expected on-orbit dynamics. Structural models are built to define the physical geometry and material properties of the spacecraft; optical models define the light paths and performance requirements. Of particular interest are models of the disturbances; the identification of potential disturbance sources, whether from on-board reaction wheels, cryocoolers, fuel sloshing, or from external solar pressures or gravity gradients, is followed by the modeling of these ex-

citations to simulate their effects on-orbit. The basic integrated models may also contain control loops for either attitude control systems or optical light-path actuators.

The implementation of these models, whether performed using discrete time domain simulations or continuous frequency domain mathematics, invariably makes use of matrices and such common mathematical tools as transformations, eigensolvers, or a host of other routines based in linear algebra. After paying particular attention to accurately modeling the spacecraft, optical paths, or disturbance sources, it is equally important to ensure that the models themselves are properly assembled and handled, so that any of these matrix routines do not change the basic dynamics under study. Considering the old idiom of “garbage in, garbage out,” it is important that the model quality be managed so that the results can be trusted.

The purpose of this work is to run through an entire disturbance to performance analysis for several spacecraft, all the while considering the effect of model quality on the results. This must also take into account the size of the models. The most typical form for the models is in first-order states-space:

$$\begin{aligned}\dot{x} &= Ax + Bu \\ y &= Cx + Du\end{aligned}\tag{1.1}$$

where the vector of states  $x$  represent the displacements and velocities of the individual nodes of a finite-element model,  $u$  represents the forces applied at one or several nodes, and  $y$  represents the displacements, velocities, or accelerations measured at one or several nodes. Typical linear system operations are fast and effective when  $x$  has only tens or a couple of hundred elements. Many of the spacecraft models have many more states than this, however. High fidelity structural finite element models, coupled with modern controllers and disturbance models, can grow from many hundreds to several thousands of states. The size of these systems can create numerical difficulties that either require large amounts of computational resources, or that can cause the linear system operations to fail. The goal of this work is to show computational and reduction steps that can be performed on large systems, so that they can still be analyzed using a disturbance analysis framework and produce meaningful results.

## 1.2 Dynamics, Optics, Controls, Structures (DOCS)

### Framework

A suite of tools has been developed at the MIT Space Systems Laboratory for the purpose of completely analyzing the effects of disturbances on a spacecraft, and for examining the manner in which performances react to excitations. The collection of these tools is named DOCS, and describes all aspects of integrated modeling including **D**ynamics, **O**ptics, **C**ontrols, and **S**tructures (see Figure 1-1). The basic framework was developed by Gutierrez [22] and consists of a series of MATLAB functions. Given a state-space structural system and any one of several types of disturbance models, these functions will determine the expected performances, identify critical modes that contribute to performance degradation, determine the sensitivity of both modal and physical parameters to the disturbances, and follow model uncertainties through the analysis. The primary tool used in this work will be the disturbance analysis; along with determining whether or not a particular performance requirement is met, it also allows critical modes to be identified and can determine which disturbance inputs are providing the most energy to a mode. In this manner the DOCS functions provide more than just final performance results. Rather, they are designed for the purpose of iterative spacecraft design. By examining how the disturbances interact with a flexible spacecraft, and then by examining the sensitivities to determine which spacecraft parameters should be changed to most benefit the performance, exact design changes can be proposed and implemented.

Along with the basic disturbance and sensitivity functions, several other tools have been prepared at MIT to assist with spacecraft analysis and design. Identifying and modeling the disturbances is a key component of integrated modeling. The greatest contributor to spacecraft vibrations is expected to be the reaction wheels, used to slew and to hold the attitude of a spacecraft. Based on empirical data and analytical approximations, Master-son [28] has developed disturbance models that capture the key reaction wheel dynamics. These models will be used in the disturbance analysis of this work. Mallory [27] developed a controller tuning technique to improve upon baseline controllers. He also developed a method to determine which sensor/actuator combinations are suitable for a particular application, for example, system identification of a spacecraft's modeshapes. de Weck [15] has developed an iso-performance analysis to complement the sensitivity analysis. Whereas

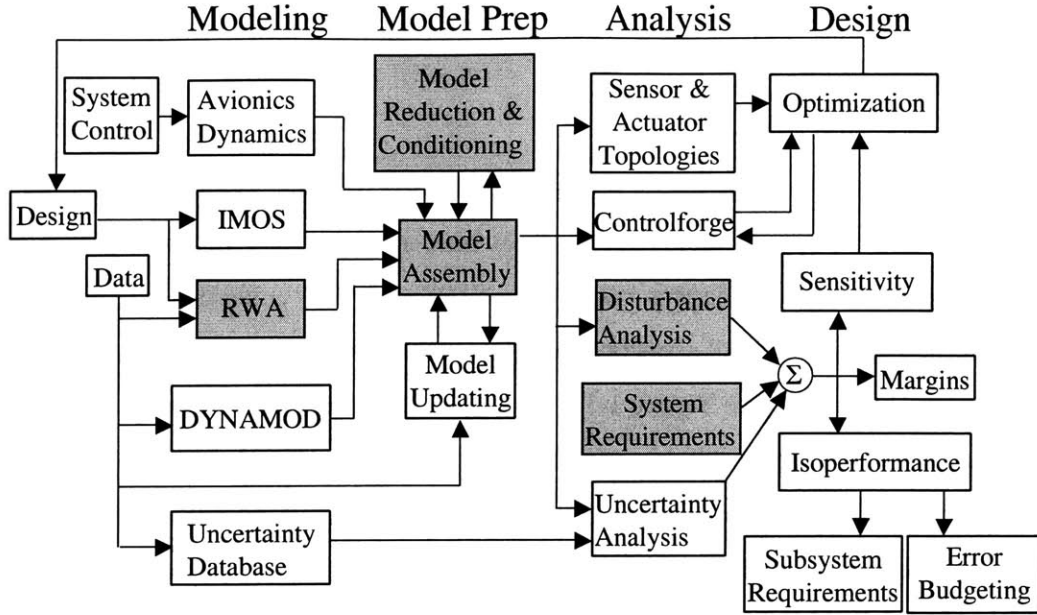


Figure 1-1: An overview of the DOCS framework. Those areas used by or created by this thesis are highlighted.

the sensitivities show how the performances can change based on variations in the modal or physical parameters, the iso-performance curves show how parameters can change while maintaining constant performance. This would be used at a higher level of design, after the requirements have been met, to trade performance errors between components in an effort to minimize costs (weight, monetary, or other).

One of the goals of the DOCS toolbox was to make it spacecraft-independent. It is designed as a generic tool that can be applied to any model framed in a state-space manner. Space observatories already examined include the original SIM model version 1.0 by Gutierrez [22] and a low-fidelity model of NGST by de Weck [14]. This work will apply the disturbance tools to a proposed NGST precursor mission named Nexus, as well as to the latest SIM model, version 2.2.

### 1.3 State Space Balancing and Reduction Routines

The critical step in working with large order models is reducing them to a more manageable size. For any given set of inputs and outputs, many of the elements in the state vector  $x$  can not be controlled and/or observed. Since these states do not affect the transfer function

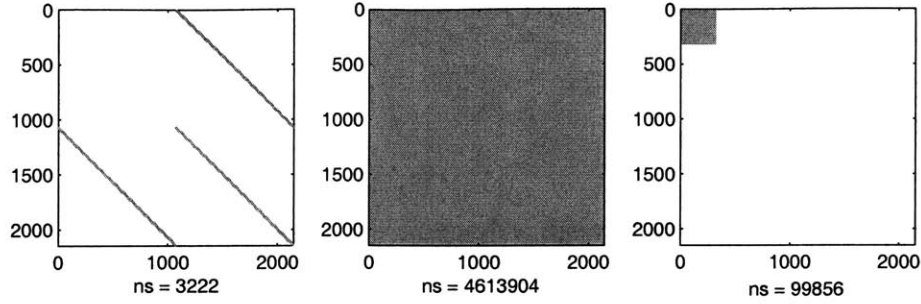


Figure 1-2: Structure of the SIM state-space  $A$  matrices: original sparse second order modal form (left) with 2148 states, fully populated balanced system (center), and fully populated reduced system with 316 states.

that describes the output for a given input, their presence in the system adds unnecessarily to the computational burden.

Several reduction routines have been proposed. Skelton has a series of papers that described Modal or Component Cost Analysis [23, 45, 46, 44]; a cost functional ranks each state, and those with the lowest costs can be removed. Another popular method is gramian balancing. This was first proposed by Moore [35], with extensions and modifications by Laub [25] and Gregory [19]. The *gramians* of a system describe the amount that states are controllable or observable. By transforming the system so that the gramians are equal, or *balanced*, the states are equally controllable *and* observable. The least controllable and observable can then be removed. As shown in Figure 1-2, balancing has the unfortunate result of turning a sparse matrix into one fully populated, but the reduction in number of states offsets this disadvantage. The fully populated balanced matrix is also better numerically conditioned than the sparse diagonal.

Despite its popularity, gramian balancing is difficult to implement on large-order models, if indeed the routine will run at all. Numerical ill-conditioning and the inversion of very small singular values can affect the accuracy of the final balanced model. Gregory recommends several approaches that can be taken, and Laub remarks on the difficulty of solving for the gramians. Neither of these papers explicitly provide any extensions on the basic algebraic transformation. Mallory [27] describes a method whereby large models can be balanced by removing some of the smallest singular values. This approach, termed *balanced truncation*, will be examined here. In order to improve the overall numerical quality of the system, several other steps will be discussed that improve numerical conditioning, or are required for gramian balancing. Once the system is balanced, additional reduction can still take

place. Examples of the resulting transfer functions will be provided.

## 1.4 Thesis Overview

This thesis describes the steps through a dynamic disturbance analysis, with emphasis on the model quality and conditioning, balancing, and reduction. An outline of the steps is provided in Figure 1-3. The chapter number that is associated with each block is given on the side. The first step, building a finite element (FE) model of a space observatory, involves taking the spacecraft design and modeling it using nodes, beams, plates, et cetera. This was done in all cases at the respective NASA facilities. The basic architecture of all three observatories, NGST, SIM, and Nexus, as well as a description of their FE models, is provided in Chapter 2. The mass  $M$  and stiffness  $K$  matrices that result are run through the basic dynamic eigenproblem in order to find the natural frequencies  $\omega$  and the structural modeshapes  $\Phi$ . Some basic properties of the eigenproblem are provided in Chapter 3. Once damping is added to a system, the equations of motion can be cast into first order, state-space form, where the spacecraft dynamics, inputs and outputs are described by Equation 1.1.

As well as reviewing the eigenproblem, Chapter 3 also describes two popular linear algebra routines: the Singular Value Decomposition (SVD) and the Lyapunov equation. These routines are important for both the gramian balancing algorithm and for one type of disturbance analysis, so their basic properties and applications should be understood. In the case of the Lyapunov equation, a faster solver is also proposed that makes use of the structure of the  $A$  matrix.

Chapter 4 continues with the spacecraft analysis by performing some basic and necessary routines on the spacecraft model to prepare it for balancing. The idea of model quality management is emphasized here, where numerical conditioning, the nature of the inputs and outputs, and checks that can be run to track model quality are proposed. These steps are critical for the balancing of a large model.

A description of gramian balancing follows in Chapter 5. Because of the difficulties involved in inverting highly ill-conditioned matrices, balanced truncation is used. It is first necessary to define a tolerance for this truncation before the model can be balanced. The model is then reduced to a desired level; any one of several methods can be used to

determine the level of reduction. The balanced and reduced models can be compared to the original. If numerical difficulties either prevent the model from balancing or fail to produce an acceptable balanced model, a new truncation tolerance can be set and the balancing routine run again.

Once the model is successfully balanced and reduced, the integrated model can be assembled. This first involves preparing models that describe the disturbance sources. Reaction wheels will be used as the exclusive disturbance source for this analysis; an overview of their behavior and models is provided in Chapter 6. Models are prepared where wheel speed is treated as a stochastic random variable, and for actual discrete wheel speeds. Attitude control systems and optical control loops are added to the system in Chapter 7. For these analyses, no additional reduction is performed on the closed-loop models. As the flow diagram shows, however, ideally the entire closed loop system would be reduced. A first round of balancing and moderate reduction should be performed on the open loop system to provide numerical stability. The control loops can be closed, and the system reduced down to the desired model size.

A description and the implementation of the disturbance analysis is included in Chapter 7. The first disturbance analysis performed for the Nexus testbed is shown and the results are compared to its successor, NGST. This is followed by the first disturbance analysis performed for the newest SIM model, version 2.2. Finally, in Chapter 8, the results of the SIM analysis are used to compare the version 2.2 model to the original SIM Version 1.0 model, whose analysis was performed in [22].

Chapter 9 concludes the thesis by describing the next steps in a dynamics analysis of a space observatory, and suggesting future work for the model quality control efforts.

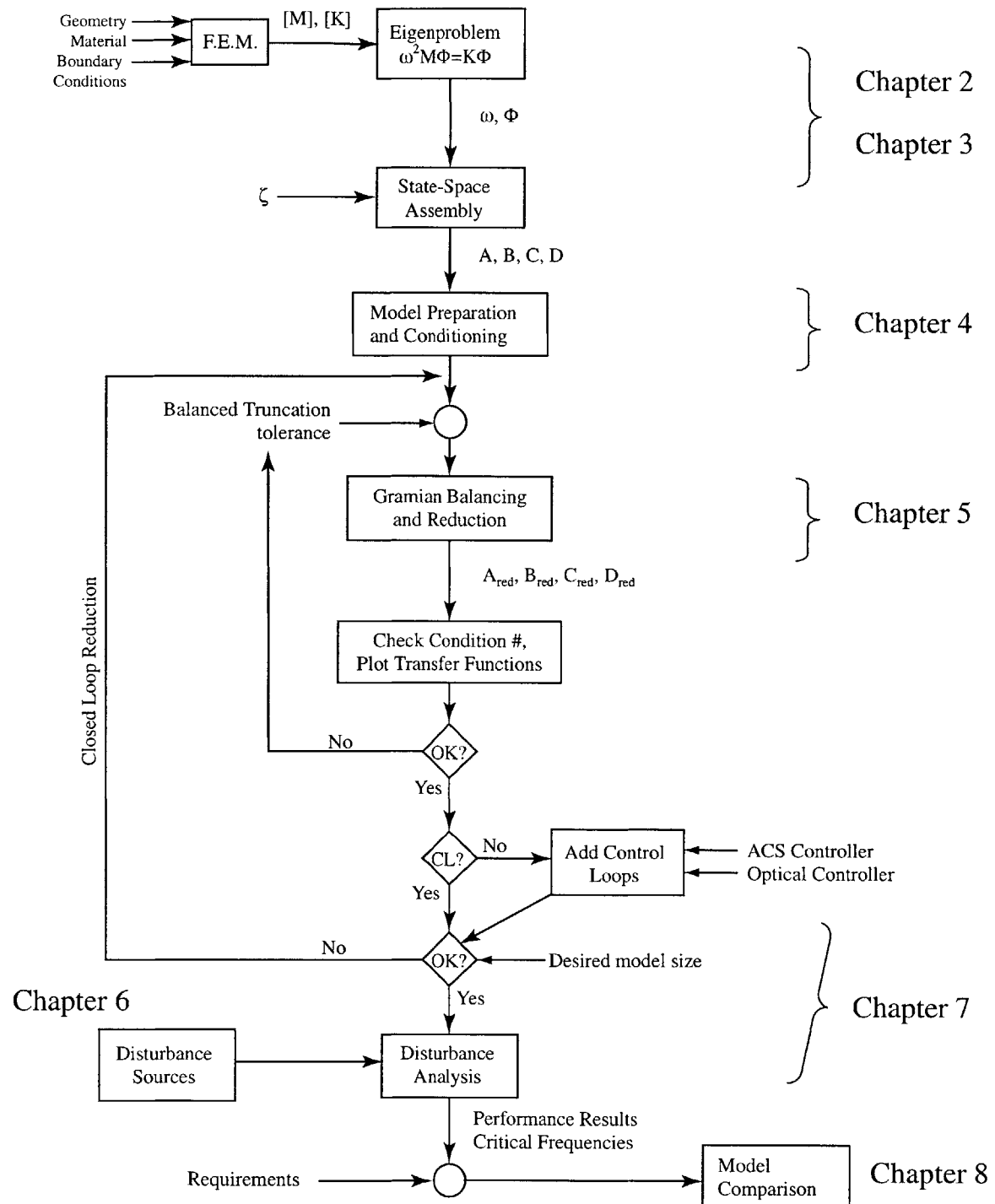


Figure 1-3: Thesis Outline



## Chapter 2

# Space Telescope Descriptions

As part of its Origins Program, NASA centers are currently developing several advanced space telescopes far more powerful and capable than the Hubble Space Telescope (HST) now in orbit. These spacecraft generally have more stringent pointing and wave front requirements than HST and will rely upon technology still in development including lightweight mirrors, optical interferometry in space, and advanced optical controls, to meet these goals.

Two of the space telescopes are being developed by NASA Goddard. The Next Generation Space Telescope (NGST) is an infrared observatory currently scheduled to launch around 2009. To alleviate some of the unknowns in the wave front control and mirror technologies of this mission, Goddard engineers were concurrently developing the Nexus spacecraft<sup>1</sup>. Nexus was to have been a smaller space telescope that would be used as an on-orbit testbed. It has many of the same features as NGST, including lightweight mirrors and a large sunshield, but its primary mission was to demonstrate technologies and verify models that will be used for NGST. The third spacecraft, the second true Origins spacecraft, is the Space Interferometry Mission (SIM) being designed at JPL. As the name implies, SIM is an optical interferometer, to be launched around 2006.

The spacecraft models were all acquired from the respective NASA centers, and all went through the reduction routine described in Chapter 5. A brief overview of each spacecraft's architecture and model is presented here.

---

<sup>1</sup>Nexus was cancelled in December, 2000 in a rescoping of the NGST mission.

## 2.1 Next Generation Space Telescope (NGST)

NGST is being planned as the next large observatory after Hubble. It was initially proposed by the HST and Beyond Committee to search in the “Dark Zone” of time between 100 million and 1 billion years after the Big Bang [47]. Hubble’s optics can resolve adolescent galaxies that formed several billion years after the Big Bang, and the Cosmic Background Explorer (COBE) produced images of the structure of the universe 300,000 years after the Big Bang. To observe the beginnings of galaxy formation between these times, however, a new spacecraft is needed.

The light from these early galaxies has been red-shifted because of their recession away from Earth, so their wavelengths are in the infrared. It was decided that an infrared telescope, cooled to below 50K with a primary mirror diameter of at least 4 meters, was required to examine this period of galaxy formation. The proposed orbit was around the L2 Lagrangian point, located on the line extending from the Sun through the Earth, on the anti-Sun side of the Earth (Figure 2-1). This distances the telescope from the gravity and atmospheric effects around Earth, plus it isolates the thermal effects of the Sun, Earth, and Moon to one side of the spacecraft.

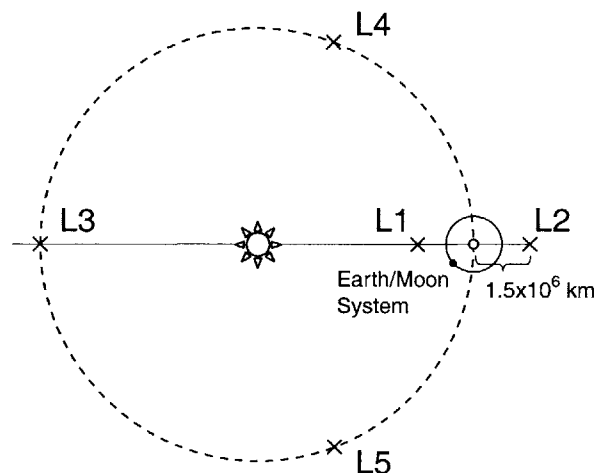
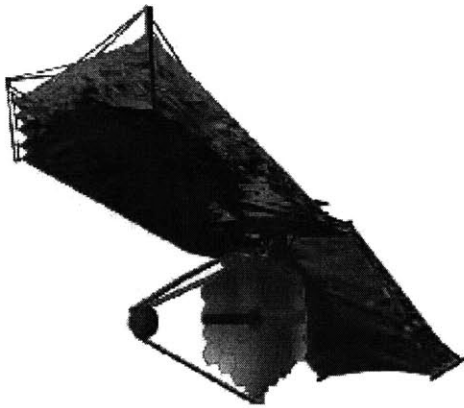


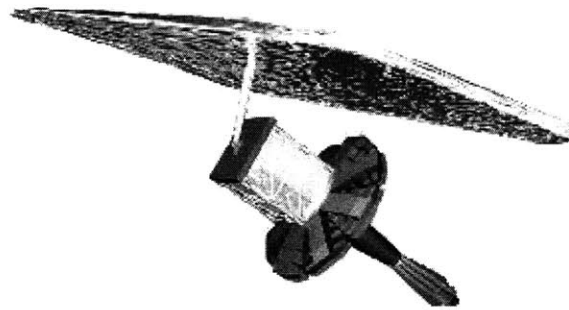
Figure 2-1: Earth-Sun Lagrangian points. NGST is planned to orbit L2.

NASA Goddard began to design a possible architecture for this Next Generation Space Telescope, as did teams from Lockheed Martin and TRW/Ball Aerospace. Each of their designs is illustrated in Figure 2-2. The actual telescope will be designed and built by either Lockheed Martin or TRW, whoever wins the final down-select, scheduled for summer

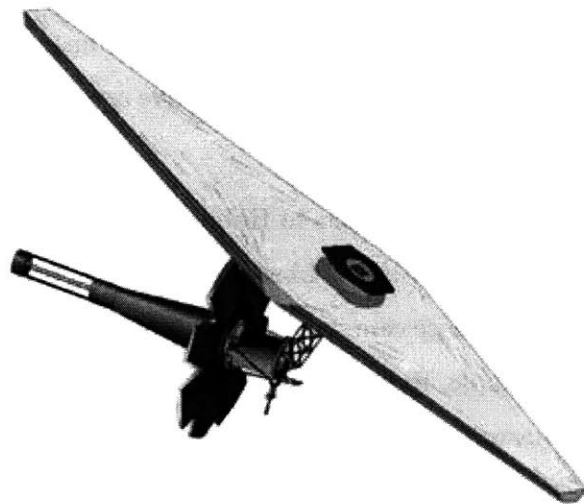
2001. The purpose of the Goddard “Yardstick” design is to explore technical issues of the spacecraft including thermal design, disturbance sources, and wave front control. It also allows NASA engineers to develop requirements and error budgets, and to develop tools with which to examine the final contractor design. MIT was given this Yardstick model to examine. The initial DOCS analysis for the Yarkstick was performed by de Weck in [14].



(a) TRW/Ball Aerospace



(b) Lockheed-Martin



(c) GSFC Yardstick

Figure 2-2: NGST designs proposed by the contractor candidates and GSFC [5]

### 2.1.1 NGST Mission Architecture

Each of the three NGST designs employs a primary mirror (PM) over three times as large as Hubble's: 8 meters compared to 2.4 meters. Current plans are to launch NGST on an Atlas IIAS-type booster [5]. Since such a large aperture would not fit within its launch shroud, the Yardstick primary mirror consists of 8 separate petals that would be stowed against the spacecraft during launch, and would deploy on orbit. They direct the science light to a secondary mirror located at the end of the long boom seen in Figure 2-2(c), which then directs the light to science instruments. These include a Near Infrared (NIR) instrument (wavelength  $\lambda = 1 - 5\mu m$ ), and a Mid Infrared (MIR) instrument ( $\lambda > 10\mu m$ ) [47].

The thermal environment of the optical components is one of the leading drivers in the spacecraft design. The Optical Telescope Assembly (OTA), which consists of the primary and secondary mirrors, along with the Integrated Science Instrument Module (ISIM), must remain cooled between 30-50K. To achieve this, NGST makes use of a large sunshield. The telescope remains in the cool shadow of this sunshield, while the bus instruments, and attitude and propulsion systems remain on the warm side. Mass and volume considerations require that the sunshield be lightweight; this also means that it will be very flexible, with a fundamental frequency around 0.3 Hz. This means that NGST will be much more dynamically active at low frequency than is HST. The MIR instrument will require further cooling to 6-8K. This will have to be achieved using active cryocoolers, despite the harmonic disturbances they transmit to the spacecraft.

The requirements for NGST are similar to Hubble (see Table 2.1); the challenge is that NGST is a much more flexible spacecraft. Line-of-sight (LOS) RMS relates to the pointing accuracy of the center of the science camera. The allowed jitter in the LOS is approximately 1/10 the resolution. For example, Hubble's resolution is 0.06 arcseconds [asec], and the LOS jitter requirement is 0.007 asec, or 7 milli-arcseconds (mas) [1]. The resolution for NGST will be 0.05 asec, with an associated jitter requirement of 5 mas ( $1\sigma$ ) [36]. The RMS wavefront error (WFE) is a measure of the different lengths traveled by two rays of light that enter the optics at the same time. The differences in pathlength can be caused by either static effects from aberrations in the mirror, quasi-static effects such as thermal warpage, or dynamics effects from vibrations. The WFE requirement for NGST in units of wavelength is  $\lambda/14$ , or  $0.157\mu m$  at 2.2 microns wavelength.

In order to achieve this stability, active optical control of wavefront and pointing is required. Although optical control loops have been written for NGST, they are not used here. All of the NGST transfer functions that will be shown in this work are entirely in the open loop, so will not meet optical requirements. The purpose of the NGST disturbance analysis will be to determine the dynamic similarity of that observatory with Nexus. Since the Nexus model will not be closed loop either, the absence of a controller should not be a factor.

Table 2.1: Comparison of telescopes

	Hubble	NGST
Aperture [m]	2.4	8
Wavelength $\lambda$ [ $\mu\text{m}$ ]	0.11 to 2.6	1 to 5
Resolution $\theta$ [asec]	0.06	0.05
LOS requirement (RMS) [mas]	7	5
WFE Requirement (RMS) [ $\mu\text{m}$ ]	0.0272 @ $\lambda=0.633 \mu\text{m}$	0.157 @ $\lambda=2.2 \mu\text{m}$

### 2.1.2 NGST Structural Finite Element Model

Several finite element (FE) models were created for NGST using JPL's Integrated Modeling of Optical Systems (IMOS) modeling software. IMOS is a MATLAB based toolbox that builds a FE model using elements similar to those found in Nastran, but that allows the entire modeling process to remain in the MATLAB environment. Several models were created, including `ngst810`<sup>2</sup>, a 109 node model used in the previous MIT analysis [14]. This was based on the `ngst603`<sup>3</sup> model, with 995 nodes. A variation of this model, `ngst603ss`, was used in place of the current Nexus model for disturbance studies, after Nexus underwent significant design changes. (explained in detail in Section 2.2). `Ngst603ss` includes an more detailed model of the sunshield, and as a result has many more low-frequency modes than its predecessors.

`Ngst810` had been designed as a small model that could be worked with quite easily; few numerical problems were encountered with mathematical routines, and the turnaround time between analysis and design iteration could be reduced to hours. No additional re-

---

<sup>2</sup>Created on 8/10/98

<sup>3</sup>Created on 6/03/97

duction beyond simplifying the FE model was performed. The purpose of the balancing and reduction framework is to take a large state space representation of a spacecraft and reduce it to a size that allows fast and accurate results. For the purpose of testing these algorithms, a larger, more complex model is preferred to begin with. Ngst603ss better suits this purpose and will be used in subsequent chapters.

The ngst603ss model is shown in Figure 2-3. Most of the detail has gone into the OTA, with a simple Spacecraft Support Module (SSM) and ISIM comprised of several bar elements and concentrated masses. All of the reaction wheels are assumed to be collocated at the SSM node (node #10291). For a disturbance analysis, this means that the individual disturbance contributions from each wheel must be summed together, and the disturbances from the entire assembly applied at that single node (see Section 6.1). The cryocooler disturbances, three forces and one torque [14], act at the ISIM node where the MIR instrument would be located (node #825).

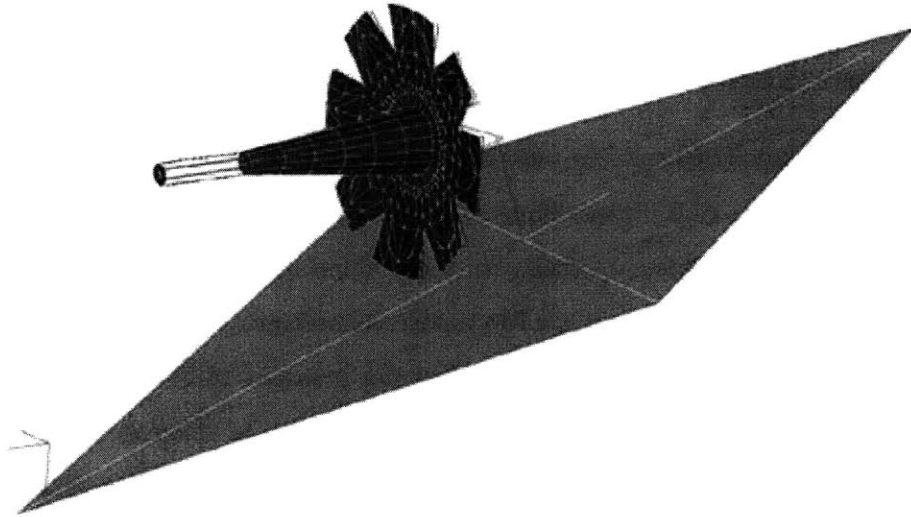


Figure 2-3: ngst603ss FE Model

The first six modes of this model are rigid body modes, three translational and three rotational. The lowest flexible frequency is the first sunshield mode at 0.301 Hz, and most of the lower frequencies belong to sunshield modes [24]. Even these low modes are expected to drop in frequency with more realistic modeling of the sunshield [36]. The first bending mode of the Secondary Mirror support structure is at 4.9 Hz, and the first Primary Mirror

mode is at 5.1 Hz. These imply a much more flexible spacecraft than Hubble. Whereas Hubble is stiff enough such that it can rely entirely on its reaction wheels and rigid body controllers for optical pointing, NGST will require active optical actuators. Once the finite element model is prepared, an optics model is required to compute the optical performances.

### 2.1.3 NGST Optical Performance

The FE model of NGST provides nodal displacements. Although useful for determining strains or other displacement-dependent values, these do not provide much insight as to whether the spacecraft meets its optical requirements. These requirements were mentioned at the start of this subchapter: LOS jitter at or below 5 mas and RMS WFE of  $\lambda/14$ .

The integrated model determines these optical metrics using linear combinations of nodal displacements and rotations from distinct nodes in the FE model that represent optical components (mirrors and optical instruments). These displacements and rotations are multiplied by the optical sensitivities to the movements. These sensitivities are found using MACOS (Modeling and Analysis for Controlled Optical Systems [10]), a ray-tracing program designed originally at JPL. The wavefronts for representative light rays and the image centroid in the x- and y-axes are found as each reference node is perturbed one degree of freedom at a time. Two sensitivity matrices are thus computed, the centroid linear sensitivity matrix  $\partial C/\partial u$  and the wavefront linear sensitivity matrix  $\partial W/\partial u$ , where  $u$  is a vector of generalized displacements from the reference nodes. These matrices allow calculation of wavefront and centroid RMS for a given  $u$  displacement vector.

$$\begin{aligned} C &= C_o + \frac{\partial C}{\partial u}u \\ W &= W_o + \frac{\partial W}{\partial u}u \end{aligned} \tag{2.1}$$

Redding, in Reference [40], provides an in-depth discussion of how the sensitivity matrices are computed.

The MACOS model provided for NGST uses eleven reference nodes: eight at the centers of each primary mirror (PM) petal plus one at the center of the entire PM structure (nodes #900-908), one at the secondary mirror (node #829) and one at the ISIM (node #825). These nodes are multiplied by the sensitivities to provide two centroid values for  $x$  and  $y$  in mas (so that  $\partial C/\partial u$  is a  $2 \times 11$  matrix). They also provide 2440 WFE's in nanometers for a total of 2442 performance outputs (so that  $\partial W/\partial u$  is  $2440 \times 11$ ). In the case of the WFE

sensitivity matrix, it should be noted that there are more columns than rows. This means that the columns in the matrix are not linearly independent, or the column space has not been reduced to its basis vectors [48]. Reference [13] provides a technique to reduce these matrices to a minimal basis using the singular value decomposition method. This allows the same amount of information to be examined using smaller matrices.

Using the structural FE model along with the optics model, an integrated disturbance to performance model of NGST can be built. This model will be cast into state-space form and reduced by the techniques described in Chapter 5. After that the DOCS tools can be applied. Because of the technical challenges associated with NGST, Nexus was to have been used as a validation testbed. It will be described next.

## 2.2 Nexus

The Nexus space telescope was being developed by NASA Goddard as a precursor and technology demonstrator mission for NGST, many of whose technologies have never been demonstrated in space. Several critical areas of uncertainty have been recognized for NGST [11]. They include fabrication and verification of the OTA, integration of the cryo-cooled instruments with the spacecraft thermal design, uncertain dynamics of the flexible sunshield, and wave front sensing and control (WFSC). To mitigate the risks associated with these uncertainties, Goddard engineers planned to build and fly Nexus. It would be a smaller telescope than NGST, but have many of the same features such as ultra-lightweight mirrors with image-based WFSC; a deformable mirror to compensate for wave front errors; a deployable, flexible sunshield; cryogenic actuators; and deployable optics (primary mirror).

Several flexible testbeds have already been flown in space, including the Middeck 0-gravity Dynamics Experiment (MODE) [8] and the Middeck Active Control Experiment (MACE) [30], both supported by MIT and launched in the Shuttle middeck. The Interferometry Program Flight Experiments (IPEX I&II) free-flying testbeds were designed by JPL to study microdynamics of structures in space [26]. All of these were simple truss/boom structures. Nexus would be a full-fledged space telescope. The quality of its images would only have been on-par with Hubble, but the optics and spacecraft would be a technical validation of segmented infrared telescopes. The spacecraft would be instrumented with sensors and actuators (including accelerometers, shakers, heaters, and temperature gages),



to provide a complete dynamical and thermal characterization. This would allow, for example, verification of disturbance models (reaction wheels and cryocoolers) developed at MIT.

### 2.2.1 Nexus Mission Architecture

Nexus went through several design changes as the mission was refined. Because all of the MIT analyses were performed on the older version of Nexus, also dubbed Horizon, this will be described first. The most current version, designed to more closely approximate NGST, will be described thereafter.

A partnership between the space science and Earth observing teams at Goddard led to the first Nexus design. The Earth Observing 3 (EO3) Redeye mission was combined with Nexus to create the Horizon spacecraft (Figure 2-4). Initial plans were to launch Horizon from the Space Shuttle in LEO, and boost it to GEO so that the telescope would not be disturbed by the changing thermal environment of low Earth orbit. For stellar observation mode, Horizon was to have an accuracy of 2 asec and jitter of 1 asec. For Earth observing mode accuracy was to be 10 asec and jitter  $<0.5$  asec [42].

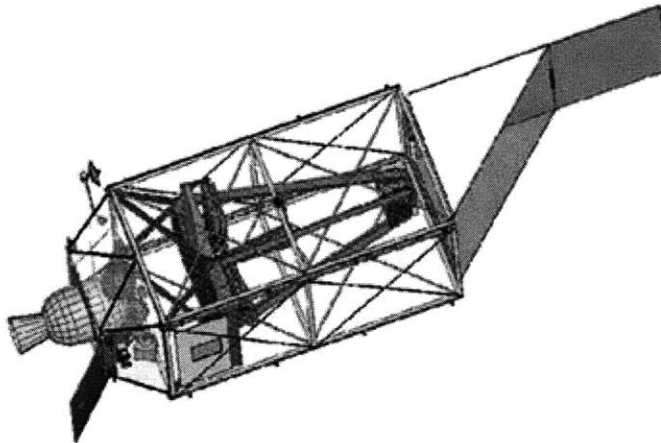


Figure 2-4: Original Nexus/Horizon spacecraft (image from NASA Goddard Space Flight Center [38])

The primary mirror was made of three petals, similar in design to the eight petals on NGST. There was no sunshield, so the lowest structural mode was an order of magnitude higher in frequency than on NGST. Baffles covered by thermal blankets surrounded the entire OTA structure, and a door at the top of the baffles would be opened on-orbit to

allow light in. The lack of sunshield and rigid structure meant that Horizon would be dynamically stiffer than NGST. No cryo-coolers would be used, so their model validation and disturbance effects could not be examined. There would be four reaction wheels to maintain attitude and perform slews.

After funding difficulties were encountered, the EO3 and Nexus missions were separated. Nexus was redesigned to look like a 1/3-scaled model of NGST (compare Figures 2-5 and 2-2). The architecture included a flexible sunshield and cryo-cooled instruments as described in the previous section. The three-petal primary mirror from Horizon was retained. Its effective diameter was 2.8 meters. The baffles around the mirror were removed. The requirements are less stringent than NGST: 15 asec pointing accuracy with 1 asec jitter over 1000 seconds [43], with only 0.5 asec jitter allocated to reaction wheel disturbances.

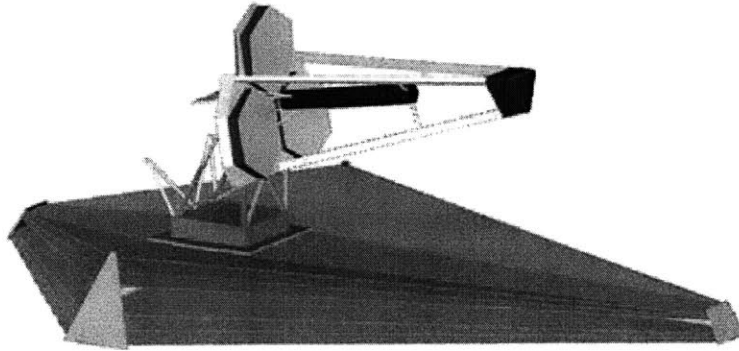


Figure 2-5: Current Nexus design (image from NASA Goddard Space Flight Center [11])

Plans were to launch Nexus to L2 on either a Delta II or Delta IV expendable booster. This provided the most similarity between the planned operating environment of NGST. Figure 2-6 shows the spacecraft in its stowed configuration, and gives an idea of how compactly NGST must be stowed.

### 2.2.2 Nexus Structural Finite Element Model

The only available FE model for Nexus was the original Nexus/Horizon model, displayed in Figure 2-7. This was used for an initial disturbance analysis described in Chapter 7. Later examinations of how the new Nexus design would behave used the `ngst603` model.

The Horizon model contains 2681 nodes. The OTA nodes are particularly dense as the OTA model was built for thermal as well as dynamical analysis. This disparity in nodal

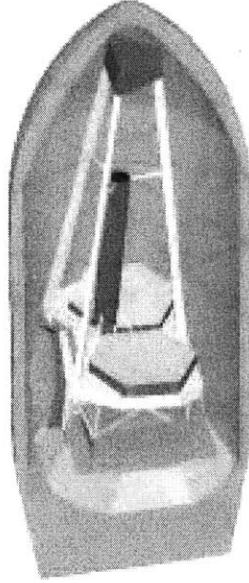


Figure 2-6: Nexus stowed configuration in a Delta II fairing. Note the stowed deployable primary mirror petal. (image from NASA Goddard Space Flight Center [11])

density is unwarranted for a dynamics solution, and the size of the corresponding  $M$  and  $K$  matrices would greatly increase the computational cost of a physical parameter sensitivity analysis. A smaller model was created by removing modes from the spacecraft. The number of modes was reduced from 2681 to 779 nodes. The FE pre-processor program FEMAP was used for this purpose. The primary mirror nodes after reduction are shown in Figure 2-8. The modal frequencies of the two models are plotted over each other in Figure 2-9. This shows that the dynamics remain fairly constant. The FEMAP model was then converted to NASTRAN for a normal modes analysis. The MATLAB program `nas2imos.m` can be used to convert the NASTRAN `.dat` file to IMOS format. From there the  $M$  and  $K$  matrices can be built and used in the MATLAB environment.

Reaction wheel disturbances enter this model through four separate nodes (#'s 634, 640, 688, 694), representing each of the four reaction wheels. This differs from the NGST model with one node representing all of the reaction wheels. Nodes representing individual optical elements are included for the optics model.

The first flexible mode is at 1.9 Hz compared to 0.2 Hz for NGST. The structural differences will also be apparent in the disturbance analysis in Section 7.3.

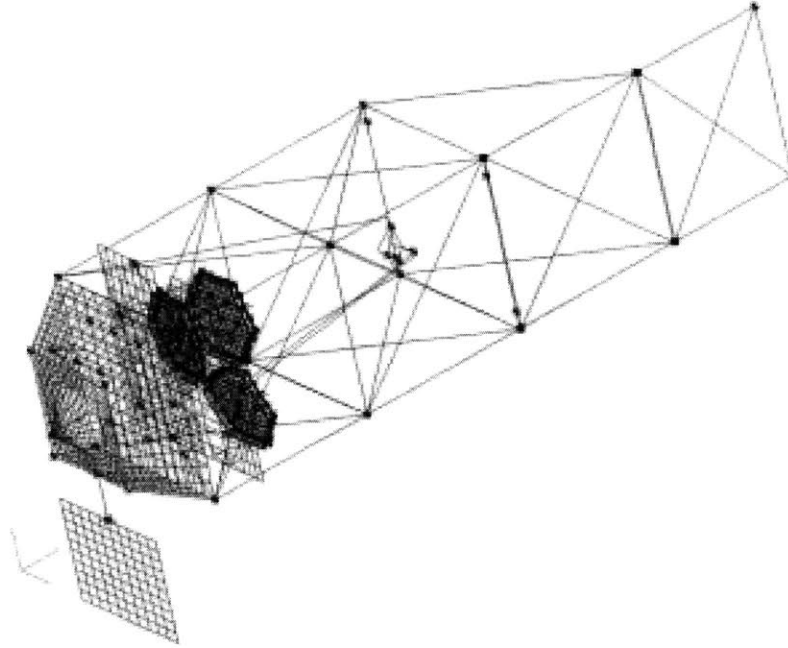


Figure 2-7: Nexus/Horizon Finite Element Model

### 2.2.3 Nexus Optical Performance Metrics

A JPL-built MACOS optics model was used to compute performances for Nexus given the structural FE displacements. The initial disturbance analysis, using the 2681 node model, computed only three performance metrics using six degrees of freedom at each of four nodes. The node at the secondary mirror and three nodes from the primary mirror petals, one at the center of each, were multiplied by the optical sensitivities to the motions of those points. The performance metrics were centroid jitter in both the  $x$ - and  $y$ -axes in meters, and the WFE of only one ray in meters.

Note that centroid jitter is given in units of length and not angle in the sky. To convert to arcseconds of angle requires the plate scale of the CCD detector, missing here. The plate scale specifies the angle in the sky that each pixel can view, and since the jitter is actually the movement of a guide star or extended source image over the pixels in the plane perpendicular (approximately) to the incoming light, it can be described using units of length. In order to specify the pointing stability of the telescope however, the movement of the pixels is converted to the angle affected by that movement.

A more complete analysis requires the plate scale and use of more than one ray for a WFE analysis. The integrated model can still be used to show general behavior of the

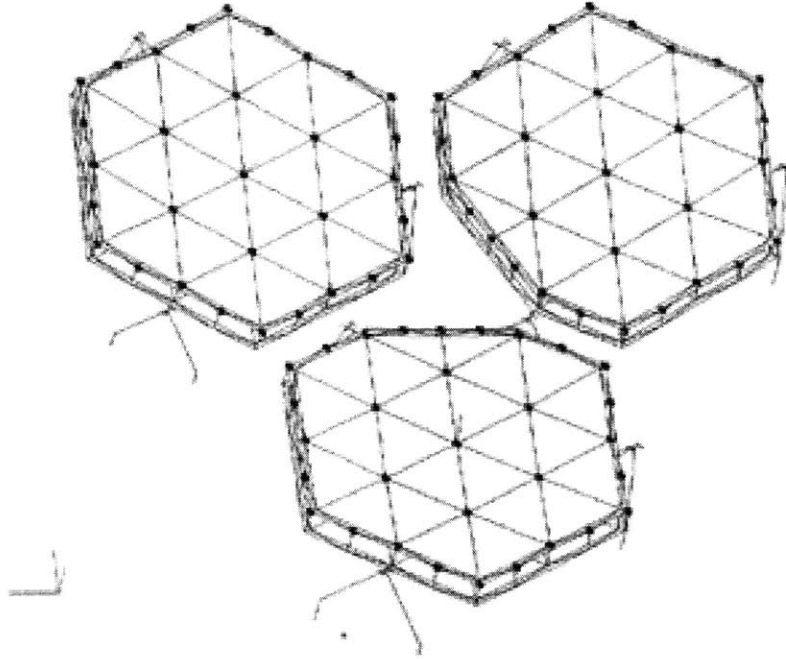


Figure 2-8: Primary Mirror of the Reduced Nexus/Horizon FEM

Nexus/Horizon model, and can compare the dynamics of Nexus/Horizon with those of NGST. Since the full-order model will be used in the disturbance analysis of Chapter 7, the integrated model will not be taken through the reduction routines of Chapter 5.

The next and final spacecraft considered will be a visual interferometer, the Space Interferometry Mission.

## 2.3 Space Interferometry Mission (SIM)

The final spacecraft examined is the Space Interferometry Mission being designed at JPL (Figure 2-10). SIM will be the first space telescope to employ optical interferometry for precision astrometry, or the measurement of the exact position of stellar objects. It will be able to detect the position of a stellar object to about  $4 \mu\text{as}$  (micro-arcseconds), or about a billionth of a degree [7, 49]. This will give scientists a far greater understanding about the formation of planets and galaxies. For example, by detecting the wobble of stars relative to reference stars, SIM will be able to detect extra-solar planets smaller than those found thus far; it should even be able to determine the existence of terrestrial planets only several times larger than Earth orbiting nearby stars [49]. It can use parallax, or triangulation from observing locations on opposite sides of the sun, to determine the distance to any star in

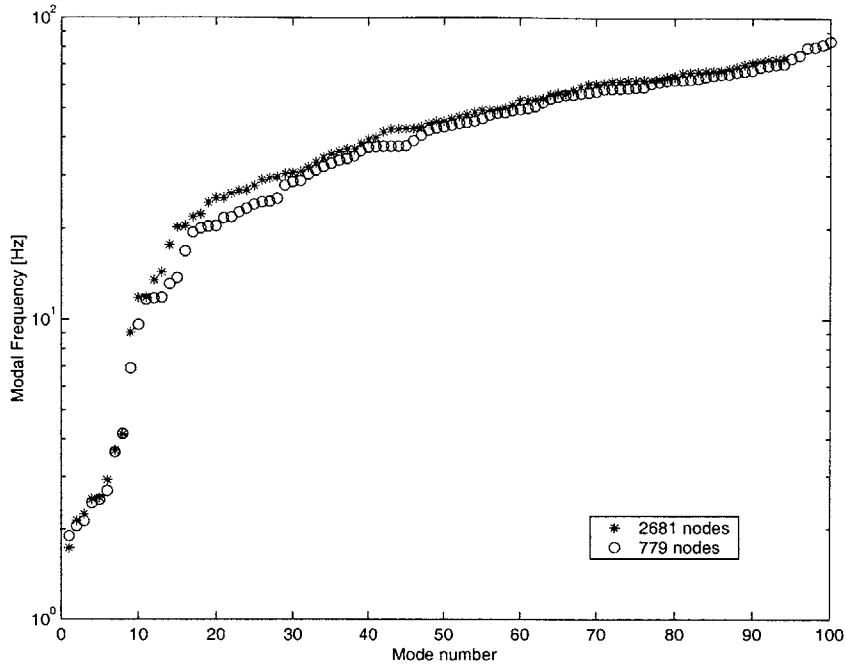


Figure 2-9: Comparison of modal frequencies between high- and low-fidelity Nexus/Horizon models

our galaxy brighter than  $18^{th}$  magnitude. Observations of distant galaxies will enable more precise estimates of the Hubble constant and the age of the universe.

Not only will SIM return valuable scientific data, but it will also demonstrate space-based interferometry for a new generation of telescopes. For example, the Terrestrial Planet Finder (TPF) [37] will rely on destructive interference of science light to block the light of a star, allowing the habitable range for terrestrial planets to be observed. TPF and its kin may rely on light gathered from multiple spacecraft moving in formation. SIM will still use telescopes located on a single spacecraft.

### 2.3.1 SIM Mission Architecture

At its core SIM will consist of a 10 meter baseline Michelson interferometer [7, 6]. Eight telescopes, called siderostats, will be placed linearly along the main structure of the spacecraft, the Precision Support Structure (PSS). The light from any combination of two telescopes can make an interferometer. The collected light is passed through a switchyard to determine which light beams will be combined. Optical delay lines are used to ensure the distances traveled by two coplanar light rays are equal. The light is finally directed to beam combiners for interference. The furthest two telescope bays will nominally make up the science

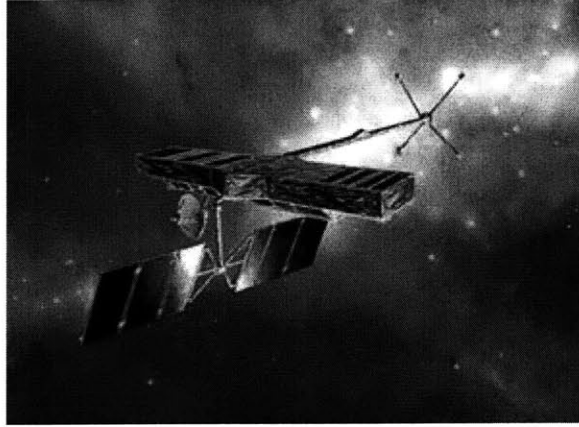


Figure 2-10: An artist's drawing of the Space Interferometry Mission [6]

interferometer with the full 10 meter baseline (distance between the mirrors). Two other pairs of telescopes make up two guide interferometers. This architecture allows a multitude of baselines by changing which telescopes are used as the science interferometer<sup>4</sup>. The remaining two telescopes are kept in reserve<sup>5</sup>.

Each telescope bay will contain a gimballed siderostat mirror to aim the science light at 33 cm primary mirrors. They reflect the light to secondary mirrors, which reflect a 3 cm collimated beam of light to the switchyard. Each interferometer takes a beam from either side of the PSS, passes a beam from only one side through an optical delay line, and combines both. White light fringes should occur when the pathlengths from either side are equal. The optical delay line controls the pathlength using a combination of voice coils and piezoelectric translator (PZT) mechanisms for varying stroke requirements [21].

For astrometry, the main purpose of SIM, the exact position of a science object is found by knowing the angle between the incoming science light and the physical baseline vector, labeled **B** in Figure 2-11. The *physical baseline* is the distance between a reference point, or fiducial, on each mirror. This is determined using an internal metrology system of laser beams which are sent from the optical assembly and bounced off of corner cube mirrors physically located on the siderostat mirrors.

The external delay in light collected by the siderostat on the left in Figure 2-11 is  $B \cos \theta$ .

<sup>4</sup>The architecture described is known as SIM Classic. An alternate architecture known as Son of SIM clustered the mirrors for each interferometer at either end of a long spacecraft. This allows the relative angles between baselines (science and the guides mirrors) to be more easily determined. However it would be more difficult to change baseline lengths. For this and other reasons, SIM Classic was chosen over Son of Sim.

<sup>5</sup>The exact number of reserve telescopes has changed. In this configuration there are two.

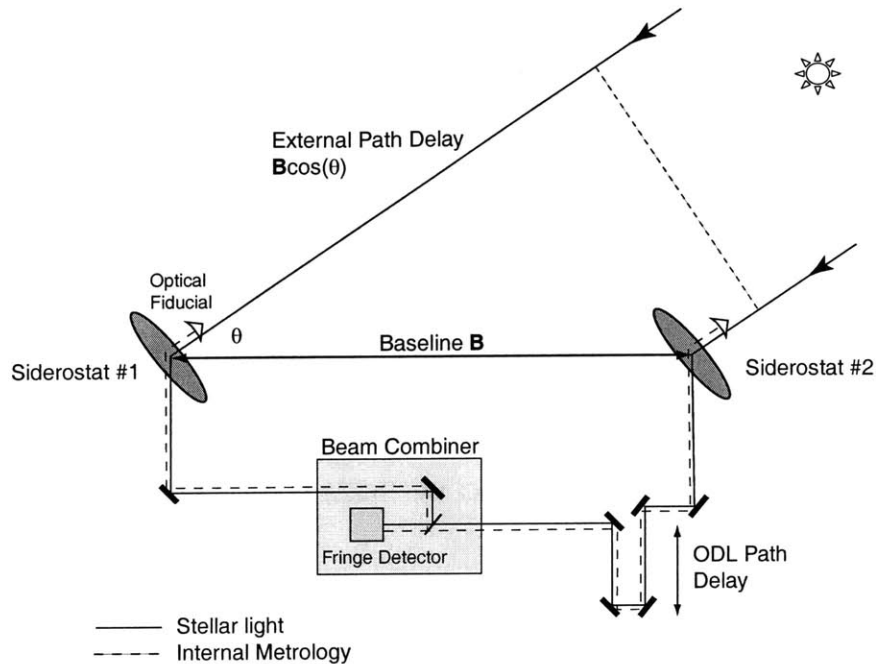


Figure 2-11: Basic elements of the SIM interferometer

Knowing the difference in pathlength to within a fraction of a wavelength of light will allow the angle  $\theta$  to be found. The next step in determining the exact position of a stellar object is to find the angle between it and a reference star. The two guide interferometers are used for this purpose. They will each be fixed on nearby reference stars, and a similar angle  $\theta$  found for each. The final step is to accurately determine the relative orientations of all three baselines. This is done using the external metrology system. Lasers are bounced off of fiducials located on the external metrology boom, directly in front of the spacecraft (see Figure 2-12), and the fiducials on the siderostat mirrors. By determining all of the distances between mirrors, the orientation of the scientific baseline and the relative position of the science object are determined.

All of this requires nanometer optics stabilization and picometer measurement of the wavefront. Fast steering mirrors (FSM) are used to control the tilt of the light beams. The voice coils and PZT actuators in the optical delay lines previously mentioned will control the pathlength (Figure 2-13).

The avionics and attitude control subsystems are contained in two "backpacks" located directly below the PSS. One backpack contains the optical instruments and sensors, and the other contains the spacecraft subsystems. SIM is supposed to be launched on a Delta III in 2005 to an Earth-trailing heliocentric orbit. The spacecraft model is considered next.



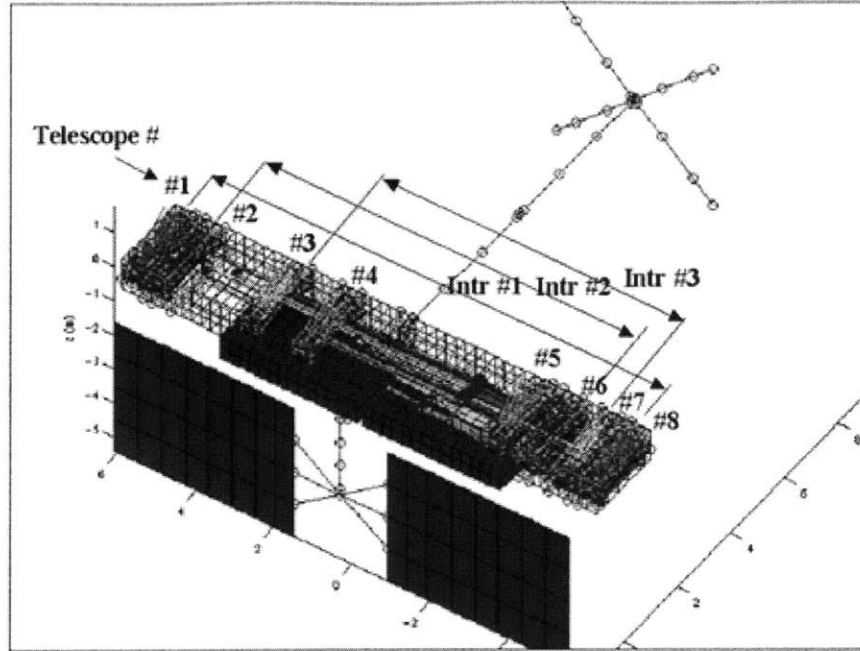


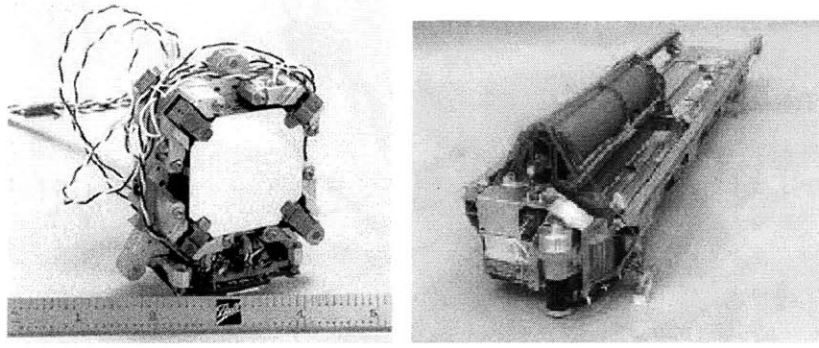
Figure 2-12: SIM Finite Element Model

### 2.3.2 SIM State-Space Model

The finite element model for the entire SIM spacecraft was assembled from component FE models built at JPL, TRW, and Lockheed Martin. Figure 2-12 shows the complete spacecraft. As shown in the figure, the outermost telescopes (#1 and #8) comprise interferometer #1, the science interferometer. Telescopes #2 and #6 make interferometer #2 (the Guide 1 interferometer), and telescopes #3 and #7 make interferometer #3 (the Guide 2 interferometer). The last two telescopes are to be held in reserve. The model is more detailed than either NGST or Nexus. Altogether there are over 27,000 degrees of freedom in the model, which corresponds to approximately 4500 nodes.

Because of the size of this model, the actual finite element  $M$  and  $K$  matrices were not used by MIT. Rather, prepared state-space models were provided by JPL. SIM Version 2.0 was provided in the form of a MATLAB .mat file, `classic_integratework_nom.mat`<sup>6</sup>. It included  $A$ ,  $B$ ,  $C$ , and  $D$  matrices with 2162 states, 20 disturbance and actuator inputs, and 103 performance and sensor outputs. The model was in second-order form, where the  $A$  matrix was arranged as follows.

<sup>6</sup>Version 1.0 was a 1300 node SIM "stick" model that was examined by Gutierrez in the first SIM disturbance/sensitivity analysis [22].



(a) Fast Steering Mirror [3]

(b) Optical Delay Line [21]

Figure 2-13: Devices used in SIM's optical train

$$A = \begin{bmatrix} 0 & I \\ -\Omega^2 & -2Z\Omega \end{bmatrix} \quad (2.2)$$

$\Omega$  is a diagonal matrix of modal frequencies and  $Z$  a diagonal matrix of damping coefficients. Damping varies between  $\zeta = 0.001$  to  $\zeta = 0.09$ , though the majority of states have  $\zeta = 0.0025$ . The model was open loop for both optics and attitude control system (ACS) and no disturbances states had been appended to the model.

The inputs include six reaction wheel disturbances and both voice coil and PZT stack actuators on each of the four interferometers (Science, Guide 1, Guide 2, and the spare). The outputs include optical pathlength differences (OPD) for both star and internal metrology, the external metrology pathlength, wavefront tilt angles at both the back end (WFT) and front end (FEC) cameras located in the siderostat bays for each of the eight telescopes, and rigid body spacecraft attitude angles and rates. The only inputs actually used were the six reaction wheel disturbances, listed in Table 2.2. As was done for NGST, the sum of the forces and torques from four reaction wheels were applied at a single node on the SIM model.

Of the 103 outputs, only 31 performances of interest were computed for the first three interferometers. The three attitude angles were also included to close a simple ACS controller for rigid body stabilization. All of the 34 outputs are listed in Table 2.3. The first six OPD outputs and the External Metrology Pathlength were treated as individual performance channels. The  $x$  and  $y$  WFT and FEC outputs from each interferometer were

Table 2.2: SIM v2.0 inputs for analysis

No.	Symbol	Description	Units
1	RWAFx	Reaction Wheel Assembly Force in x-direction	[N]
2	RWAFy	Reaction Wheel Assembly Force in y-direction	[N]
3	RWAFz	Reaction Wheel Assembly Force in z-direction	[N]
4	RWATx	Reaction Wheel Assembly Torque about x-axis	[Nm]
5	RWATy	Reaction Wheel Assembly Torque about y-axis	[Nm]
6	RWATz	Reaction Wheel Assembly Torque about z-axis	[Nm]

root-sum-squared (RSS) together to compute the final performance. This is illustrated in Equation 2.3.

$$\begin{aligned}
\sigma_{z,\text{Star DWFT \#1}} &= [\sigma_{z,7}^2 + \sigma_{z,10}^2 + \sigma_{z,13}^2 + \sigma_{z,16}^2]^{1/2} \\
\sigma_{z,\text{Star DWFT \#2}} &= [\sigma_{z,8}^2 + \sigma_{z,11}^2 + \sigma_{z,14}^2 + \sigma_{z,17}^2]^{1/2} \\
\sigma_{z,\text{Star DWFT \#3}} &= [\sigma_{z,9}^2 + \sigma_{z,12}^2 + \sigma_{z,15}^2 + \sigma_{z,18}^2]^{1/2} \\
\sigma_{z,\text{FEC DWFT \#1}} &= [\sigma_{z,19}^2 + \sigma_{z,22}^2 + \sigma_{z,25}^2 + \sigma_{z,28}^2]^{1/2} \\
\sigma_{z,\text{FEC DWFT \#2}} &= [\sigma_{z,20}^2 + \sigma_{z,23}^2 + \sigma_{z,26}^2 + \sigma_{z,29}^2]^{1/2} \\
\sigma_{z,\text{FEC DWFT \#3}} &= [\sigma_{z,21}^2 + \sigma_{z,24}^2 + \sigma_{z,27}^2 + \sigma_{z,30}^2]^{1/2}
\end{aligned} \tag{2.3}$$

An updated SIM model was also provided to MIT. SIM Version 2.2 included stiffened mirror mounts in the siderostats, and the stiffness of the external metrology boom root was changed. The state space model contained 2184 states. The inputs and outputs of interest remained the same as listed in Tables 2.2 and 2.3, which allows a comparison of results between this model and SIM Version 2.0. This comparison is included in Chapter 8.

The original SIM version 2.0 analysis is described in references [34] and [31]. Unit-intensity white noise, run through a band-pass filter, was injected into each of the RWA input channels in place of realistic reaction wheel disturbances. An updated analysis using SIM version 2.2 and realistic RWA models was presented to the SIM Technical Advisory Committee (SIMTAC) in October, 2000 [32]. This also included a discrete reaction wheel speed disturbance analysis as described in Section 6.1.

Table 2.3: SIM v2.0 outputs for analysis

No.	Symbol	Description	Units
1	Star Opd #1	Starlight Optical Pathlength Difference Int. 1	[nm]
2	Star Opd #2	Starlight Optical Pathlength Difference Int. 2	[nm]
3	Star Opd #3	Starlight Optical Pathlength Difference Int. 3	[nm]
4	Int. Met. Opd #1	Internal Metrology Pathlength Difference Int. 1	[nm]
5	Int. Met. Opd #2	Internal Metrology Pathlength Difference Int. 2	[nm]
6	Int. Met. Opd #3	Internal Metrology Pathlength Difference Int. 3	[nm]
7	Star X WF1 Tilt #1	Starlight Wavefront Tilt X-axis Side 1 for Int. 1	[asec]
8	Star X WF1 Tilt #2	Starlight Wavefront Tilt X-axis Side 1 for Int. 2	[asec]
9	Star X WF1 Tilt #3	Starlight Wavefront Tilt X-axis Side 1 for Int. 3	[asec]
10	Star Y WF1 Tilt #1	Starlight Wavefront Tilt Y-axis Side 1 for Int. 1	[asec]
11	Star Y WF1 Tilt #2	Starlight Wavefront Tilt Y-axis Side 1 for Int. 2	[asec]
12	Star Y WF1 Tilt #3	Starlight Wavefront Tilt Y-axis Side 1 for Int. 3	[asec]
13	Star X WF2 Tilt #1	Starlight Wavefront Tilt X-axis Side 2 for Int. 1	[asec]
14	Star X WF2 Tilt #2	Starlight Wavefront Tilt X-axis Side 2 for Int. 2	[asec]
15	Star X WF2 Tilt #3	Starlight Wavefront Tilt X-axis Side 2 for Int. 3	[asec]
16	Star Y WF2 Tilt #1	Starlight Wavefront Tilt Y-axis Side 2 for Int. 1	[asec]
17	Star Y WF2 Tilt #2	Starlight Wavefront Tilt Y-axis Side 2 for Int. 2	[asec]
18	Star Y WF2 Tilt #3	Starlight Wavefront Tilt Y-axis Side 2 for Int. 2	[asec]
19	FEC X WF1 Tilt #1	Front End Camera X-axis WFT Side 1 for Int. 1	[asec]
20	FEC X WF1 Tilt #2	Front End Camera X-axis WFT Side 1 for Int. 2	[asec]
21	FEC X WF1 Tilt #3	Front End Camera X-axis WFT Side 1 for Int. 3	[asec]
22	FEC Y WF1 Tilt #1	Front End Camera Y-axis WFT Side 1 for Int. 1	[asec]
23	FEC Y WF1 Tilt #2	Front End Camera Y-axis WFT Side 1 for Int. 2	[asec]
24	FEC Y WF1 Tilt #3	Front End Camera Y-axis WFT Side 1 for Int. 3	[asec]
25	FEC X WF2 Tilt #1	Front End Camera X-axis WFT Side 2 for Int. 1	[asec]
26	FEC X WF2 Tilt #2	Front End Camera X-axis WFT Side 2 for Int. 2	[asec]
27	FEC X WF2 Tilt #3	Front End Camera X-axis WFT Side 2 for Int. 3	[asec]
28	FEC Y WF2 Tilt #1	Front End Camera Y-axis WFT Side 2 for Int. 1	[sec]
29	FEC Y WF2 Tilt #2	Front End Camera Y-axis WFT Side 2 for Int. 2	[asec]
30	FEC Y WF2 Tilt #3	Front End Camera Y-axis WFT Side 2 for Int. 3	[asec]
31	Attitude Angle X	Used for ACS design	[rad]
32	Attitude Angle Y	Used for ACS design	[rad]
33	Attitude Angle Z	Used for ACS design	[rad]
34	Ext. Met.	External Metrology Pathlength	[m]

## 2.4 Summary

Next Generation Space Telescope and the Space Interferometry Mission are two of the upcoming space observatories to assist scientists in determining the origins of planets and galaxies. Nexus was to have been a testbed in space, allowing engineers to test mirrors, control laws, and to verify models for this new class of space instrument.

All of these spacecraft are similar in that they are large, highly flexible, modally dense structures, each with highly sensitive optics that must be controlled to within fractions of the wavelength of light. Understanding the interaction between structures and controls is vital to the success of these missions. The disturbance analysis described in Chapter 7 is a first step in determining whether a finite-element model of each spacecraft can meet the optical requirements. Once the models are built, the next step is to reduce them to a size that allows fast and accurate computations.



## Chapter 3

# Numerical Tools

The balancing routines in the following chapters are based on several mathematical routines and solvers such as the Singular Value Decomposition (SVD) and solutions of the Lyapunov equation. Most dynamics problems also require solving an eigenvalue problem to determine the natural frequencies and modeshapes. Because of the importance of these routines, this chapter will discuss their basic properties and how they are used in the structures/controls environment.

One of the difficulties that will also be addressed is solving these equations for large order systems. As the size of a  $n \times n$  matrix grows from  $n$  equals several hundred to  $n$  equals several thousand, exact solutions become difficult if not impossible to find. Numerical errors as well as bounds on floating point accuracy limit the users' ability to produce accurate solutions to some problems. Another problem is that of speed; as the size of a matrix grows the length of time it takes to solve any of these equations expands from minutes to hours. From a practical standpoint, this dramatically slows down a disturbance/sensitivity analysis and makes rapid iterations on a design difficult. Especially in solving the Lyapunov equation, this chapter will address some of these issues and recommend methods to obtain fast, accurate results.

This chapter will not go into detail on the solutions of these problems. For a mathematically rigorous approach to each equation, consult a linear algebra or advanced controls text. Unless otherwise noted, Strang's text [48] was used for most of the linear algebra properties in this chapter.

### 3.1 Eigenvalues

The eigenvalue diagonalization  $AS = S\Lambda$ , where  $A$  is the matrix being diagonalized,  $\Lambda$  is the diagonal matrix of eigenvalues, and  $S$  is the matrix of eigenvectors, is undoubtedly the most important routine in structural dynamics. The natural frequencies  $\omega_i$  and modeshapes  $\phi_i$  of a structure are found through solving the generalized eigenproblem

$$\Omega^2 M \Phi = K \Phi \quad (3.1)$$

with mass matrix  $M$ , stiffness matrix  $K$ , and  $n$  modes.

$$\Phi \equiv \begin{bmatrix} \phi_1 & \cdots & \phi_n \end{bmatrix} \quad \Omega \equiv \begin{bmatrix} \omega_1 & & 0 \\ & \ddots & \\ 0 & & \omega_n \end{bmatrix}$$

Eigenproblems are also of importance for controlled structures since the eigenvalues of a state-space  $A$  matrix are either pairs of complex-conjugate poles or single real poles of the system, and are the roots of the characteristic equation. If complex eigenvalues are plotted on the complex plane, the magnitude is the modal frequency  $\omega$  with damping  $\zeta$  (see Figure 3-1). The stability of a system can be determined by ensuring that all of the poles have negative real parts, or are in the left-half of the complex plane [50, 41].

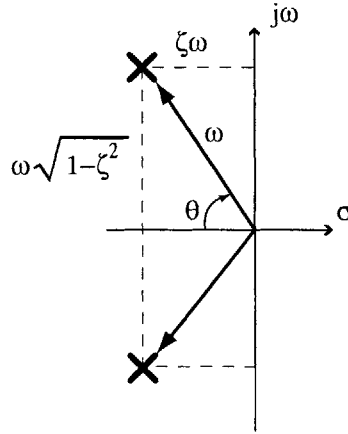


Figure 3-1: Complex conjugate poles on the complex plane. Both represent a single mode with frequency  $\omega$ .

The literature on the subject of eigenvalues is comprehensive; reference [39] is recommended as a starting point for understanding the computational difficulties of solving



eigenproblems. The basic properties of symmetric matrices are discussed here.

The  $M$  and  $K$  matrices in the eigenvalue equation 3.1 are most often real symmetric<sup>1</sup>. The symmetric eigenvalue problem has several properties worth mentioning. First, all of the eigenvalues are real, so they represent the actual frequencies. This compares to the complex eigenvalues of the  $A$  matrix, in which the magnitudes of the complex numbers equal the frequencies. Second, a real symmetric matrix has *orthogonal* eigenvectors, so  $\phi_i \cdot \phi_j = 0$  for  $i \neq j$ . Although the magnitude of these eigenvectors is not specified, they can be chosen to be *orthonormal*<sup>2</sup>, where  $\phi_i \cdot \phi_j = 1$  for  $i = j$ . More often they may be mass-normalized where  ${}^o\phi_i = \phi_i / (\phi_i^T M \phi_i)$ . An advantage of working with orthonormal matrices is that their inverse is equal to their transpose. This can be quickly proved by writing  $\Phi \Phi^T = I$  and therefore  $\Phi^T = \Phi^{-1}$ . This allows an eigenvalue decomposition to be written as

$$A = S \Lambda S^{-1} = S \Lambda S^T \quad (3.2)$$

when  $A$  is symmetric. The complexity of an inverse is replaced by the simplicity of a matrix transpose. This result will be used in Section 3.3 to illustrate a solution of the Lyapunov equation. For the balancing routines of Chapter 5, the singular value decomposition is used more often than the eigenvalue decomposition. This alternate diagonalization routine is described next.

## 3.2 Singular Value Decomposition

The Singular Value Decomposition (SVD) is a useful tool in matrix analysis, and will be used extensively by the balancing routines in Chapter 5. Unlike the eigenvalue diagonalization, an SVD can be performed on any  $m \times n$  matrix, and it always produces an orthonormal basis. The relative sizes of the singular values will also provide a measure of numerical conditioning for the models.

---

<sup>1</sup>Exceptions would occur if there were additional terms on the acceleration or displacement state vectors in the equation of motion. One of the SIM models not considered used complex damping, which creates a non-symmetric  $K$  matrix. All of the other spacecraft models (including other SIM models) used linear proportional damping, allowing  $M$  and  $K$  to remain symmetric.

<sup>2</sup>Strang [48] suggests that any square matrix with orthonormal columns is properly called *orthogonal*, and that the term *orthonormal matrix* is not used. For the sake of clarity however, that term will be used herein.

### 3.2.1 Properties of SVD matrices

The standard form of the SVD on a matrix  $A$  is:

$$AV = U\Sigma \quad (3.3)$$

Rewrite this by inverting  $V$ .

$$A = U\Sigma V^{-1} \quad (3.4)$$

Note the similarity between this and the eigenvalue factorization  $A = SAS^{-1}$ . In the case that  $U = V$ , the SVD simply becomes an eigenvalue decomposition. However whereas the eigenvector matrix  $S$  is generally not orthonormal<sup>3</sup> the singular value matrices  $V$  and  $U$  always are. This means that

$$\begin{aligned} V^T V &= I \\ U^T U &= I \end{aligned} \quad (3.5)$$

where  $I$  is the identity matrix; therefore

$$\begin{aligned} V^T &= V^{-1} \\ U^T &= U^{-1}. \end{aligned} \quad (3.6)$$

Equation 3.4 can be rewritten by replacing  $V^{-1}$  with  $V^T$ . This can be further generalized by considering complex orthonormal matrices, or *unitary* matrices. The transpose operator  $(\cdot)^T$  is replaced by the complex-conjugate transpose, or *Hermitian*, operator  $(\cdot)^H$ .

$$A = U\Sigma V^T \quad (\text{or}) \quad A = U\Sigma V^H \quad (3.7)$$

The final matrix of the SVD,  $\Sigma$ , is a real diagonal matrix containing the singular values,  $\sigma_i$ , or zeros if there are linearly dependent columns<sup>4</sup>. In Equation 3.8, the  $n \times n$  matrix  $\Sigma$

---

<sup>3</sup>The situation described in the previous section, in which  $A$  is symmetric, is an obvious exception

<sup>4</sup>Only the non-zero values along the diagonal of  $\Sigma$  are termed “singular values.”

has  $p$  linearly independent columns and  $r$  dependent columns.

$$\Sigma = \begin{bmatrix} \begin{bmatrix} \sigma_1 & & \\ & \ddots & \\ & & \sigma_p \end{bmatrix}_{p \times p} & \\ & \begin{bmatrix} 0 & & \\ & \ddots & \\ & & 0 \end{bmatrix}_{r \times r} \end{bmatrix} \quad (3.8)$$

The matrix  $A$  is thus factorized into an orthonormal times a diagonal times an orthonormal matrix. These matrices can be calculated using the principals of orthogonality. To calculate  $V$ , multiply Equation 3.7 by  $A^H$ , and recognize that  $U^H U = I$ .

$$A^H A = (U \Sigma V^H)^H (U \Sigma V^H) = (V \Sigma^H U^H U \Sigma V^H) = V \Sigma^2 V^H \quad (3.9)$$

Since  $\Sigma$  is real and diagonal,  $\Sigma^H = \Sigma$ . The above equation is in the form of another eigenvalue problem, where  $\Sigma^2$  contains the eigenvalues  $\sigma_i^2$  of  $A^H A$ , and  $V$  is the matrix of eigenvectors of  $A^H A$ . In a similar manner,  $U$  is the matrix of eigenvectors of  $A A^H$  with the same eigenvalues  $\sigma_i^2$ . Those eigenvectors in  $V$  (and similarly in  $U$ ) associated with zeros in  $\Sigma^2$  are filled by vectors in the nullspace of  $A$ , described by the solutions of:

$$A v_{null,i} = 0 \quad (3.10)$$

for all  $i = (p + 1), \dots, (p + r)$ . In such cases where nullspace vectors exists,  $A$  has linearly dependent columns and is singular. So a singular  $A$  matrix means that some of the singular values will always be zero. In the balancing routines described in Chapter 5, very small singular values will indicate matrices that are nearly singular.

One last property discussed here about singular values is their usefulness in computing the inverse of a singular matrix. Generally speaking, an inverse does not exist for singular matrices. However by taking advantage of orthogonality, it is possible to compute the *pseudoinverse*, also known as the Moore-Penrose inverse, represented here by  $(\cdot)^\dagger$ . First compute the SVD of a singular matrix,  $A = U \Sigma V^H$ , and separate the singular values (defined as always non-zero) from the zero terms along the diagonal of  $\Sigma$ .

$$\Sigma = \begin{bmatrix} \Sigma_{sv} & 0 \\ 0 & 0 \end{bmatrix} \quad (3.11)$$

Then the pseudoinverse is just  $A^\dagger = V\Sigma^\dagger U^H$  with

$$\Sigma^\dagger = \begin{bmatrix} \Sigma_{sv}^{-1} & 0 \\ 0 & 0 \end{bmatrix} \quad (3.12)$$

### 3.2.2 Condition Number of Matrices

One of the uses of singular values for model quality purposes is to compute the matrix condition numbers, or the ratio of the largest to smallest singular values.

$$c = \frac{\sigma_{max}}{\sigma_{min}} \quad (3.13)$$

More generally the condition number is defined by  $c = \|A\| \|A^{-1}\|$ , where  $\|\cdot\|$  is the matrix *norm*. This provides an measurement of the relative size of a matrix, just as a vector is described by its length  $\|\mathbf{x}\|$ . The norm of  $A$  is defined as the square root of the maximum eigenvalue of  $A^T A$ . Likewise the norm of  $A^{-1}$  is one over the square root of the minimum eigenvalue of  $A^T A$ , so that

$$c = \sqrt{\lambda_{max}(A^T A)} \cdot \frac{1}{\sqrt{\lambda_{min}(A^T A)}} \quad (3.14)$$

The previous section showed that the eigenvalues of  $A^T A$  are simply the singular values of  $A$ , which leads to Equation 3.13 above.

The usefulness of the condition number is that its size provides an indication of the numerical robustness, or numerical conditioning of a matrix. Larger condition numbers mean a greater difference between the maximum and minimum singular values, and represent an ill-conditioned system. To illustrate, consider two second-order systems defined by the following A-matrices, with natural frequency  $\omega$  and damping  $\zeta$ .

$$A_1 = \begin{bmatrix} 0 & 1 \\ -\omega^2 & -2\zeta\omega \end{bmatrix} \quad (3.15)$$

$$A_2 = \begin{bmatrix} -\zeta\omega & \omega\sqrt{1-\zeta^2} \\ -\omega\sqrt{1-\zeta^2} & -\zeta\omega \end{bmatrix} \quad (3.16)$$

The first equation is in the familiar second-order form, while the second is in real-modal form. Both describe the exact same system. Consider the condition numbers of each when  $\omega = 100$  rad/sec and  $\zeta = 0.01$ .

$$A_1 = \begin{bmatrix} 0 & 1 \\ -10000 & -2 \end{bmatrix}$$

$$\text{cond}(A_1) = 10000$$

$$A_2 = \begin{bmatrix} -1 & 99.995 \\ -99.995 & -1 \end{bmatrix}$$

$$\text{cond}(A_2) = 1$$

The first matrix is numerically ill-conditioned with a 1.0 on the off-diagonal facing an  $\omega^2$ . The second matrix is numerically better conditioned, since each diagonal is on the order of  $\omega$ . For a system with multiple modes, a large difference between the smallest and largest frequencies could compound these numerical issues. This can become a serious problem with very large matrices across a wide spread of frequencies. The relative floating point accuracy in MATLAB (`eps.m`) is  $\varepsilon = 2.22 * 10^{-16}$ . This represents the smallest distance beyond 1.0 that MATLAB can recognize. As will be seen in following chapters, it is possible that singular values smaller than  $10^{-16}$  will be carried along with values greater than  $10^0$ . Since this results in a very large condition number, steps are needed to improve the numerical conditioning of systems. This will be addressed in the next chapter.

### 3.3 Lyapunov Equation

The final equation described is the steady-state *Lyapunov* equation, shown below. This will be used first to calculate the controllability and observability gramians of a state-space system. It will be used again in Chapter 7 to obtain the state covariance matrix  $\Sigma_q$  in a Lyapunov-based disturbance analysis. A fast Lyapunov solver is developed for systems whose  $A$  matrix has a diagonal structure. References [41] and [52] were valuable for this section.

$$AX + XA^T + Q = 0 \quad (3.17)$$

#### 3.3.1 Controllability and Observability Gramians

Given a state space system described by 3.18, it is often useful to know the amount that each state in  $x$  is controllable and observable. If a state is neither, its usefulness in a system of equations is reduced. In the case of controllability, the particular question is whether or not  $x$  can be driven to a particular  $x_f$ , and if so how much control energy would be required to drive it.

$$\begin{aligned} \dot{x} &= Ax + Bu \\ y &= Cx + Du \end{aligned} \quad (3.18)$$

The Lyapunov equation helps determine the controllability and observability of a system by computing the controllability and observability *gramians*<sup>5</sup>. The eigenvalues of the gramian matrices provide a relative measure of the ability of a state to be controlled or observed. So if  $\lambda_{min}$  for the controllability gramian is very small, it would be very difficult or require a great deal of control energy to reach a particular state. Similarly, if  $\lambda_{max}$  for the observability gramian is large, that state is highly observable in the system outputs  $y$ .

The controllability gramian,  $W_c$ , is derived by determining a control input that drives  $x(t)$  to any given state  $x(t_{final})$ . In integral form, the gramian is:

$$W_c(t) = \int_0^t e^{A\tau} B B^T e^{A^T \tau} d\tau \quad (3.19)$$

---

<sup>5</sup>An alternate spelling is *grammians*. Both have been seen in literature, and the author is unaware which is considered more correct.

where for  $n$  states,  $W_c$  is an  $n \times n$  matrix.  $W_c$  can also be described by the solution to the differential Lyapunov equation

$$\frac{d}{dt}W_c(t) = AW_c(t) + W_c(t)A^T + BB^T. \quad (3.20)$$

If the system is stable, or if all of the poles (or real parts of the eigenvalues) of  $A$  are in the left-half of the complex plane, then  $W_c$  will approach its steady state value and the derivative in Equation 3.20 goes to zero.

$$\lim_{t \rightarrow \infty} W_c(t) = W_{c,ss} \quad (3.21)$$

$$0 = AW_c(t) + W_c(t)A^T + BB^T \quad (3.22)$$

This steady-state Lyapunov solution is used to compute the gramians in the balancing routines. A similar derivation is used for the observability gramian.

$$0 = A^TW_o(t) + W_o(t)A + C^TC \quad (3.23)$$

For a given rectangular matrix  $R$ , the matrix multiplications  $R^TR$  and  $RR^T$  both produce symmetric *but different* matrices. So the products  $BB^T$  and  $C^TC$  are both symmetric. If the  $Q$  term in Equation 3.17 is symmetric, so will be the Lyapunov solution  $X$ . This produces the first of several useful facts, listed below.

1.  $W_c(t)$  and  $W_o(t)$  are symmetric for  $t \geq 0$ .
2.  $W_c > 0$  (positive definite) if  $BB^T > 0$  and  $W_o > 0$  if  $C^TC > 0$ .
3. Given  $BB^T \geq 0$ , (positive semi-definite)  $(A, B)$  is completely controllable if and only if  $W_c > 0$ , or has full rank.
4. Given  $C^TC \geq 0$ ,  $(C, A)$  is completely observable if and only if  $W_o > 0$ , or has full rank.
5. The controllability gramian  $W_c$  is also equal to the state covariance matrix  $\Sigma_q$

Especially important are items 3 and 4. As will be discussed in Chapter 5, the rank of the gramians will determine whether traditional balancing routines will work or not. The

symmetry described in item 1 will be used by the fast Lyapunov solver described in the next chapter. It is also most important to remember that solutions to this steady-state Lyapunov equation require stable systems. So rigid body modes in a model must be either stabilized or removed before balancing can proceed. This will be discussed in the next chapter.

### 3.3.2 Analytical Solution

This section will provide a brief description of how to solve the Lyapunov equation. The algorithm is not provided as a recommended means of solving the equation, but rather will lead to a faster method of solving certain large-order problems. Reference [23] and [45] for explicit solutions to the gramians of state-space systems described using normal-modes with  $\omega$  and  $\zeta$ .

Consider the Lyapunov equation described by 3.17. Diagonalize  $A$  using its eigenvectors<sup>6</sup>,  $A = SAS^{-1}$ . Substitute this matrix product for  $A$  in Equation 3.17, pre-multiply by  $S^{-1}$  and post-multiply by  $S^{-T}$ .

$$\begin{aligned} S^{-1} \left( (SAS^{-1})X + X(S^{-T}\Lambda S^T) + Q \right) S^{-T} &= 0 \\ \underbrace{S^{-1}S}_{=I} \Lambda S^{-1} X S^{-T} + S^{-1} X S^{-T} \Lambda \underbrace{S^T S^{-T}}_{=I} + S^{-1} Q S^{-T} &= 0 \end{aligned}$$

Redefine the matrix products as follows.

$$\Lambda \underbrace{S^{-1} X S^{-T}}_{\equiv \tilde{X}} + \underbrace{S^{-1} X S^{-T}}_{\equiv \tilde{X}} \Lambda + \underbrace{S^{-1} Q S^{-T}}_{\equiv \tilde{Q}} = 0 \quad (3.24)$$

This is now a new Lyapunov equation with the matrix definitions given. The important property is that  $\Lambda$  is diagonal. For a simple  $2 \times 2$  case, the matrices can be described in the following fashion.

$$\begin{bmatrix} \lambda_1 & 0 \\ 0 & \lambda_2 \end{bmatrix} \begin{bmatrix} \tilde{x}_{11} & \tilde{x}_{12} \\ \tilde{x}_{21} & \tilde{x}_{22} \end{bmatrix} + \begin{bmatrix} \tilde{x}_{11} & \tilde{x}_{12} \\ \tilde{x}_{21} & \tilde{x}_{22} \end{bmatrix} \begin{bmatrix} \lambda_1 & 0 \\ 0 & \lambda_2 \end{bmatrix} + \begin{bmatrix} \tilde{q}_{11} & \tilde{q}_{12} \\ \tilde{q}_{21} & \tilde{q}_{22} \end{bmatrix} = 0 \quad (3.25)$$

---

<sup>6</sup>Note that MATLAB uses a Schur decomposition as described in [9]. In practice, the eigenvalue method described may be unstable if the matrices are ill-conditioned. It is used in this description because of the familiarity of eigenproblems.



$\lambda_i$  are the diagonal values of  $\Lambda$ , and the  $\tilde{x}_{ij}$  are the scalar entries in each  $(i, j)$  element of  $\tilde{X}$ . Note that unless the original  $Q$  matrix is symmetric, the Lyapunov solutions  $X$  or  $\tilde{X}$  will not be symmetric. By multiplying the matrices out, the diagonal nature of  $\Lambda$  succeeds in decoupling the entire set of equations.

$$\begin{bmatrix} \lambda_1 \tilde{x}_{11} + \tilde{x}_{11} \lambda_1 + \tilde{q}_{11} = 0 & \lambda_1 \tilde{x}_{12} + \tilde{x}_{12} \lambda_2 + \tilde{q}_{12} = 0 & \cdots \\ \lambda_2 \tilde{x}_{21} + \tilde{x}_{21} \lambda_1 + \tilde{q}_{21} = 0 & & \\ \vdots & & \end{bmatrix}$$

The resulting equations are uncoupled, so that solving for each  $\tilde{x}_{ij}$  requires no more than solving a simple algebraic equation  $\lambda_i \tilde{x}_{ij} + \tilde{x}_{ij} \lambda_j + \tilde{q}_{ij} = 0$ .

$$\tilde{x}_{ij} = -\frac{\tilde{q}_{ij}}{(\lambda_i + \lambda_j)}. \quad (3.26)$$

After solving for all of the  $\tilde{x}_{ij}$ , they can be incorporated into  $\tilde{X}$ , which in turn can be substituted into the original matrix product  $X = S\tilde{X}S^T$ . This finally produces the Lyapunov solution  $X$ .

### 3.3.3 Fast Lyapunov Solvers

The balancing routines and disturbance analyses will require that several Lyapunov equations be solved. In a large system where the  $n \times n$  solution  $X$  has  $n > 2000$ , this one computation may take upwards of an hour to complete and involves over  $10^{11}$  floating point operations<sup>7</sup>. Running a spacecraft through the entire DOCS code takes tens of hours as a result. As computer speeds continue to increase these times will fall. This is an inelegant solution to the problem, however, and fails to help once larger spacecraft models are used. Although the Lyapunov equation is not the only roadblock to faster results (solving for the eigenvalues can take even more time), its form permits a faster solution in certain cases.

Consider again the Lyapunov form outlined in Equation 3.25. The diagonal nature of  $\Lambda$  permits the individual equations to decouple for each  $\tilde{x}_{ij}$ , thus allowing many simple, independent solutions to build the entire  $n \times n$  matrix. This same idea can be applied when  $\Lambda$  is block diagonal instead of diagonal. Using the variable  $A$  in place of  $\Lambda$ , consider

---

<sup>7</sup>Most of the work presented here was performed on a 850 MHz Pentium III processor running WindowsNT.

the general Lyapunov form described by Equation 3.17, but for the case where  $A$  is  $2 \times 2$  matrix-block diagonal. Assume that  $Q$  is symmetric.

$$\begin{bmatrix} A_1 & 0 \\ 0 & A_2 \end{bmatrix} \begin{bmatrix} X_{11} & X_{12} \\ X_{12}^T & X_{22} \end{bmatrix} + \begin{bmatrix} X_{11} & X_{12} \\ X_{12}^T & X_{22} \end{bmatrix} \begin{bmatrix} A_1 & 0 \\ 0 & A_2 \end{bmatrix}^T + \begin{bmatrix} Q_{11} & Q_{12} \\ Q_{12}^T & Q_{22} \end{bmatrix} = 0 \quad (3.27)$$

Four matrix equations result.

$$\begin{aligned} 1) & A_1 X_{11} + X_{11} A_1^T + Q_{11} = 0 & 2) & A_1 X_{12} + X_{12} A_2^T + Q_{12} = 0 \\ 3) & A_2 X_{12}^T + X_{12}^T A_1^T + Q_{12}^T = 0 & 4) & A_2 X_{22} + X_{22} A_2^T + Q_{22} = 0 \end{aligned} \quad (3.28)$$

Notice that equations 1 and 4 in Equation 3.28 are just new Lyapunov equations. Equations 2 and 3 are also Lyapunov equations, though in a more general form  $AX + XB + C = 0$ . This is sometimes called the *Sylvester* equation. Each of these can be solved using whichever technique was formerly applied for the full matrix  $X$  (`lyap.m` in MATLAB was most often used here), but because of their smaller size they can individually take far less time than the full  $n \times n$  system. Also note that Equation 3 is just the transpose of Equation 2, so of the four equations only three must be solved.

The requirement on  $A$  is that it can be made into a block diagonal form. Luckily the decoupled modal form resulting from a normal modes analysis can be easily written using  $2 \times 2$  blocks given by 3.15 or 3.16. If the system is no longer in a modal form, the eigenvalues of most  $A$  matrices can be written in a diagonal *Jordan* form [41, 52]. The time and computation required to solve the eigenvalue problem would offset the gains from the fast Lyapunov solver, however.

Using the  $2 \times 2$  modal system, there are now  $n/2$  blocks along the diagonal of  $A$ . Keeping in mind the symmetry of  $X$ , this means  $\frac{\frac{n}{2}(\frac{n}{2}+1)}{2}$  separate  $2 \times 2$  Lyapunov solutions  $X_{ij}$  must be solved. One concern may be that although the computational time for each solution is fast, the number of computations and the inefficiencies of *for*-loops may not yield an overall time savings. As will be seen, the time to solve all the  $2 \times 2$  equations is less than the time required to solve the entire  $n \times n$  problem; however this is not the most efficient block size to use.

There is no reason that larger blocks can not be selected, so long as the size is an even factor of  $n$ . Using a block size of  $m$ , a general relation for the number of Lyapunov blocks

can be written.

$$N_{blocks} = \frac{\frac{n}{m}(\frac{n}{m} + 1)}{2} \quad (3.29)$$

As an example of the efficiency that can be gained, this method was run on sample problems with  $n = 600, 1000, 1500$ , and  $2000$  states. A modal system was created using  $n/2$  logarithmically even-spaced frequencies between  $10^{-3}$  and  $10^3$ . Damping of  $0.001$  was used, and an input  $B$  matrix was chosen randomly. This test was run for the  $(A, B)$  controllability gramian, although the algorithm works for any Lyapunov problem.

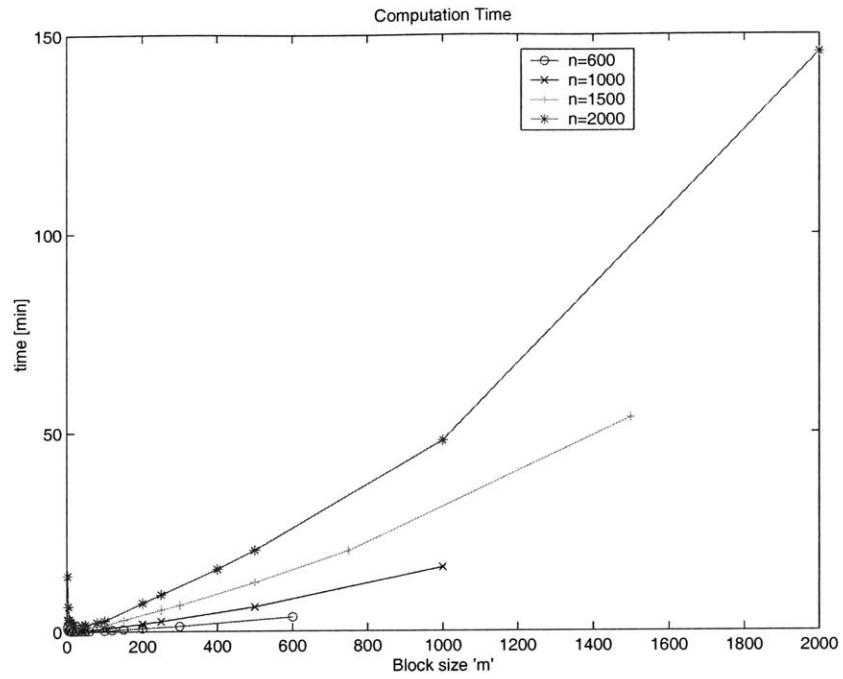
All even factors of  $n$  are chosen as possible block sizes  $m$ . For  $n = 1000$ , this allows  $m = [2 \ 4 \ 8 \ 10 \ 20 \ 40 \ 50 \ 100 \ 200 \ 250 \ 500 \ 1000]$ . Even numbers are required since the  $A$  matrix is still  $2 \times 2$  block diagonal.

Figure 3-2(a) shows the variation of CPU time in minutes versus block size  $m$  for each problem of size  $n$ . The last point on each curve represents the full  $n \times n$  Lyapunov solution. For  $n = 2000$ , nearly  $2\frac{1}{2}$  hours are required to obtain an answer. This compares to 14 minutes for  $m = 2$ . This considerable time savings is improved further with slightly larger block sizes. A minimum in all four curves (shown clearer in Figure 3-2(b)) indicates an optimum  $m$  between  $m = 20$  and  $40$ . For  $m = 40$ , the  $2000$  state model takes only 1.6 minutes to compute an answer. A summary of the results from Figure 3-2 is included in Table 3.1.

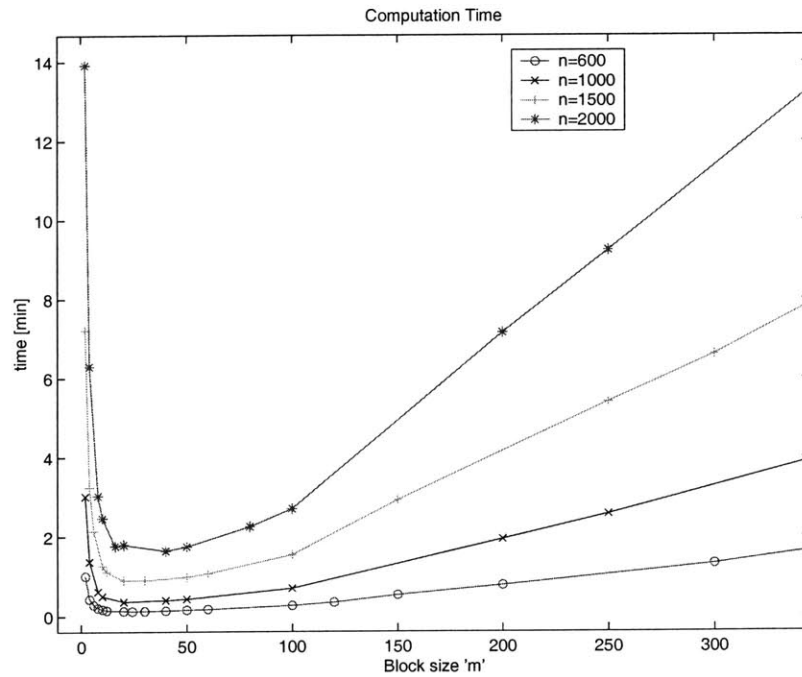
Table 3.1: Time improvements using fast Lyapunov method

$n$ states	time to solve full $n \times n$ system (minutes)	time to solve using $m \times m$ blocks (minutes)	fastest block size $m$	time savings ratio $t_{max}/t_{min}$
600	3.5	0.13	24	26.9
1000	16.1	0.37	20	43.5
1500	53.7	0.90	20	59.7
2000	145.5	1.65	40	88.2

The quality of the solution is checked by placing the answer back into the Lyapunov equation. This resultant matrix should equal zero. Due to numerical inaccuracies, the maximum value of the resultant is actually on the order of  $10^{-13}$  for all  $n$ . What is important is that the resultant for each block solution is identical to the resultant for the full  $n \times n$  solution. The solutions suffer from no additional inaccuracies.



(a) Full View



(b) Zoomed-in

Figure 3-2: CPU Time in minutes to solve a Lyapunov equation of size  $n$  using blocks of size  $m$

Another metric with which to judge the routines are the number of floating point operations, or flops, that must be performed. The advantage of measuring flops over CPU time is that flops are machine independent. The nature of MATLAB's `lyap.m` function is such that an exact flop count based on the number of required operations can not be specified. The Schur decomposition used by MATLAB requires a Gram-Schmidt factorization  $A = QR$ . This may require a different number of operations depending on intricacies of the  $QR$  factorization. Reference [9], used for the `lyap.m` function, suggests that the number of required multiplications is probably overestimated by

$$(5.5 + 4\sigma)n^3$$

where  $\sigma$  is an average number of steps in the factorization, dependent on the matrix  $A$ . Reference [16] empirically found that the number of flops goes by  $50n^3$ .

Using the fast Lyapunov method, a single  $50n^3$  operation is replaced by many  $50m^3$  operations, with  $n \gg m$ . If the number of Lyapunov equations is described by Equation 3.29, then the estimated number of flops is

$$N_{flops} = 25(mn^2 + m^2n). \quad (3.30)$$

The total number of flops to solve every problem of size  $n$  with block sizes  $m$  was output for the sample problem and plotted as points in Figure 3-3. The curves plotted over the points are the approximations given in Equation 3.30 above. The approximation is shown to work very well. Further, use of the fast Lyapunov method succeeds in reducing the flop count by several orders of magnitude. For the 2000 state model, the full  $n \times n$  system requires over  $4 \times 10^{11}$  flops compared to  $4.9 \times 10^8$  flops when a block size of  $m = 2$  is used. The number of flops for those blocks sizes with the fastest times (as given in Table 3.1) are provided in Table 3.2.

This method has been coded into a MATLAB function `newgram.m`, that solves for either the controllability or observability gramian based on the inputs  $(A, B)$  or  $(C, A^T)$ . It is used successfully in the balancing routines of Chapter 5.

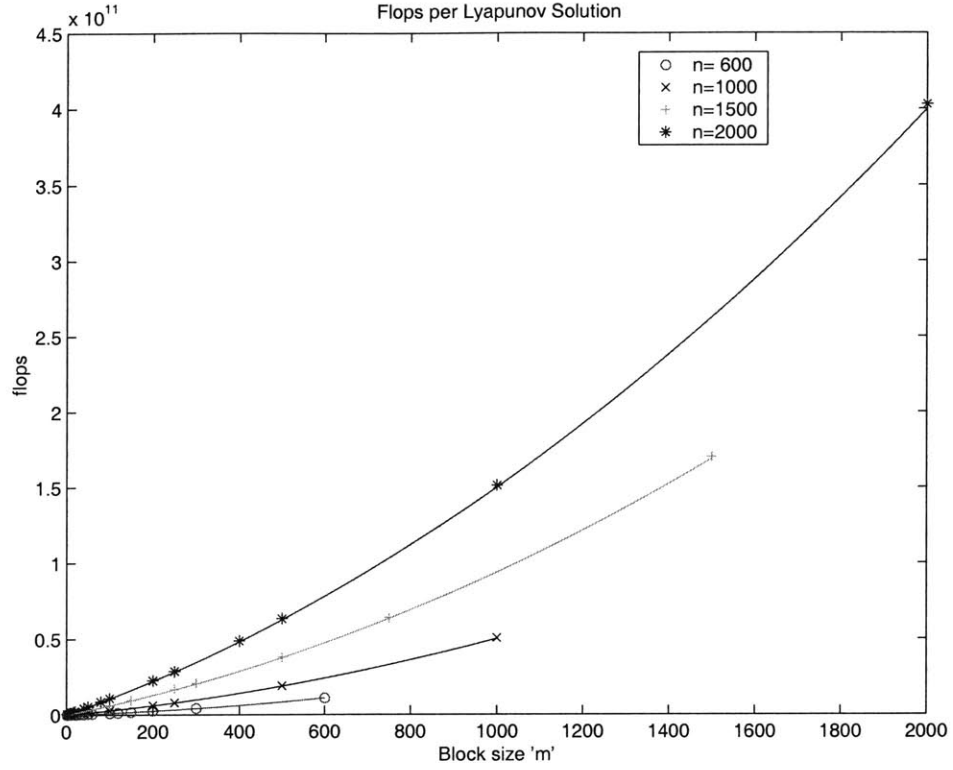


Figure 3-3: Number of flops for the sample problem, along with curves showing the flop count approximation

Table 3.2: Improvements in flop counts using fast Lyapunov method

$n$ states	# flops for full $n \times n$	# flops using $m \times m$ blocks	fastest block size $m$
600	$1.1 \times 10^{10}$	$2.4 \times 10^8$	24
1000	$5.0 \times 10^{10}$	$5.6 \times 10^8$	20
1500	$1.7 \times 10^{11}$	$1.3 \times 10^9$	20
2000	$4.0 \times 10^{11}$	$4.3 \times 10^9$	40

### 3.4 Summary

The eigenvalue problem, singular value decompositions, and the Lyapunov solution are three mathematical problems used quite frequently in structural dynamics analysis, and all are important tools in the DOCS framework. The eigenvalue problem is used particularly with the initial finite element  $K$  and  $M$  matrices; for linear systems it is also used to find the complex poles in the system  $A$  matrix. Both the SVD and Lyapunov problems will be relied upon heavily in Chapter 5 to perform system balancing. The fast Lyapunov solver described will speed up the balancing routines, as well as the disturbance analyses of Chapter 7. Because routines such as the Lyapunov solver will only work on stable systems, the next step is to ensure that the spacecraft models are stable. Assuming that the plant is not basically unstable, as would result from a destabilizing controller, only the marginally stable rigid body modes must be dealt with.

It is important to keep in mind that the results provided by the equations in this chapter are only as numerically sound as the matrices that are provided to them. In the next chapter several steps will also be taken to ensure that the spacecraft models are numerically well-conditioned.





## Chapter 4

# Methods for Maintaining Model Quality

Given a state-space model that needs to be reduced, there are a number of steps that should first be taken to improve the numerical quality of the matrices. Some of these, such as the scaling and choice of inputs and outputs, are designed primarily to improve the numerical conditioning of the matrices. Others, such as the removal or stabilizing of rigid body modes, are required before the model can be balanced. Many of these steps are performed routinely for the models that have been studied. When dealing with large models of several hundred to several thousand states, it is more critical that the steps are adhered to before any balancing is attempted. Basic routines to track the quality of a matrix are also briefly discussed. A overview of the steps the are performed in the DOCS model preparation routines is illustrated in Figure 4-1.

### 4.1 Model Preparation

The first choice to make in preparing a model to be reduced is which model to use? The final integrated model that will be analyzed will include an ACS controller, closed optics loops, and may have states describing the disturbance inputs appended directly into the state matrices. This is obviously the most complete system, of which the most important states should be retained in reduction. The purely open loop system describes the spacecraft, but the states have not been weighted by the disturbance inputs or the control loops. By exciting certain modes or attenuating frequency ranges, both of these processes can change

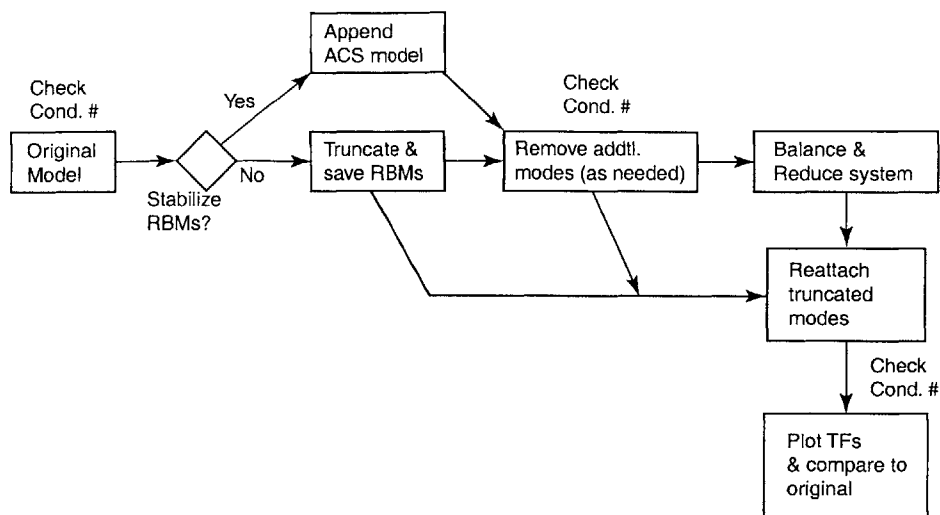


Figure 4-1: Block diagram outlining the model preparation steps.

each state's importance.

There are equal disadvantages to reducing the entire system. If a separate disturbance analysis is performed for many reaction wheel speeds, the final integrated model will change each time. The balancing routine can take over an hour for each model, so the total amount of time to run a range of wheel speeds could quickly grow prohibitively large. The other difficulty, that will be discussed in this section, is the numerical conditioning of a closed loop system. In order to successfully balance a model, the matrices must be well-conditioned. ACS loops often add low frequency poles, which tend to worsen, not better, a system's conditioning, and optical controllers add on even more states. As a result, all of the balanced systems shown here have open ACS and optics loops and only such modifications as will be described.

Given an open loop model, a state space system made from  $A$ ,  $B$ , and  $C$  matrices can be manipulated in several ways to improve numerical quality. This is necessary because for large systems, poor numerical conditioning can at best cause routines such as eigen- and Lyapunov solvers to produce highly inaccurate results. At worst these routines will fail to run. Using the SIM models (Versions 2.0 and 2.2) as examples, several steps are listed in the attempt to improve the numerical characteristics of a system. The first step, stabilizing or removing the rigid body modes, is also required before system can be balanced.

### 4.1.1 Rigid Body Modes

Six rigid body modes result for systems with free-free boundary conditions, such as a spacecraft in a zero-gravity environment. These modes are represented in a system by frequencies of zero and are represented in the  $A$  matrix by blocks of the form:

$$A_{rbm} = \begin{bmatrix} 0 & 1 \\ 0 & 0 \end{bmatrix}. \quad (4.1)$$

The poles lie directly on the origin of the complex plane so the system is only marginally stable. In order to find a solution to the Lyapunov problem, which is used in the balancing routine and in one of the disturbance analysis methods, the rigid body modes must be stabilized.

For the spacecraft in orbit, these modes are controlled using thrusters or reaction wheels as part of the attitude control system (ACS). For the model of the spacecraft, one method to control the modes is to include an ACS control loop around the main spacecraft plant. The controller takes the spacecraft attitude angles and rates and outputs commands to the reaction wheels; the firing of thrusters excites the structures beyond the level where science can be performed. As a result they are ignored in a disturbance-to-performance analysis. Once the spacecraft model has been balanced and reduced, this will be the path taken for further work. However before the system has been balanced, it can be easier not to incorporate an ACS controller just yet.

Another option is to eliminate the rigid body modes entirely. Although the rigid body *rotation* of an observatory is obviously critical to its pointing ability<sup>1</sup> and cannot be eliminated without grossly affecting the system dynamics, the *translational* rigid body modes are much less important. For a science object that is effectively located at infinity, the stellar light rays are practically parallel, so translational movement does not change the observatory's view. Since these modes are unobservable, they will eventually be directly truncated from the system.

The third option is to remove and save the rigid body modes for balancing only. This option makes use of the decoupled nature of normal modes. The system  $A$  matrix can be written in a  $2 \times 2$  block diagonal form, where each block describes a mode in either second

---

<sup>1</sup>Hubble uses only its rigid body controller to point itself.

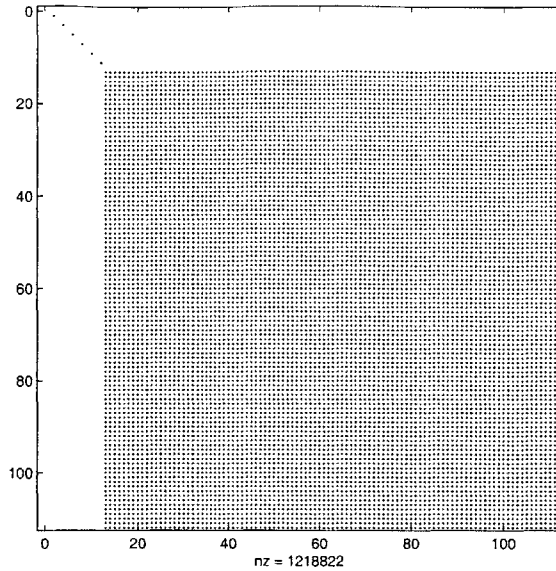


Figure 4-2: Structure of the system  $A$  matrix after appending rigid body modes to the reduced flexible modes (zoomed in to upper left corner of matrix).

order form or real modal form, Equations 3.15 and 3.16. Since each mode is decoupled from the others, it can be removed from the system without affecting any other mode.

The rigid body modes are thus separated from the flexible modes, which are then balanced and reduced. Although the resulting flexible  $A_{flex}$  matrix is fully populated, and the flexible modes that remain after reduction are coupled to one another, they are all still uncoupled from the rigid body modes. These can be appended back into the system. The structure of the resulting  $A_{red}$  matrix is shown in Figure 4-2. The six rigid body modes are still in uncoupled  $2 \times 2$  form.

#### 4.1.2 Low- and High- Frequency Modes

The rigid body modes had to be removed in order to stabilize the system; other modes can be removed if desired to improve the conditioning of the  $A$  matrix. The condition number is directly related to the magnitude between the highest and lowest modal frequencies (which represent the poles, or eigenvalues of the system). An ACS controller typically adds very low frequency poles, usually at least a decade below the lowest flexible frequency. While these stabilize the rigid body modes, they also increase the condition number, thereby decreasing the numerical stability. This is the primary reason that an ACS controller is not added until after the system is balanced and reduced.

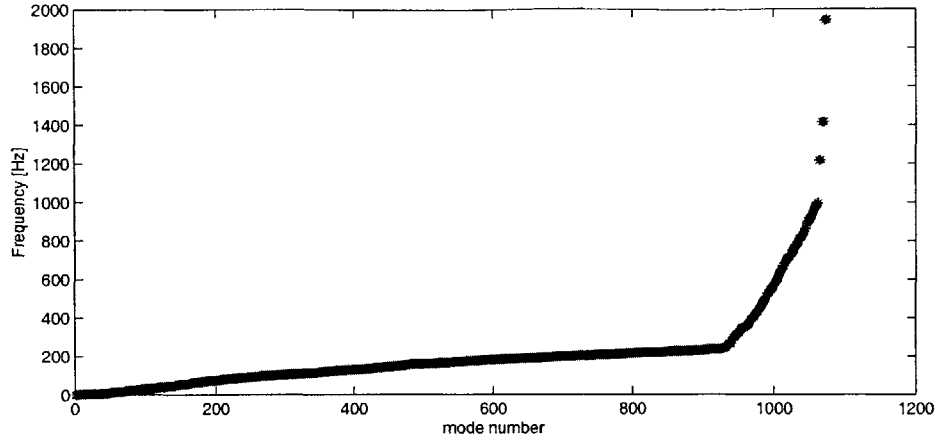


Figure 4-3: Distribution of modal frequencies in SIM Version 2.0. Modal density decreases after 240 Hz around mode #930. The twelve highest modes are all above 1 kHz.

The same effect is evident with very high frequency poles. Consider for example the highest modal frequencies of SIM Version 2.0, seen in Figure 4-3. The great majority of the 1075 structural modes are below 1000 Hz (the “kink” in the curve occurs since the modal density decreases at 240 Hz). Twelve of the frequencies, belonging to the delay line actuator modes, are above this level however. The highest of these is at 1947 Hz. Despite their small quantity, these few poles would still affect the numerical quality of the system. They too can be removed from the uncoupled system, which is subsequently balanced and reduced. Unless it is determined that these modes are uncontrollable/unobservable, they should be appended back into the reduced system in the exact same manner as the rigid body modes had been.

Although this is a relatively simple procedure, care should be taken in deciding whether to remove modes to improve the balancing. The purpose of balancing is to arrange the modes such that the least important can be eliminated. By removing and reattaching modes in the manner described, modes are being retained that from a reduction standpoint should perhaps be removed. Only in such a situation as this, where the number of modes separated out is much less than the total, and where there is an obvious numerical advantage, should such high (or low) frequency modes be removed.

#### 4.1.3 Input/Output Selection

All of the steps taken thus far to improve a system’s numerical quality have involved its modes. Although removing rigid body and high frequency states requires manipulation of

the  $B$  and  $C$  matrices, the basic procedures were based entirely around the  $A$  matrix. If an eigenvalue problem is solved to find the complex conjugate frequencies of the system, then only the  $A$  matrix is required. This changes when solving a Lyapunov problem for the gramians; the quality of the input and output matrices must also be considered.

The first most basic step is scaling the input and output values. This is as simple as changing the units so that the values are on or near the order of 1.0. For example, many of the performance outputs are in meters for optical pathlength difference or wave front error, and in radians for wave front tilt. The actual performance values are most often on the order of nanometers or milli-arcseconds. By keeping the original units, an extra  $10^{-9}$  (m/nm) or  $4.85 \times 10^{-9}$  (rad/mas) are carried along needlessly in the calculations.

Another reason for scaling the units around 1.0 is to normalize the weights of the modes. Consider two cases where the performances units are many orders of magnitude apart: nanometers versus radians. As shown in the example transfer functions of Figure 4-4, the second mode, though barely observable for the first performance (OPD), dominates the second performance (WFT). It is obvious that the second mode should be retained in any reduction, but through the units it would be reduced out since the WFT in radians ( $2.06 \times 10^8$  mas) is much smaller than the OPD in nanometers.

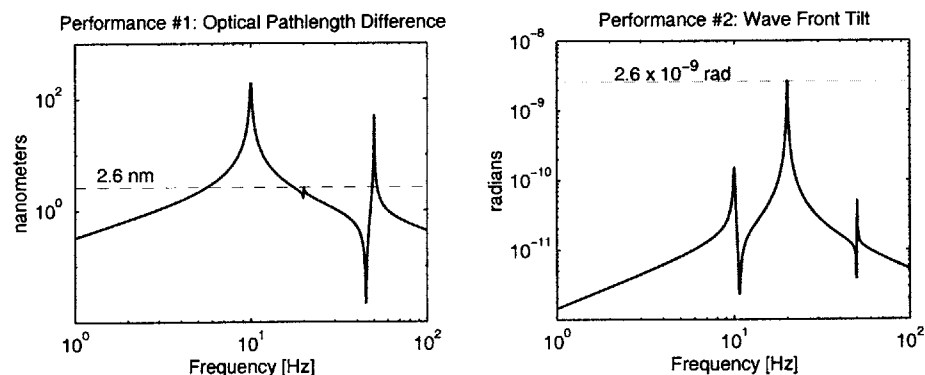


Figure 4-4: Sample transfer functions show the effect of units on the relative importance of modes.

These units can easily be changed by multiplying the appropriate row of the  $C$  matrix by the unit conversion factor. The same can be done for the columns of the  $B$  matrix; reaction wheel forces given in Newtons can be converted to milli-Newtons or micro-Newtons, as is warranted. Since the input magnitudes are usually closer to 1.0, in practice they were left in units of Newtons.

Another aspect of the conditioning of the  $B$  and  $C$  matrices is the choice of which inputs and outputs to use. This will certainly be dictated by what input/output relationship is under study. The choice (if one is available) will affect the balancing routines since the different transfer functions in a MIMO system may hold different modes to be more or less important. As the number of transfer functions grows, the list of modes which are considered important for any one of the relationships may grow. The list of modes which can be safely eliminated from all relationships naturally may shrink, constraining the amount the system can be reduced.

There is another factor in the input/output choice based on the balancing routine described in the next chapter. In the balanced truncation method of Section 5.3.2, only a certain number of states will be retained after balancing based on the relative magnitude difference between their singular values and the maximum singular value of the controllability gramian. That maximum value will change based on which control inputs are used. Take for example the controllability gramian singular values for SIM Version 2.0, the top 70 of which are shown in Figure 4-5. When only reaction wheel disturbances are input, the maximum value is  $6.4 \times 10^5$ ; when the PZT and voice coil actuator inputs are added, the maximum singular value jumps to  $1.3 \times 10^8$ , an increase of three orders of magnitude.

The controllability gramian singular values give an indication of how controllable individual states are. This jump in the values makes sense when the type of inputs are considered. The reaction wheel disturbances affect the states indirectly and do not have the authority to provide direct control on the optical train. The role of the optical actuators is exactly to provide direct control over part of the spacecraft, and their control authority is much greater; hence their larger singular values. Mallory provides a more in-depth look at sensor/actuator topology in [27].

If the number of states truncated is dependent on the maximum value, it is obvious that raising the threshold will cause more states to be removed. This is indeed the case. Using only the reaction wheel disturbance inputs, 1321 states will remain after balanced truncation. If the actuator inputs are included, that number will drop to 1104.

Besides preparing a system for balancing, model quality management also involves tracking the progress of a system through the various balancing and reduction routines. This will briefly be described next.

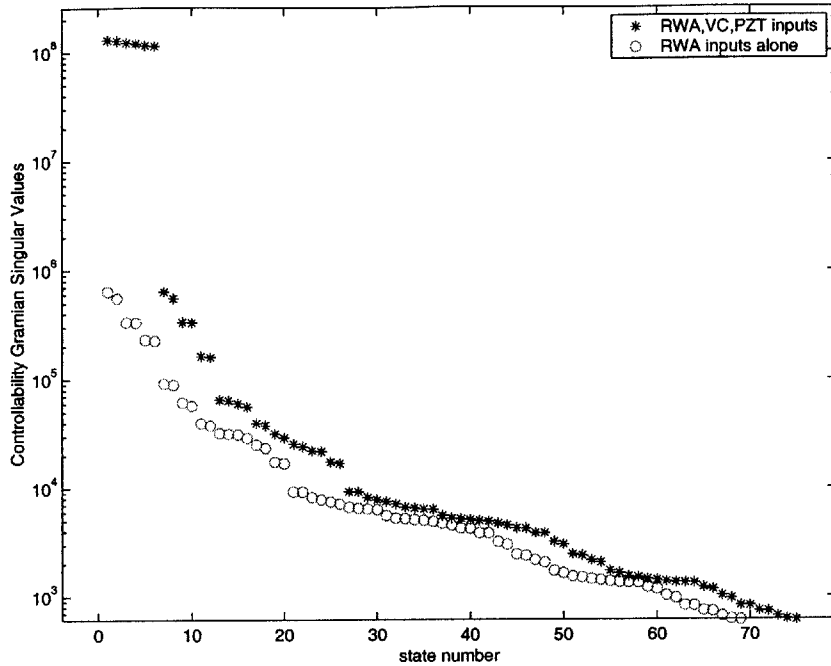


Figure 4-5: SIM Version 2.0 controllability gramian singular values, comparing reaction wheel inputs alone to reaction wheel and PZT and voice coil actuators.

## 4.2 Tracking Numerical Quality

Tracking numerical quality is not a complex process; indeed the basic metrics used in the DOCS analysis are quite simple. The purpose in including it is to recognize that any model may be grossly altered through the mathematical and transformation steps outlined in this and the next chapters. This alteration need not be the result of an error in implementation; if the system is too ill-conditioned, it is possible that solving for a balanced system that accurately maintains the shape of the original function is impossible. The previous section listed steps that can be taken to prevent this from happening. This section suggests simple tasks to identify a problem if it does occur.

The most simple device is to plot the transfer functions and compare the balanced and reduced systems with those of the original. This will be the approach most often used here. It allows a visual check to see if the frequencies, damping, and backbones have been accurately reproduced. The quality required is obviously dependent on the application of the system. Figure 4-6 is an example transfer function for SIM Version 2.2, showing the reaction wheel force disturbance in the x-direction to the Star OPD #1 performance output. The original, balanced, and reduced systems are all included. Though decibels are often



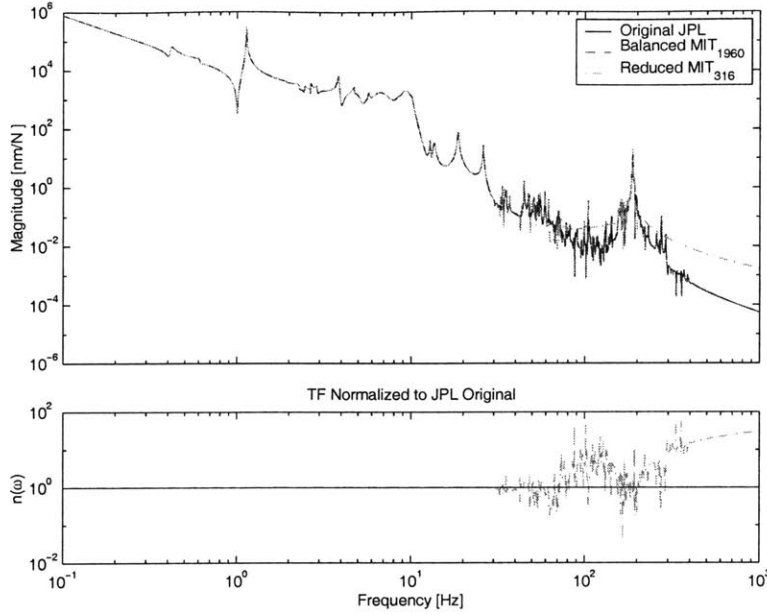


Figure 4-6: Transfer function of RWA  $F_x$  to Star OPD #1 for SIM model v2.2

used for proper Bode plots, transfer function magnitude  $|G(\omega)|$  will be used here. The plots are computed by solving the matrix equation,

$$G(\omega) = C(j\omega I - A)^{-1}B + D \quad (4.2)$$

through the frequencies  $\omega$ . The MATLAB `bode.m` command will be used most often to generate these plots.

In order to quantify the deviation from the original of a balanced or reduced system, the normalized value of the new transfer function to the original is plotted below the Bode plot.

$$n(\omega) = \frac{G_{orig}(\omega)}{G_{bal/red}(\omega)} \quad (4.3)$$

A value of 1.0 is maintained for zero deviation. As the dereverberated transfer function, or backbone of the reduced system drifts from the original, the normalized value will likewise drift from 1.0. Unless an exact match of every mode is required, the very first deviation is not necessarily indicative of the frequency beyond which the new system is unreliable. It is altogether probable that modes will be missing from a reduced system. The frequency at which the backbone deviates from 1.0 will, in general, be considered the limit of the system

accuracy. In the example figure, the 316-state reduced model seems to reach this point above 80 Hz, although it succeeds in capturing the strong mode at 187 Hz. No deviations are visible for the 1960-state balanced model; it is identical to the original.

The last method for tracking model quality is through the condition number, described in Section 3.2.2. Good numerical conditioning has been identified as a prerequisite for a system being balanced. The condition number allows this to be measured and can assist in the decision whether to eliminate low- or high-frequency modes. The desired value depends on the model and the circumstances; no attempt will be made to specify what the final number should be. In practice, values above  $10^{20}$  are considered very poor and will likely cause numerical difficulties for balancing routines. For instance, standard balancing routines routinely fail when the controllability and observability gramians have condition numbers as great as  $10^{34}$ . Values between  $10^{10}$  and  $10^{20}$  are preferred for gramian matrices, but are considered high for system  $A$  matrices. For an  $A$  matrix, Lyapunov solvers and eigensolvers work best when the condition number is less than  $10^{10}$ . Any order of magnitude reductions are desirable, and post-balancing condition number are usually less than  $10^5$ .

For example, Figure 4-7 shows the non-zero singular values for the SIM Version 2.2 model for two cases: one with RBMs and high-frequency actuator modes attached, and the other after these modes have been removed. The removal of the RBMs does not affect the condition number since it is defined by the non-zero singular values. Greater benefit comes from removing the high-frequency modes. The condition number falls from  $1.50 \times 10^8$  to  $3.93 \times 10^7$ . After balancing, the value will decrease further to  $2.43 \times 10^3$ . At this level no numerical difficulties are expected. Tracking the condition number will continue through the balancing routines of Chapter 5.

### 4.3 Summary

The quality of a model is defined here not in terms of whether it accurately captures the dynamics of the system it represents, but rather from the numerical standpoint of whether the model can successfully be run through various mathematical routines. The Lyapunov solver is of particular concern since it is required for gramian balancing. Preparatory steps can be taken on the model  $A$ ,  $B$ , and  $C$  matrices to improve their conditioning. Several basic metrics of tracking model quality are also mentioned. These are critical since the

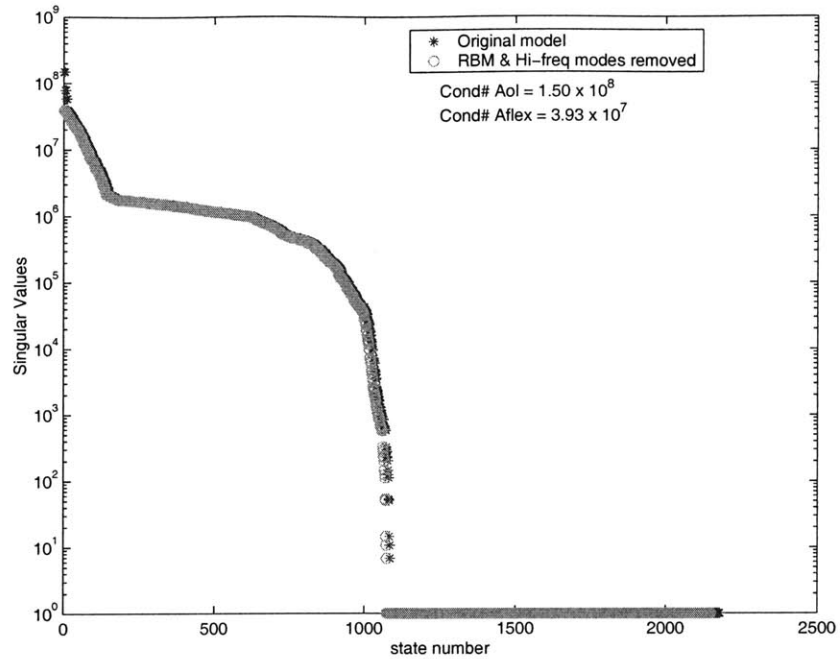


Figure 4-7: Singular values of SIM model v2.2  $A$  matrices. Original model with RBMs and high-frequency modes attached is compared to the model with those modes removed.

quality of the results from any analysis is only as good as the quality of the model used. Model quality management should be followed not only to ensure that various routines such as an eigensolver or Lyapunov solver work, but also to promote confidence in the final results.



## Chapter 5

# Balancing and Model Reduction

The primary goal of the balancing and reduction routines is to produce a model of lower order that still contains all of the relevant dynamics of the original model. When working with state-space systems, a reduction in the number of states translates to smaller  $A$ ,  $B$  and  $C$  matrices. Since the performances are usually sensitive to only a small subset of the state vector, the removal of extra states usually has little effect on the final analysis results.

There are several computational reasons for working with reduced models. Routines such as eigenvalue or Lyapunov solvers take on the order of  $n^3$  operations, where  $n$  is the number of states. Any reduction in the number of the states can save considerable time and computational expense. This dramatically speeds up the DOCS analysis such that iterations on a design can be examined in hours instead of days. Reduction also saves computer memory. For example, the full order  $A$  matrix for the SIM model takes over 37 megabytes of memory in MATLAB. Since it is not uncommon to have several models in the workspace at the same time, even computers with generous amounts of RAM can be quickly overwhelmed during calculations. Finally, balancing a model often improves the numerical conditioning of the matrices, whether or not the model is reduced thereafter. This helps prevent numerical errors that have nothing to do with the model itself, but rather the computational implementation.

### 5.1 Methods of Model Reduction

Model reduction can occur at many places once a FE model is constructed. Methods such as Guyan Reduction and Component Mode Synthesis [12] can be used to reduce the finite

element degrees of freedom directly. Guyan Reduction reduces the  $M$  and  $K$  matrices by eliminating those degrees of freedom (DOFs) whose inertia effects or masses are negligible. Component Mode Synthesis is used to describe the dynamics of an assembled structure when individual components are modeled separately. For example, the FE models for SIM's optical elements were made separate from those for the bus and instrument backpacks. A subset of the modes from the individual components are used to assemble the complete  $M$  and  $K$  matrices, and since not all modes are used, the size of the resulting matrices are thus reduced.

Once a model in second order form  $M\ddot{q} + C\dot{q} + Kq = F$  is cast into the state-space first order form  $\dot{x} = Ax + Bu$ , other methods of reduction can be employed. Internal Balancing Theory was first proposed by Moore [35] in 1981. The states are *balanced* so that the least controllable states are also the least observable, and can be removed. The balanced system is also numerically better conditioned. References [25, 52] describe implementations of this theory. Reference [19] describes a methodology for choosing which states to remove and derives analytical expressions for the Hankel Singular Values (described in the next section) given a system in modal form.

$$\ddot{\eta} + 2\zeta\omega\dot{\eta} + \omega^2\eta = \phi^T f \quad (5.1)$$

Moore's theory is one of the most popular methods for reduction and in the following sections a variant will be applied to large systems.

Another method for reduction is Component Cost Analysis (CCA) or a derivative called Modal Cost Analysis (MCA), described in a series of papers by Skelton [23, 45, 46, 44]. MCA determines the cost of each *component* of a system, where the components are usually individual modes. The cost can be defined in terms of the performance outputs  $y(t)$ ,

$$V = \lim_{t \rightarrow \infty} \mathcal{E}[v(t)] = \lim_{t \rightarrow \infty} \mathcal{E}[y^T(t)Qy(t)]$$

where  $\mathcal{E}$  is the expectation operator and  $Q$  is a weighing matrix. Individual components have cost  $V_i$ , and those modes with the lowest costs can be eliminated.

Reference [23] in particular suggests methods for using these reduction techniques on larger models where the typical balancing approach may fail. A comparison between

MCA/CCA techniques and the balancing methods described next would be useful, though was not attempted here.

## 5.2 Balancing Routines

Moore's internal balancing theory assumes that the spacecraft dynamics can be represented by a linear, time-invariant model of the form:

$$\begin{aligned}\dot{x} &= Ax + Bu \\ y &= Cx + Du.\end{aligned}\tag{5.2}$$

The  $A$  matrix is of the block form:

$$A = \begin{bmatrix} 0 & I \\ -\Omega^2 & -2Z\Omega \end{bmatrix}\tag{5.3}$$

where  $\Omega$  is the diagonal matrix of modal frequencies,  $Z$  is the diagonal matrix of damping coefficients, and  $I$  is the identity matrix. In this form the modes are uncoupled from one another and each is described by two states<sup>1</sup>  $[x_i, \dot{x}_i]^T$ . The goal of reduction is to remove the states which are the least important to the system. The relative importance of each state is determined by first computing the controllability and observability gramians of the system. These can be found by solving the steady state Lyapunov equations for  $W_c$  (controllability) and  $W_o$  (observability), as was done in Equations 3.22 and 3.23. These are rewritten here for convenience.

$$AW_c + W_c A^T + BB^T = 0\tag{5.4}$$

$$A^T W_o + W_o A + C^T C = 0\tag{5.5}$$

In control theory, controllable and observable are terms used to define the authority of a control actuator on a mode, and the observability of a mode to a feedback sensor. In this work, where the objective is to retain those modes that best couple the disturbance

---

<sup>1</sup>Note that the actual order of the states for the system described by Equation 5.3 is  $[\mathbf{x}, \dot{\mathbf{x}}]^T$ , where  $\mathbf{x}$  and  $\dot{\mathbf{x}}$  are vectors. The Real Modal Form, described by Equation 3.16, orders the individual modal displacement and velocity states next to each other.

source to the performance metrics, controllable refers to modes that are most disturbable and observable refers to those that participate most in the performance metrics.

The relative sizes of the eigenvalues of  $W_c$  then correspond to the amount that each state can be controlled/disturbed [41]. Similarly, the relative sizes of the eigenvalues of  $W_o$  correspond to the amount that each state can be observed or the amount it participates in the performance. Individual states that may only be slightly controllable may still be highly observable and vice versa. Removing the states that are only slightly controllable but very observable, for example, could affect the resulting transfer function and the input/output dynamics of the system. It should be recognized that the states themselves are mathematical entities that often do not directly represent the physical behavior of the spacecraft. A physical representation comes from the product of the state matrices  $A$ ,  $B$ , and  $C$  through

$$G(\omega) = C(sI - A)^{-1}B. \quad (5.6)$$

Since the states are mathematical constructs, they can be transformed in any manner desired just as long as the resultant behavior still produces the output  $G(\omega)$ . A state vector in which all of the elements are highly observable (a predominance of the  $C$  matrix) could be transformed such that the new state vector is highly controllable, (a predominance of the  $B$  matrix), with both states describing the same physical system whose physical modes may or may not be controllable by the actuators or observable by the sensors.

Ideally the states would be transformed in such a manner that the (mathematically) most controllable are also the most observable (or more appropriately, the states that are the most disturbable are also the most performable). The least controllable and observable could then be identified and safely eliminated. Internal balancing performs this step by setting both gramians equal to a single diagonal matrix. Since the eigenvalues of a diagonal matrix are simply the values along the diagonal, those values provide a direct measure of the relative importance of each state. Two methods to compute this *balanced* gramian are presented.

### 5.2.1 Gramian Transformations

Several methods are available to compute the balanced realization. All of them make use of basic transformation algebra in which a transformation matrix  $T$  changes the state vector



$x$ , usually in uncoupled modal form, to a new vector<sup>2</sup>  $\tilde{x}$ . The new vector can be of different length than the original, depending on the application. In basic balancing theory, the number of states is invariant to transformation. The basic relation between original and transformed state vectors follow.

$$\begin{aligned} x &= T\tilde{x} \\ \tilde{x} &= T^{-1}x \end{aligned} \tag{5.7}$$

By plugging this state vector into the state equations, Equation (5.2), the entire system transforms to:

$$\begin{aligned} \dot{\tilde{x}} &= T^{-1}AT\tilde{x} + T^{-1}Bu \\ y &= CT\tilde{x} + Du \end{aligned} \tag{5.8}$$

New state space matrices can be defined by  $\tilde{A} = T^{-1}AT$ ,  $\tilde{B} = T^{-1}B$ , and  $\tilde{C} = CT$ . The Lyapunov equations 5.4 and 5.5 can be likewise manipulated using  $T$ . Assume that the transformed controllability and observability gramians are described by the equations:

$$\begin{aligned} \tilde{A}\tilde{W}_c + \tilde{W}_c\tilde{A}^T + \tilde{B}\tilde{B}^T &= 0 \\ \tilde{W}_o\tilde{A} + \tilde{A}^T\tilde{W}_o + \tilde{C}^T\tilde{C} &= 0 \end{aligned}$$

Substitute in the matrix multiplication terms for  $\tilde{A}$ ,  $\tilde{B}$ , and  $\tilde{C}$ . Pre- and post-multiply by  $T$ , its transpose, and its inverse, respectively, in order to reduce many of the transformation terms to the identity matrix.

$$\begin{aligned} T ( T^{-1}AT\tilde{W}_c + \tilde{W}_cT^TA^TT^{-T} + T^{-1}BB^TT^{-T} ) T^T &= 0 \\ T^{-T} ( \tilde{W}_oT^{-1}AT + T^TA^TT^{-T}\tilde{W}_o + T^TC^TCT ) T^{-1} &= 0 \end{aligned}$$

---

<sup>2</sup>Note that the usage of  $T$  does not depend on whether  $T$  changes  $x$  to  $\tilde{x}$ , or  $\tilde{x}$  to  $x$ . As long as the chosen notation is followed, the algebra remains the same.

Simplify this and recognize the original Lyapunov Equations 5.4 and 5.5.

$$\underbrace{A \widetilde{W}_c T^T}_{W_c} + \underbrace{T \widetilde{W}_c T^T}_{W_c} A^T + B B^T = 0$$

$$\underbrace{T^{-T} \widetilde{W}_o T^{-1}}_{W_o} A + A^T \underbrace{T^{-T} \widetilde{W}_o T^{-1}}_{W_o} + C^T C = 0$$

This provides a relation between the original and transformed gramians:

$$\widetilde{W}_c = T^{-1} W_c T^{-T} \quad (5.9)$$

$$\widetilde{W}_o = T^T W_o T \quad (5.10)$$

The amount each state can be controlled or observed can thus change depending on the transformation matrix  $T$ . Internal balancing theory postulates that a transformation matrix  $T$  exists *such that the transformed gramians are equal to each other* and equal to a presumed diagonal matrix  $\Sigma_H$  containing the *Hankel Singular Values*, also known as the Second Order Modes. Because the eigenvalues of a diagonal matrix are the values along the diagonal, the Hankel Singular Values (HSV) provide a direct measure of the relative controllability *and* observability of each state. The values follow the rule  $\sigma_i^H > \sigma_j^H$ , where  $i < j$ .

$$\widetilde{W}_c = \Sigma_H = \widetilde{W}_o \quad (5.11)$$

$$\Sigma_H = \begin{bmatrix} \sigma_1^H & & \\ & \ddots & \\ & & \sigma_n^H \end{bmatrix} \quad (5.12)$$

The challenge is then to find this balancing transformation  $T$ . Two approaches to solve for it will be outlined.

### 5.2.2 Eigenvalue Approach

The steps in computing the balanced transformations are reduced to finding a proper transformation matrix  $T$ . A simple method using eigenvalues starts by squaring all of the terms in Equation 5.11. Since  $\widetilde{W}_c = \widetilde{W}_o$ , this can be written as follows.

$$\Sigma_H^2 = \widetilde{W}_c \widetilde{W}_o \quad (5.13)$$

Substitute in Equations 5.9 and 5.10 for the transformed gramians.

$$\Sigma_H^2 = T^{-1} W_c W_o T \quad (5.14)$$

Finally rearrange the terms in the following manner.

$$W_c W_o = T \Sigma_H^2 T^{-1} \quad (5.15)$$

The final equation can be recognized as a simple eigenvalue problem of the form  $A = SAS^{-1}$ . The squares of the Hankel Singular Values are the eigenvalues of the matrix formed by multiplying  $W_c$  with  $W_o$ . The transformation matrix  $T$  is the associated matrix of eigenvectors. This is a conceptually simple approach, however the eigenvalue solution required may not be as robust to ill-conditioned matrices as the next method. This second method using singular value decompositions is used in practice.

### 5.2.3 SVD Approach

Actual implementations of internal balancing use a variant described by Laub [25] and again by Zhou, et alia [52]. The end result is still that the transformed gramians equal the Hankel Singular Values. Instead of solving for the transformation matrix  $T$  by finding the eigenvectors of  $W_c W_o$ , two singular value decompositions are performed. The first is on  $W_c$ .

$$W_c = U_c S_c V_c^T \quad (5.16)$$

The singular values of  $W_c$  are contained in the diagonal matrix  $S_c$ . Since the gramians are symmetric matrices,  $V_c = U_c$  [48]. The equation is rewritten and the matrix  $R$  is defined as follows:

$$W_c = U_c S_c U_c^T = \underbrace{(U_c \sqrt{S_c})}_{R^T} \underbrace{(\sqrt{S_c} U_c^T)}_R \quad (5.17)$$

Instead of performing a SVD on the observability gramian directly, perform one on the augmented observability matrix.

$$RW_o R^T = U_{oo} S_{oo} V_{oo}^T \quad (5.18)$$

Again the symmetry of the gramian provides that  $U_{oo} = V_{oo}$ . Also, the square roots of the singular values in  $S_{oo}$  are equal to the Hankel Singular Values in  $\Sigma_H$ , so the equation can be written as:

$$RW_o R^T = U_{oo} \Sigma_H^2 U_{oo}^T. \quad (5.19)$$

The transformation matrix between the original and balanced systems is finally:

$$T = R^T U_{oo} \Sigma_H^{-\frac{1}{2}} = U_c S_c^{\frac{1}{2}} U_{oo} S_{oo}^{-\frac{1}{4}} \quad (5.20)$$

with the inverse computed as follows.

$$T^{-1} = \Sigma_H^{\frac{1}{2}} U_{oo}^T R^{-T} = S_{oo}^{\frac{1}{4}} U_{oo}^T S_c^{-\frac{1}{2}} U_c^T \quad (5.21)$$

Although not as obvious a result as the eigenvalue approach provides, it can be checked by using Equation 5.20 in the gramian transformation of Equation 5.9, and solved for the transformed gramian.

$$\begin{aligned} \widetilde{W}_c &= T^{-1} W_c T^{-T} \\ &= S_{oo}^{\frac{1}{4}} U_{oo}^T S_c^{-\frac{1}{2}} U_c^T (U_c S_c U_c^T) U_c S_c^{-\frac{1}{2}} U_{oo} S_{oo}^{\frac{1}{4}} \\ &= \sqrt{S_{oo}} \\ &= \Sigma_H \end{aligned}$$

Using this  $T$ , the transformed gramian equals the HSV matrix. Similar steps can show that  $\widetilde{W}_o$  also equals  $\Sigma_H$ , proving that the gramians are equal to each other.

## 5.3 Balancing Routines on Large Models

Although the balancing routine is relatively straightforward, it runs into difficulties when faced with large models such as NGST's or SIM's, when the number of states reaches several hundred or several thousand. The inversion of small singular values in Equations 5.20 and 5.21 produces errors in the standard implementation. A description of the errors and a solution are described.

### 5.3.1 Difficulties

One popular implementation is the `balreal.m` function in MATLAB, based off of Reference [25]. To illustrate the potential difficulties, two separate models of NGST were created: a 200-state version and a 600-state version. Both were run through `balreal.m`. The 200-state model successfully balanced. The Hankel Singular Values were returned and can be used to reduce the model. They are plotted in Figure 5-1. Only the first 66 states are retained. The resulting transfer functions look nearly identical to the original, as shown in Figure 5-2. Only the smallest modes have been removed, including several pole-zero cancellations such as at 3 Hz.

When the 600-state model is input to `balreal.m` however, an error always occurs with the admonition that the “`system must be reachable`”. This unreachability, or uncontrollability, results from zero singular values of the controllability gramian,  $W_c$ . `Balreal.m` first performs a Cholesky decomposition on the gramians; since this decomposition requires positive definiteness, any zero singular values would produce an error. A zero singular value or eigenvalue represents a state that cannot be controlled. A useful test is to consider the rank of the gramian. The 200-state model has 188 states after the rigid body modes are removed, and the rank of its  $W_c$  matrix is 188, or full rank. The 600-state model has 588 flexible states, but its rank is only 556. This rank-deficiency is indicative of uncontrollable states.

As the size of the system grows larger, numerical inaccuracies may give some finite value to the singular values of these uncontrollable states. These values may still be many orders of magnitude smaller than those of truly controllable states, however. This causes errors in the previously described balancing routine. The transformation matrix  $T$  from Equation 5.20 requires an inversion of the HSV matrix, or more precisely of the singular values  $S_{oo}$  of the

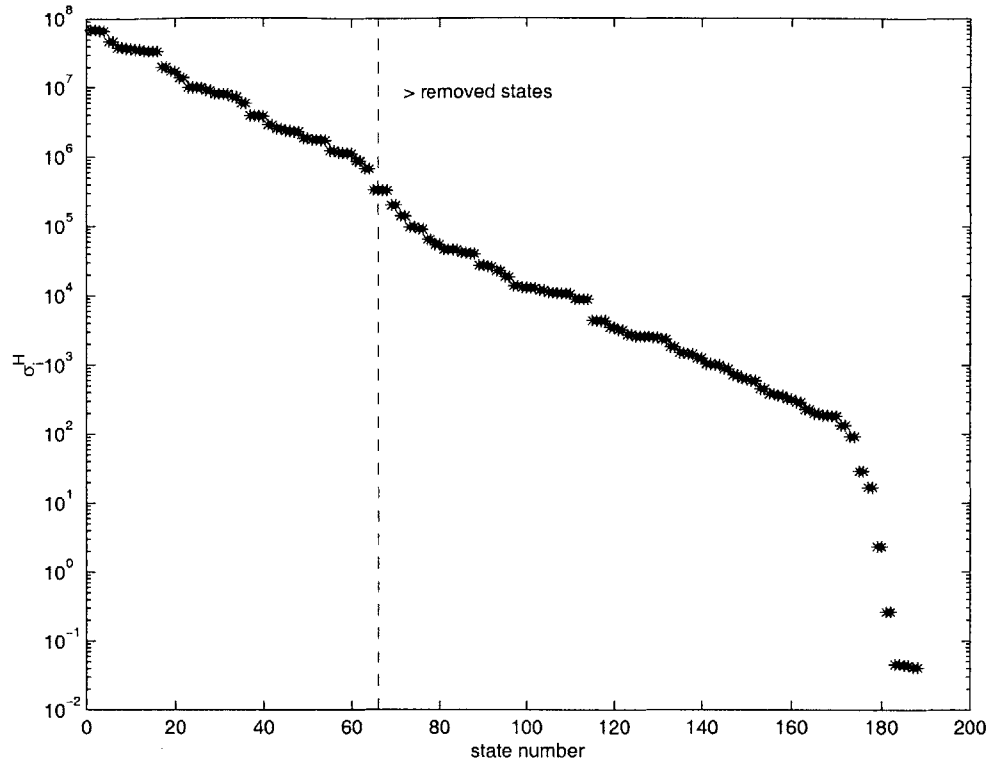


Figure 5-1: Hankel Singular Values for ngst603ss 200-state model

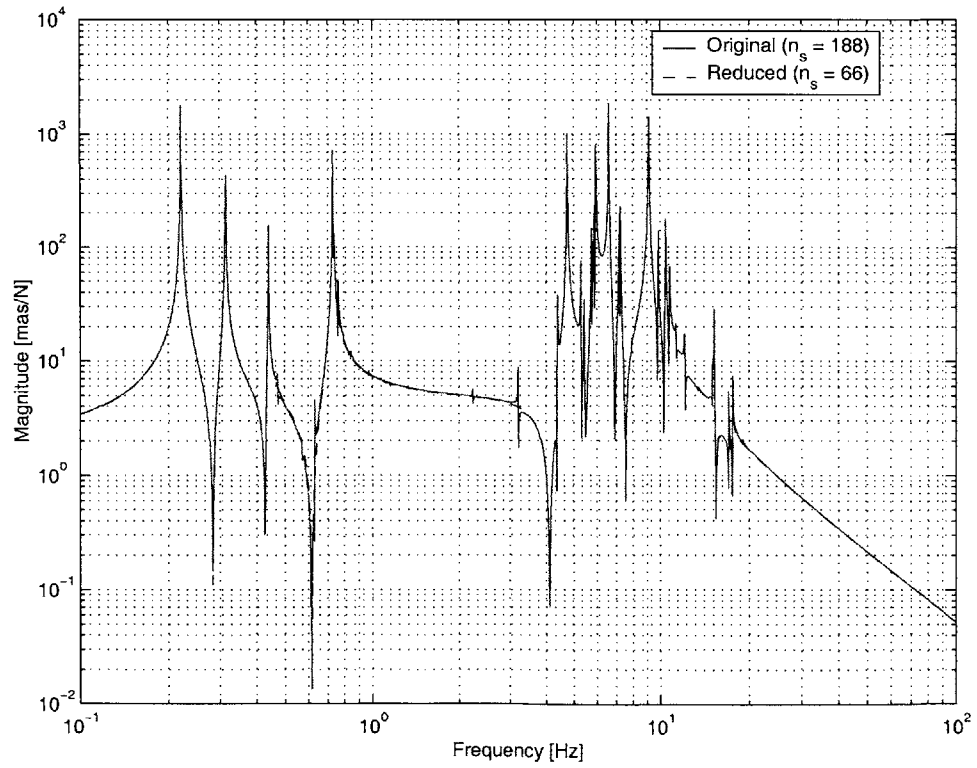


Figure 5-2: RWA force X to centroid X transfer function for ngst603ss 200-state model

augmented observability gramian  $RW_oR^T$ . A zero singular value would not allow a solution at all, where a very small singular value may produce a result, but that result could be highly inaccurate. In effect, the smallest and most numerically uncertain values would dominate the transformation. For example, the augmented observability singular values  $S_{oo}$  for the 600-state model are plotted in Figure 5-6. The values drop from a magnitude of  $10^{15}$  to  $10^{-22}$ . Since the relative floating point accuracy of MATLAB is only  $2.22 \times 10^{-16}$ , a 37 order of magnitude difference from largest to smallest values means that the smallest values are not guaranteed to be accurate<sup>3</sup>.

In order to balance large models then, it is necessary to account for these uncontrollable states with very small singular values. A method to do this is described next.

### 5.3.2 Balanced Truncation Method

In order to successfully balance an ill-conditioned model, Mallory [27] developed the *balanced truncation* method, illustrated in Figure 5-3. The method builds the transformation matrix  $T$  by eliminating the smallest gramian singular values *before* balancing takes place. Pre-balancing operations on the system ensure that no important states are removed at this step. Once the problematic singular values have been removed, a pseudo-inverse can be used in place of the inverse in Equation 5.20 to build the transformation matrix  $T$ .

Since the least controllable states corresponding to the smallest singular values would likely be eliminated from the system during reduction anyway, a check is incorporated into the method once the controllability singular values (Equation 5.16) are computed. Those values less than a user-defined tolerance are set equal to zero:

$$\bar{S}_c = \text{diag}[\sigma_{c_1}, \sigma_{c_2}, \dots, \sigma_{c_m}, 0, \dots, 0] \quad (5.22)$$

where for all  $i \leq m$ ,  $\sigma_{c_i} > \text{tol}_c$ . The key assumption is that the least controllable states are also not highly observable, so would not be retained in a reduced model even after balancing. This is further ensured by *pre-balancing* the system before the computation of any gramians.

The pre-balancing option takes a system whose  $A$ -matrix is in  $2 \times 2$  block diagonal form,

---

<sup>3</sup>Note that the largest and smallest numbers *possible* in MATLAB are on the order of  $10^{\pm 308}$ . The floating point accuracy is the limit between two numbers such that one can be added to the another and their sum recognized by MATLAB.

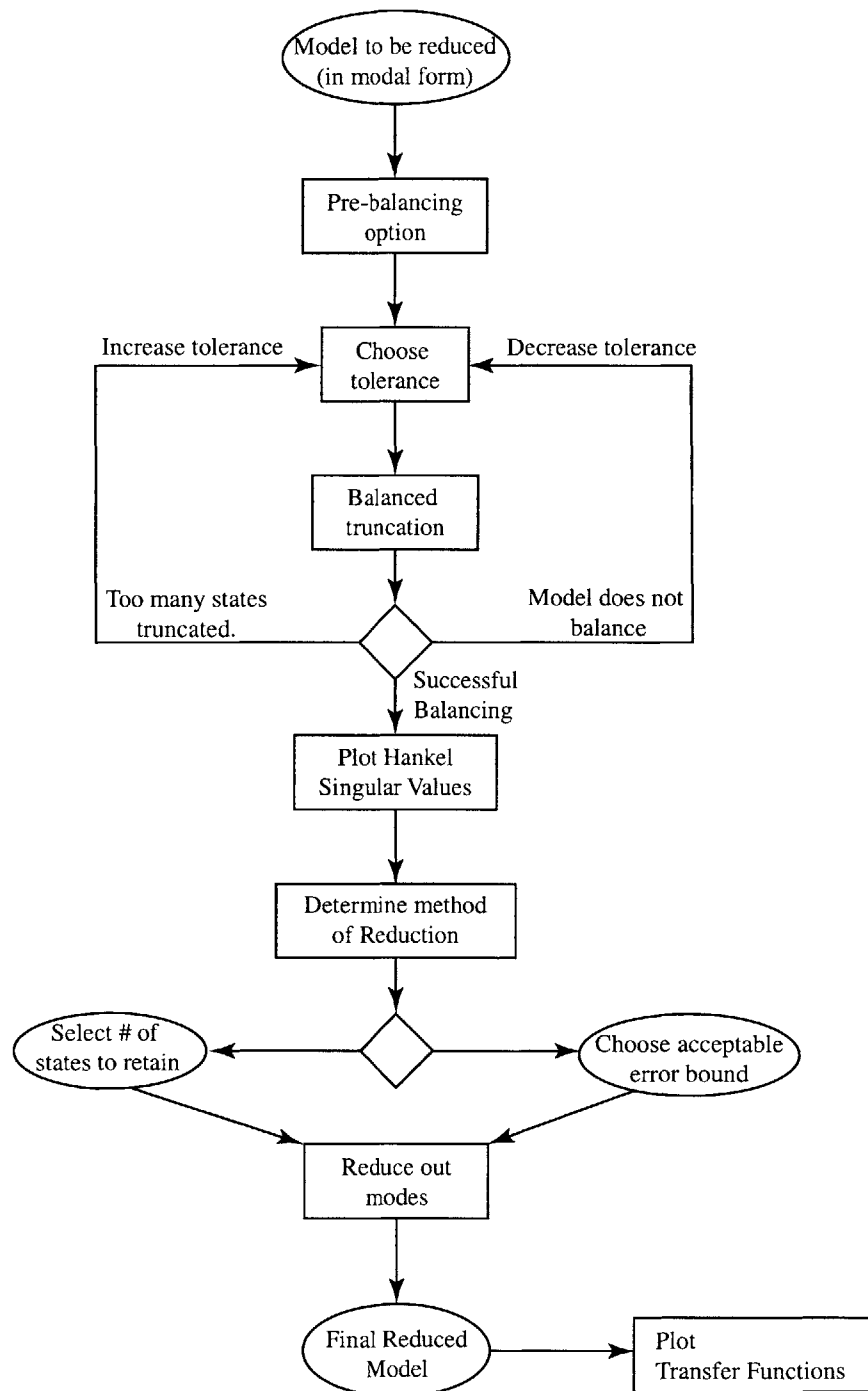


Figure 5-3: Outline of the balanced truncation routine.



such as a  $2^{nd}$  order modal or real modal form (see Equations 3.15 or 3.16 for examples) and balances the inputs and outputs of each mode using the standard routines. This transforms most of the states so that none are strongly observable yet lightly controllable. Those blocks that are entirely uncontrollable or unobservable are not pre-balanced. This ensures that these states will be easily identified by the truncation tolerance. Once the entire system gramians are computed, the pre-balanced states will already be transformed so that no highly observable states are truncated in Equation 5.22.

The next step is to calculate the augmented observability gramian via:

$$(\bar{S}_c^{\frac{1}{2}} U_c^T) W_o (U_c \bar{S}_c^{\frac{1}{2}}) = U_{oo} S_{oo} V_{oo}^T \quad (5.23)$$

and those augmented observability singular values below a certain tolerance are similarly set equal to zero.

$$\bar{S}_{oo} = \text{diag}[\sigma_{oo1}, \sigma_{oo2}, \dots, \sigma_{ooq}, 0, \dots, 0] \quad (5.24)$$

where for all  $j \leq q$ ,  $\sigma_{ooj} > \text{tol}_{oo}$ .  $\text{tol}_c$  is usually set less strict than  $\text{tol}_{oo}$  to lessen the chance of removing a lightly controllable but still strongly observable state. This results in  $q < m$ ; fewer singular values remain after the second truncation than after the first.

The inverses of the diagonal matrices  $\bar{S}_c$  and  $\bar{S}_{oo}$  can be computed using the pseudo-inverse of Section 3.2.1.

$$\bar{S}_c^\dagger = \text{diag}[\frac{1}{\sigma_{c1}}, \frac{1}{\sigma_{c2}}, \dots, \frac{1}{\sigma_{cm}}, 0, \dots, 0] \quad (5.25)$$

$$\bar{S}_{oo}^\dagger = \text{diag}[\frac{1}{\sigma_{oo1}}, \frac{1}{\sigma_{oo2}}, \dots, \frac{1}{\sigma_{ooq}}, 0, \dots, 0] \quad (5.26)$$

This allows calculation of the transformation matrix  $T$  and its inverse via Equations 5.20 and 5.21. Zeros in the singular value matrices would produce columns of zeros in  $T$ , so the final step is to produce a truncation matrix  $T_t$  which eliminates these needless zero columns.

$$T_t = \begin{bmatrix} I_{q \times q} \\ 0_{(n-q) \times q} \end{bmatrix} \quad (5.27)$$

The final transformation matrix and its pseudo-inverse are,

$$\bar{T} = U_c \bar{S}_c^{\frac{1}{2}} U_{oo} (\bar{S}_{oo}^\dagger)^{\frac{1}{4}} T_t \quad (5.28)$$

$$\bar{T}^\dagger = T_t^T \bar{S}_{oo}^{\frac{1}{4}} U_{oo}^T (\bar{S}_c^\dagger)^{\frac{1}{2}} U_c^T \quad (5.29)$$

Instead of a  $n \times n$  square transformation matrix, the final transformation matrix is rectangular  $n \times (n - q)$ . This means that the transformed  $\tilde{A}$  matrix will be  $q \times q$  (Figure 5-4). So instead of a balanced realization with the same number of states as the original system, the new realization will have fewer. In return for a numerically conditioned model that can be successfully balanced, some information about the system is lost. Further reduction will usually be necessary, since no more states should be removed than are necessary for successful balancing. This further reduction can happen on the open loop structural plant model, or preferable after disturbance and control states have been appended to the open loop model, so that the modes in the final disturbance-to-performance system are properly weighted.

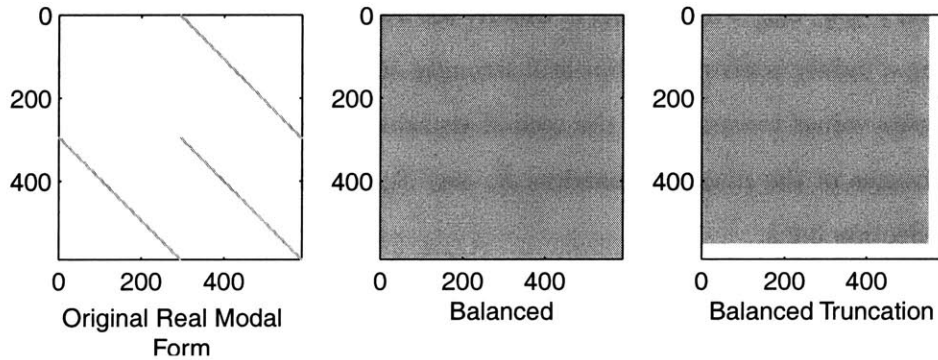


Figure 5-4: Structure of  $A$  matrices through balancing. The original matrix in real modal form is sparse. Complete balancing would produce a fully populated matrix. The balanced truncation method creates a fully populated matrix of smaller size.

## 5.4 Reducing the Model

Since the number of states remaining after balanced truncation is likely to be larger than desired for a dynamics analysis, reduction is still required. The amount of reduction can be chosen based on the Hankel Singular Values, plotted for `ngst603ss` in Figure 5-6. Since the relative magnitude of the HSVs indicates the relative importance of each state, those values

which are much smaller than others can be safely removed. For smaller order problems there can exist distinct steps in the curve that denote the boundary between important and extraneous states. For larger models, the values tend to slope continuously downward with no abrupt steps. The challenge is how to determine the number of states to remove.

There are three principal methods for this determination:

1. Reduce to a necessary level
2. Maintain transfer function accuracy
3. Allow a given performance error

The first method is to reduce the model to whichever size is necessary for further analysis. For example, the size of modern state-based controllers depends on the number of states in the plant being controlled. In order to design a controller with a minimum number of states, a small plant state vector is required. Another reason may be computational; if a great many analyses must be run with a model, such as a disturbance analysis at many reaction wheel speeds, then the necessary time and resources would be reduced if a smaller design model could be used. Although removing the majority of states from a large model may truncate many modes in the transfer function, the most important will always remain by virtue of the gramian balancing. Even in a large model, most of the performances are affected by only a small number of critical modes, as will be seen in Chapter 7. As long as these modes are retained, such aggressive reduction of a system may be permissible, but should always be checked by plotting and examining transfer functions.

The second method is to reduce the model to the smallest number of states required to keep the transfer functions nearly identical to the original, full-state system. Any unobservable modes would not appear in the transfer function, so there would be no errors if they are removed. Whether very small modes can be removed depends on the required level of fidelity. At lower frequencies, smaller modes may be reduced out due to near pole-zero cancellations. This was the case with the NGST 200-state model in Figure 5-2. At higher frequencies, the roll-off of the dereverberated transfer function, or the transfer function backbone, reduces the relative magnitude and hence the importance of many modes. This is often the area where differences between the original and reduced models are first noticeable; many of the NGST and SIM reduced models lose fidelity at higher frequencies. This

loss is considered acceptable since the rolloff also lessens the effects of the higher frequency modes on the performances<sup>4</sup>. Also, because of numerical inaccuracies with eigensolvers, the highest frequency modes will usually not be as accurate, so the impetus to keep them in a reduced model is less.

Both of these reduction methods rely on subjective inputs from the user. The question, “how many retained states are good enough?” depends on how the model will be used, what role different frequency regions play in the analysis, and ultimately on engineering judgement.

The final method of reduction is more quantitative in nature. It computes the number of states to retain by finding the RMS errors that will result because of reduction. Given an acceptable amount of error, the amount of reduction is automatically calculated. This procedure begins by computing the RMS performances as will be done in the disturbance analysis of Chapter 7. For the  $i^{th}$  performance metric, the RMS performance can be given as

$$\sigma_{z_i} = (C_{zd,i} \Sigma_q C_{zd,i}^T)^{\frac{1}{2}} \quad (5.30)$$

where the matrix  $C_{zd}$  provides the disturbance-to-performance outputs from a system described by Equation 5.2, and  $\Sigma_q$  is the state covariance matrix found using the Lyapunov equation

$$A_{zd} \Sigma_q + \Sigma_q A_{zd}^T + B_{zd} B_{zd}^T = 0. \quad (5.31)$$

Note that this equation is identical to Equation 5.4 which computes the controllability gramian  $W_c$ , meaning that  $\Sigma_q = W_c$ .

Balancing is a similarity transformation, which means that the transformation changes the states, but should not change the input-output relationship. The *balanced* state covariance matrix  $\Sigma_{\tilde{q}} = \tilde{W}_c = \Sigma_H$  should produce output results identical to the original system.

$$\sigma_{z_i} = \tilde{\sigma}_{z_i} = (\tilde{C}_{zd,i} \Sigma_{\tilde{q}} \tilde{C}_{zd,i}^T)^{\frac{1}{2}} \quad (5.32)$$

---

<sup>4</sup>As will be seen, the high frequency region around 187 Hz does contribute in the SIM model. However because those modes have higher HSVs, they are successfully retained in all reduced models.

Although the outputs from the original and balanced systems are equal to each other, this will not be the case for the reduced system. By removing the states related to the lowest  $\sigma_i^H$ 's, the contributions of those states to the total output values are also lost<sup>5</sup>. The output relation for the reduced system is written

$$\bar{\sigma}_{z_i} = (\bar{C}_{zd,i} \Sigma_{\bar{q}} \bar{C}_{zd,i}^T)^{\frac{1}{2}} \quad (5.33)$$

but  $\bar{\sigma}_{z_i} \neq \sigma_{z_i} = \tilde{\sigma}_{z_i}$ . Since  $\Sigma_{\bar{q}}$  is computed using the reduced  $\bar{A}$  and  $\bar{B}$  matrices, it no longer is equal to  $\tilde{W}_c$  or  $\Sigma_H$ , nor are the matrices the same size. The next step is to determine how large an error results from eliminating a given number of states.

Reference [16] describes a method whereby this relationship is computed. The error between the performances  $\tilde{\sigma}_{z_i}$  of the balanced system and those from the reduced system,  $\bar{\sigma}_{z_i}$  with  $k$  retained states, can be written as

$$\varepsilon_{RMS} = \Delta\sigma_{z_i} = \tilde{\sigma}_{z_i} - \bar{\sigma}_{z_i} = (\bar{\sigma}_{z_i}^2 + \tilde{C}_{zd,i} \Sigma_E \tilde{C}_{zd,i}^T)^{\frac{1}{2}} - \bar{\sigma}_{z_i} \quad (5.34)$$

where  $\Sigma_E$  contains only those Hankel Singular Values that represent states eliminated from the balanced system.

$$\Sigma_E = \begin{bmatrix} 0 & & & & & \\ & \ddots & & & & \\ & & 0 & & & \\ & & & \sigma_{k+1}^H & & \\ & & & & \ddots & \\ & & & & & \sigma_n^H \end{bmatrix} \quad (5.35)$$

The relative error between balanced and reduced systems can be found via

$$\frac{\Delta\sigma_{z_i}}{\sigma_{z_i}} = \frac{\Delta\sigma_{z_i}}{\tilde{\sigma}_{z_i}} = 1 - \frac{\bar{\sigma}_{z_i}}{(\bar{\sigma}_{z_i}^2 + \tilde{C}_{zd,i} \Sigma_E \tilde{C}_{zd,i}^T)^{\frac{1}{2}}}. \quad (5.36)$$

This relation requires that the reduced RMS performances  $\bar{\sigma}_{z_i}$  already be computed. Since the goal is to determine how many states should be retained *before* reduction takes place,

---

<sup>5</sup>Contributions would also be lost by truncating states in the balancing routine. Because of the limited number of states that are reduced at that point, and because of their relative unimportance, their contribution is assumed negligible.

Reference [16] derives a conservative error bound on the change in RMS performance over the *reduced* performances, based on the Hankel Singular Values themselves.

$$\frac{\Delta\sigma_{z_i}}{\bar{\sigma}_{z_i}} < \frac{1}{2} \frac{\sum_{i=k+1}^n \sigma_i^H}{\sum_{i=1}^k \sigma_i^H} \quad (5.37)$$

This error bound uses the  $1^{st}$  through  $k^{th}$  retained HSVs, as well as the  $(k+1)^{th}$  through  $n^{th}$  eliminated HSVs, where  $n$  is the number of states of the balanced truncated system. This relation says that for  $k$  retained states, the resulting error of the RMS performance due to the reduction of states will be  $100 \times (\Delta\sigma_{z_i}/\bar{\sigma}_{z_i})$  percent. Tables 5.1 and 5.2 list several percentage errors and the number of resulting states for both the NGST and SIM models. Not ice in these table that tolerable errors ( $< 1\%$ ) result even after substantial reduction. This shows how the final performances usually are driven by only a small subset of the total state vector.

Once a vector of eliminated states is decided upon, the actual reduction can be performed using either brutal truncation or static condensation. As the name implies, brutal truncation directly removes a state from the system by removing those rows and columns of the  $\tilde{A}$ ,  $\tilde{B}$ , and  $\tilde{C}$  matrices related to that state. This can be done in MATLAB using the `modred.m` function, or can be performed by multiplying the full state matrix by a truncation matrix  $T_e$ .

$$\begin{aligned} \bar{x}_{(1 \times k)} &= T_e \tilde{x}_{(1 \times n)} \\ T_e &= \begin{bmatrix} I_{k \times k} & 0_{k \times (n-k)} \end{bmatrix} \end{aligned}$$

The reduced state matrices are  $\bar{A} = T_e^T \tilde{A} T_e$ ,  $\bar{B} = T_e^T \tilde{B}$ , and  $\bar{C} = \tilde{C} T_e$ . Note that  $T_e^{-1} = T_e^T$ .

Static condensation attempts to include the DC gain of each eliminated state in the response of the system. If the system is written in terms of (R)etained and (E)liminated states,

$$\begin{aligned}
\begin{bmatrix} \dot{x}_R \\ \dot{x}_E \end{bmatrix} &= \begin{bmatrix} A_{RR} & A_{RE} \\ A_{ER} & A_{EE} \end{bmatrix} \begin{bmatrix} x_R \\ x_E \end{bmatrix} + \begin{bmatrix} B_R \\ B_E \end{bmatrix} u \\
y &= \begin{bmatrix} C_R & C_E \end{bmatrix} \begin{bmatrix} x_R \\ x_E \end{bmatrix}
\end{aligned} \tag{5.38}$$

Static condensation assumes that the dynamics of the eliminated states are very fast and quickly reach steady state.

$$\dot{x}_E = 0$$

This constrains the lower matrix equation of Equation 5.38 so that,

$$0 = A_{ER} x_R + A_{EE} x_E + B_E u$$

or rewriting this,

$$x_E = -A_{EE}^{-1} (A_{ER} x_R + B_E u). \tag{5.39}$$

Substituting this back into the upper matrix equation of Equation 5.38 yields the reduced system,

$$\begin{aligned}
\dot{x}_R &= [A_{RR} - A_{RE} A_{EE}^{-1} A_{ER}] x_R + [B_R - A_{RE} A_{EE}^{-1} B_E] u \\
y &= \begin{bmatrix} C_R & -C_E A_{EE}^{-1} A_{ER} \end{bmatrix} x_R + [-C_E A_{EE}^{-1} B_E] u
\end{aligned} \tag{5.40}$$

Note that a  $\bar{D}$  term results from this calculation. This can be removed using a technique described in [22].

Despite the apparent advantage of static condensation, in practice brutal truncation worked much better. No DC gain loss was seen since most of the reduced modes are at higher frequencies with small DC gain contributions. In fact, static condensation produced a worse fit to the transfer function at high frequencies. An example is shown in Figure 5-13. It is possible that for a very flexible spacecraft, even the eliminated states violated the “fast

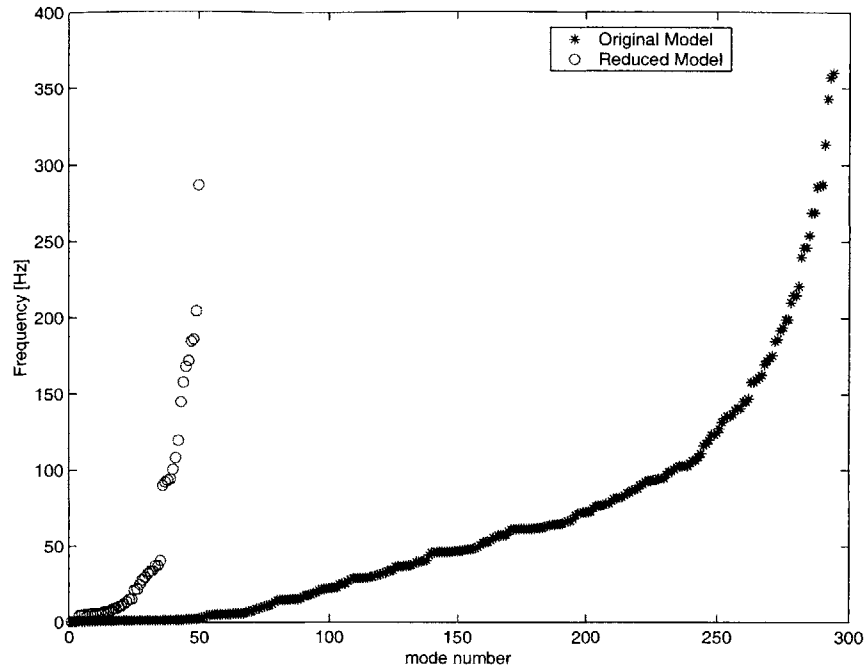


Figure 5-5: Modal Frequencies of the `ngst603ss` 600-state and reduced 100-state models.

dynamics” assumption by having long settling times. An investigation into the reasons for static condensation’s poor performance was not attempted here, but would be worthwhile. All of the systems used in the DOCS analysis were reduced using brutal truncation.

## 5.5 Spacecraft Examples

The reduced models of two space telescopes, NGST and SIM, are provided as examples of the balanced truncation routines. Both are large models that could not be balanced using the traditional `balreal.m`. Using the techniques described, the number of states in each model could be reduced to nearly 1/6 of the original number and produce a good fit to the original transfer functions.

### 5.5.1 NGST

The 600-state NGST model (with 588 states after rigid body mode (RBM) removal) has 294 flexible modes between 0.2210 Hz and 360.4 Hz. The modal frequencies are plotted in Figure 5-5. The first 50 modes are all below 3 Hz; most of these are sunshield modes coming from the expanded sunshield model included in `ngst603ss`.



As was described in the previous section, the numerical ill-conditioning of the gramians prevents standard routines from successfully balancing this model. The singular values of the controllability gramian  $W_c$  and of the augmented observability gramian  $W_{oo} = RW_oR^T$  are plotted in Figure 5-6. Since the ratio of the largest to smallest singular values gives the condition number, a quick look at the maxima and minima of the curves indicates how numerically poor the matrices are. The singular values for  $W_c$  drop from nearly  $10^8$  to under  $10^{-11}$  for a condition number of  $4.04 \times 10^{18}$ . The singular values for  $RW_oR^T$  have a much wider spread; they drop from nearly  $10^{16}$  to  $10^{-21}$ , for a condition number of  $7.83 \times 10^{36}$ . It was these very small values that caused the Cholesky decomposition in `balreal.m` to produce an error.

These small values will be removed by the balanced truncation method in order to get the system to balance. The tolerances used to determine which to remove are based on the distance a value is below the largest singular value. A tolerance of  $tol_c$  for the controllability gramian would cause all those singular values less than  $\sigma_{c,max} \cdot tol_c$  to be set to zero. To ensure that strongly observable modes are not prematurely removed,  $tol_c$  is always set to be less strict than the tolerance for the augmented observability gramian. In the present routine,  $tol_c = tol_o/100$ . To balance the NGST 600-state model,  $tol_o = 10^{-20}$  and  $tol_c = 10^{-22}$ . This means that all of those controllability singular values below  $\sigma_{c,max} \cdot tol_c = (9.09 \times 10^7) \cdot 10^{-22} = 9.09 \times 10^{-14}$  are set to zero. Since there are no singular values this small, none are removed.

Because no controllability singular values were removed, there is a full set of augmented observability singular values  $S_{oo}$ . Their threshold for truncation is  $\sigma_{o,max} \cdot tol_o = (7.77 \times 10^{15}) \cdot 10^{-20} = 7.77 \times 10^{-5}$ . All values of the curve  $S_{oo}$  less than this were removed. As can be seen in the Figure 5-6, the resulting Hankel Singular Values are fewer in number than  $S_{oo}$ . Of the original 588 states, only 552 remain after balanced truncation, meaning that 36 were considered too unobservable to keep in the system. Note that since the HSVs are the square root of  $S_{oo}$ , no value is less than square root of  $7.77 \times 10^{-5}$ , or  $8.81 \times 10^{-3}$ .

It should not be goal of balanced truncation to remove many states; only the fewest number than will allow balancing should be eliminated at this stage. If a tolerance is chosen so large (closer to  $\sigma_{c,max}$  for  $S_c$ ) that too many states are removed, it should be decreased so that more states are retained. Likewise, if the tolerance is too small (further from  $\sigma_{c,max}$  for  $S_c$ ) so that many of the very small singular values are retained, the system

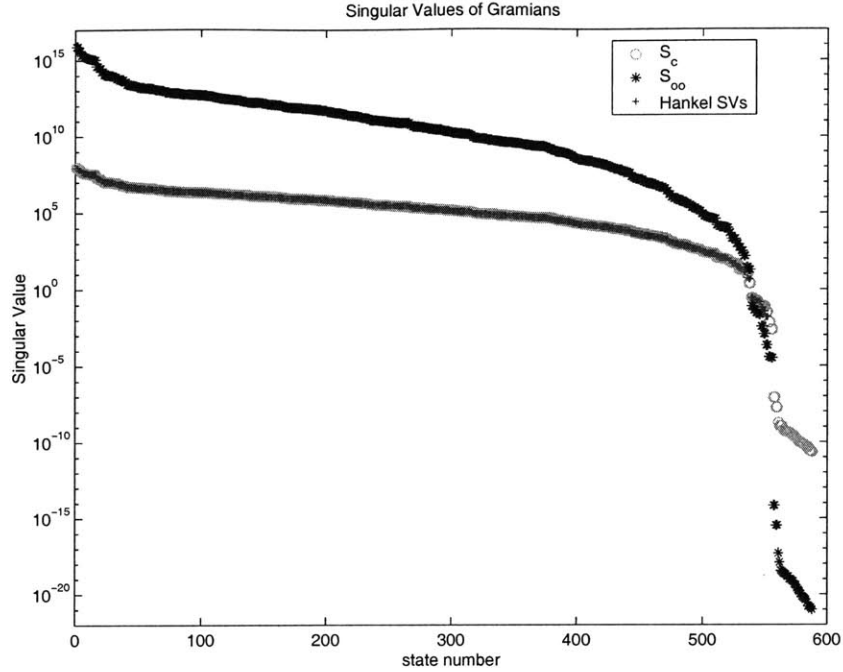


Figure 5-6: Singular Values of the controllability and augmented observability gramians, compared to the final Hankel Singular Values

still may fail to balance. The level of tolerance can be iterated on to produce an appropriate balanced model.

The transformation matrix is computed and the truncated balanced system with 552 states is realized. The first benefit of balancing is the improved conditioning of the system  $A$  matrix, as shown by its singular values in Figure 5-7. The condition number has dropped from  $5.13 \times 10^6$  to 1631, an improvement of over three orders of magnitude. Likewise the condition number of both gramians, now both equal to the HSV matrix, is  $5.97 \times 10^9$ . The quality of the balanced transfer functions is seen in Figure 5-8, where the legend subscripts specify the number of states. For the input/output pair of reaction wheel force  $X$  to centroid  $X$ , the balanced transfer function with 564 states (552 flexible states plus 6 RBMs) matches the original 600-state model perfectly. The removal of states has not changed any of the dynamics in any of the transfer functions.

It is of interest to note that all of the gramian calculations used the fast Lyapunov solver described in Section 3.3. The  $2 \times 2$  block diagonal states were divided into larger blocks of  $28 \times 28$  for faster results. The two gramian calculations took 7.8 and 8.8 seconds, respectively.

This balanced model is reduced using brutal truncation. Equation 5.37 can be used to

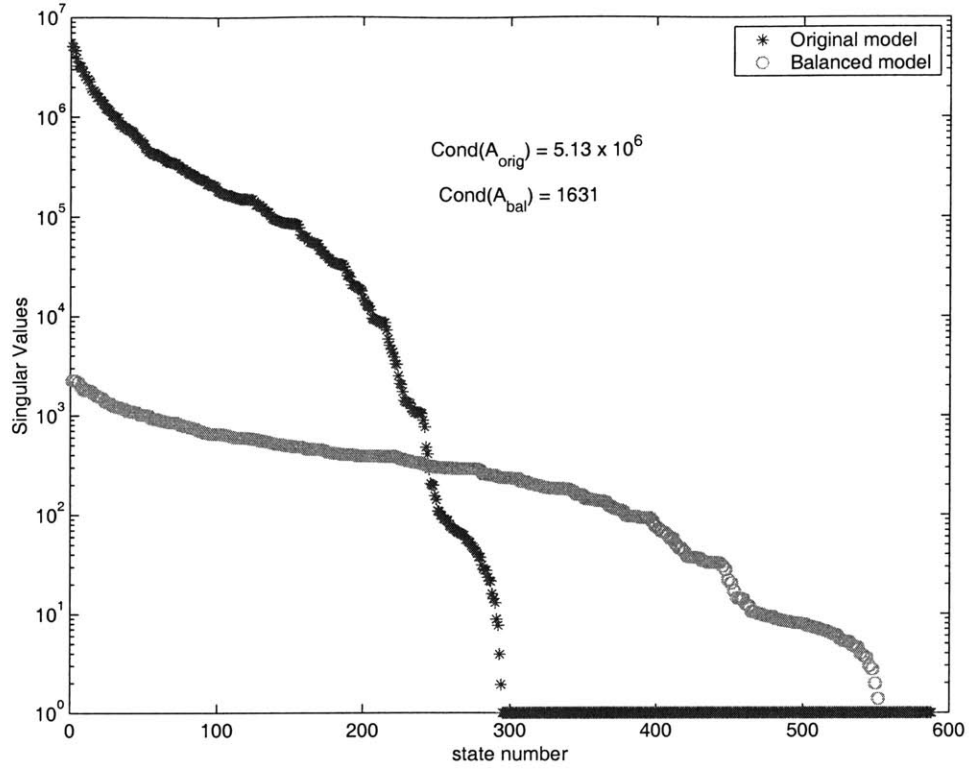


Figure 5-7: Original and balanced  $A$ -matrix singular values for `ngst603ss`.

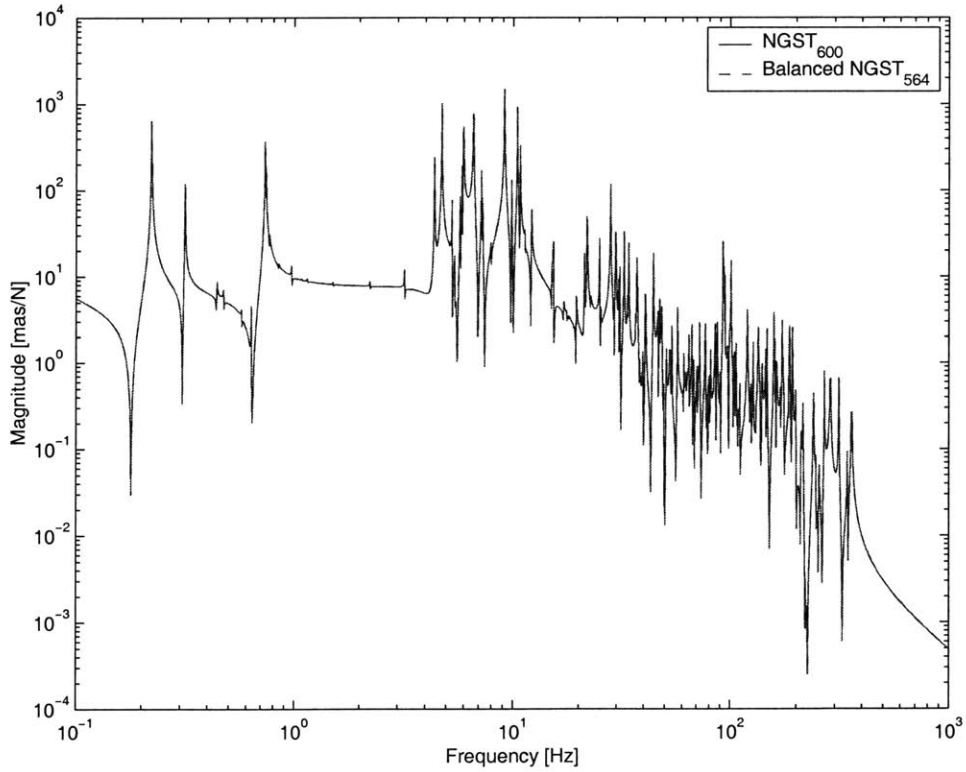


Figure 5-8: Full order versus Balanced Transfer Function: RWA  $F_x$  to Centroid X

determine what the maximum RMS output error would be as a result of removing states. Table 5.1 lists the percentage errors for a given number of retained states. A dramatic reduction from 600 to 25 states would create nearly a 30% error; for most applications this would likely be considered unacceptable. The error due to reduction to 100 states is only 7% which, depending on the application, may be permissible, and removing half of the states causes less than a 1% error. This indicates that the majority of the states do not contribute significantly to the outputs, so their removal should not effect the analysis results.

Table 5.1: Effects of number of kept states for the NGST 600-state model

# Retained States	% RMS Error <
25	27.1
50	14.7
100	6.94
150	3.33
300	0.254
350	0.0944

Figures 5-9 though 5-12 are representative transfer functions (TFs) for a system reduced to 100 states. For low frequencies (below 10 Hz), most of the highly observable modes are retained. Those that are eliminated include slightly observable modes and near pole-zero cancellations. For higher frequencies (above 10 Hz) the modal density dramatically increases in each plot. This increase occurs as the transfer function backbone begins to rolloff. The smaller magnitudes of many of these higher frequency, densely packed modes makes them less important to the final outputs. With only 100 states kept, these higher modes are expected to be the first observable modes to be eliminated. As seen in the figures, this is indeed the case; this reduced system captures less than half of the higher frequency peaks. For the modes that are retained, high frequency and low, the reduced model succeeds in capturing the frequencies and damping very well. The backbone of each transfer function is also captured well, as can be seen in the normalized magnitude plots below each transfer function. Although each missing mode produces a brief spike on the normalized plots, there are few regions in which a broader deviation of the normalized curve indicates a deviation in the backbone.

The amount of reduction depends on how many modes need to be kept. For accurate,

high authority control design, more modes should be kept since removing modes not only eliminates their magnitude information, but also eliminates the phase loss they contribute. Since this is critical in the assessment of stability robustness, the elimination of the higher frequency modes would be unacceptable, and the 100-state system obviously inadequate. For a disturbance analysis in which only several critical modes contribute to the final results, this system is a good representation of the full-order model.

Figure 5-13 shows a comparison of brutal truncation versus static condensation between models reduced to the same number of states. The two methods agree with each other reasonably well through 40 Hz. Beyond that the discrepancies begin to grow, although the peaks of the largest modes are captured equally well. At higher frequencies static condensation fails to maintain the backbone of the curve as well as brutal truncation. This grows worse beyond 200 Hz, as the statically condensed system fails entirely to roll off. This behavior was also noticed with the SIM model. One possible reason could be the presence of a state-space  $D$  term in the statically reduced system. This feed-through term acts as a constant in the transfer function, preventing the system from rolling off beyond a certain level. While incorporating the  $D$  term back into the  $A$ ,  $B$ , and  $C$  matrices (using a method in [22]) should theoretically allow further roll-off, no changes were evident when this process was attempted (see Figure 5-13). Further examination of the assumptions inherent in static condensation are required for a greater understanding of this behavior.

### 5.5.2 SIM

The DOCS tools were used on several models of the SIM spacecraft. In the present work, both versions 2.0 and 2.2 of the model were examined. Both were of a size that required reduction before any of the DOCS tools could be employed. A description of the balancing and reduction for both models follows herein, along with representative transfer functions showing the quality of the reduction.

#### SIM Version 2.0

The version 2.0 SIM model has 2150 flexible modes. A plot of the non-zero frequencies, first plotted in Figure 4-3 is included again in Figure 5-14. The high-frequency modes described in Section 4.1.2 are plainly visible above 1000 Hz. As described in that section, these 12 modes (24 states) are removed prior to balancing for better numerical conditioning of the

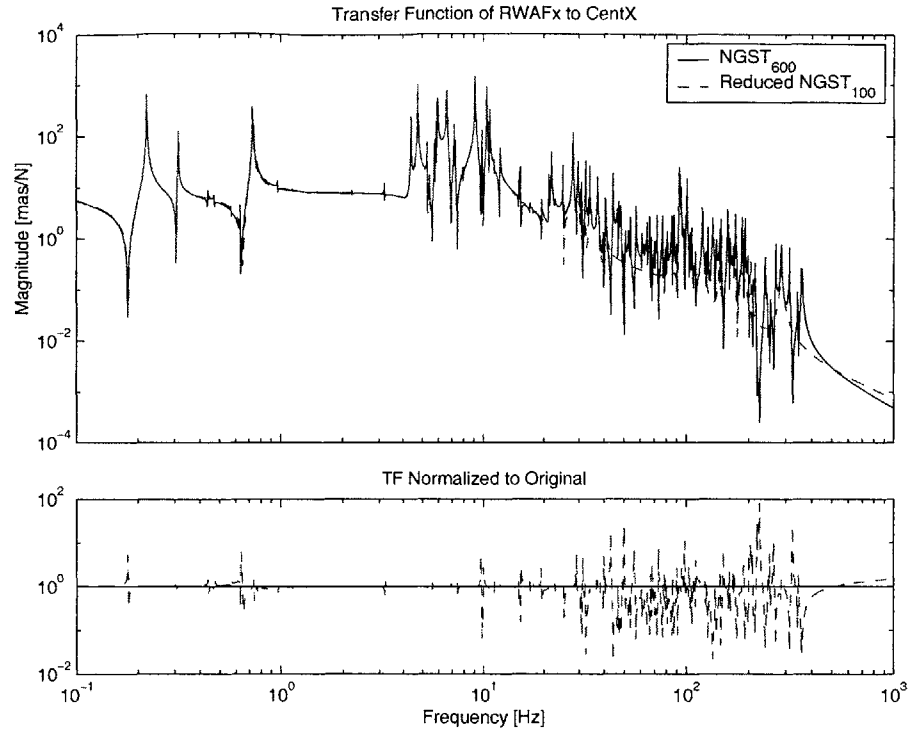


Figure 5-9: Transfer Function between RWA force X and centroid X, NGST 100-state reduced model.

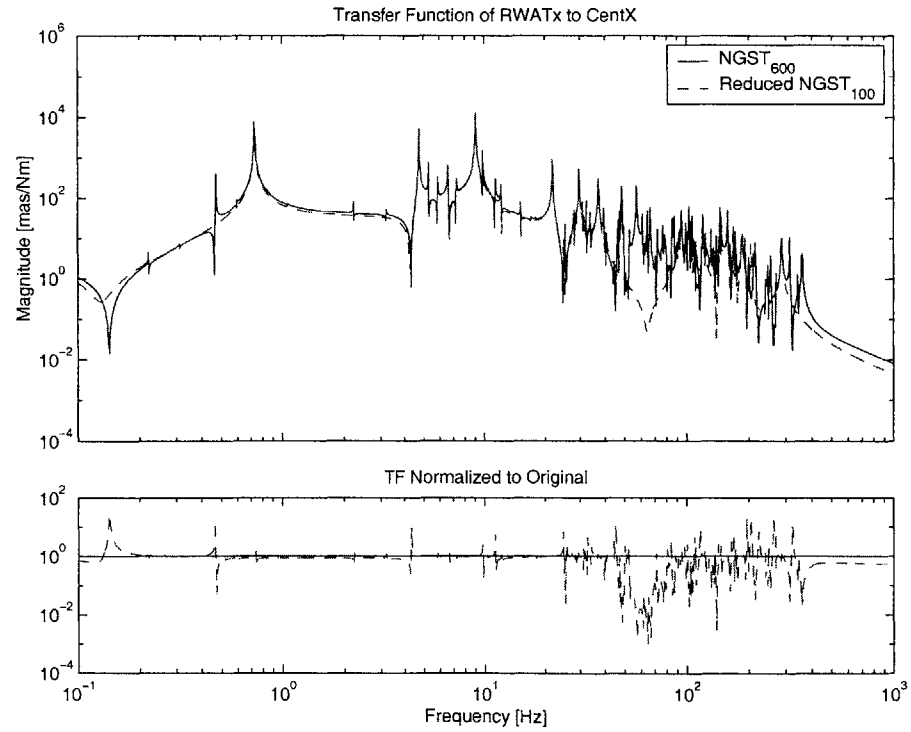


Figure 5-10: Transfer Function between RWA torque X and centroid X, NGST 100-state reduced model.

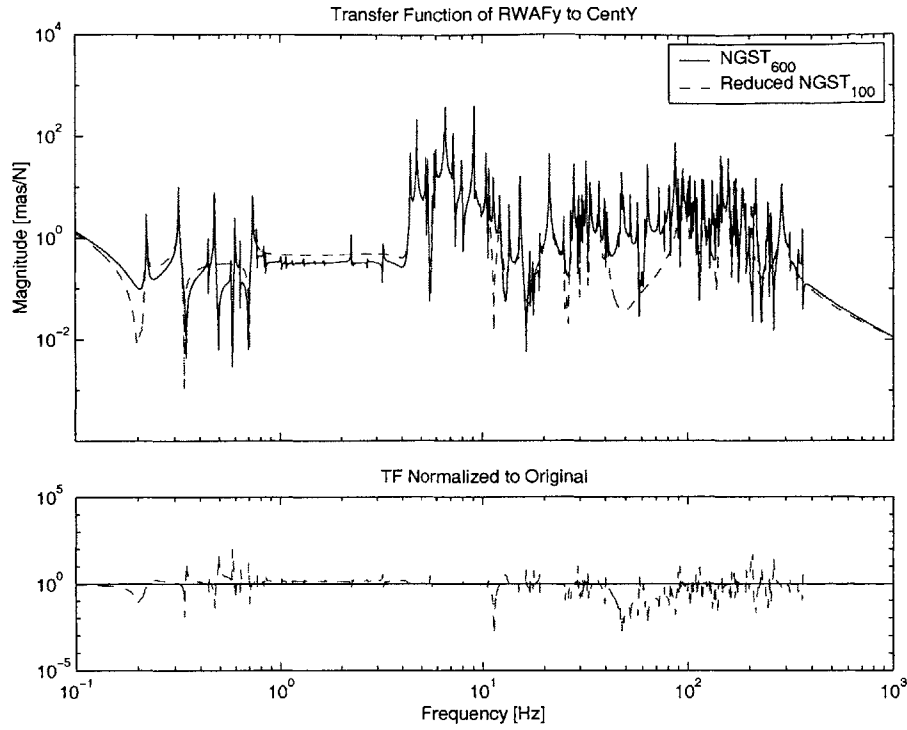


Figure 5-11: Transfer Function between RWA force Y and centroid Y, NGST 100-state reduced model.

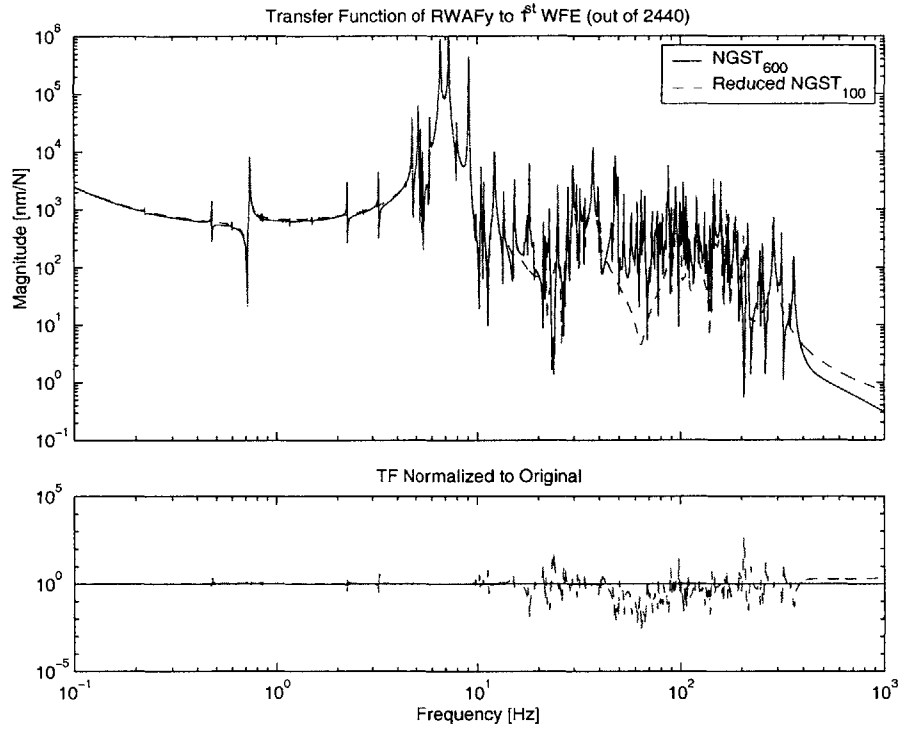


Figure 5-12: Transfer Function between RWA force Y and the first ray's WFE, NGST 100-state reduced model.

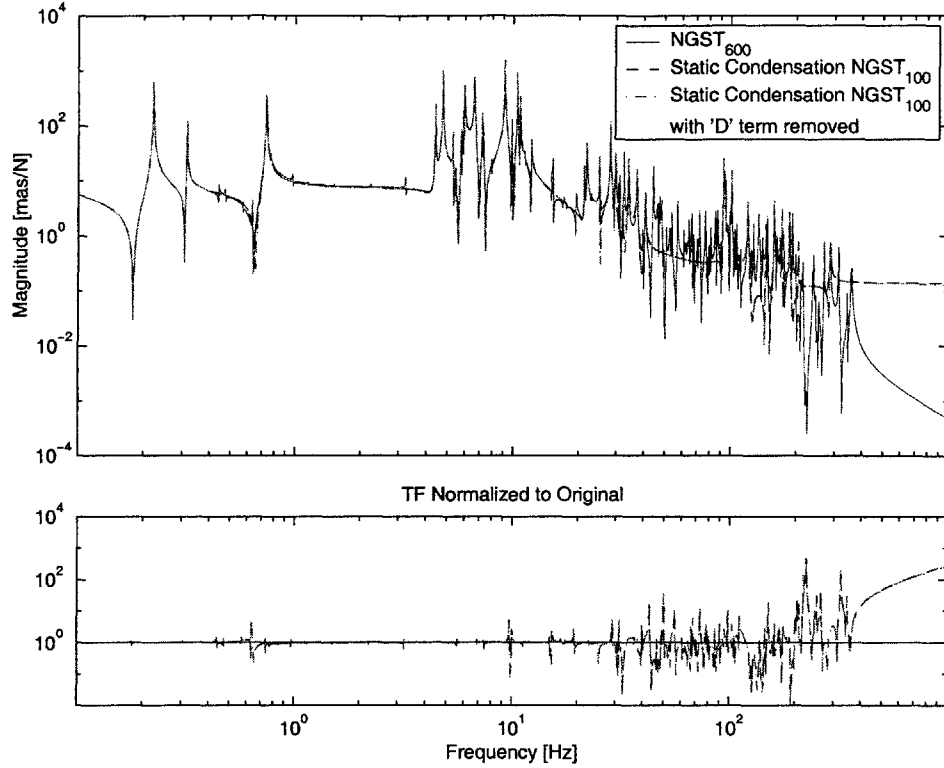


Figure 5-13: A comparison of reduction methods: brutal truncation versus static condensation for the NGST 600-state model, RWA force X to centroid X.

system, so that only 2126 states are balanced. The majority of the modes are below 240 Hz. The reduction in modal density after this frequency causes the “kink” in the curve around mode #930. Between 100 Hz and 240 Hz the modal density results from mirror mount modes randomly scattered through the range [20].

The singular values of the controllability and augmented observability gramians are shown in Figure 5-15. The condition number of  $W_c$  is  $2.66 \times 10^{28}$ , and the condition number of  $W_{oo} = RW_oR^T$  is  $2.34 \times 10^{40}$ . Because this model will be examined with optical loops closed, the system inputs are the reaction wheel disturbances plus the voice coils and PZT stack actuators. The choice of inputs was discussed in Section 4.1.3, and by including the actuators the maximum controllability singular value, and hence the controllability gramian condition number, is increased. This accounts in part for the very poor conditioning of these matrices.

The tolerance was set low in order to retain many modes. For the controllability singular values  $S_c$ ,  $tol_c$  was set to  $10^{-22}$  (1/100 of the tolerance for  $S_{oo}$ ). With a maximum singular value of  $1.30 \times 10^8$ , all singular values less than  $\sigma_{c,max} \cdot tol_c = 1.30 \times 10^{-14}$  would be



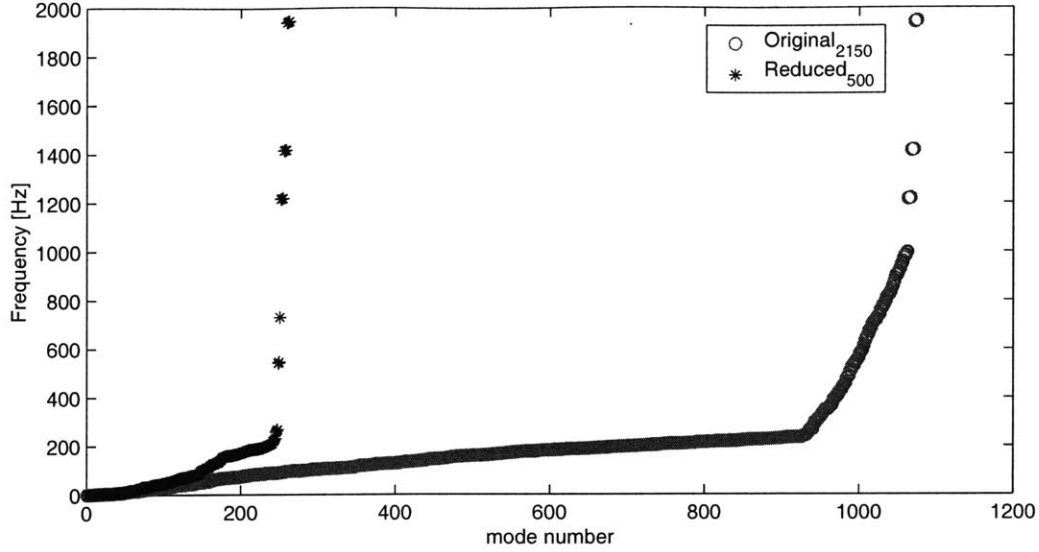


Figure 5-14: Comparison of original and reduced frequencies for SIM v2.0.

truncated. In this case there were 16 essentially uncontrollable states that fell below this threshold and were removed. Because the augmented observability gramian is formed using the controllability singular values, this reduction means that  $S_{oo}$  will be smaller than  $S_c$ ; there are 2120 non-zero singular values in  $W_{oo}$  compared to 2126 in  $W_c$ .

The great difference between the largest and smallest values in  $S_{oo}$  means that many values will be truncated even with a tolerance as relatively small as  $tol_o = 10^{20}$ . The maximum singular value is  $1.68 \times 10^{16}$ , so that all values below  $\sigma_{o,max} \cdot tol_o = 1.68 \times 10^{-4}$  are removed. Of the original 2126 states, this leaves only 1104 remaining after the balanced truncation. The Hankel Singular Values, plotted over the gramian singular values in Figure 5-15, abruptly end at state number 1104. Balancing has already reduced the model by nearly half. It is interesting to note that had only the reaction wheel disturbances been input into the system, the resulting improvement in the gramian condition numbers would have allowed 1321 states to be retained. More states could be retained by lowering the tolerance further, but care must be taken to ensure that the system is not so ill-conditioned as to not balance.

The conditioning of the system  $A$  matrix improves by four orders of magnitude due to balancing (Figure 5-16). Reducing the system to 500 states only marginally improves the condition number.

Table 5.2 shows that the effect of reduction on the final RMS errors is very slight. The

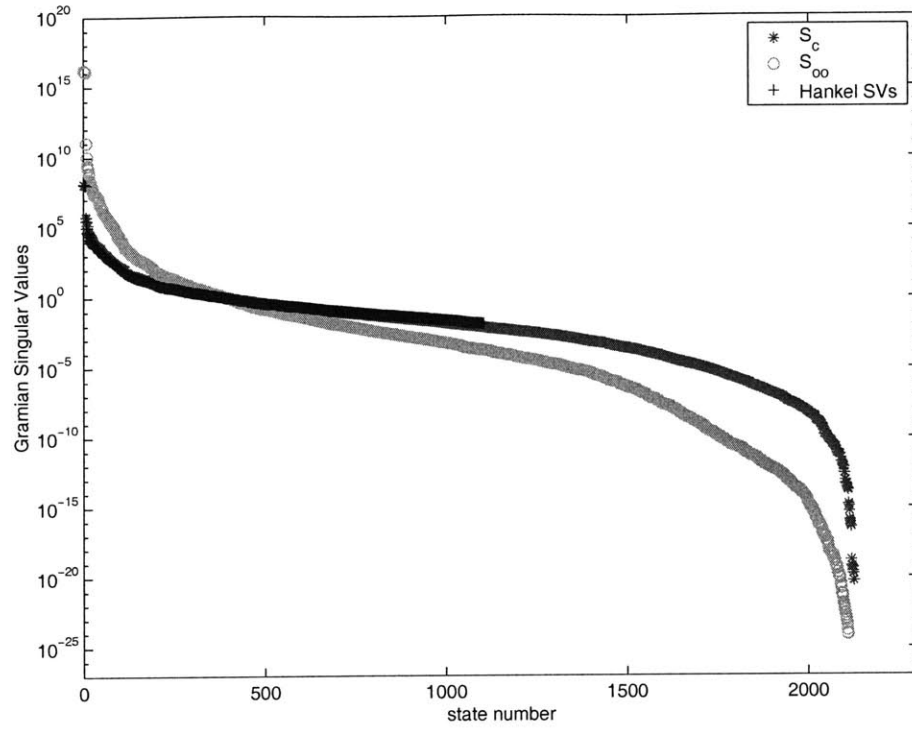


Figure 5-15: Controllability and augmented observability singular values and Hankel Singular Values for SIM v2.0

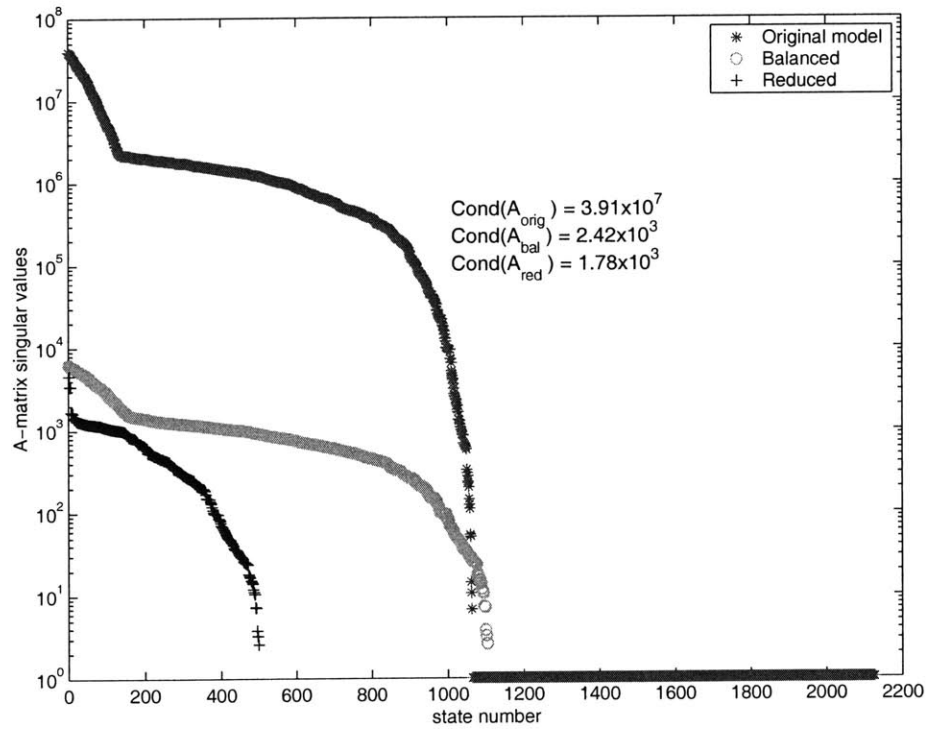


Figure 5-16: Singular values of the system  $A$  matrices.

system can be reduced to as few as 25 states and the error should be no greater than 0.01% of what it would be with the balanced system. Compare this with the reduction errors of NGST, Table 5.1, which are much more sensitive to the number of states removed. In both systems the high frequency modes are among the first to be eliminated. Comparing the high frequency dynamics of the two spacecraft, NGST's transfer functions (Figures 5-9 through 5-12) roll off slower than SIM's (Figure 5-17 through 5-19). The higher modes are stronger and more important for NGST, so it can be expected that their absence will have a stronger affect on the final results. Except for the frequency region around 187 Hz, most of SIM's high frequency modes are many orders of magnitude smaller than those at lower frequencies, so their removal is not as much of a concern.

The SIM model was finally reduced to only 500 states with an associated error of less than 0.00001%. This was chosen over the more aggressive levels of reduction because the weighting of the modes by the controllers and disturbance sources has not yet occurred. This level maintains the accuracy of the transfer functions while still reducing the system to a more manageable size.

Table 5.2: Effects of number of kept states on the SIM Version 2.0, 2148-state flexible model.

# Retained States	% RMS Error <
25	$9.06 * 10^{-3}$
50	$2.26 * 10^{-3}$
100	$3.00 * 10^{-4}$
150	$1.09 * 10^{-4}$
300	$1.93 * 10^{-5}$
500	$4.21 * 10^{-6}$

The modes that remain are shown in the plot of natural frequencies, Figure 5-14. The first 21 frequencies modes are all retained and the frequencies are nearly identical to those of the original 2150 state (1075 mode) system. Modes start to be missed after this point, though the remaining frequencies still match up with frequencies of the original. Nearly all of the retained modes are below 270 Hz; beyond that frequency only three modes have survived the reduction. As will shortly be seen in plots of the transfer functions, there are very few observable modes above this point even in the original system. Note that the 24 states corresponding to those modes above 1 kHz have been appended to the 500 state

reduced model.

Both balanced and reduced plots of three representative transfer functions are shown in Figures 5-17, 5-18, and 5-19. They are compared to transfer functions provided by JPL of the full order system. The balanced transfer functions all closely match the originals. Small deviations due to the truncation are evident, but are isolated to individual modes that are missing; there is no gross deviation of the curves. All of the reduced models are nearly identical to the originals up to 100 Hz. Beyond that point the effect of missing modes becomes more evident, and, for Figures 5-17 and 5-18, large deviations appear at frequencies above 200 Hz.

Despite these deviations, all of the critical frequencies are captured. Specifically, note the large peaks in the transfer functions between 180 and 200 Hz. In Chapter 7, this high frequency range will be shown to be critical to performance. The frequencies and damping of these peaks are successfully captured in all of the reduced transfer functions. The disturbance analysis will show that the critical frequencies result from several low-frequency modes, and those high-frequency modes around 187 Hz, all of which are captured.

## **SIM Version 2.2**

The same reduction routine was performed on the SIM Version 2.2 model. This new system has 2184 states. Before reduction, 12 rigid body modes and 24 modes above 1 kHz were all removed. The remaining 2148 states were reduced using a tolerance of  $10^{-25}$  for  $W_{oo}$  and  $10^{-27}$  for  $W_c$ . This tolerance is much lower compared to previous examples, and indeed is much lower than the floating point accuracy of MATLAB. In practice however, it did not seem to affect the accuracy of the final transfer functions and it allows for more states to be retained in the balanced realization. After balancing, a total of 1960 states remain. Lowering the tolerance meant that only a tenth of the states were truncated, compared to nearly a half in the previous example.

Three separate levels of reduction were computed to illustrate the gradual worsening of the system accuracy as more modes are eliminated. Figure 5-20 shows a relatively mild reduction, to only 1000 flexible states (1063 states after RBMs and high-frequency modes are reattached). Figure 5-21 shows a more aggressive reduction to 0.001% RMS error, which results in 572 retained flexible states (608 states in the complete system). Finally, Figure 5-22 shows the most aggressive reduction to 0.01% RMS error, which results in 280 retained

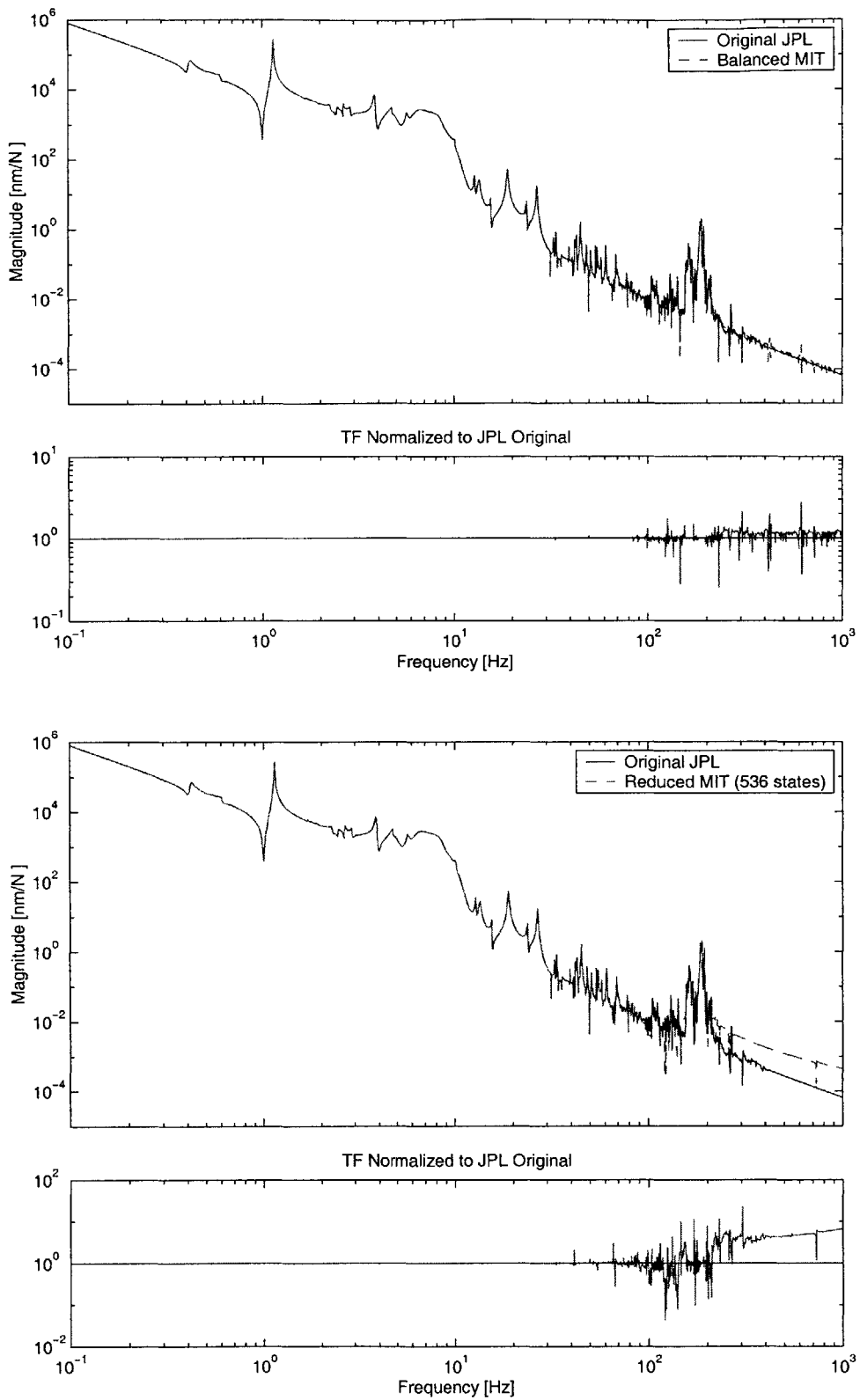


Figure 5-17: Balanced and Reduced transfer functions of RWA Force X to Star OPD #1, SIM v2.0

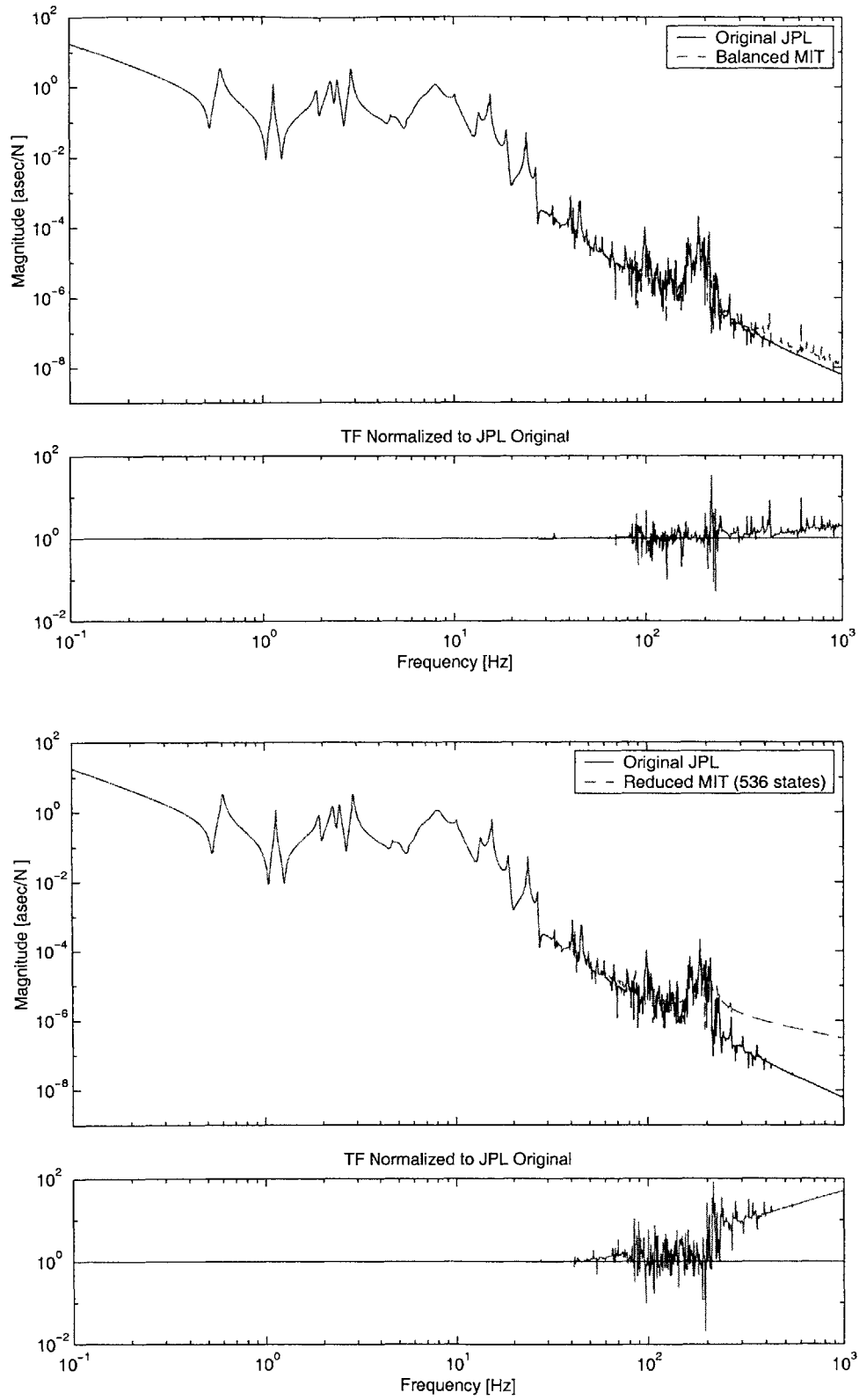


Figure 5-18: Balanced and Reduced transfer Functions of RWA Force X to Star X WF1 Tilt #1, SIM v2.0

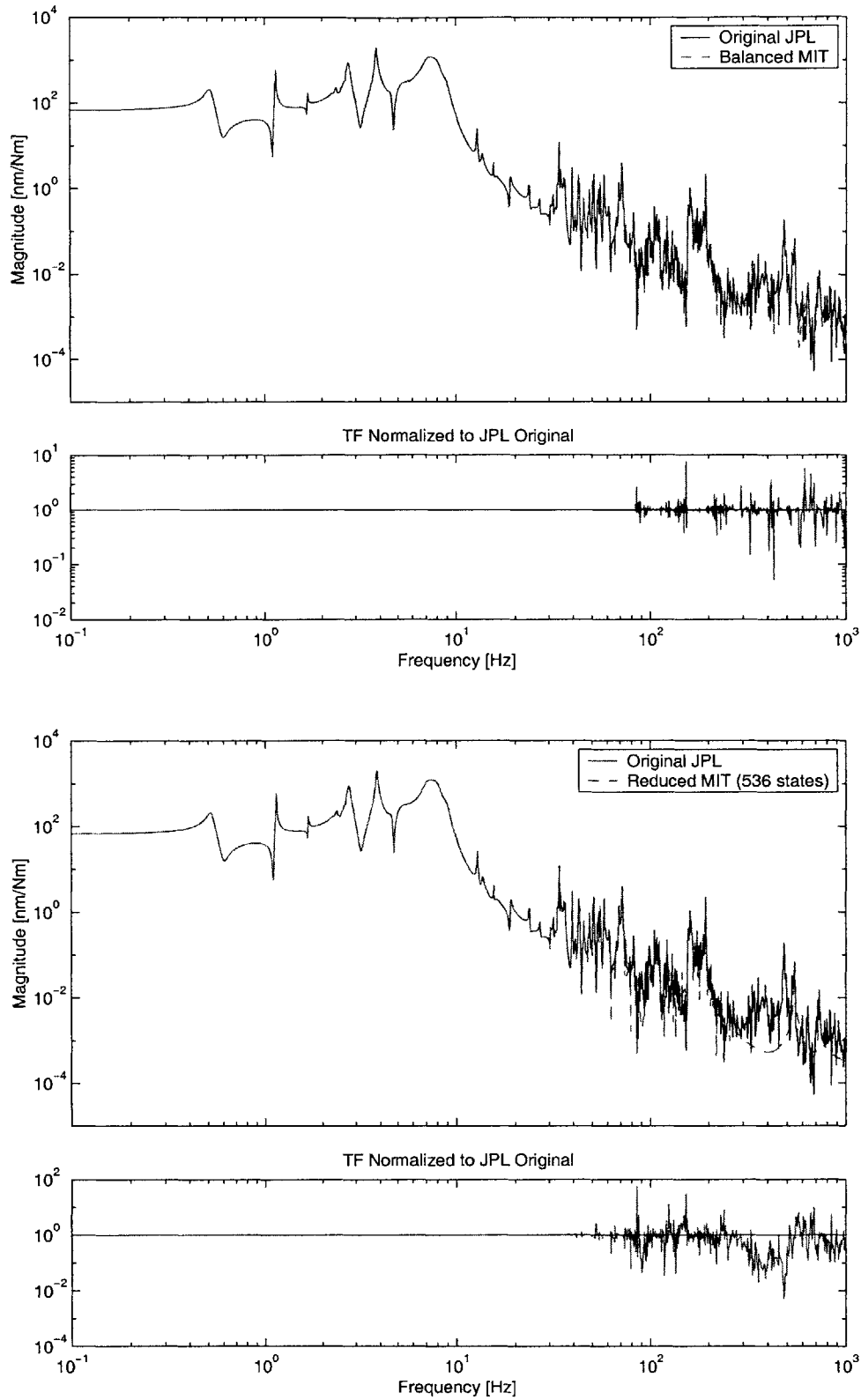


Figure 5-19: Balanced and Reduced transfer Functions of RWA Torque X to Internal Metrology Opd #1, SIM v2.0

flexible states (316 states in the complete system).

The 1063 state model is, not surprisingly, the most accurate approximation of the original with only small, slightly observable modes missing. The 608 state model shows more discrepancies as further modes are eliminated from the system. The high frequency roll-off is also less steep than in the original system. This is the effect of losing the modal contributions to the DC gain. The 316 state model is the least accurate, with observable modes above 40 Hz missing. The backbone of the reduced transfer functions also deviates from the original between 70 Hz and 150 Hz. These are the same modes that were determined not to be important by the error analysis in Table 5.2, however. Despite these problems, the critical frequency regions below 20 Hz, and around the 180 Hz peaks are captured in each of these transfer functions. The strongest high-frequency modes around 187 Hz have the proper frequency and damping.

Because these most critical areas are retained in even the smallest model, and considering the computational savings of running a 316 state versus a 1063 state model (a factor of 38 reduction in flops for  $n^3$  problems), the 316-state model will be used for the disturbance analysis described in the next chapter.

## 5.6 Summary

The balancing and reduction of state-space models using internal balancing theory was reviewed in order to reduce the size and improve the numerical conditioning of the spacecraft models under study. Due to numerical difficulties, the routines can often fail on large models of several hundred to several thousand states. In order to accomplish the balanced reduction, a variation to the full-state balancing was described in which the least controllable and observable states are removed prior to the proper balancing. The balanced system is then slightly smaller than the original. The resulting Hankel Singular Values can be used to reduce the system to a desired level based on a number of methods. Examples were shown for both the NGST model and for two variations of the SIM model. The performance errors due to reduction should be less than 7% for NGST, and less than 1% for the SIM models. The sample transfer functions succeeded in capturing all of the low-frequency behavior. The loss of modes in frequency regions of high modal density resulted in deviations between the reduced and original systems, but in all cases modes of critical concern were retained in the



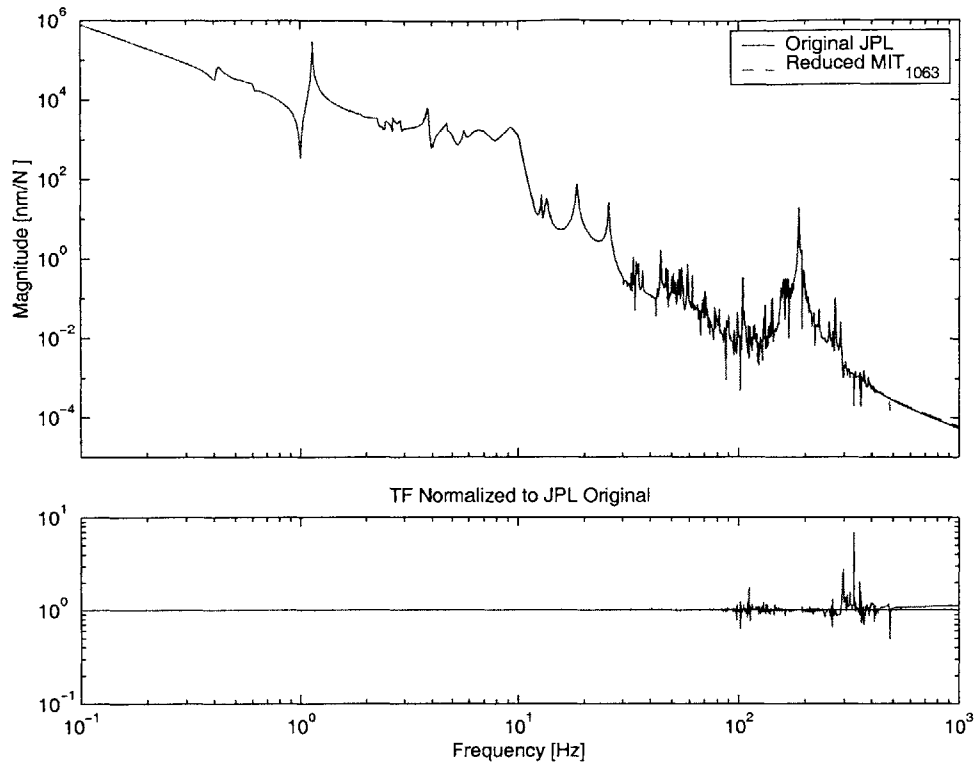


Figure 5-20: 1063 state TF of RWA Force X to Star Opd #1 for SIM model v2.2

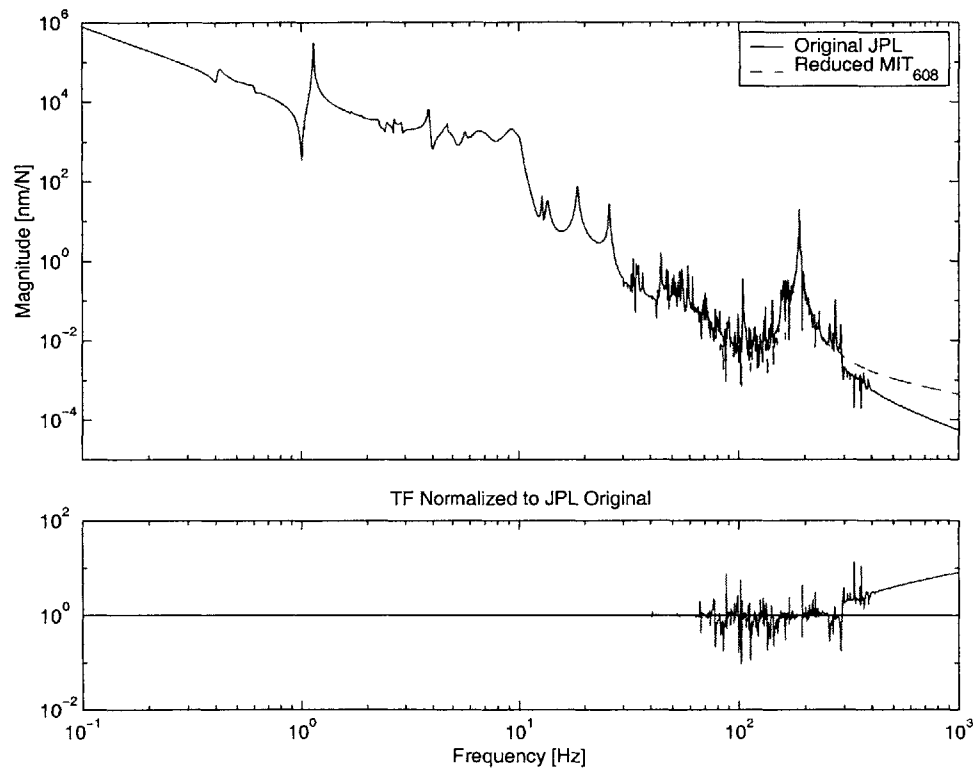


Figure 5-21: 608 state TF of RWA Force X to Star Opd #1 for SIM model v2.2

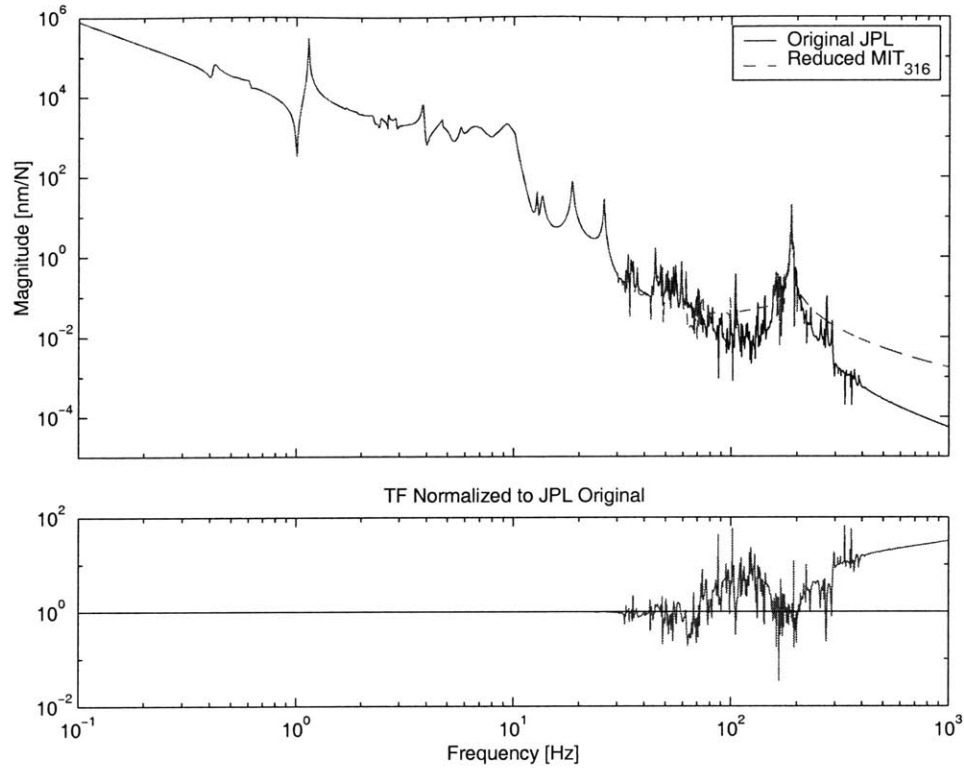


Figure 5-22: 316 state TF of RWA Force X to Star Opd #1 for SIM model v2.2

reduced open loop model.

Models of the disturbances will be described and generated in the next chapter. This will be followed by the assembly of the reduced open loop models, disturbances, and ACS and optical controllers into the integrated models in Chapter 7. These integrated models will finally be run through the DOCS disturbance analysis.

## Chapter 6

# Disturbance Sources

The disturbance analyses of Chapter 7 necessitate accurate modeling of the many types of disturbance sources. These can include vibrations from cryocoolers or tape drives. Closed loop controllers can introduce mechanical disturbances in the control path due to actuator and sensor noise. Fuel slosh can be a major source of vibration immediately following a thruster firing, although it tends to damp out quickly through the use of diaphragms and baffles in the fuel tanks. Reference [18] provides a good overview of many types of on-orbit disturbances.

Though most of these sources have been examined, the only disturbances in this study come from reaction wheel assemblies (RWAs). Reaction wheels tend to contribute the strongest disturbance forces and torques, so as a result there has been considerable attention paid to modeling them using both empirical data and analytical models. This chapter will review the work behind RWA disturbance models and describe the coupling of those models with the overall spacecraft models.

### 6.1 Reaction Wheel Disturbances

Attitude control and slewing maneuvers of most large space telescopes, including NGST, Nexus, and SIM, are to be performed almost entirely by reaction wheel assemblies. Flywheels spinning at several hundred to several thousand RPM generate angular momentum to withstand low-frequency or DC external torques such as from atmospheric drag or solar pressure. The spacecraft are made to slew as the wheel speed is increased or decreased, which changes the angular momentum vector and creates a resulting torque. The use of

reaction wheels is generally preferred over thrusters since no propellant is required and since the impulsive excitation from a thruster firing prevents precise science observations for many tens of minutes after the event. On station the thrusters are used only when required to offload momentum stored in the reaction wheels, or for periodic orbit maintenance.

A standard reaction wheel is shown in Figure 6-1. It typically includes the flywheel floating on ball-bearings, driven by a DC motor, and contained in a housing. Several types of reaction wheels are being considered for NGST and SIM. The Ithaco Type E wheel, shown in the figure, may be used on NGST. Teldix wheels are proposed for SIM<sup>1</sup>.

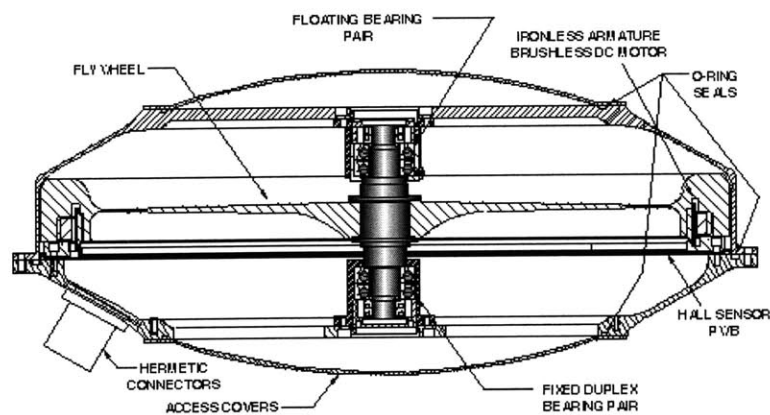


Figure 6-1: Ithaco Type E reaction wheel [2]

Although preferred over thrusters, reaction wheels are also a leading source of spacecraft disturbances; external disturbances such as solar pressure are considered negligible in comparison. Because of this, there has been much interest in understanding and modeling the dynamics of reaction wheels. Masterson [28] developed both empirical and analytical models of wheel disturbances based on test data from the HST and Ithaco wheels. References [22] and [14] also describe wheel modeling as performed at MIT. What follows is a brief overview of the primary sources of disturbance.

The primary wheel disturbances are caused by the fact that mass around the wheel is not symmetrically distributed. The *static imbalance* results from the fact that the center of mass is not exactly on the spin axis. It is modeled as an extra mass  $m$  being located a distance  $r$  from the spin axis. This creates a radial centripetal force,

<sup>1</sup>The SIM analyses at MIT, however, have used models of the HST reaction wheels in place of Teldix models.

$$F_r = m r \omega^2 = U_s \omega^2 \quad (6.1)$$

where  $U_s = mr$  is a property of a wheel and is usually given in [gcm]. This force can be reduced by accurate balancing of the wheel, performed by shaving extra mass off of the heavier side. Unless a wheel is very carefully balanced the static imbalance will most often be the primary source of vibrations. The *dynamic imbalance* is caused by a slight angular misalignment of the principal moment of inertia from the spin axis. This can be modeled as two equal masses on either side of the flywheel, separated by a distance  $d$  along the spin axis. A torque is created as these masses spin about each other.

$$T_r = m r d \omega^2 = U_d \omega^2 \quad (6.2)$$

The dynamic imbalance  $U_d = mrd$  is another property of the wheel. Table 6.1 provides the specifications for both the Ithaco E-wheel, the Ithaco B-wheel, and the Honeywell/Sperry wheels that flew on Hubble (here called the HST wheels).

Table 6.1: Reaction Wheel Specifications [2, 14]

	Speed Range	Momentum Capacity	Reaction Torque	Static Imbalance	Dynamic Imbalance	Mass
	[RPM]	[Nms]	[mNm]	[g-cm]	[g-cm <sup>2</sup> ]	[kg]
Ithaco						
E-wheel	±3850	>50	>300	<1.8	<60	<13.9
TW-50E300						
B-Wheel	±5100	>16.6	>32.0	<1.5	<40	<5.9
TW-16B32						
HST wheel	±3400	264	800	0.38*	4.88*	41
						* average

Since both of these imbalances result from the spinning of the flywheel, the fundamental harmonic lies at the frequency of the wheel speed, where  $\text{Hz} = \text{RPM}/60$ . Aside from the fundamental imbalances there exist higher harmonics as well as subharmonics that result from the flexibility of the wheel, bearing imperfections, motor disturbances, and other nonlinear sources. These harmonics are not dependent on the mass distribution, so balancing the wheel will not remove their effects. For wheels that are accurately balanced,

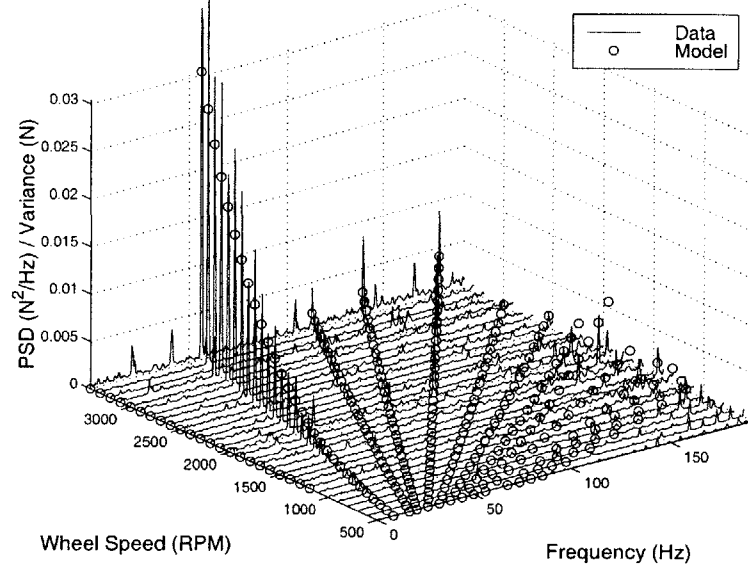


Figure 6-2: Waterfall plot derived from measured data showing Ithaco B-wheel  $F_x$  data and the radial force model

such as the HST flight wheels, the higher and sub-harmonics may actually produce a stronger disturbance than the fundamental.

Describing the harmonics is made easier with the use of a waterfall plot, such as in Figure 6-2. The  $x$  and  $y$  axes show the wheel speeds in RPM against the frequencies in Hz. The  $z$  axis shows the strength of the excitation in the form of a Power Spectral Density (PSD) [51]. For any given wheel speed, the PSD of the disturbance dynamics (forces or torques) is a slice of the waterfall plot at that wheel speed, along the frequency axis.

Models of the disturbances assume that the forces and torques can be represented by summations of sinusoidal terms. The generalized disturbance  $m_{ijk}$ , as proposed by Melody [29], can be written as:

$$m_{ijk} = C_{jk} f_i^2 \sin(2\pi h_{jk} f_i t + \phi_{ijk}) \quad (6.3)$$

where,

- $m$  = disturbance force ( $j=1,2,3$ ) or torque ( $j=4,5,6$ )
- $i$  = individual wheel number, ( $1 \rightarrow N_w$  wheels)
- $j$  = disturbance number ( $1 \rightarrow 6$ )
- $k$  = harmonic number ( $1 \rightarrow N_j$ ) harmonics for the  $j^{th}$  disturbance component

$C_{jk}$  = amplitude coefficient for  $k^{th}$  harmonic of  $j^{th}$  disturbance;  
 assumed to be the same for all wheels  
 $f_i$  = wheel speed of the  $i^{th}$  wheel in Hz  
 $h_{ijk}$  = frequency ratio of the  $k^{th}$  harmonic of the  $j^{th}$  disturbance to the frequency  
 of the wheel rotation; assumed to be the same for all wheels  
 $\phi_{ijk}$  = phase angle of the  $k^{th}$  harmonic of the  $j^{th}$  disturbance of the  $i^{th}$  wheel

It is assumed that  $f_i$  and  $\phi_{ijk}$  are independent random variables. Given reaction wheel force and torque data, the coefficients  $C_{jk}$  and  $h_{jk}$  can be found empirically. Masterson [28] describes MATLAB functions that identify the harmonics in experimental data and fit the coefficients. For each wheel, there may only be a small number of identified harmonics. The Ithaco E-wheel, for instance, has only five. This information has been collected for each wheel, and is stored in three files `rwamodel_axi.m`, `rwamodel_rad.m`, and `rwamodel_tor.m`. The reason there are only three files for the six force and torques is that given a wheel coordinate system with  $z_w$  along the spin axis, the radial forces in  $x_w$  and  $y_w$  are assumed to be identical and  $90^\circ$  out of phase; the same is true for the torques. Also, the torque disturbance about the spin axis  $z_w$  is assumed negligible compared to the torque disturbances about the radial axes. Note that the *total* torque about the  $z_w$  axis is the greatest, since that axis is used to control the spacecraft. The torque used for control is not modeled as a disturbance, but instead is input through the attitude controller.

Using the coefficients, PSDs or amplitude spectra for a single wheel can be determined at any given wheel speed. The next step is to combine several wheels into one reaction wheel assembly.

## 6.2 Reaction Wheel Assemblies

All of the disturbances described by Equation 6.3 are for a single wheel in its own coordinate frame. In order to keep attitude for a spacecraft at least three wheels are needed to control each axis; four or more are usually provided to give greater flexibility in wheel speeds and for redundancy.

Depending on the mission, the reaction wheels may be clustered together, or may be positioned separately around the spacecraft bus. The wheels for NGST are clustered to-

gether in a pyramid, all in the Spacecraft Support Module (SSM). The wheels on SIM will be separated from one another in different locations around the spacecraft backpack, below the siderostat boom. Most often the individual wheels are not aligned exactly with the spacecraft coordinates. The disturbances as expressed in the wheel frame must be transformed using Euler angles to the spacecraft frame in which they act. The effects of multiple wheels may also have to be summed together for the model, depending on the fidelity of the FE model. For both NGST and SIM, a single node was selected to act as the reaction wheel assembly, so all effects of multiple wheels must be applied at this one point. In the case of Nexus, individual nodes were included for each wheel, so that only the coordinate transformation is required. The coordinate transformation and multiple wheel summation, described by [22], will be outlined.

The forces and torques are defined in the wheel frame by the components of the generalized disturbance vector  $m$ .

$${}^w m_i(t) = \left\{ \begin{array}{c} F_x(t) \\ F_y(t) \\ F_z(t) \\ M_x(t) \\ M_y(t) \\ M_z(t) \end{array} \right\}_i \quad (6.4)$$

To transform these into the spacecraft frame, assume that the wheel is first oriented with its axes aligned with the spacecraft axes,  $X_{s/c}$ ,  $Y_{s/c}$ ,  $Z_{s/c}$  in Figure 6-3. The Euler angles are defined by rotating the wheel from these coordinates, to the wheel coordinates  $x_w$ ,  $y_w$ ,  $z_w$ , in the following order.

$\alpha$  = angle of rotation about original  $Z_{s/c}$  axis

$\theta$  = angle of rotation about new  $y$  axis after previous rotation

$\gamma$  = angle of rotation about new  $x$  axis after previous rotation

Any vector  ${}^w \mathbf{p}$  in the  $i^{th}$  wheel frame can be transformed to the spacecraft frame  ${}^{s/c} \mathbf{p}$  using the  $3 \times 3$  rotation matrix  $R_i$ , where  ${}^{s/c} \mathbf{p} = R_i {}^w \mathbf{p}$ .



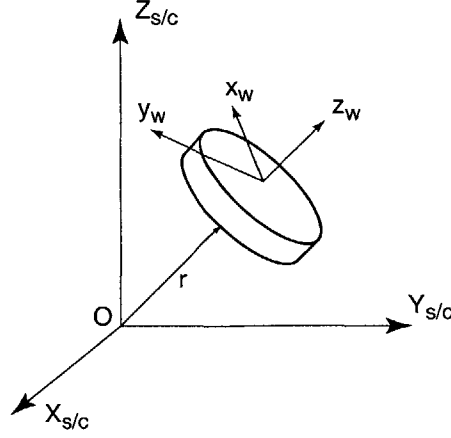


Figure 6-3: Reaction wheel frame  $x_w, y_w, z_w$  within the spacecraft frame  $X_{s/c}, Y_{s/c}, Z_{s/c}$

$$R_i = \begin{bmatrix} \cos \alpha_i \cos \theta_i & \cos \alpha_i \sin \theta_i \sin \gamma_i - \sin \alpha_i \cos \gamma_i & \cos \alpha_i \sin \theta_i \cos \gamma_i + \sin \alpha_i \sin \gamma_i \\ \sin \alpha_i \cos \theta_i & \sin \alpha_i \sin \theta_i \sin \gamma_i + \cos \alpha_i \cos \gamma_i & \sin \alpha_i \sin \theta_i \cos \gamma_i - \cos \alpha_i \sin \gamma_i \\ -\sin \theta_i & \cos \theta_i \sin \gamma_i & \cos \theta_i \cos \gamma_i \end{bmatrix} \quad (6.5)$$

Next assume that the wheel is offset from a point of disturbance application  $O$ , by a distance  $d$ . The vector  $\mathbf{r}$  in Figure 6-3 represents the location of the wheel. If the spin axis intersects the point  $O$ , then  $\mathbf{r}$  can be written in the wheel frame as  ${}^w\mathbf{r} = [0 \ 0 \ d]$ , and this can be transformed to the spacecraft frame using

$${}^{s/c}\mathbf{r} = R_i ({}^w\mathbf{r}).$$

Since the wheel's forces will create additional torques about  $O$ , use  ${}^{s/c}\mathbf{r}$  as the moment arm in the following cross product:

$${}^{s/c}\mathbf{r} \times R_i \begin{Bmatrix} F_x \\ F_y \\ F_z \end{Bmatrix}$$

Since  ${}^w[F_x \ F_y \ F_z]$  are components of  ${}^w\mathbf{m}_i$  for the  $i^{th}$  wheel, the disturbance transformation from  ${}^w\mathbf{m}_i$  to  ${}^{s/c}\mathbf{m}_i$  can be written:

$${}^{s/c}m_i(t) = \begin{bmatrix} R_i & 0_{3 \times 3} \\ {}^{s/c}\mathbf{r}_i \times R_i & R_i \end{bmatrix} {}^w m_i(t) = T_i \cdot {}^w m_i(t) \quad (6.6)$$

Once the forces and torques for all wheels are transformed to the same spacecraft frame, they are summed together to give the total disturbances at a point.

$${}^{s/c}m(t) = \sum_{i=1}^{N_w} {}^{s/c}m_i(t) \quad (6.7)$$

A variation of this algorithm can also be used with PSDs of the disturbances as functions of frequency. It has been coded into the MATLAB function `multi_wheel_psd.m`; disturbance PSDs are transformed into the spacecraft frame given the number of wheels, the Euler angles  $\alpha$ ,  $\theta$ , and  $\gamma$  for each wheel, and the distance of each wheel from the origin. A  $(6 \times 6 \times n_{freq\ pts})$  matrix is output to be used by the disturbance analysis.

### 6.3 Broadband Wheel Speed Model

The application of the wheel disturbance models to the spacecraft can proceed in one of two ways. The disturbance at a single wheel speed can be generated using Equation 6.3, and an appropriate PSD matrix generated. This will be done in the next section. Because of the large number of wheel speeds that must be examined, another method is to treat the wheel speed  $f$  as a random variable. The cumulative disturbance effect is computed and a broadband wheel speed PSD matrix is created. The final disturbance PSD matrix looks like:

$$S_{s/cm}(\omega) = \sum_{i=1}^{N_w} T_i \begin{bmatrix} S_{m_1}(\omega) & S_{m_1 m_2}(\omega) & & & & \\ S_{m_2 m_1}(\omega) & S_{m_2}(\omega) & & & & \\ & & S_{m_3}(\omega) & & & \\ & & & S_{m_4}(\omega) & S_{m_4 m_5}(\omega) & \\ & & & S_{m_5 m_4}(\omega) & S_{m_5}(\omega) & \\ & & & & & S_{m_6}(\omega) \end{bmatrix} T_i^T \quad (6.8)$$

where the  $S_{m_j}$  are the PSD vectors in frequency for the  $j^{th}$  disturbance, and the  $S_{m_{j_1} m_{j_2}}$

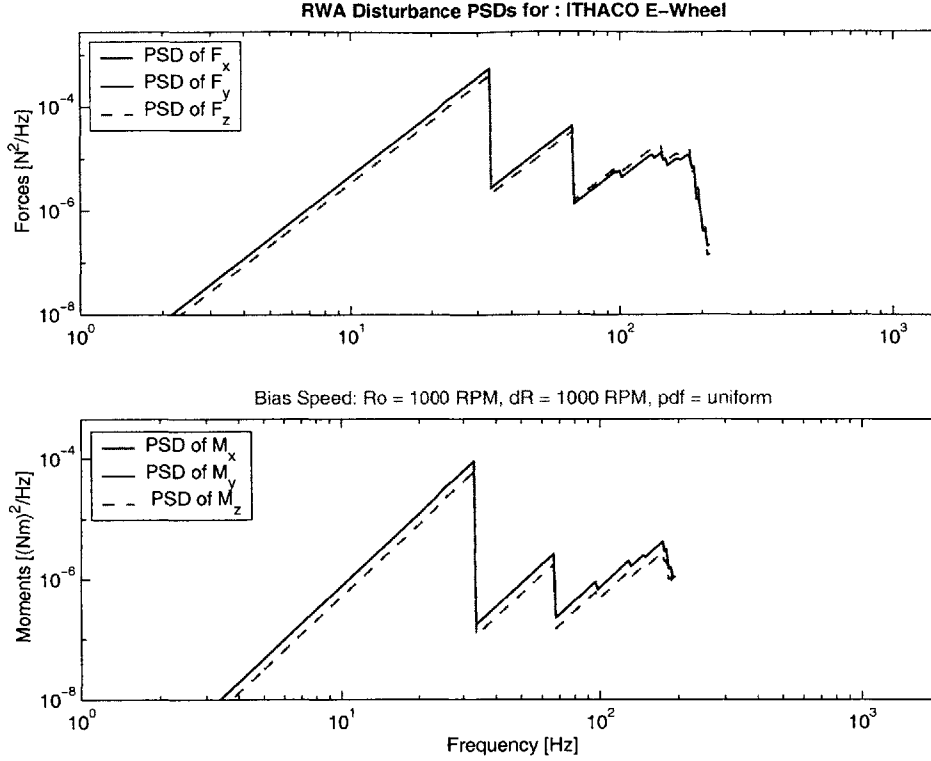


Figure 6-4: Sample broadband wheel speed PSD

are the cross-spectra density functions of the  $j_1^{th}$  and  $j_2^{th}$  radial-to-radial force and torque disturbances. A procedure to build this matrix has been implemented in MATLAB (see [22]). As an example, consider a single wheel such as will be used on Nexus. The Ithaco E-type wheel will be used, and a uniform probability density function is assumed for the wheel speed. The information in Table 6.2 is provided. The  $S_{m_j}$  spectra are computed and plotted across frequency in Figure 6-4.

Table 6.2: Variables to produce broadband wheel disturbance PSDs

Bias wheel speed	1000 RPM
Variation of wheel speed	$\pm 1000$ RPM
Euler angles	$\alpha = 45^\circ$ , $\theta = 135^\circ$ , $\gamma = 0^\circ$
Wheel offset	$d = 0$

The “sawtooth” pattern in the figure is typical for broadband PSDs with a large variation in wheel speeds and results from wheel harmonics sweeping through the frequencies; the peaks occur at frequencies where a harmonic lies at the maximum wheel speed. If no speed

variation were allowed and the PSD for a single speed were computed, individual tones at distinct frequencies would be the only remaining disturbances. This case is examined next.

## 6.4 Discrete Wheel Speed Model

The broadband wheel model allows a single disturbance analysis to cover all possible wheel speeds, but by spreading the disturbance energy over the frequency spectrum, it provides only “on-average” disturbance energy and fails to capture actual dynamics at any particular wheel speed. Across the speed range of a wheel (see Table 6.1 for examples) most points will not excite the structure to any large degree. Those particular speeds which do, however, may cause stronger disturbances than any that result from the broadband model. In order to capture these worst-case scenarios, the alternative to the broadband model is to run a disturbance analysis for many individual wheel speeds. This can take more time than a single broadband analysis, but it provides a more realistic picture of the disturbance dynamics.

The disturbances can be pictured as discrete slices of the particular waterfall plot (Figure 6-2) pertaining to each channel. Based on Equation 6.3, only those tones associated with an identified  $h_{jk}$  and  $C_{jk}$  are modeled. Unlike the PSDs in Figure 6-4, which are continuous in frequency, the tonal disturbance models have all of their energy at a finite number of discrete frequencies. Since the tonal PSDs are no longer true “densities” across continuous frequency ranges, they have units of  $[N^2]$  instead of  $[N^2/Hz]$ . An example of the tonal disturbances for one channel is shown in Figure 6-5. In this case, the amplitude spectra in units of  $[N]$  are plotted instead of the PSD. For the wheel models provided by `rwamodel_axi.m`, `rwamodel_rad.m`, and `rwamodel_tor.m`, the relationship between PSD and amplitude is<sup>2</sup>:

$$PSD = \frac{Amp^2}{2}. \quad (6.9)$$

These disturbances can be combined into a  $(6 \times 6 \times n_{tones})$  matrix and applied to the structural model directly using the PSD-based disturbance analysis described in the next

---

<sup>2</sup>This relationship may change depending on how the PSD is defined, in rad/sec or Hz, double-sided or single sided. It is recommended that the reader consult a random vibrations book such as Reference [51] for further study.

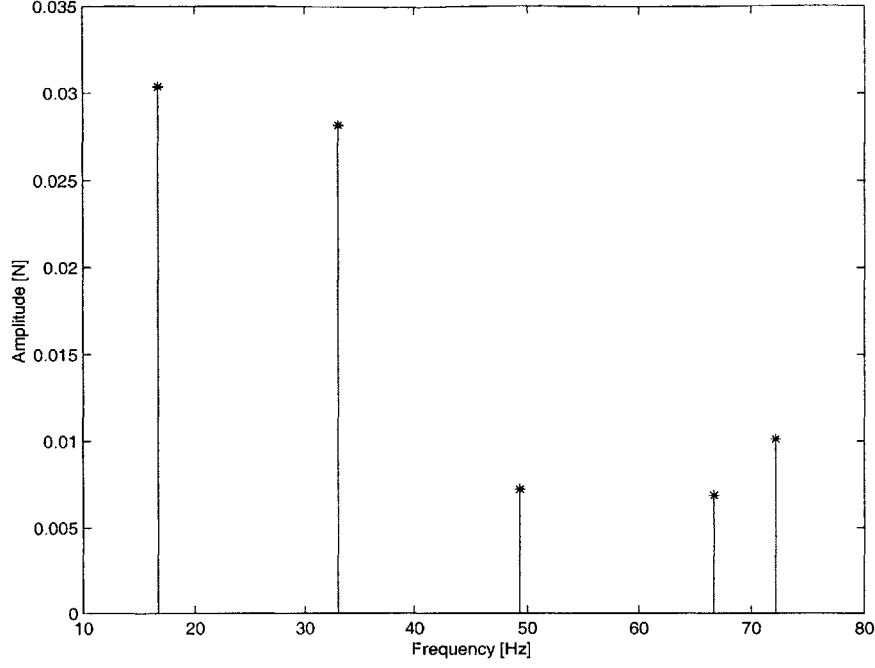


Figure 6-5: Ithaco E-wheel axial disturbance force amplitude spectra: tones at 1000 RPM

chapter.

An alternative approach is to create a state-space model for the tonal disturbances. This form is required for the DOCS sensitivity analysis, and will be used here in a Lyapunov disturbance analysis, also described in the next chapter. The Lyapunov analysis requires that the disturbance can be modeled as a filter that inputs zero mean, unit intensity white noise processes and outputs the disturbance energy. In building such a filter, the output energies must be equal to the energy contained in the PSDs. Only the six power spectral densities  $S_{m_j}$  will be considered in this case; the cross spectral densities  $S_{m_{j_1}, m_{j_2}}$  are assumed negligible.

By modeling the disturbances in state-space, a continuous function must be made to capture discrete tones. This is achieved by treating each tone in the amplitude spectra as a lightly damped harmonic. Assume that the  $i^{th}$  tone can be described by the following transfer function,

$$G_i(s) = \frac{K_i s}{s^2 + 2\zeta_i \omega_i s + \omega_i^2} \quad (6.10)$$

where  $K_i$  is a gain,  $\zeta_i$  is the damping, and  $\omega_i$  is the frequency of that particular tone. The frequency and amplitude of each tone are given in Figure 6-5, so what remains is to solve

for  $K_i$  and  $\zeta_i$ . The first constraint is that the amplitude of the function match the given amplitude  $|G(j\omega_i)|$  at frequency  $\omega_i$ .

$$|G(j\omega_i)| = \frac{K_i\omega_i}{2\zeta_i\omega_i^2} \equiv A_i \quad (6.11)$$

The second constraint is that the energy of the tone remain the same. This involves calculating the RMS value of the disturbance. Recognize that the force or torque of the tone can be described by the sinusoidal equation

$$F_i(t) = A_i \sin(\omega_i t + \phi_i). \quad (6.12)$$

The RMS of this function is

$$\sigma_{x_i} = \frac{\sqrt{2}}{2} A_i. \quad (6.13)$$

The area under a PSD also equals the RMS value. In the case of the discrete PSDs shown, the square root of the value of the PSD at each tone is equal to that tone's contribution to the total RMS. By the PSD-to-amplitude relationship of Equation 6.9, the RMS can be also calculated using

$$\sigma_{x_i} = \sqrt{\frac{\text{Amp}^2}{2}} = \frac{\sqrt{2}}{2} A_i. \quad (6.14)$$

This matches Equation 6.13 above. Next the PSD of the continuous transfer function  $G_i(s)$  is required. If the input to the function is described by the PSD  $S_w(\omega)$ , where  $\omega$  is the frequency in rad/sec, the output PSD is

$$S_X(\omega) = G(\omega)S_w(\omega)G^H(\omega) \quad (6.15)$$

and since the input to the disturbance filter is unit intensity white noise,  $S_w(\omega) = 1$ .  $S_X(\omega)$  is a continuous function in frequency so integration under the curve provides the total area and hence the RMS value. The variance of  $S_X(\omega)$  is defined by

$$\sigma_x^2 = \frac{1}{2\pi} \int_{-\infty}^{\infty} S_X(\omega) d\omega \quad (6.16)$$

which is also the mean square value for zero mean processes. The square root of the variance

$\sigma_x^2$  is then the root-mean square (RMS). Next substitute Equation 6.15 for  $S_X(\omega)$ .

$$\sigma_x^2 = \frac{1}{2\pi} \int_{-\infty}^{\infty} |G(\omega)|^2 d\omega \quad (6.17)$$

The solution of this when  $G(s)$  is in the form of Equation 6.10 is provided in [51]. At the frequency  $\omega_i$  the mean square value can be written as:

$$\sigma_{x_i}^2 = \frac{K_i^2}{4\zeta_i\omega_i}. \quad (6.18)$$

The second constraint equation is formed by setting this equal to the square of Equation 6.14.

$$\frac{k_i^2}{4\zeta_i\omega_i} = \left( \frac{\sqrt{2}}{2} A_i \right)^2 \quad (6.19)$$

Solving Equations 6.11 and 6.19 simultaneously for  $K_i$  and  $\zeta_i$  yields

$$K_i = A_i \quad (6.20)$$

$$\zeta_i = \frac{1}{2\omega_i} \quad (6.21)$$

With these values in hand, the individual  $G_i(s)$  can be converted into state-space form using a controller canonical realization,

$$\{\dot{x}_i\} = \begin{bmatrix} 0 & 1 \\ -\omega_i^2 & -2\zeta_i\omega_i \end{bmatrix} \{x_i\} + \begin{bmatrix} 0 \\ 1 \end{bmatrix} d \quad (6.22)$$

$$w_i = \begin{bmatrix} 0 & K_i \end{bmatrix} \{x_i\} + [0] d \quad (6.23)$$

where  $d$  is a white noise input and  $w$  is the disturbance output for that channel. Each tone in a single channel is described by a system of the form of Equation 6.22. Each is driven by the same white noise input  $d$  and produces part of the same disturbance output  $w$ . The entire state-space system for a single channel is a SISO system with  $2 \cdot n_{tones}$  states. Using the MATLAB `ode.m` command, a sample transfer function (Figure 6-6) is generated and plotted over the pure tones of Figure 6-5.

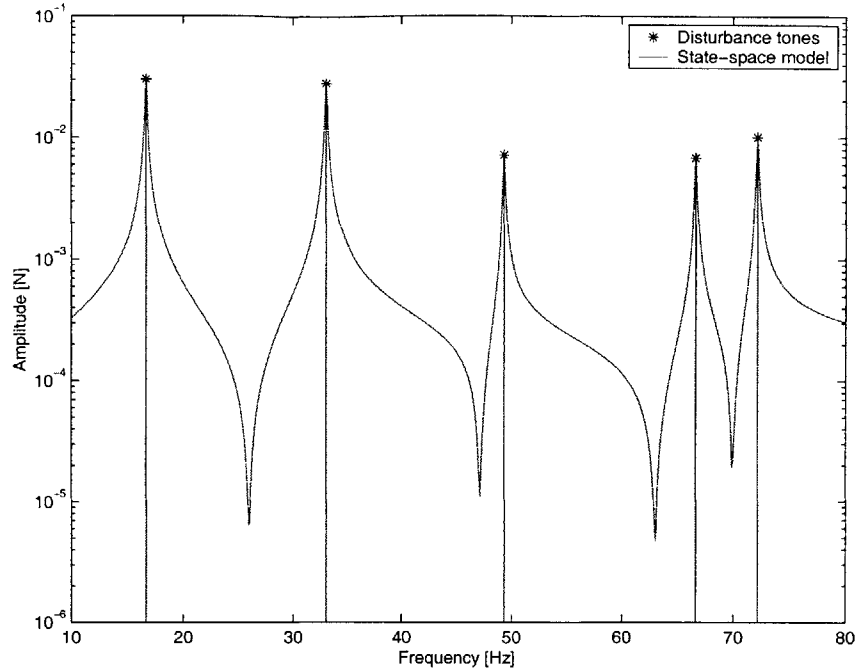


Figure 6-6: Ithaco E-wheel axial disturbance force amplitude spectra: tones and state space model at 1000 RPM

To ensure that the energy remains the same, a PSD plot was also generated along with the cumulative RMS curve (Figure 6-7). For the original tones, the cumulative RMS curve is a step function, while for the state-space model it is increasing with frequency in a differentiable manner. The models match very well, and both produce a final RMS of 0.0310 N for this disturbance force.

In order to reduce the non-physical low-frequency energy of the system as the transfer function rolls up, it is also possible to add a high pass filter (HPF) with a corner frequency near the first tone. This tends to decrease the strength of the first tone, however. As the sample problem shows, most of the energy of the disturbance is contained within that first tone, so care should be taken not to attenuate it too much. In practice, a 4<sup>th</sup> or 6<sup>th</sup> order HPF with corner frequencies around  $0.8\omega_1$  were used.

All six reaction wheel channels are appended together in a single system driven by six white noise sources. If there are many tones in a wheel disturbance, the size of this system can become large ( $n_{tones} \cdot 2 \frac{\text{states}}{\text{tone}} \cdot 6$  wheels), however it allows a Lyapunov analysis for discrete wheel speed RWA disturbances.



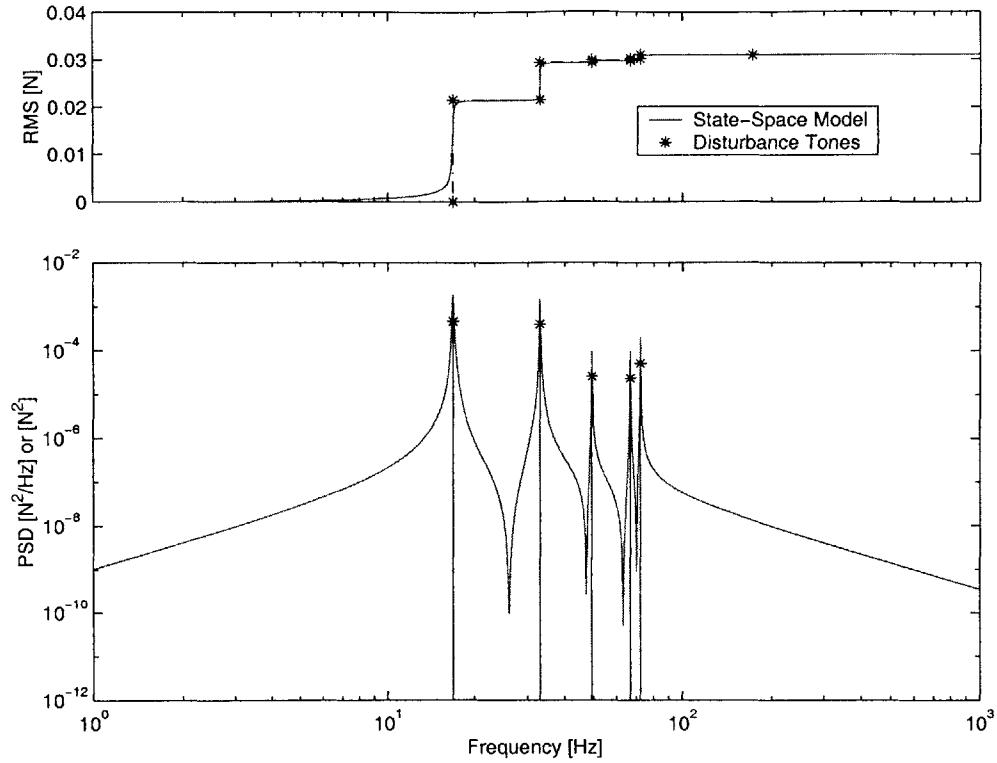


Figure 6-7: Ithaco E-wheel axial disturbance force PSD below, and RMS above: tones and state space model at 1000 RPM

## 6.5 Summary

Several types of reaction wheel disturbance models have been prepared. These include both broadband wheel speed models, in which the effect of changing wheel speed is captured, and discrete speed models that model the disturbances at a specific speed. All of the models are based on the power spectral densities of the disturbances. These PSDs can either be directly applied to the spacecraft system, or state-space shaping filters can be computed that output the proper disturbance signals. The next step is to apply these forces and torques to the spacecraft to determine how they will affect the final performances.



## Chapter 7

# Disturbance Analysis

The goal of the disturbance analysis is first to determine whether, in the presence of the reaction wheel disturbances previously modeled, the optical performances meet their requirements. More importantly however, it is to investigate why they might *fail* to meet requirements, and what aspects of the design require further refinement. This involves a closer examination of the dynamics of the disturbances and of the frequency content of the resulting performances.

The complete integrated model will first be assembled using the separate models of the physical spacecraft, optics, and disturbances, along with the addition of ACS and optical controllers. An overview of the disturbance analysis framework will follow, along with the application of the analysis techniques on Nexus, NGST, and SIM.

### 7.1 Integrated Modeling

The previous chapters have described the various models that comprise different aspects of a spacecraft. The structural models describe the mass distributions and stiffness; the optical models define the light paths, and the disturbance models capture the forces and torques that a disturbance source transmits to a structure. The next step is to incorporate attitude controllers and possibly optical controllers, and finally to assemble all of these models together. The concept of integrated modeling is that the output of multiple disciplines: dynamics, optics, controls, and structures (DOCS), get combined into a single integrated model that can simulate the behavior of a complete spacecraft and produce meaningful results. Before beginning the disturbance analysis, a brief overview of how these different

pieces are brought together will be described.

### 7.1.1 Structural, Optical, and Disturbance models

For the frequency domain analysis performed here, the structural FE model is most often transformed into a state-space representation

$$\begin{aligned} \dot{q}_p(t) &= A_p q_p(t) + B_p w(t) \\ y(t) &= C_p q_p(t) + D_p w(t) \end{aligned} \tag{7.1}$$

which defines the force and torque disturbance inputs  $w$  and the displacement, velocity, or acceleration outputs  $y$ , at given nodes on the spacecraft plant, described by the states  $q_p$ . Since the metrics of interest are optical performances and not nodal displacements, the optics models described in Chapter 2 must be attached. The optical sensitivity matrices of Equation 2.1 must be multiplied by the proper displacements  $y$  to produce the performances  $z$ . For Nexus and NGST, these include the centroid location and the wave front error (WFE). Define  $K_z$ :

$$K_z = \begin{bmatrix} \frac{\partial C}{\partial y} \\ \frac{\partial W}{\partial y} \end{bmatrix}$$

so that

$$\begin{aligned} z(t) &= K_z y(t) \\ &= [K_z C_p] q_p(t) \end{aligned} \tag{7.2}$$

The disturbances can be applied directly to this system through  $w(t)$ . This is the approach that is taken in the PSD disturbance analysis, discussed in the next section. The alternative is to use a state-space white-noise shaping filter, as was built in Section 6.4. The filter can be described by

$$\begin{aligned}\dot{q}_d(t) &= A_d q_d(t) + B_d d(t) \\ w(t) &= C_d q_d(t)\end{aligned}\tag{7.3}$$

which inputs white noise  $d(t)$  and outputs the disturbances  $w(t)$ . Assume that  $D_d$  is zero, otherwise  $w(t)$  would have infinite energy (as the white noise feeds through). This system can be put in series with the structural plant to build the white-noise input and performance output system.

$$\begin{aligned}\begin{Bmatrix} \dot{q}_d(t) \\ \dot{q}_p(t) \end{Bmatrix} &= \begin{bmatrix} A_d & 0 \\ B_p C_d & A_p \end{bmatrix} \begin{Bmatrix} q_d(t) \\ q_p(t) \end{Bmatrix} + \begin{bmatrix} B_d \\ 0 \end{bmatrix} d(t) \\ z(t) &= \begin{bmatrix} D_p C_d & C_p \end{bmatrix} \begin{Bmatrix} q_d(t) \\ q_p(t) \end{Bmatrix}\end{aligned}\tag{7.4}$$

Note that  $D_p$  is most often zero, and in the situation that they are not, it is possible to remove the  $D$  term [22]. The integrated model can now more simply be described by:

$$\begin{aligned}\dot{q}(t) &= A_{zd} q(t) + B_{zd} d(t) \\ z(t) &= C_{zd} q(t).\end{aligned}\tag{7.5}$$

Controllers are the next items to be added to the model.

### 7.1.2 ACS and Optical Controllers

A detailed attitude control system model is not available for any of the spacecraft, but in order to accurately model the disturbances the rigid body modes must be stabilized. In the ACS open loop system, small force and torque disturbances could still produce large responses in the final performances due to uncontrolled rigid body rotations. The system must also be asymptotically stable in order to solve the Lyapunov problem in one of the disturbance methods. For these reasons, the rigid body modes were stabilized either indirectly by adding stiffness to the zero frequency rigid body modes, or directly through

the use of a simple attitude controller.

Because translational rigid body modes cannot be controlled by the reaction wheels or observed in the performance metrics, they are directly removed from the system. Only the zero frequencies of the rotational rigid body modes are retained in the  $A$  matrix. The indirect method of stabilization involves adding stiffness to these modes to make them stable. Low frequency, critically damped ( $\zeta = \sqrt{2}/2$ ) poles are placed a decade below the lowest structural mode. This “pseudo-controller” is non-physical, but it allows a fast and simple ACS implementation. This was done for both the Nexus and NGST models. An example of the ACS open and closed loop system is provided in Figure 7-1

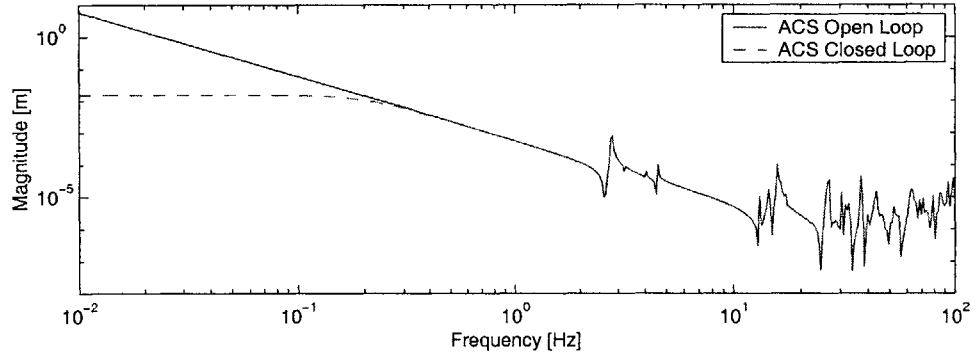


Figure 7-1: Effect of ACS “pseudo-controller” on Nexus/Horizon plant, RWA force X to centroid X.

The more realistic alternative is to construct an actual ACS controller loop. de Weck [32] built a simple loop for SIM that uses three parallel proportional-derivative (PD) channels along with a second order low-pass filter (LPF), to control the three rigid body rotations. The transfer function for a single channel is of the form

$$K_{acs}(s) = \frac{[K_r s + K_p] \omega_l^2}{s^2 + 2\zeta_l \omega_l s + \omega_l^2} \quad (7.6)$$

where  $K_r$  and  $K_p$  are the derivative and proportional gains, respectively;  $\zeta_l$  is the damping and  $\omega_l$  is the LPF corner frequency. Critical damping of  $\zeta_l = 0.707$  is used, and  $\omega_l$  is set above the crossover frequency, which is a decade below the first structural mode at 0.41 Hz. The controller inputs the three spacecraft attitude angles (as was listed in the table of SIM outputs, Table 2.3) and outputs commands to the three reaction wheel torques. The effective bandwidth of the controller is about 0.04 Hz, as seen Figure 7-2.

The optical controllers are the last pieces to be added to the integrated model. The

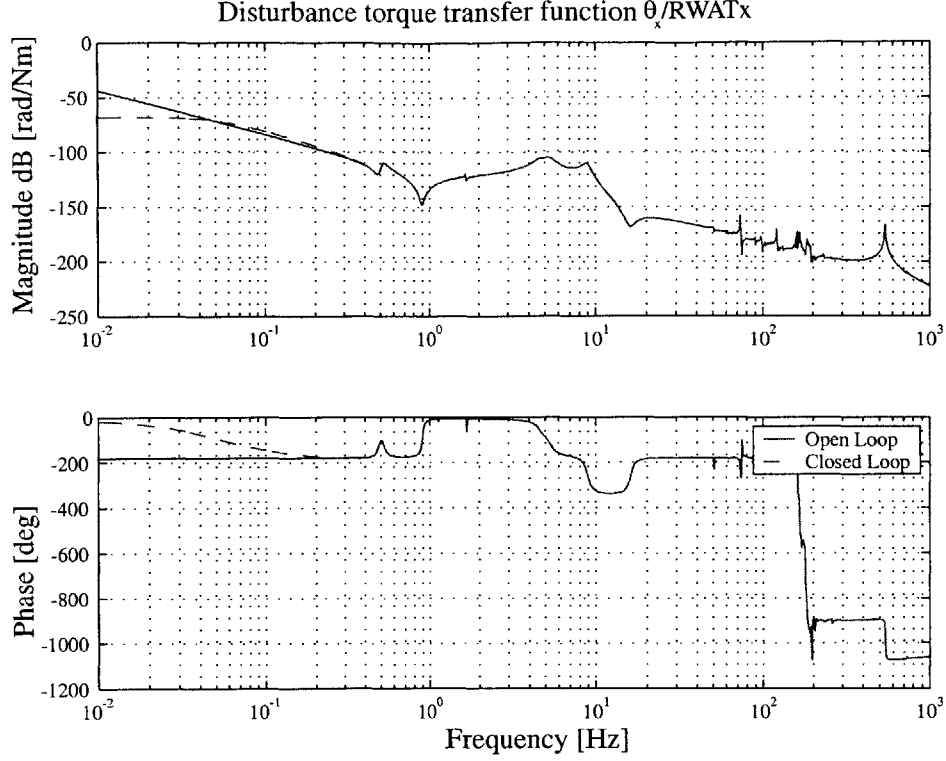


Figure 7-2: Effect of simple ACS controller on SIM plant

precise pathlength and wavefront control for both NGST and SIM cannot be attained without the use of robust optical controllers. None of the control loops have been developed yet for these spacecraft, however. For Nexus and NGST, the disturbance analyses will therefore be entirely in the open loop. In the case of SIM, a high pass filter (HPF) pseudo-controller will be used in place of an actual control loop. The high pass filter is of the form

$$K_{opt}(s) = \frac{s^2}{s^2 + 2\zeta_o\omega_o s + \omega_o^2} \quad (7.7)$$

where  $\zeta_o = 0.707$  and the optical control bandwidth  $\omega_o/2\pi$  is set at 100 Hz. This has the effect of flattening the open loop transfer function below 100 Hz. One problem that will be seen with SIM is that many of the modes affecting the performance are above this frequency and are unaffected by the optical controller.

Both the ACS controller and the optical HPF are cast into state-space form using a controller canonical realization, and are put into series with the system plant in a manner much similar to Equation 7.4. With these last components in place, the integrated open and

closed loop models are complete. The disturbance analysis can now be run on the entire system.

## 7.2 Disturbance Analysis Methodology

The DOCS disturbance analysis was developed by Gutierrez [22] and the routines were coded into a MATLAB file `dist_analysis.m` that runs one of three analyses based on the nature of the disturbance input. The three methods of applying the disturbances are by using time histories, PSD matrices in the frequency domain, or by appending a state space shaping filter to the plant in order to solve a Lyapunov problem. The latter two approaches will be run for Nexus, NGST, and SIM. A brief description of each analysis follows.

It is assumed that the spacecraft plant model, consisting of structural and performance (optics) models, can be written in the form

$$\begin{aligned}\dot{q}(t) &= A_{zw} q(t) + B_{zw} w(t) \\ z(t) &= C_{zw} q(t) + D_{zw} w(t)\end{aligned}\tag{7.8}$$

where  $w(t)$  are the disturbance inputs (whether from a reaction wheel or another source) and  $z(t)$  are the performance outputs (displacements, optical metrics, et cetera as desired). The state vector  $q(t)$  can include the plant states  $q_p(t)$ , the disturbance states  $q_d(t)$ , and any controller states  $q_c(t)$  that have been added.

The time history approach assumes that disturbance time histories  $w(t)$  exist. These can be from measured data, or simulated examples. The differential equation in Equation 7.8 can then be numerically integrated using any one of a multitude of integration schemes. Reference [17] describes many of the popular methods.

The frequency domain approach simplifies the analysis into multiplication of matrices. It assumes the disturbances can be described by a spectral density matrix  $S_{ww}(\omega)$  of size  $n_w \times n_w \times n_{freq\ pts}$ . For the reaction wheel models, this matrix is in the form of Equation 6.8.  $S_{ww}(\omega)$  can be either continuous in frequency, as in the broadband reaction wheel case, or consist of discrete tones. A frequency domain transfer function representing the plant, Equation 7.8, can be described by



$$G_{zw}(\omega) = C_{zw}(j\omega I - A_{zw})^{-1}B_{zw} + D_{zw} \quad (7.9)$$

where  $\omega$  is the frequency in rad/sec. As was done in Equation 6.15, given an input PSD, the performance output PSD can be found by the matrix multiplication

$$S_{zz}(\omega) = G_{zw}(\omega)S_{ww}(\omega)G_{zw}^H(\omega) \quad (7.10)$$

The PSD of the  $i^{th}$  performance is contained in the  $[S_{zz}(\omega)]_{i,i}$  vector of the three dimensional array  $S_{zz}(\omega)$ . This captures all of the frequency content of the signal, and using the cumulative RMS curves the modes which contribute most to the performance degradation can be identified. The RMS performance errors are found in the same manner as Equation 6.22, by integrating under the PSD curve (assuming zero mean processes) and taking the square root.

$$\sigma_{z_i}^2 = \frac{1}{2\pi} \int_{-\infty}^{\infty} [S_{zz}(\omega)]_{i,i} d\omega \quad (7.11)$$

While the integral to infinity will produce the final RMS value, an integral up to any frequency  $\omega_j$  will give the contribution to the RMS of the frequencies to that point. By sweeping across the entire frequency range in this manner, the cumulative RMS curve can be drawn. It should be seen that the function will be monotonically increasing, and that any large jumps in the curve will indicate frequencies that strongly contribute to the error. The disturbance routine allows the user to identify the critical modes at those frequencies. The sensitivity analysis that is included in the DOCS package then examines the performance sensitivity to these modes and provides insight into which changes could improve performance.

The final approach is a Lyapunov analysis. It solves for the final performance RMS values directly using several matrix operations. All frequencies are taken into account without having to sum contributions along a specified frequency vector; as a result it does not suffer from frequency resolution issues as the PSD method may. The analysis requires that the disturbances be described in the form of a white noise state space shaping filter, as described by Equation 7.3. The disturbance states must be appended to the spacecraft plant  $G_{zw}$ , to create the white noise input to performance output transfer function  $G_{zd}$ ,

described by Equation 7.5. The system must be stable to solve the Lyapunov equation, so rigid body controllers are necessary.

The system covariance matrix  $\Sigma_q$  is found by solving the steady-state Lyapunov problem,

$$A_{zd}\Sigma_q + \Sigma_q A_{zd}^T + B_{zd}B_{zd}^T = 0 \quad (7.12)$$

and the performance covariance matrix is found from

$$\begin{aligned} \Sigma_z &= \mathcal{E} [zz^T] \\ &= \mathcal{E} [C_{zd} qq^T C_{zd}^T] \\ &= C_{zd} \mathcal{E} [qq^T] C_{zd}^T \\ &= C_{zd} \Sigma_q C_{zd}^T \end{aligned} \quad (7.13)$$

where  $\mathcal{E}[\cdot]$  is the expectation operator. Each diagonal entry of  $\Sigma_z$  corresponds to one of the performance outputs of interest. The RMS values are the square roots of these diagonal entries.

$$\Sigma_z = \begin{bmatrix} \sigma_{z_1}^2 & \sigma_{z_1 z_2} & \cdots & \sigma_{z_1 z_{n_z}} \\ \sigma_{z_2 z_1} & \sigma_{z_2}^2 & & \vdots \\ \vdots & & \ddots & \\ \sigma_{z_{n_z} z_1} & \cdots & & \sigma_{z_{n_z}}^2 \end{bmatrix} \quad (7.14)$$

The Lyapunov approach is convenient since it requires only one Lyapunov solution (which can be made faster using the fast Lyapunov solver of Section 3.3.3, provided that  $A_{zd}$  is block-diagonal), and two matrix multiplications to provide a final RMS result. The disadvantage compared to the PSD frequency domain method is that no frequency information is provided. Only the final RMS value for each performance is output.

The PSD and Lyapunov disturbance methods will be used on the spacecraft model. Using the reaction wheel disturbances developed previously, the PSD frequency domain approach will be used on all three observatories. The Lyapunov approach will be applied only to SIM.

### 7.3 PSD Analysis on Nexus & NGST

The frequency domain PSD disturbance method was applied to Nexus/Horizon in an early attempt to compare the dynamics of that spacecraft with NGST. Due to the dynamic dissimilarities between them, Nexus was later redesigned to behave more like NGST. This analysis shows the differences between the spacecraft and demonstrates the DOCS disturbance procedure.

The Nexus/Horizon FEM provides nodes at each of the four wheel locations. Since each wheel contributes three forces and three moments, a total of 24 disturbance inputs will be required. Based on mechanical drawings of the spacecraft bus, the chosen wheel Euler angles in terms of  $\alpha$ ,  $\theta$ , and  $\gamma$  are  $[45^\circ, -45^\circ, -135^\circ, 135^\circ]$ ,  $[135^\circ, 135^\circ, 135^\circ, 135^\circ]$ , and  $[0^\circ, 0^\circ, 0^\circ, 0^\circ]$ . The Ithaco E-wheel model will be used since that type of wheel is a candidate for use on NGST. Only three performance outputs were considered: centroid X, centroid Y, and the wave front error (WFE) for a single representative ray.

Since the purpose of the analysis is to compare Nexus/Horizon with NGST, a similar disturbance analysis will also be performed using the `ngst810` model, though a more complete NGST disturbance analysis can be found in [14]. For the NGST model, the effects of all four wheels are colocated at a single node. The distance from each wheel to the node is  $d = 0.5\text{m}$  and the Euler angles of the assembled wheels are  $\alpha = [-135^\circ, 180^\circ, 135^\circ, 0^\circ]$ ,  $\theta = [-90^\circ, 0^\circ, 90^\circ, 0^\circ]$ , and  $\gamma = [0^\circ, 45^\circ, 0^\circ, -135^\circ]$ .

The broadband RWA model will be applied first, followed by a sample discrete wheel speed case. It should be noted for the discrete case that all wheels are modeled as running at the same speed. In reality this will most often not be the case. Because of this, the results should be reviewed as being the worst-case.

#### 7.3.1 Broadband wheel speeds

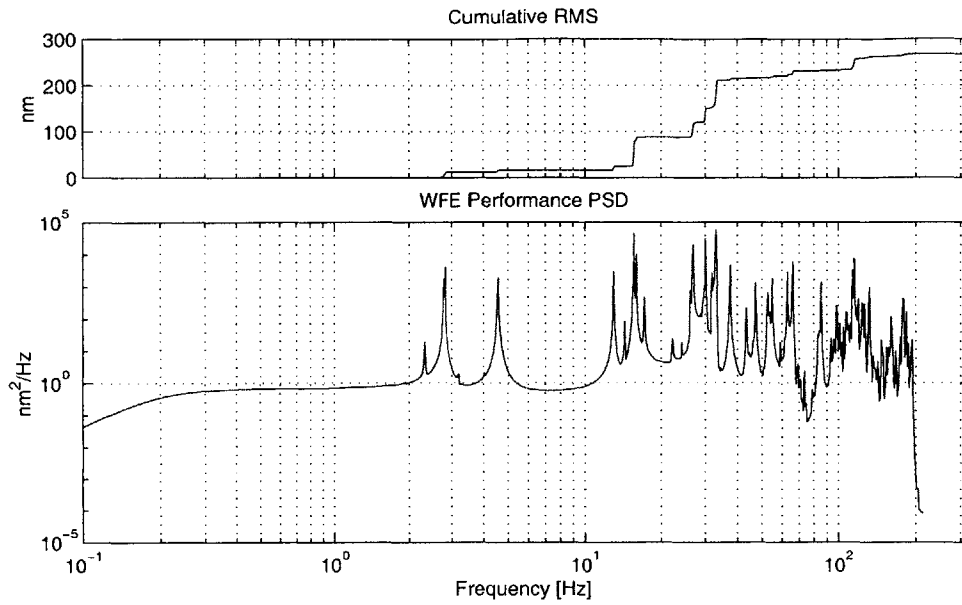
Broadband wheel speed disturbance PSDs such as those plotted in Figure 6-4 were applied to the two spacecraft. The WFE performance PSD outputs are shown in Figure 7-3 (the plots for centroid X and Y are in Appendix A). They are continuous functions of frequency with the spacecraft modes emphasized or attenuated depending on the strength of the wheel disturbances at a particular frequency. Above each PSD plot is its cumulative RMS curve. The final value on this curve is the total RMS performance value to be compared with the

requirements (though no requirements had been yet specified for Nexus, and both of these modes have open optics loops). One apparent difference between the spacecraft is that the frequencies contributing to Nexus' WFE RMS are much higher than for NGST. The cumulative RMS curve is still increasing near 200 Hz, beyond which point no further modes were computed. This suggests that more modes should be extracted for the Nexus model; ideally the RMS curve would asymptote to its final value well before the modes end, such as in the NGST cumulative RMS plot.

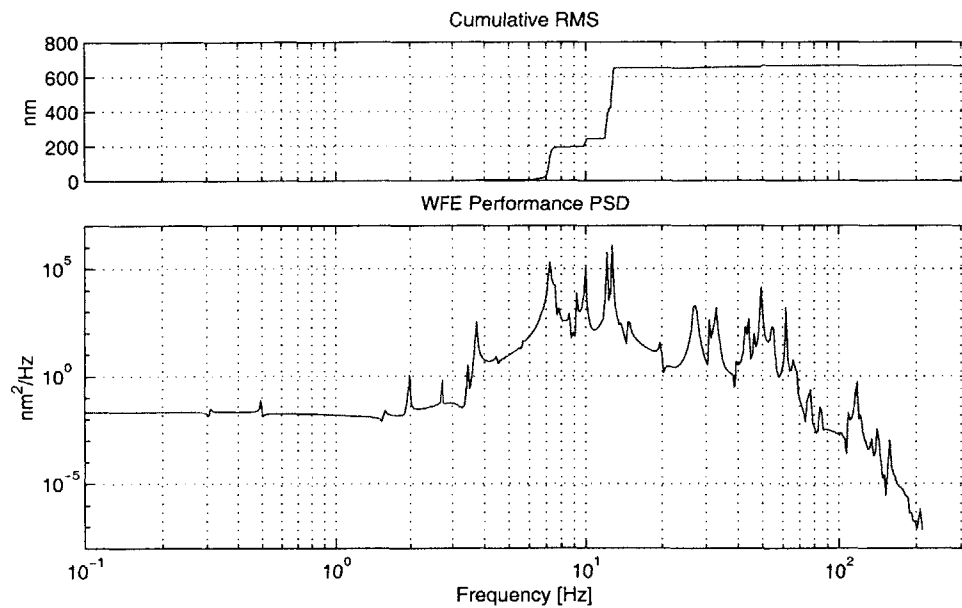
The frequency content of the curve can be examined to yield valuable information on the role individual modes play in the performance. The DOCS disturbance analysis provides steps to identify the critical frequencies and to determine which disturbance inputs contribute the most at those frequencies. The RMS plots are normalized to 1.0 and re-plotted to highlight jumps in the curve. This is shown in Figure 7-4. Assuming that the critical modes are lightly damped, each step corresponds to a frequency or small cluster of frequencies that can be mapped to a distinct mode of the system. The excitation of that mode (or modes) is responsible for the rise in performance RMS. The DOCS user can manually select those steps that appear the greatest for further examination. A separate, quantitative approach to selecting the critical frequencies is described in Reference [33]; it examines the contribution to the total RMS of each modal  $2 \times 2$  block in the system  $A_{zd}$  matrix.

These curves show the difference in frequency contribution between the two spacecraft much more concisely. A range of frequencies between 15 Hz to over 100 Hz contribute to Nexus' total performance RMS, while for NGST nearly the entire RMS rise occurs at 12 Hz. Once the critical frequencies are identified, the percentage contribution of each disturbance source to the total RMS error is computed. These are shown in Figure 7-5.

Because of the large number of disturbance inputs to Nexus, Figure 7-5(a) appears rather crowded. Upon closer examination, the  $F_z$ ,  $M_x$ , and  $M_z$  wheel disturbances contribute the most at 32.96 Hz, with the  $F_x$  and  $F_y$  disturbances contributing more at the lower frequencies. Overall a plurality of Nexus disturbance sources contribute to the WFE. Figure 7-5(b) is rather different. One mode at 12.72 Hz contributes over 80% of the entire WFE RMS, and of that 80% half is caused by the  $M_z$  disturbance, with most of the remainder from the  $M_x$  and  $F_y$ . Reference [14] describes this critical mode in more detail. Overall, a much more select group of disturbances affects NGST's WFE performance, and

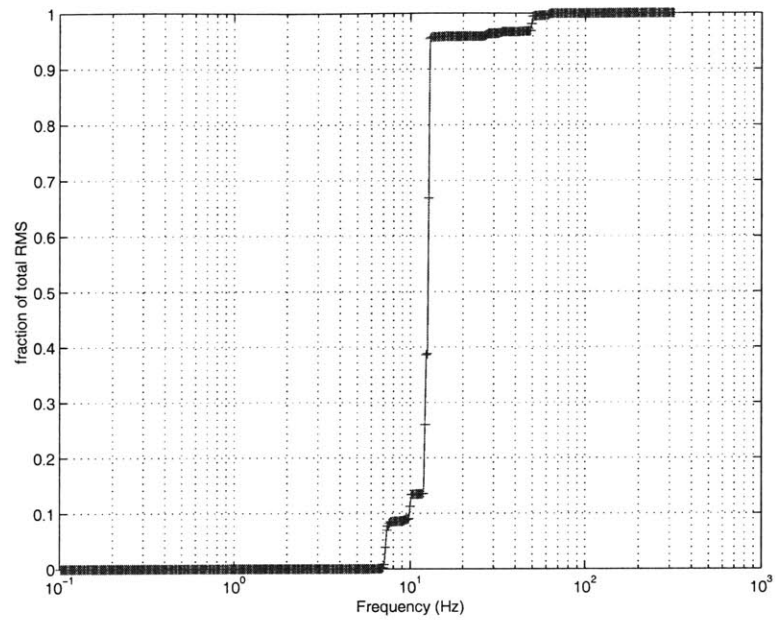


(a) Nexus/Horizon

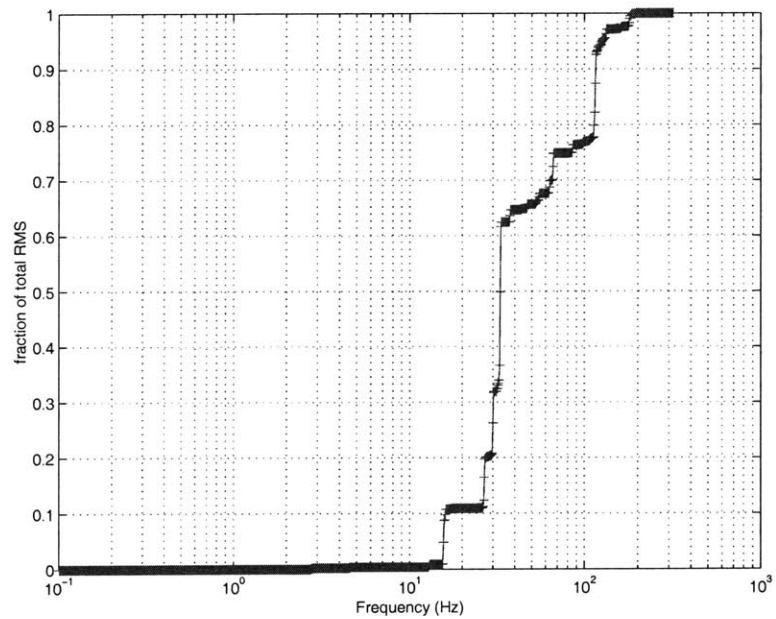


(b) NGST

Figure 7-3: Wave Front Error PSD and cumulative RMS plots for NGST and Nexus; broad-band wheel speeds

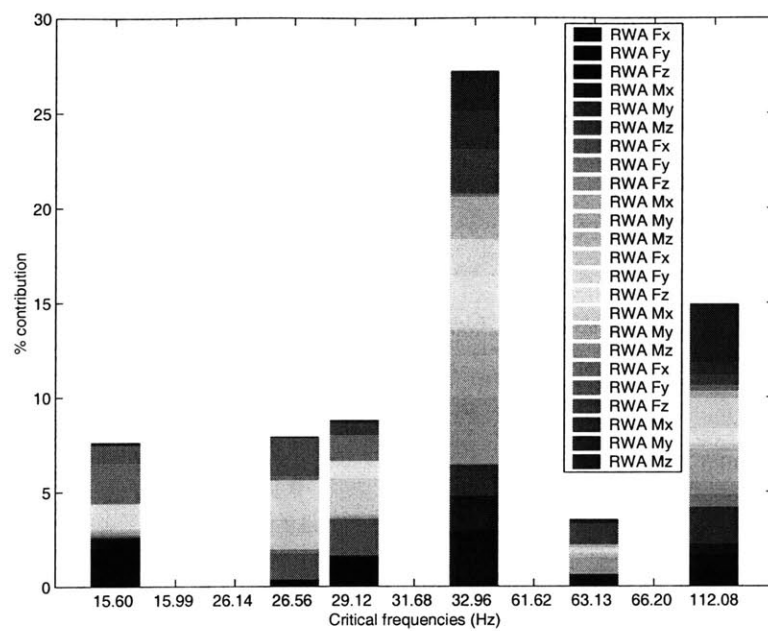


(a) Nexus/Horizon

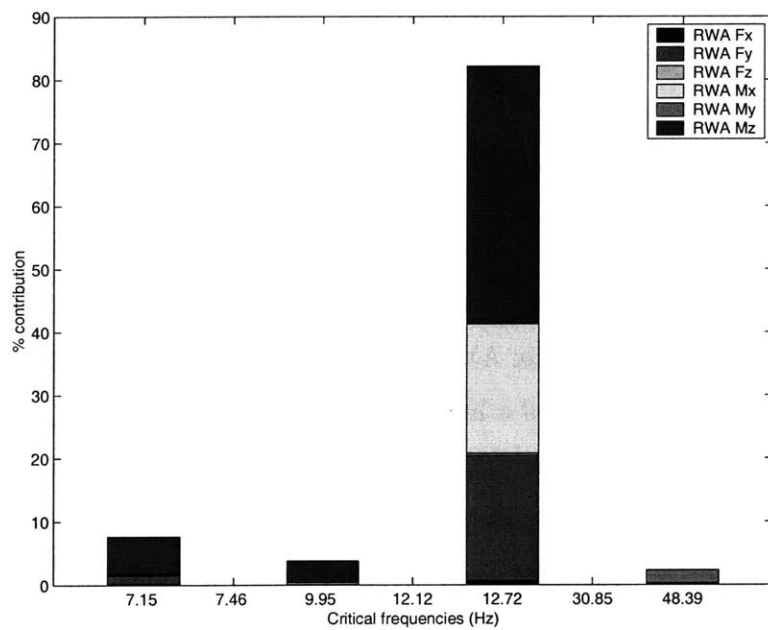


(b) NGST

Figure 7-4: Normalized Cumulative RMS WFE curves



(a) Nexus/Horizon



(b) NGST

Figure 7-5: Disturbance contributions to Critical WFE Frequencies

nearly all of the performance degradation is caused by a single mode.

Those frequencies listed in Figure 7-5 but without any contributions to the WFE have corresponding contributions to the centroid X and Y performances. Table 7.1 lists all of the critical frequencies identified for these performances. All but two of NGST's critical frequencies lie below those of Nexus. This suggests that NGST is a much more flexible spacecraft than Nexus and that the control bandwidths or vibration isolation requirements for each spacecraft will be different.

Table 7.1: Critical Frequencies in Hz

Nexus/Horizon	NGST
15.60	7.15
15.99	7.46
26.14	9.95
26.56	12.12
29.12	12.72
31.68	30.85
32.96	48.39
61.62	
64.13	
66.20	
112.1	

### 7.3.2 Discrete wheel speeds

A PSD-based disturbance analysis using discrete wheel speed tones was also performed. An example of the performance PSD at 1000 RPM is shown in Figure 7-6 (the plots for centroid X and Y are in Appendix A). Because the PSD consists of a series of tones at discrete frequencies, the outputs of a linear system are themselves only a series of tones at those frequencies. The cumulative RMS curve is formed of pure steps; each tone adds a specific amount to the final value. The analysis was run repeatedly between 100 RPM and 2500 RPM (the expected operating range) to produce the performance versus wheel speed plots of Figure 7-7.

These plots identify wheel speeds at which the spacecraft are susceptible to disturbances. For instance, 1000 RPM is a relatively quiet speed for both. Hence the final Nexus RMS value in Figure 7-6 is much less than for the broadband PSD plot, Figure 7-3(a) (264nm for the broadband versus 175nm for the discrete wheel speed case). Stronger excitations



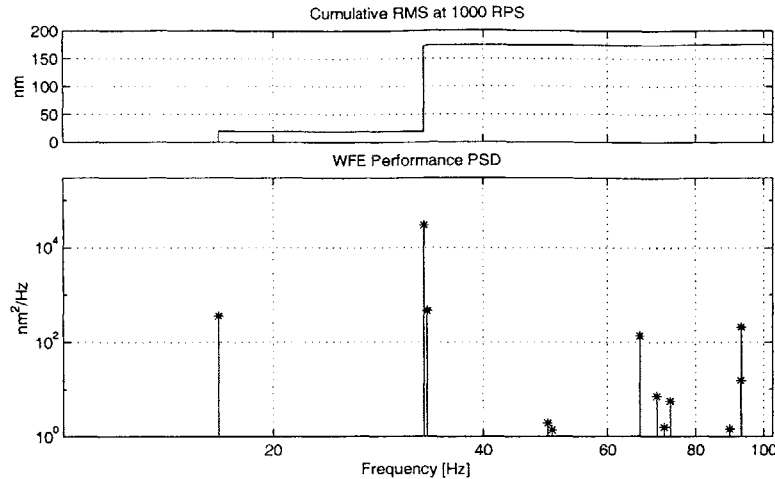
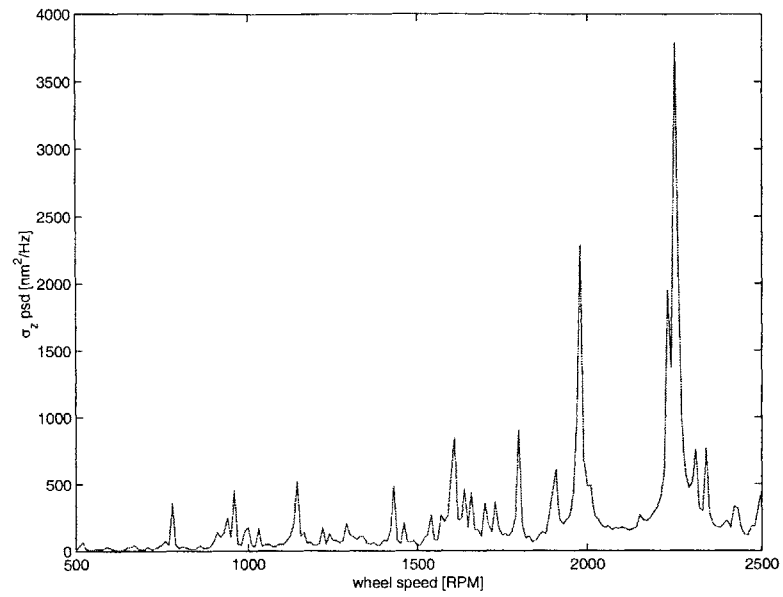


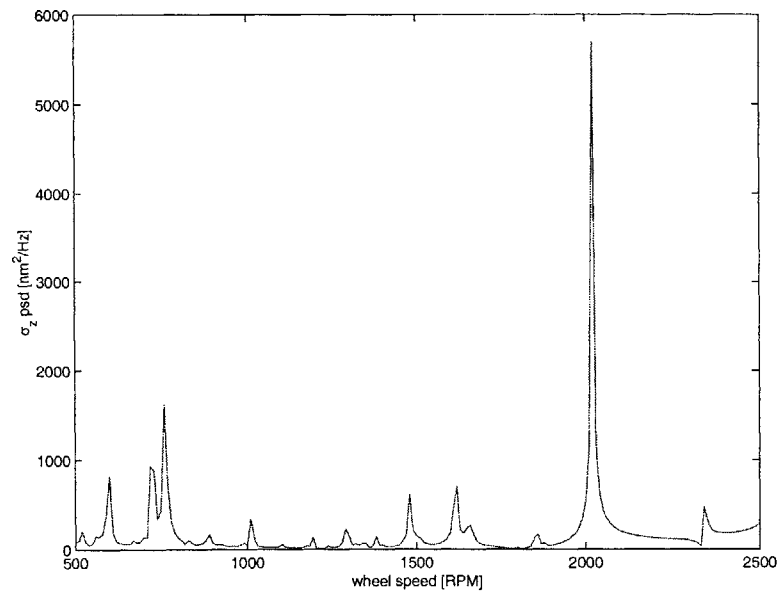
Figure 7-6: WFE performance PSD for Nexus/Horizon using a tonal RWA model at 1000 RPM

occur at other speeds; note in particular the strong peak at 2020 RPM for NGST, and the peaks at 1980 RPM and 2250 RPM for Nexus. Comparing the two plots, Nexus seems to be excited at many more wheel speeds than NGST, and the speeds that do excite NGST are more widely separated from each other. One basic approach to reducing the disturbance errors is to restrict the speeds at which the wheels may spin. NGST's dynamics would allow a wider range of acceptable speeds.

It would still be useful to examine the frequency content at each critical wheel speed, to determine which modes are contributing to the performance degradation. This would involve computing the discrete performance PSDs, as in Figure 7-6, at multiple wheel speeds. Although this would be impractical for the entire range, the performance versus RPM plots could be used to identify the critical speeds. The broadband results suggested that Nexus has many more critical modes than NGST. The interaction of wheel harmonics with all of these modes could cause the behavior seen in Figure 7-7(a), namely a multitude of critical wheel speeds. Likewise if only a single mode drives NGST's performance, then only when a harmonic crosses that one frequency would a strong disturbance be evident in Figure 7-7(b). Although NGST is a much more flexible spacecraft, the control problem may be less than for Nexus, since only one critical mode must be targeted for active control.



(a) Nexus/Horizon



(b) NGST

Figure 7-7: WFE performance versus wheel speed

### 7.3.3 Nexus/NGST Analysis Summary

Although intended as a testbed leading to NGST, the Nexus/Horizon model shows a dynamically dissimilar spacecraft. It is much stiffer than NGST, its critical frequencies are much higher, and the manner in which disturbances excite the structure are different. Nexus seems to require general isolation of the reaction wheels, while NGST could improve from isolation of particular wheel axes. If active optical control is used, NGST may actually be an easier spacecraft to work with, since only one mode at a low frequency (beneath most optical control bandwidths) would have to be controlled. Further examination of the frequency content at critical wheel speeds is recommended. This will be done for SIM in the next section.

## 7.4 Lyapunov and PSD Analysis on SIM

The RWA disturbances on SIM will result from at least three Teldix reaction wheels, one oriented along each of the three spacecraft axes. Because the Teldix wheel model was not available, HST wheels were considered sufficiently similar to be used in their stead. The effects from all three wheels were co-located at a single node, so the disturbance summation method, described previously, was employed. The Euler angles for the three wheels in terms of  $\alpha$ ,  $\theta$ , and  $\gamma$  are  $[0^\circ, 90^\circ, 0^\circ]$ ,  $[90^\circ, 90^\circ, 0^\circ]$ , and  $[0^\circ, 0^\circ, 0^\circ]$ . Since that node represents a reaction wheel, the distance  $d$  of the wheel to the point of application was zero. The wheels will be run between 10 and 66 RPS, or between 600 and 3960 RPM. As in the Nexus/NGST discrete analysis, all wheels are assumed to be run at the same speed. This is unlikely to actually occur, so the results may be considered worst-case.

The SIM model used for this analysis is SIM Version 2.2. The discrete wheel speed disturbance model in the form of either a Lyapunov shaping filter or PSD tones will be used. A high pass filter approximation to the optical control loops has been applied to closed the optics loop around the Star OPD, Internal Metrology OPD, and Wave Front Tilt (WFT) performances (for a . The Front End Camera (FEC) and External Metrology performances are left solely in the open loop.

One factor in both the open and closed loop performances will be the dynamics of the HST wheels. Unlike the Ithaco E- and B-wheels, the fundamental harmonic is not dominant. Figure 7-8 shows the  $C_i$  versus  $h_i$  ( $i^{th}$  harmonic) for the axial and radial force components of

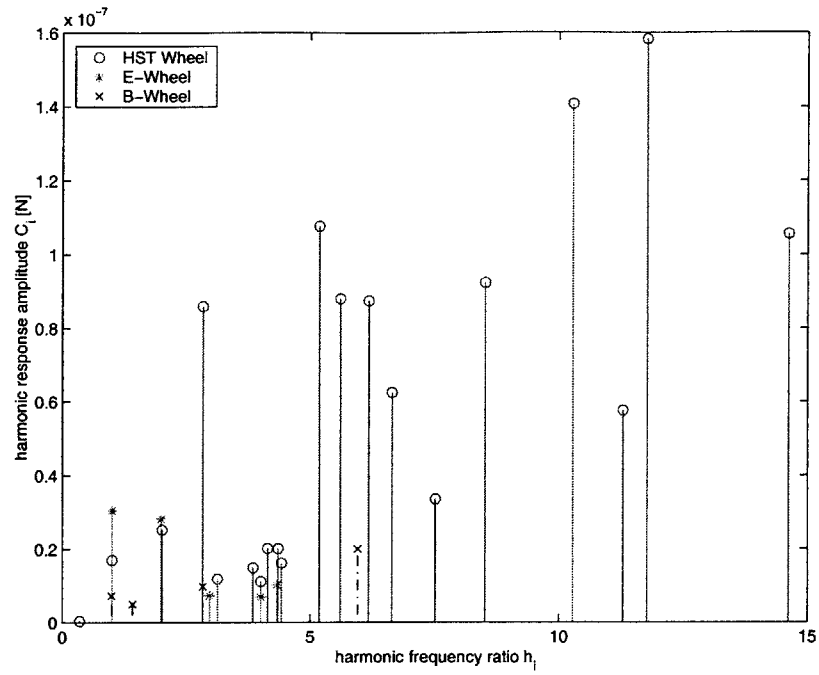
the two Ithaco wheels and the HST wheel. The  $h_i$  represent the ratio of harmonic frequency to fundamental frequency, so  $h_i = 1$  is the fundamental,  $h_i < 1$  is the subharmonic, and  $h_i > 1$  are the higher harmonics. The  $C_i$  are amplitudes of the harmonic response in [N] or [N-m].

One obvious feature of the HST wheel in Figure 7-8, is the larger number of harmonics compared to the Ithaco wheels. For the axial disturbance component, the Ithaco E-wheel has five harmonics and the B-wheel has four, while the HST wheel has twenty. The frequency content of the wheel is also much higher. The largest axial  $h_i$  for the B-wheel is 5.95, compared to 14.62 for the HST wheel. What is also surprising about the wheel is the strength of those higher harmonics. For both the B-wheel and HST wheel the  $C_i$  for the higher harmonics are greater than for the fundamental; this is more pronounced for the HST wheel however. The strongest axial harmonic is nearly ten times as great as the fundamental. All of this suggests that the higher harmonics will dominate the HST disturbance. Since even at the lowest wheel speeds (10 RPS) the highest harmonics will be above the controller bandwidth (100 Hz), optical control will be unable to attenuate their effects, as will be seen.

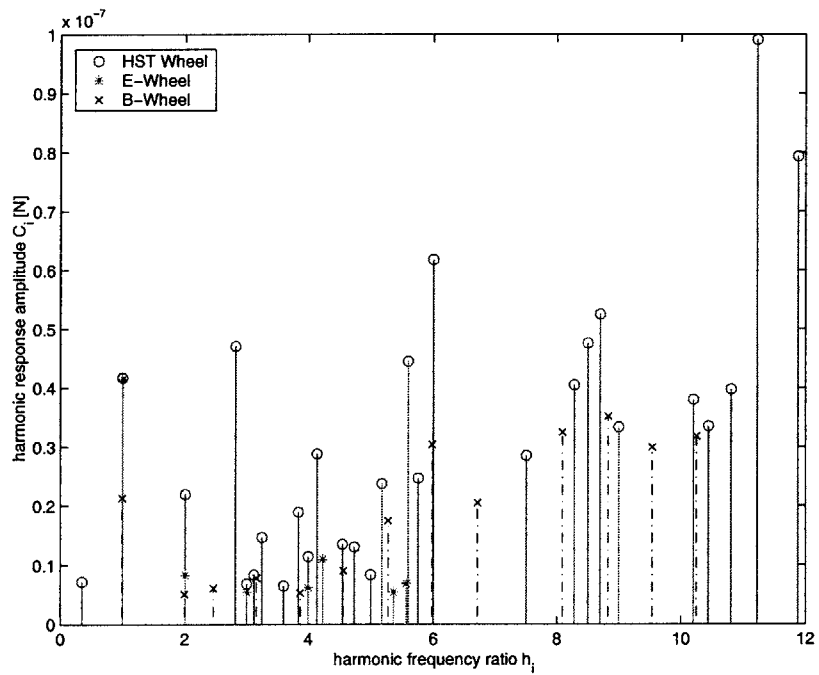
#### 7.4.1 Lyapunov Analysis

The Lyapunov disturbance method was applied first. The analysis output is a vector that contains the final RMS performance for each performance at a given wheel speed. The analysis is then repeated through the wheel speeds. The  $\Delta$ RPS is 0.2 RPS. Figure 7-9 is an example output, that shows both the open and closed loop RMS results across wheel speeds. Also plotted are the average values of the performance errors, along with the given performance requirement (6 nm for Star OPD).

Figure 7-9 is typical of the open and closed loop behavior of the Star OPD and Internal Metrology OPD results. Open loop results exceed the requirement for over half of the wheel speed range, particularly at lower speeds. Speeds at 11 and 19.8 RPS illicit strong responses. At higher wheel speeds, the results overshoot the requirements between 56.4 and 60.4 RPS, and above 64.8 RPS. When the optics loop is closed, all of the low-speed excitation is attenuated, but the high speed response above 30 RPS remains the same as with the open loop. These responses are caused by higher wheel harmonics above the 100 Hz optical bandwidth. Since the optical errors excited by these harmonics are not attenuated by control, the structural response is nearly the same as without any optical control. This



(a) Axial Disturbances



(b) Radial Disturbances

Figure 7-8: Wheel harmonic numbers  $h_i$  versus wheel harmonic coefficients  $C_i$  for the Ithaco E- and B-wheels and the HST wheel.

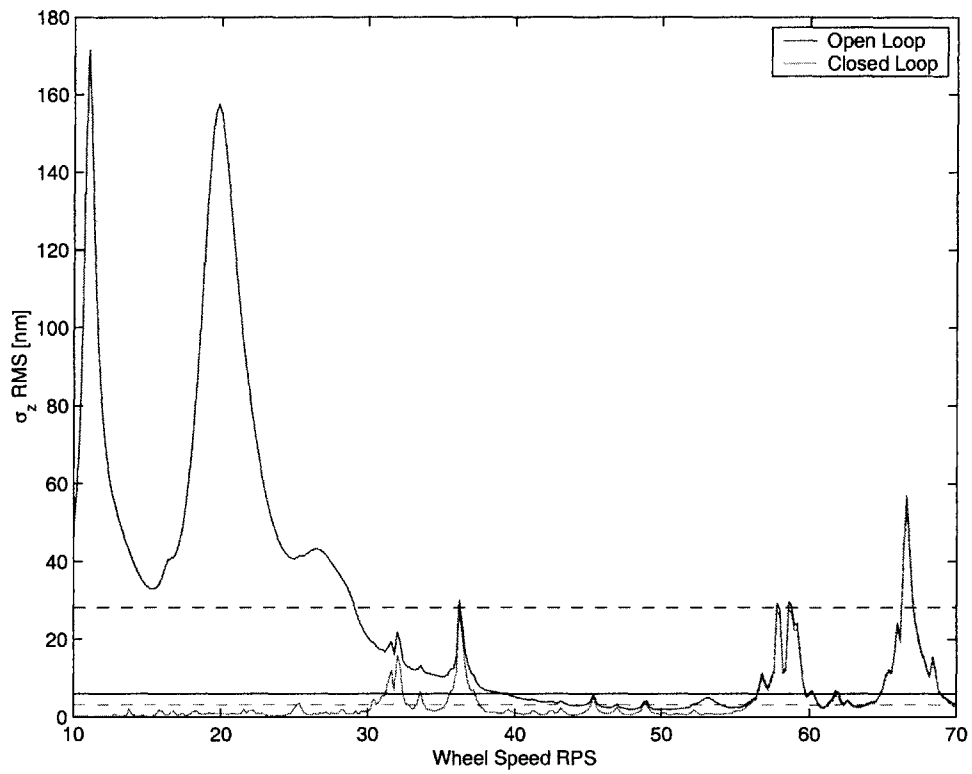


Figure 7-9: Open and Closed Loop performance RMS versus RPM for Star OPD #1. Dashed horizontal lines indicate average values; solid horizontal line indicates requirement.

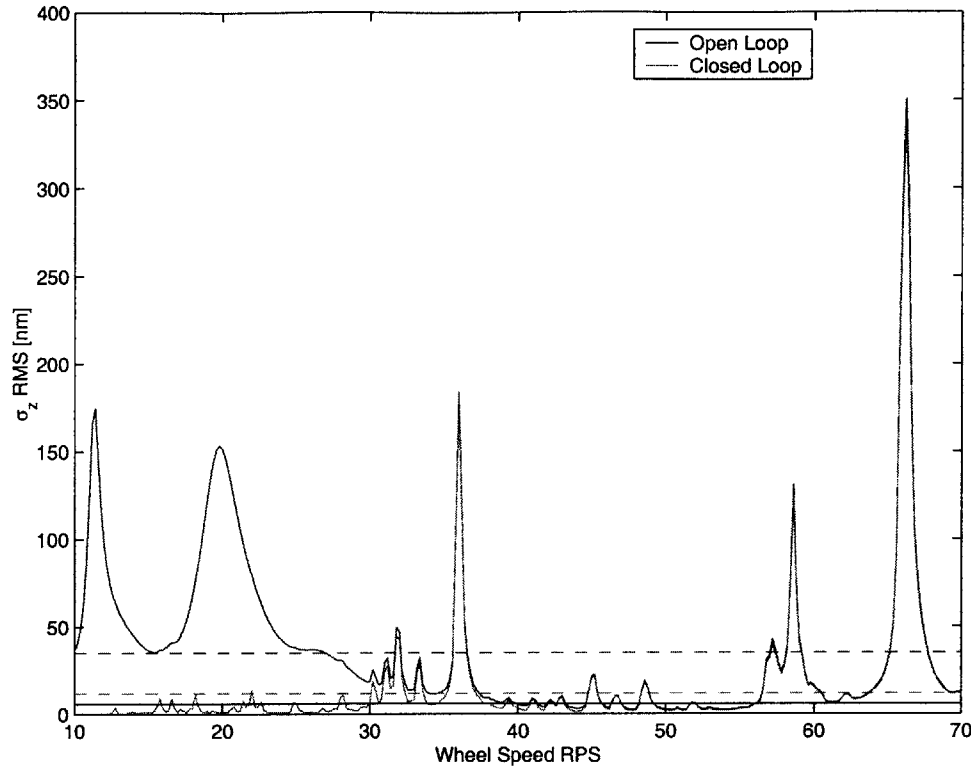


Figure 7-10: Open and Closed Loop performance RMS versus RPM for Star OPD #2. Dashed horizontal lines indicate average values; solid horizontal line indicates requirement. Note the stronger responses at high speeds compared to Star OPD #1.

will be seen more clearly with the frequency-based PSD plots coming up.

One interesting feature that these plots show is a variation between the responses of interferometer #2 and those of interferometers #1 and #3. For the Star and Internal Metrology OPD, the regions of open and closed loop excitation are the same as were just observed, but the magnitude of the response at higher wheel speeds is greater. Figure 7-10 illustrates this. This same behavior was seen in a broadband analysis of the model [32], so it appears to be a feature of the finite element model and not the disturbance implementation. Because the finite element model was not provided, the reason for this behavior is unknown. A possible reason is if one or both of the siderostats that make up interferometer #2 sit in a dynamically active region of the spacecraft Precision Support Structure.

A representative Wave Front Tilt performance plot is provided in Figure 7-11. The performance meets requirements even in the open loop. Closed loop behavior resembles the open loop above 30 RPS again illustrating the limitation of control at these speeds due to the high frequency, uncontrolled harmonics. Neither the Front End Camera nor the

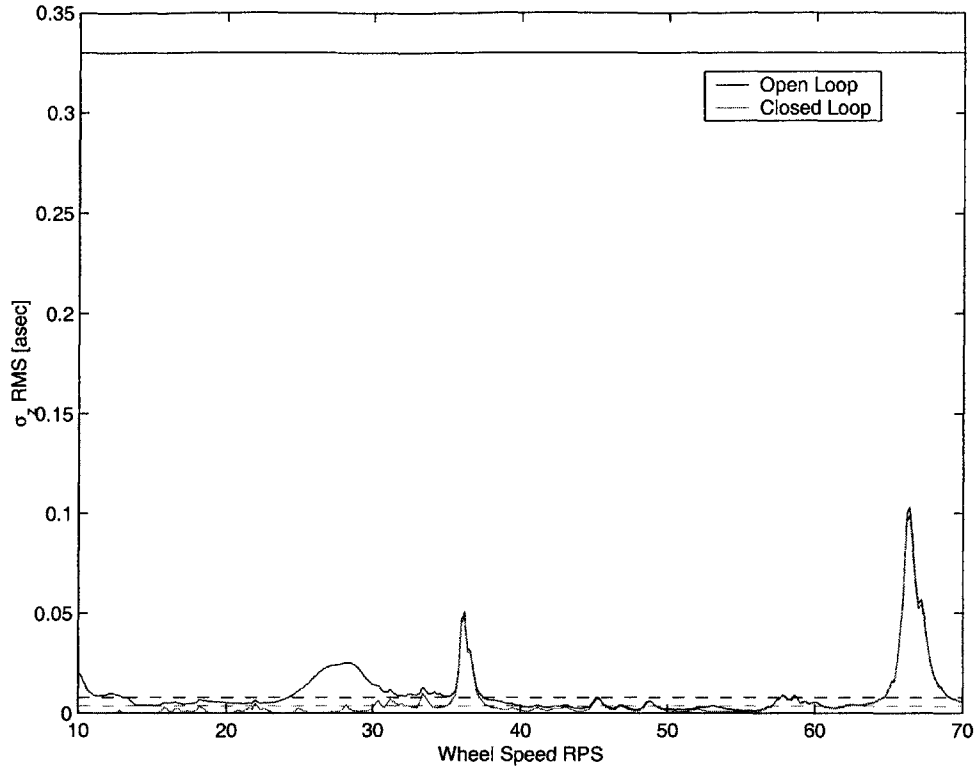


Figure 7-11: Open and Closed Loop performance RMS versus RPM for Star X WFT #1. Dashed horizontal lines indicate average values; solid horizontal line indicates requirement.

External Metrology have closed optics loops, and requirements are not set for either. Plots of all the performances can be found in Appendix B. Table 7.2 summarizes the average and maximum RPS results.

#### 7.4.2 Reaction Wheel Comparison

Since the performance dynamics depend on the dynamics of the reaction wheel disturbances, and because the HST wheels are not the actual wheels that are being baselined for SIM, analyses were also run with several other RWA models. The purpose was to examine how the performance dynamics change with the amount of reaction torque and with different frequency ratios  $h_i$ . The goal is to determine which characteristics of a wheel drive the performances. If these characteristics are found in the Teldix wheel model, then the disturbance analysis results using the HST wheel model may accurately reflect the baselined spacecraft. A sample RMS performance versus wheel speed plot is shown in Figure 7-12. It compares the closed loop response of Star OPD #3 given HST, Ithaco E-, and Ithaco B-wheel models.

There is an obvious difference in magnitude between wheel models; both Ithaco wheels



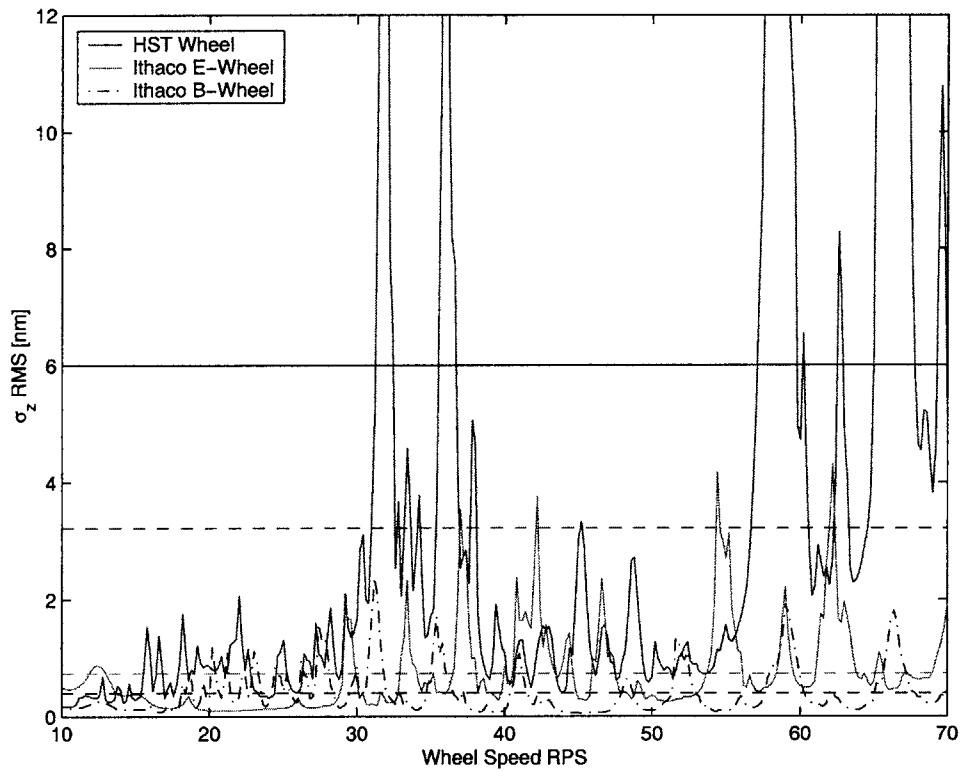


Figure 7-12: Closed Loop performance RMS versus RPM for Star OPD #3 for the Ithaco E- and B-wheels and the HST wheels. Dashed horizontal lines indicate average values; solid horizontal line indicates requirement.

Table 7.2: Summary of RMS Performances from SIM Lyapunov Analysis

Performance	Req.	Open Loop		Closed Loop	
		Average $\sigma_z$	Max. $\sigma_z$	Average $\sigma_z$	Max. $\sigma_z$
Star OPD #1 [nm]	6	28.2	172	3.17	27.8
Star OPD #2 [nm]	6	34.9	295	11.8	284
Star OPD #3 [nm]	6	28.9	186	3.23	38.2
Int. Met. OPD #1 [nm]	na	49.5	342	6.43	57.1
Int. Met. OPD #2 [nm]	na	65.9	588	23.4	565
Int. Met. OPD #3 [nm]	na	52.2	371	6.41	76.1
Star WFT #1 [asec]	0.21	0.0080	0.062	0.004	0.060
Star WFT #2 [asec]	0.21	0.0082	0.073	0.004	0.070
Star WFT #3 [asec]	0.21	0.0082	0.089	0.005	0.085
FEC Tilt #1 [asec]	na	0.0080	0.060		
FEC Tilt #2 [asec]	na	0.0076	0.065		
FEC Tilt #3 [asec]	na	0.0082	0.092		
Ext. Met. [nm]	na	18.9	197		

would apparently meet the performance requirement. This may be deceiving since the amount of torque (and hence the strength of the disturbances, see Figure 7-8) is less than the HST wheels (see Table 6.1); the wheels may in effect meet disturbance requirements while failing to meet the necessary torque requirements. Note however that the average performance values from the Ithaco wheels only differ by a factor of two, even though the torque they produce differs by a factor of ten. On the other hand, comparing the HST and Ithaco E-wheels, the average performance values differ by a factor of five and the maximum values differ by a factor of ten, even though the torques they produce differ only by a factor of three. The conclusion is that the relative difference in the amount of reaction torque does not seem to correspond to a similar difference in performance.

If torque is not a deciding factor in the magnitude of the response, then perhaps the dynamics of the wheels are important. It was previously observed in Figure 7-8, how the disturbance dynamics of the HST wheel differed from the Ithaco wheels in terms of frequency content and relative magnitude. The higher harmonics were more numerous and pronounced for the HST wheels. As will be seen in the next section, these higher harmonics will interact with high frequency modes to drive the closed loop performance. The strength and frequency content of the wheels seems to be much more important than their size; a wheel whose dynamics are similar to the HST wheels may produce similar responses no

matter what the torque is. In deciding whether the Teldix wheels would produce similar performance behavior, the harmonics should first be compared with the HST wheels.

Another difference between the wheels is the range of speeds that excite the structure. Worst-case peaks for the Ithaco wheels are distributed more evenly across the range, while for the HST wheels they tend to be clustered at mid-range and high-range speeds. This latter distribution may be preferable from the standpoint of the reaction wheel ACS controller. Assuming that some speeds will always excite the structure beyond acceptable levels, an easy way of staying within requirements is simply not to spin the wheels at those speeds. Although the worst case peaks of the HST wheels exceed requirements, there are relatively wide ranges where the performance is within limits. If there are redundant wheels, then a wheel speed control law can probably be designed to provide full authority while avoiding certain speeds. If this solution is unacceptable based on operational aspects, other solutions may be further isolation, or the use of magnetic wheel bearings to reduce the strength of the harmonics.

The differences indicate that the final performance is dependent on the wheel model chosen. A wheel of similar size as the HST wheel may not produce similar results; the disturbance dynamics of the wheel will be an important factor in the type of response that should be expected.

### 7.4.3 Frequency-based PSD Analysis

The Lyapunov analysis can indicate which wheel speeds will cause the worst performance, but it fails to provide any frequency information that specifies which modes are excited thereby causing the worst performance. This information can be provided by a PSD analysis. The white noise shaping filters are used to create continuous frequency PSDs such as that of Figure 6-7. As was done for Nexus and NGST in the previous section, performance PSDs and cumulative RMS curves are output from which the critical modes can be identified.

A PSD analysis for every wheel speed examined in the Lyapunov analysis would produce a surfeit of plots, many of which would correspond to uninteresting speeds that do not excite the structure. Though a performance waterfall plot may highlight dynamics not obvious by looking at PSDs for a single speed and should be considered for future work, this was not attempted here. The Lyapunov RMS versus RPS plots such as Figures 7-9 through 7-11

Table 7.3: Selection of SIM Critical RWA Speeds

	Open Loop		Open & Closed Loop			
	[RPS]		[RPS]			
Star OPD #1	11.0	19.8	31.6	36.2	58.6	66.0
Star OPD #2	11.4	19.8	31.8	36.0	58.6	66.0
Star OPD #3	11.6	19.8	31.6	36.0	58.0	66.0
Star WFT #1		28.2		36.2		66.0
Star WFT #2		28.2		36.0		66.0
Star WFT #3		28.2		36.0	58.6	66.0

and those included in Appendix B, are used to identify only those speeds that warrant closer examination. For Star OPD and WFT, a subset of the critical wheel speeds in both open and closed loop are provided in Table 7.3. The results are similar between Star OPD and Internal Metrology OPD, and between WFT and FEC.

It is obvious from Table 7.3 that there are several wheel speeds that affect all performances equally. The speeds around 36 RPS, 66 RPS, and to some extent 58 RPS all excite both pathlength and wavefront tilt performances. In addition, the speeds around 11 RPS, 19.8 RPS, and 28.2 RPS are important for the open loop performance. A PSD analysis was run for these speeds in order to understand the disturbance to structure interaction.

Figures 7-13 through 7-16 show examples of the Star OPD #1 performance PSD. Plots for the remaining performances can be found in Appendix C. Unlike the tonal PSD plots from the Nexus/NGST analysis, the entire frequency range is covered. All of the densely packed modes above 30 Hz are still visible, although unless a harmonic is passing over one of their frequencies, their relative importance should remain weak. Because the shaping filter is still modeling discrete tones, only those modal frequencies that match a tone should be excited in a linear system. This is seen by examining the cumulative RMS plots above each PSD plot. Consider Figure 7-13 which shows the open loop Star OPD #1 at 11.0 RPS. The final RMS value of 172 nm is identical to the value on the open loop curve in Figure 7-9 at 11.0 RPS and is the worst-case performance listed in Table 7.2. The PSD provides the additional information that nearly all of that value is produced in a single step at 3.84 Hz.

This excitation at 3.84 Hz results from the wheel subharmonic passing through structural modes at that frequency. The wheel harmonics shown in Figure 7-8 indicate a single subharmonic with an  $h_i$  of 0.35. For a wheel spinning at 11.0 RPS the fundamental will be

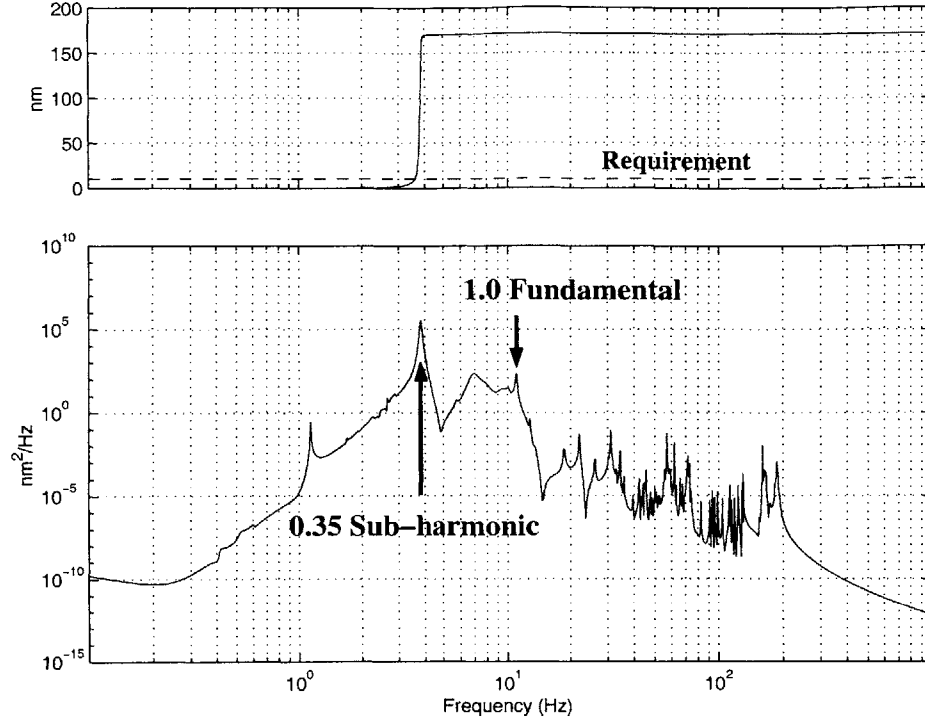


Figure 7-13: Star OPD #1 open loop at 11 RPS; PSD and cumulative RMS plot. Prominent RWA tones are highlighted.

at 11 Hz, and the subharmonic should be at:

$$f_{sub} = (RPS) \cdot h_{sub} = 11 \cdot 0.35 = 3.85 \text{ Hz}$$

which agrees with the observed response. It is interesting to note that the fundamental, which for most wheels causes the strongest disturbance, excites the structure far less than the subharmonic (both indicated by arrows in the figure) and has a negligible effect on the final RMS. This is the case for all of the speeds examined; the fundamental never adds an appreciable amount to the total RMS.

The subharmonic is also the driving disturbance for the Star OPD performances at 19.8 RPS , and for the WFT at 28.2 RPS. At higher wheel speeds, those unaffected by the optical control loop, the higher harmonics begin to play a more dominant role. Consider Star OPD #1 at 36 RPS (Figure 7-14). Four prominent peaks are indicated, although only two of these have a meaningful contribution to the total RMS, and of these one is dominant. The largest peak corresponds to the 5.18 harmonic passing through 186.48 Hz. The 2.0 harmonic passing through 72 Hz also affects the performance, though to a lesser

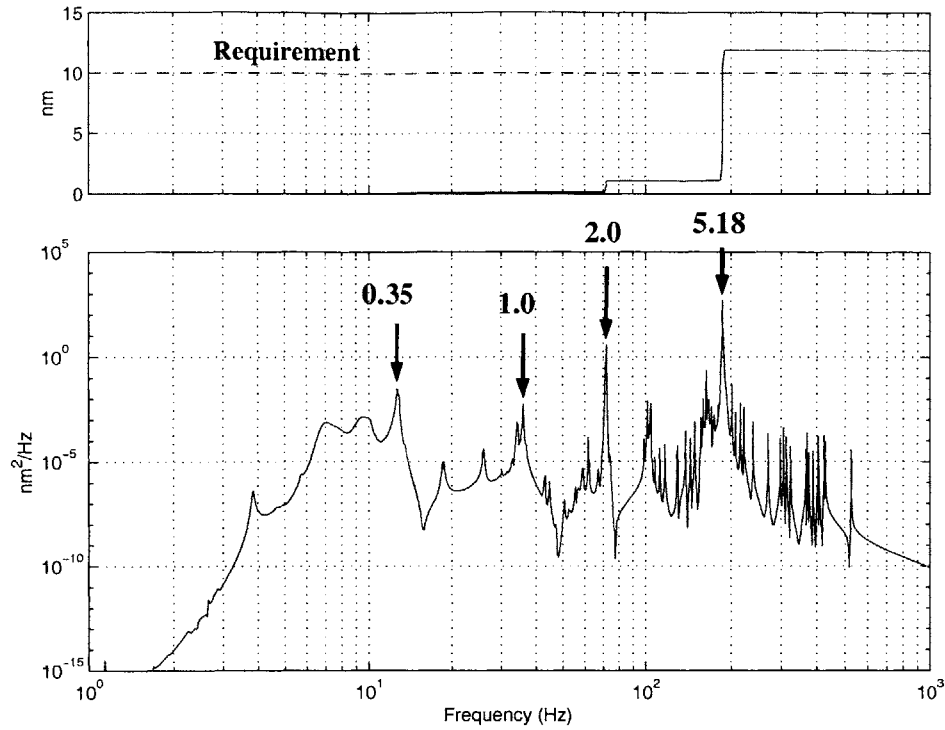


Figure 7-14: Star OPD #1 closed loop at 36 RPS; PSD and cumulative RMS plot. Prominent RWA tones are highlighted. In order from left to right are the 0.35 subharmonic, the fundamental, the 2.0 harmonic, and the 5.18 harmonic.

degree. The subharmonic and fundamental are indicated, but they do not contribute at these speeds. Figure 7-15 shows the condition at 58 RPS, with the main contribution coming from the 2.82 harmonic passing through 163.56 Hz. Figure 7-16 shows the highest anticipated wheel speed, 66 RPS, where the main disturbance is from the 2.82 harmonic now passing through 186.12 Hz. Based on all of the PSD plots in Appendix C, a listing of the critical frequencies and the associated harmonic number is provided in Table 7.4.

The high frequency dynamics of SIM, particularly in the area of 183 Hz to 193 Hz, was observed during balancing as a prominent feature of the transfer functions. It is shown now to be a major disturbance contributor in the closed loop. High HST harmonics interact with SIM's high-frequency modes to push the performance error beyond the allowable limits. This is troubling since this is beyond the optical control bandwidth and knowledge of the plant dynamics is poor at these high frequencies.

By using the Lyapunov disturbance method to identify critical wheels speeds, and the PSD disturbance method to identify at which frequencies the RMS “jumps”, critical modes of the spacecraft have been found. A modal contribution plot can be generated to precisely

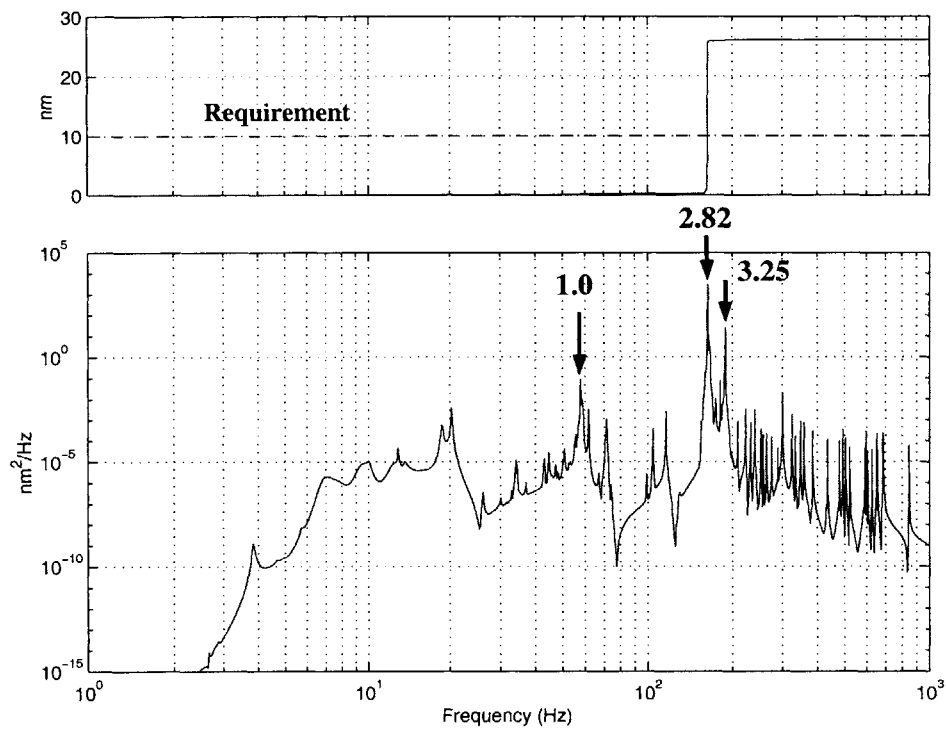


Figure 7-15: Star OPD #1 closed loop at 58 RPS; PSD and cumulative RMS plot. Prominent RWA tones are highlighted. In order from left to right are the fundamental, the 2.82 harmonic, and the 3.25 harmonic.

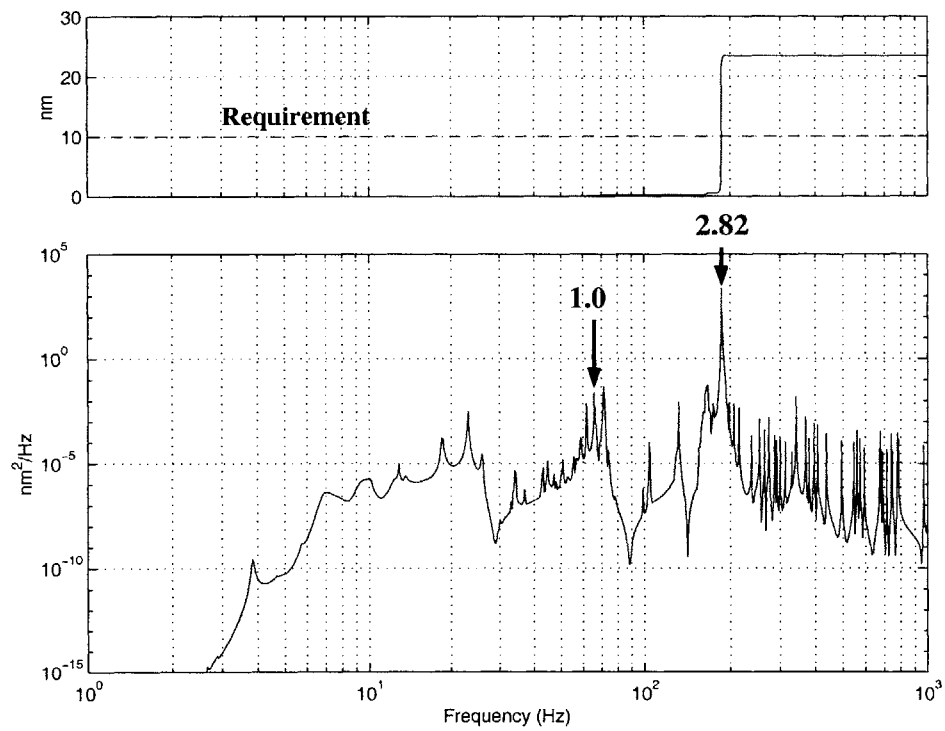


Figure 7-16: Star OPD #1 closed loop at 66 RPS; PSD and cumulative RMS plot. Prominent RWA tones are highlighted. In order from left to right are the fundamental and the 2.82 harmonic.



Table 7.4: SIM v2.2 Critical Frequencies

Wheel Speed [RPS]	Open Loop			Closed Loop				
	11.0	19.8	28.2	36.0	36.2	58.0	58.8	66.0
Star OPD								
$h_i$	0.35	0.35		5.18	5.18	2.82	2.82	2.82
frequency [Hz]	3.85	6.93		186.48	187.52	163.56	165.25	186.12
WFT								
$h_i$			0.35	5.18				
frequency [Hz]			9.87	186.48				

identify the critical frequencies. The quantitative approach in finding the critical frequencies was used in place of the manual selection described for Nexus and NGST. At 66 RPS for Star OPD #1, Figure 7-17 verifies that most of the contribution is at 186.12 Hz, and moreover results from six separate modes. An examination of the SIM  $A_{zd}$  matrix verifies that there are six modes at this frequency. Since the modeshapes for SIM are unavailable, it is impossible to say what is physically causing this behavior<sup>1</sup>.

#### 7.4.4 State-Space versus Tonal Comparison

A quick analysis was run at three wheel speeds (10 RPS, 40 RPS, and 60 RPS) using the pure PSD tones instead of the outputs of the shaping filter. At the relatively quiet speed of 60 RPS, Figure 7-18 shows the PSD and cumulative RMS plots using each method. There is a difference of 1.3 nm between the final RMS results (6.2 nm for the tonal disturbance, 4.9 nm for the shaping filter). Across the plots this is an average error; in many of the plots there is no difference at all, while in others the difference was closer to 2.5 nm for similar levels of performance. It would be preferred that the differences between methods would be a smaller percentage of the total performance, especially since the RMS disturbance levels between methods were close (see Figure 6-7).

In nearly all of the cases, the difference is the result of modal contributions from modes not aligned with a disturbance tone. Because the state-space shaping filter is continuous in time, all of the dynamics of the system can be captured, while the pure tones only excite

<sup>1</sup>Engineers at JPL suspect that it may be caused by the interaction of optical mount modes with higher order PSS modes. Since the optical mounts are not yet included in the FEM, their modes were stochastically distributed between 100 and 240 Hz [20]. When that distribution was shifted to higher frequencies, the problem disappeared.

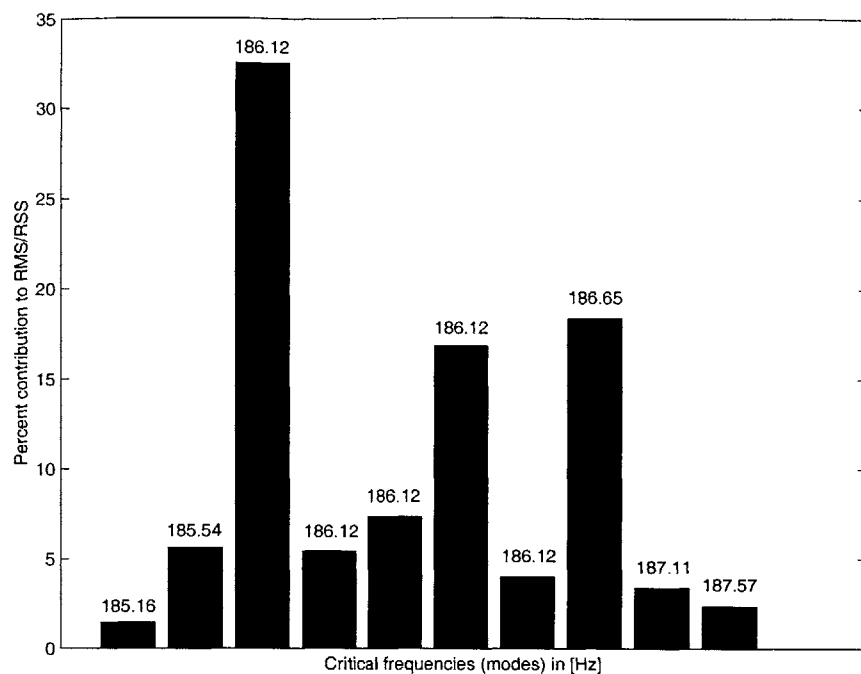


Figure 7-17: Critical frequencies of Star OPD #1 at 66 RPS.

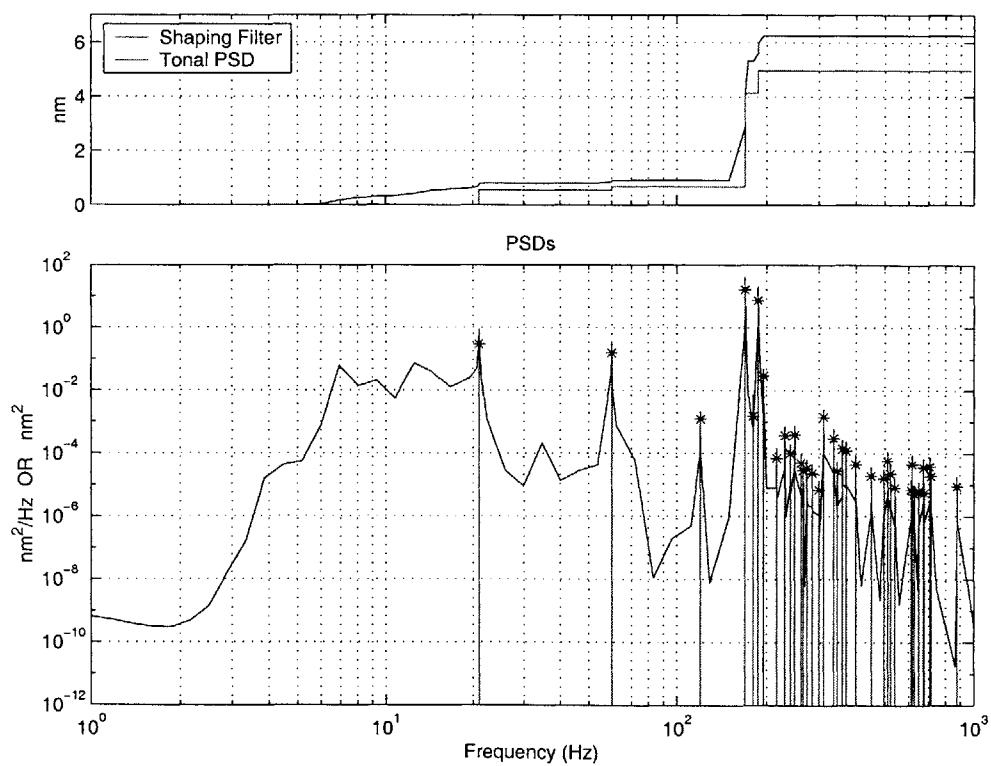


Figure 7-18: Comparison of tonal and shaping filter PSD and RMS results for Star OPD #3 at 60 RPS

the modes at their exact frequency. Although the shaping filter was built to emphasize the frequencies of the tones, a strong mode can still affect the transfer function even after multiplication with the regions of the filter between peaks. This is especially the case for the low-frequency, high magnitude structural modes, and is the reason the high pass filter was added to the disturbance model. Because these additional tones always add more energy, the shaping filter results overbound the pure tonal PSD in nearly all cases, allowing for conservative estimates of performance.

Because there were a small number of cases in which the tonal disturbance RMS overbounds the shaping filter results, the contribution of additional modes is obviously not the only problem. Special attention should also be paid to the frequency vector used with the shaping filter. The peaks of very lightly damped modes can easily be missed if the frequency point spacing is too large. This “capping” of the modes can ignore significant amounts of energy. A usual procedure is to increase the density of the frequency vector around the lightly damped modes. Although this was done for all of the analyses here, it is possible that the  $\Delta f$  must be reduced even further.

It should be recognized that the tonal disturbance model, from which the shaping filter is based, is itself only a model of the actual disturbances, and as such comes with its own limitations. For example, it fails to take into account the structural flexibility of the wheel and its mount. This can add to the disturbance magnitude at those wheel speeds and frequencies where the wheel’s flexible modes overlap the harmonics. Allowing for this uncertainty, the results between the tonal and shaping filter models are considered acceptable for this level of disturbance analysis, in which the ACS and optical control models are themselves only approximations. For a more intensive and realistic disturbance analysis, more effort may be required to eliminate the difference between the two models.

#### 7.4.5 SIM Analysis Summary

Several simplifying assumptions were used to build the SIM integrated model. These include the simplified ACS controller, the optical pseudo-controller, and the use of reaction wheels other than those baselined for the spacecraft. It is nevertheless possible to make several observations on the behavior of SIM, with these assumptions in mind.

Irregularities in the response of Star OPD #2 warrant closer inspection, to determine whether the differences between it and Star OPDs #1 and #3 are physical or are artifacts

of the model. Since each of the siderostat models is supposed to be a copy of the others, it must be the interaction of a siderostat with another part of the spacecraft, either physically or in the model, which is causing this behavior.

The most important finding of the SIM disturbance analysis was the importance of the higher wheel harmonics as they interact with modes around 186 Hz. The amplification of these harmonics pushed the performance beyond requirements even after the optics control loop was closed. Since no physical model was available, the source of those high frequency modes is unknown. When such a model becomes available, the examination of these modes should be a priority. It may be problematic if they do result from the random scattering of mirror mount modes between 100 and 240 Hz, since these are essentially un-modeled elements which drive the performance. A closer examination of the optical bench may be required to determine the actual frequencies of the mirror mounts.

The actual Teldix wheel model is also required to appreciate the effect of reaction wheels on SIM. As was seen with the Ithaco wheels, the dynamics of the harmonics play a critical role in how the structure will respond. Any wheel model that resembles the HST wheels in number and intensity of the higher harmonics may be expected to excite SIM beyond allowable levels.

## 7.5 Summary

The DOCS disturbance analysis was run to compare the behavior of Nexus and NGST, and to examine the newest SIM model. The disturbance method is a useful tool in examining the performance dynamics of a spacecraft, given any one of a number of disturbance types. It identifies the critical modes that are causing performance errors, and determines exactly which disturbance inputs are interacting with these modes. This helps determine exactly which spacecraft component requires either more study or isolation. Together with the sensitivity analysis described in [22], it is an invaluable aid in iterating on the design of an advanced, flexible space structure.

## Chapter 8

# Model Evolution

Several different versions of the SIM Classic model have been examined at MIT. This work, along with References [31, 33], have described the disturbance analyses run on versions 2.0 and 2.2. Gutierrez [22] performed the initial disturbance analysis on the first model, version 1.0. This body of information has been used separately to determine the expected level of performance of each model, and to identify critical frequencies and modes that contribute to performance errors. Examined together, these analyses provide the opportunity to compare the manner and quality in which different models describe one spacecraft. Of interest is whether or not simple first-generation “stick” models accurately capture the key dynamics seen in models of higher fidelity.

The changes between versions 2.0 and 2.2 were relatively minor, and involved mainly the stiffening of several elements; the basic model itself remained the same. The differences between the version 1.0 and version 2.2 models are much greater. Besides modeling slightly different spacecraft designs, the amount of detail in the model is much greater for version 2.2. It is assumed that this translates to a more accurate representation of the spacecraft dynamics. The comparison then will be between the SIM Version 1.0 disturbance analysis, and the version 2.2 analysis contained in the previous chapter of this work. Of interest will be whether the former model captures the dynamics seen in the latter. A brief description of SIM Version 1.0 will also be included.

## 8.1 SIM Classic Version 1.0

The initial SIM model was built at JPL using IMOS. It is a simple stick model with only 212 nodes. The main siderostat boom is modeled using Bernoulli-Euler box beams. Mirrors and optical elements are attached using rigid body elements. An illustration of the finite-element model is shown in Figure 8-1.

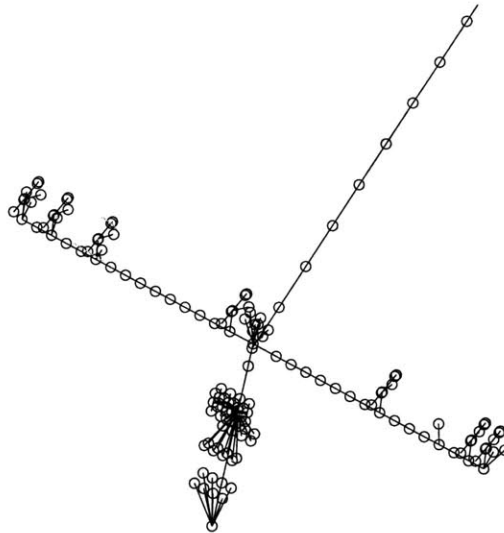


Figure 8-1: SIM Version 1.0 FE model.

By comparing the geometry to that of SIM Version 2.2, shown in Figure 2-12, it is obvious that the stick model is not just a scaled down version with fewer nodes. Although the basic design is the same, with siderostats placed along the Payload Support Structure (PSS) and an external metrology boom used to measure the orientations of the individual baselines, there are significant differences between the two models. Between version 1.0 and version 2.2 the number of siderostats increased by one. The optical switchyard in version 1.0 was located on an optical boom below the PSS. This optics boom also housed the RWA and spacecraft bus systems. In version 2.2, all of this has been replaced by the two spacecraft “backpacks” that are suspended under each spar of the PSS. Although generally similar, the two models are not of the exact same spacecraft, so variations in the dynamics may result from differences in design along with finite-element fidelity.

The integrated model used in the analysis included 0.1% modal damping, a 100 Hz bandwidth optical (fringe tracking) control loop, and reaction wheel disturbance inputs at

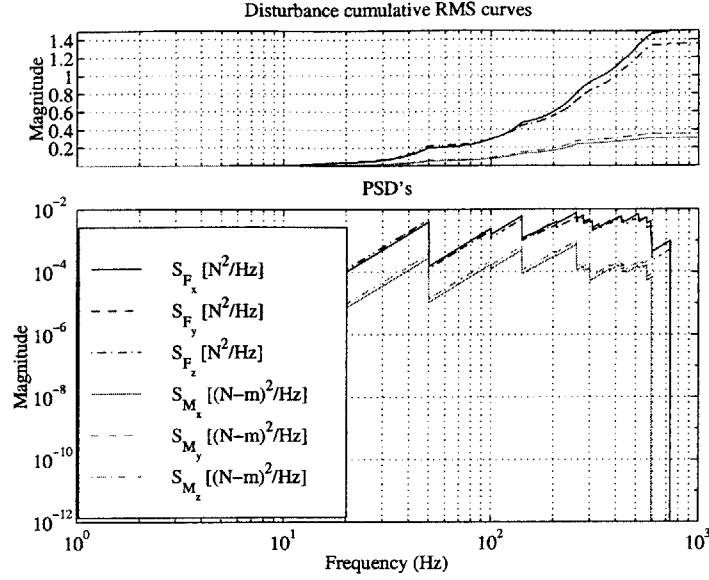


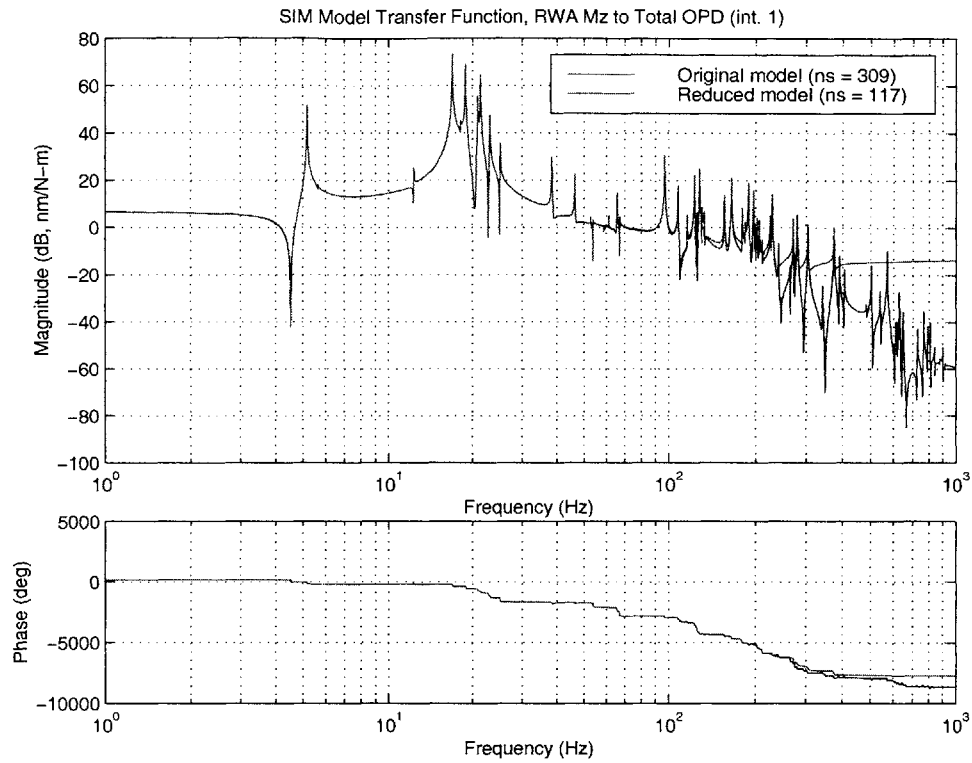
Figure 8-2: Cumulative RMS curves and PSDs for the broadband RWA disturbances

a single node. Four HST wheels are used, compared to three in version 2.2. The wheels are arranged in a pyramid fashion with each wheel's spin axis offset  $63^\circ$  from the spacecraft  $z$ -axis. Broadband wheel speed disturbances are assumed, where the random wheel speed has a uniform probability density between 0 and 3000 RPM. The performance output examined in Total OPD, which is identical to the Star OPD used for version 2.2. They are the sum of the internal and external pathlength differences. The disturbance PSDs are shown in Figure 8-2 and feature the typical broadband "sawtooth" pattern.

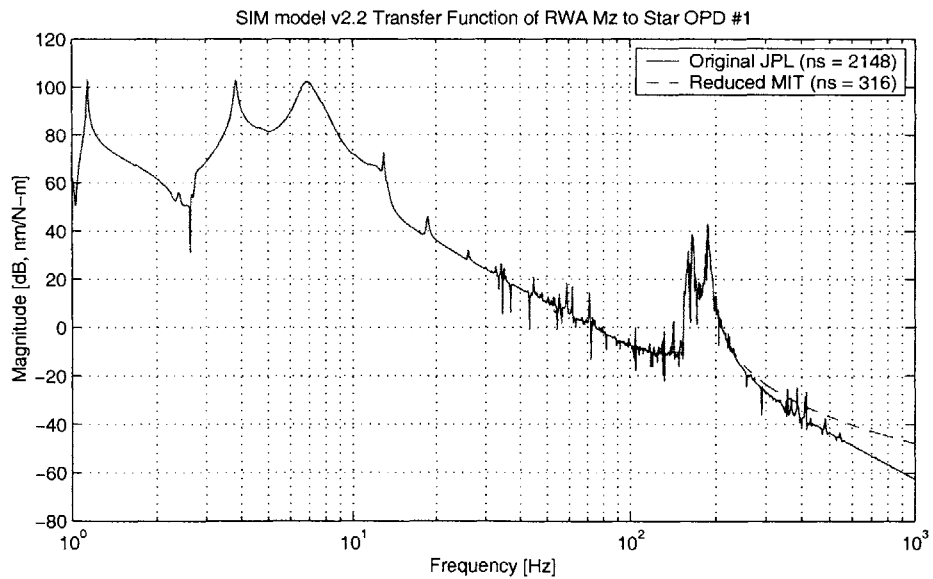
## 8.2 Model Comparison

The original version 1.0 integrated model consists of 309 states, and was reduced to 117 states. The transfer function from RWA Torque  $z$  to Total OPD is provided in Figure 8-3(a). The same transfer function for the newer system is provide in Figure 8-3(b). Although the ACS is open loop for the version 2.2 model, across the frequency range plotted there are no differences between the open and closed loop systems; the low-frequency magnitude does not roll off until 0.04 Hz, which is the bandwidth of the ACS controller.

An observation can be made about the quality of the reduction. Using the basic gramian reduction routines, there was little difficulty in reducing a 309 state model to less than half its original size. The reduced model captures the dynamics accurately through 120 Hz, and



(a) SIM Version 1.0



(b) SIM Version 2.2

Figure 8-3: Sample original and reduced transfer functions for SIM Versions 1.0 and 2.2.



large deviations are not evident until over 200 Hz. The version 2.2 model is reduced such that small deviations from eliminated modes start appearing as early as 50 Hz, but the overall transfer function matches the backbone and captures all retained modes up through 200 Hz. The frequencies that the reduced models are accurate over are similar for both systems, but using the balanced truncation method from Chapter 5, a 2148-state model was reduced to 316 states, less than a *sixth* of its original size, compared to a reduction by half for the version 1.0 model.

There are obvious differences between the dynamics of the two systems. The strongest modes for the older model seem to be between 15 and 25 Hz. After this there are clusters of highly observable modes, particularly between 100 and 200 Hz. But of these, no modes stand out and the transfer function rolls off steadily. The important dynamics all seem to be at lower frequencies.

This contrasts markedly with the newer transfer function<sup>1</sup>. There are still strong low-frequency modes around 4 and 7 Hz, but the modes around 7 Hz are highly damped. This suggests that the 0.1% damping used in version 1.0 was too aggressive for the entire structure. Compared to the relatively uninteresting high-frequency dynamics of version 1.0, one of the most critical aspects of the new model is the frequency region around 187 Hz. This very obvious feature in the transfer function was shown in the previous chapter to be a driver for the closed loop performances. To determine exactly which modes are performance drivers for the older model, consider the results from the disturbance analysis.

The version 1.0 performance PSD given a broadband wheel speed disturbance is shown in Figure 8-4. A cumulative RMS curve is included, along with a chart showing the strength of each disturbance input across frequency; darker lines indicate stronger contributions. Compare this plot to the closed loop PSDs at several critical discrete wheels speeds in Figures 7-14 through 7-16. Unlike each of those worst-case disturbances, the broadband results suggest that the total OPD would nearly meet the 6 nm requirement. This does not necessarily indicate an important difference between the models, however. Excepting the unusual behavior of OPD #2, the version 2.2 broadband results described in [33] are also much closer to the requirements than the discrete cases. The more significant difference is which frequency region contributes to the total RMS error. For the version 2.2 model using both broadband and discrete wheel speed disturbances, the critical frequencies are in

---

<sup>1</sup>Consider also the RWA  $F_x$  to Star OPD #1 transfer function in Figure 5-22

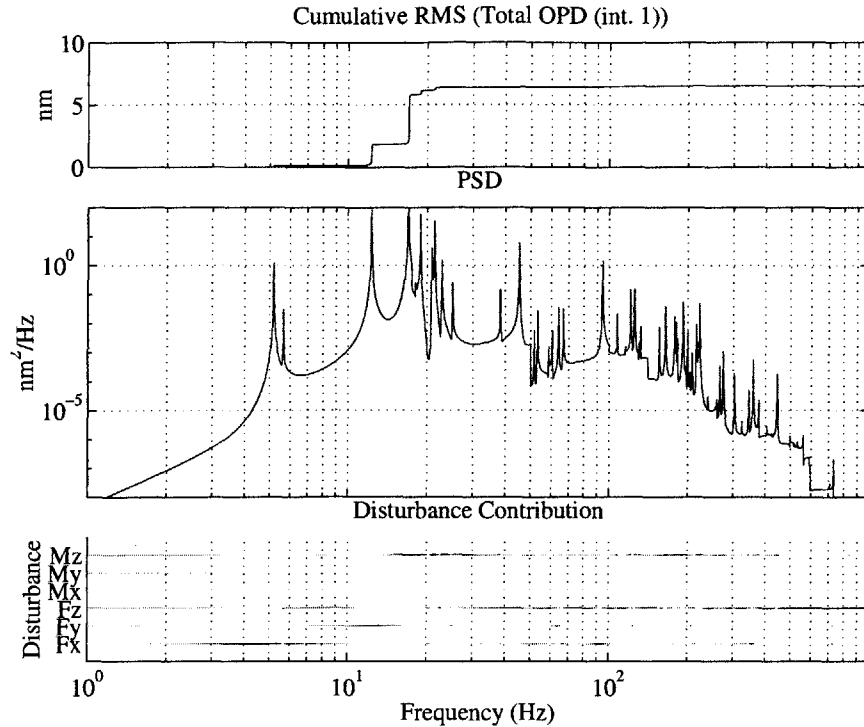


Figure 8-4: SIM Version 1.0 cumulative RMS curve, performance PSD, and disturbance contributions for Total OPD

a narrow region around 187 Hz. As the normalized RMS curve in Figure 8-5 shows, nearly 90% of the error for this model is accumulated before 20 Hz. The critical frequencies are also spread over a larger region.

By selecting the largest steps in the normalized RMS curve, the critical frequencies can be identified. Figure 8-6 indicates the relative contribution of each frequency to the total performance RMS, as well as the relative contribution of each disturbance input. The greatest contribution is from a mode at 16.97 Hz. It was identified as a problem for most of the performances, and is excited the most by the  $M_z$  disturbance component. Similar plots for SIM version 2.2 also identified the  $M_z$  component as causing the most excitation<sup>2</sup>. Since both models use HST wheels, it is possible that this behavior results from the wheel model, and not the spacecraft dynamics.

The OPD critical frequency results for both models are summarized in Table 8.1. As has been observed, the critical frequency regions are quite different. For the older model the important modes are between 12 and 22 Hz, while in the closed loop the new model is

<sup>2</sup>This is the disturbance in the spacecraft axes, which has  $z$  up from the siderostat boom for both models. See Figure 2-12.

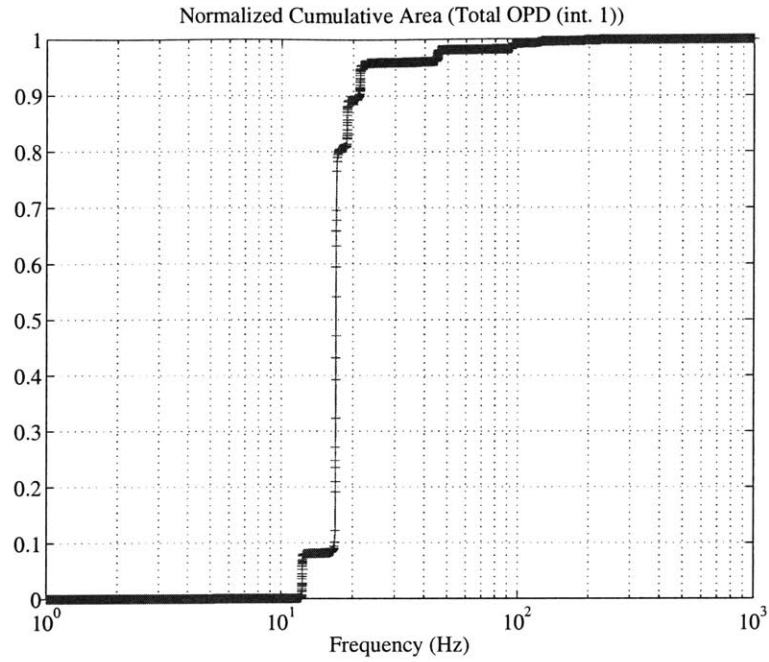


Figure 8-5: Normalized cumulative RMS curve for SIM Version 1.0, Total OPD

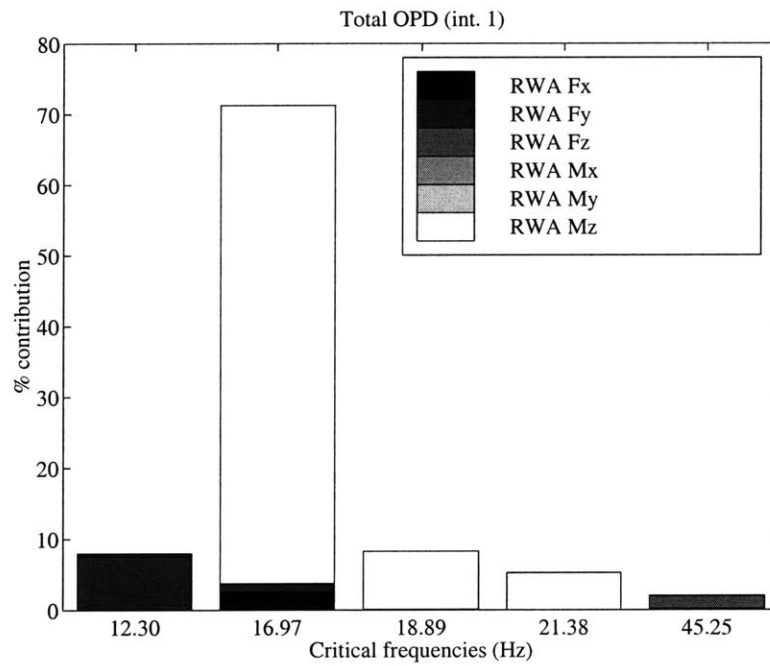


Figure 8-6: Contributions of critical frequencies and disturbance inputs to the Total OPD RMS for SIM Version 1.0.

driven by high frequency modes at and above 163 Hz. The importance of understanding where these higher frequency modes come from and how they can be attenuated is critical for SIM. Their complete absence in the version 1.0 model suggests that the older model is too different to be used in any meaningful fashion.

Table 8.1: SIM closed loop OPD critical frequencies [Hz]

Version 1.0	Version 2.2
12.30	163.56
16.97	165.25
18.89	186.12
21.38	186.48
45.25	187.52

### 8.3 Summary

Comparing the evolving SIM models side-by-side shows that many dynamical features have changed. In particular, the closed loop behavior of the SIM Version 2.2 model is dominated by prominent high-frequency modes not observed in Version 1.0. The control problem that these modes represent was not even a factor with the older model, all of whose critical frequencies were below 50 Hz with a 100 Hz control bandwidth. Although it can be expected that modal frequencies or damping may change as models are updated, this critical feature could not have been guessed at using the original model.

Although this comparison does not reflect positively on the use of stick models for initial dynamics analysis, variables other than the model fidelity could account for the differences. These were not two models of the exact same spacecraft. SIM, while not entirely reconfigured, went through some considerable design changes that included the location of the optical instruments and reactions wheels. The differences in dynamic behavior that were seen are just as likely the result of these changes than of the simplicity of the original model. A examination of models more alike in design is needed for a fairer comparison of fidelity.

## Chapter 9

# Conclusions

### 9.1 Overview

This thesis has examined whether a large order model can be successfully balanced, reduced, and used in the DOCS disturbance analysis. Previous theses have shown the usefulness of the DOCS tools on smaller “stick” models. Those models required little to no additional reduction. Numerical considerations have been consistently used in the work performed using DOCS, but they had not been formalized as part of the framework. The purpose of this work is to specify model preparation tasks required for all large models (and very useful for smaller models), and to implement the balanced truncation reduction routines into the formal DOCS architecture.

Chapter 2 described the three space observatories that were examined in this work. The Next Generation Space Telescope is the named successor to Hubble and will image objects in the universe’s past from an age that hitherto is beyond the reaches of modern observatories. Nexus had been planned as a testbed in space to verify whether the mirrors and optical controls designed for NGST would meet expectations, and to determine if the models being used for a highly flexible space observatory captured the true on-orbit dynamics. Space Interferometry Mission will be the first true space interferometer, and along with delivering highly accurate astrometry measurements, will prepare the way for such innovative missions as the Terrestrial Planet Finder. The models for all of these spacecraft were provided by the respective NASA centers where they are being designed. IMOS and Nastran models were provided for Nexus and NGST, so the size of the state-space models could vary depending on the number of modes that were extracted from the eigenvalue problem. The largest

model examined was SIM, whose 27,000 degrees of freedom had already been reduced to a state-space model with well over 2000 states. All three spacecraft also have associated optics models, that relate the displacements and velocities of nodes representing optical elements to the final performance metrics of wave front tilt, centroid resolution, and wave front error/optical pathlength difference.

Chapter 3 provided background information on some of the key linear algebra routines that are used in balancing and in the disturbance analysis. Basic properties of the eigenproblem, Singular Value Decomposition, and the Lyapunov equation were listed, and their uses outlined. A goal of speeding up the balancing and disturbance routines was achieved by developing a fast Lyapunov solver that utilizes the structure of the system  $A$  matrix to break one large Lyapunov problem into many smaller problems. This saves considerable time and reduces the number of computations by several orders of magnitude.

Chapters 4 and 5 encompass the “Model Reduction and Conditioning” block of the DOCS framework, Figure 1-1. Chapter 4 first prepares a model for the balancing routine, and more generally suggests steps to improve the numerical conditioning of any model. For the initial open loop system, this preparation includes stabilizing or removing and saving the rigid body modes, and removing and saving any additional modes as may help the balancing. Basic steps such as input/output scaling are suggested to prevent needless large or small numbers from being carried through the calculations. The quality of the system and the quality of the balancing and reduction is tracked through the entire process using condition numbers and transfer function comparisons of the altered models with the original.

The gramian balancing transformation is finally described and performed on NGST and SIM in Chapter 5. An overview of journal articles that describe reduction routines is provided, and the basic algorithm for gramian balancing is derived in two different fashions. The failure of this basic method to balance larger models is shown, with the primary reason being the inversion of very small controllability gramian singular values. With the assumption that the states associated with these controllability singular values are too small to be included in a reduced model, even if they are observable, they are truncated out of the system as it is being balanced. The final balanced model is smaller than the original, though further reduction may still be warranted. Those states with the smallest Hankel Singular Values are reduced out of the system. The number of eliminated states can be decided upon based on the final use of the model; fewer states should be eliminated if all

observable modes must be retained, more states can be reduced if only the most critical modes are necessary. Examples of balanced and reduced transfer functions are plotted over their original transfer functions for NGST, SIM Version 2.0, and SIM Version 2.2.

Once the open loop system has been reduced, additional pieces of the integrated model must be assembled. Chapter 6 is dedicated to reviewing and preparing reaction wheel disturbance models. Because the speed of the wheels affects the strength and dynamics of the disturbance, there are two ways of studying the effect of multiple wheel speeds. One is to treat the wheel speed as a random variable, and determine the resulting stochastic disturbance input. The alternative is to use the pure tonal disturbance of a wheel at each discrete speed, and then to run many disturbance analyses through the entire speed range. Both approaches have been taken here; the broadband model was used on Nexus and NGST, and discrete tonal models were used for Nexus, NGST, and SIM. This thesis also developed a state-space shaping filter to match the pure PSD tones of the discrete case, thus allowing the Lyapunov disturbance analysis to be run at discrete wheel speeds. This was used for SIM Version 2.2. The results closely matched those from the original PSD tones, though further refinement may be necessary to produce identical performance responses.

The complete integrated model was assembled in Chapter 7 with the addition of simple ACS controllers and, for SIM, a high pass filter “pseudo-controller” for the Star OPD and WFT optics. No optical control loops were closed for Nexus or NGST. Three types of disturbance analyses were described depending on the type of disturbance input: time histories, frequency-based PSD vectors, or state-space white noise shaping filters. Only the latter two were used. The primary goal of the Nexus/NGST analysis was to compare the dynamics of the two spacecraft. Because an older design for Nexus was used, there were noticeable differences between the two spacecraft. That version of Nexus was much stiffer than NGST, whose lowest structural frequency is around 0.3 Hz due to its flexible sunshield. Further, all of the critical frequencies that drive NGST’s performance are lower than for Nexus. This means that the physical alterations or control bandwidth required to improve the performance would be different for each spacecraft. Since one of the key goals of Nexus was to verify NGST’s optical control methods, these differences would seriously affect its usefulness as a validation testbed.

The disturbance analysis on SIM focused on specific wheel speeds and frequency ranges that excited the OPD performances beyond requirements. The closed loop analysis indi-

cated that at wheel speeds above 30 RPS, the optical controllers no longer have any authority. Plots showing the RMS performance against wheel speed indicate several regions of particular concern. Since the Lyapunov approach used to generate these plots only outputs a final RMS value, continuous time PSDs were generated from the shaping filters and used to examine the frequency content at these critical speeds. It was found that high frequency wheel dynamics were interacting with particularly strong structural modes around 187 Hz. Since the optical controller has a bandwidth of 100 Hz, these disturbances were beyond its reach. One caveat is that the wheel model used was based on the Hubble flight wheels, not the Teldix wheels that are currently baselined for SIM. The higher harmonics of the HST wheels are stronger than even the fundamental, so they dominate the disturbance. Since these were the harmonics interacting with the 187 Hz modes, another wheel whose dynamics are different from the HST wheels will likely produce different responses. One additional observation from the SIM model was that the responses from OPD #2 were much greater than for the other interferometers. Since a physical representation of the telescope was not available, a reason for this behavior remains unknown.

Chapter 8 used the results from this SIM disturbance analysis and compared them with similar results from the analysis performed on version 1.0. The purpose was to determine if that original stick model captured the dynamics of the current high fidelity model. A side-by-side comparison of the critical frequencies showed that the dynamics of the models were very different. The version 1.0 model did not contain any of the 187 Hz high frequency modes that dominate the closed loop response for version 2.2; all of the older model's critical frequencies were below 50 Hz and within the bandwidth of optical control. This does not necessarily suggest that stick models are not useful, since the design of the spacecraft had changed between models. Although the basic architecture remained the same, the locations of optical elements and reaction wheels moved. The changes in design likely contributed to the differences in dynamics. A comparison between different models of the exact same spacecraft design is needed to make a more definitive statement on the effect of model evolution.



## 9.2 Recommendations for Future Work

There are three areas of research that should be continued beyond this thesis. The DOCS “Model Conditioning and Reduction” block requires further work to prepare the codes for rigorous use. The Nexus/NGST analyses are continuing and allow investigations using the original mass and stiffness matrices, and the SIM analysis requires several updated models to be complete.

In regards to the conditioning, balancing, and reduction, possible steps include:

- Beyond scaling the inputs and outputs separately, determine whether they could be scaled together for numerical improvement. Besides the transformation of the state vector, are there transformation matrices for the input and output vectors  $\tilde{u} = T_u u$  and  $\tilde{y} = T_y y$  that could yield substantial improvements in numerical conditioning?
- The time computational burden required to balance a model are still large when the number of states grows beyond 1000. Much of the time is taken up as the routines compute the eigenvalues and the singular values. The MATLAB `eig.m` function is much slower than other solvers available. Faster solvers should be searched for and used instead.
- Other computational burdens include the multiplication of large matrices and the RAM required to hold very large matrices in the workspace. The code should be optimized for large systems to prevent difficulties in memory. The routines are currently coded as MATLAB functions. The efficiency of compiling them using the C programming language should be investigated.
- Compare the gramian balancing method with the Component or Modal Cost Analysis (CCA or MCA) methods described by Skelton [23, 45, 46, 44]. Consider the quality of the reduction results for each technique and the computational time and resources that are needed to implement each technique for large order systems.
- Determine why systems reduced using static condensation failed to roll off at high frequency, even after the feedthrough  $D$  term was removed.

- Since the controllability and observability of individual modes will change as optical control loops are implemented, the final reduction should only be performed on the closed loop system. When reducing the open loop system, it is possible that important closed loop modes would be reduced out. A proper approach would be to balance and reduce the model in stages; first reduce the open loop system to a point where the numerical conditioning has improved, add the controllers, and then reduce the model to the desired level.

Future work for the Nexus/NGST spacecraft should include:

- Use the reduced Nexus FEM in a physical parameter sensitivity study.
- Run a disturbance analysis on both the reduced Nexus FEM and the original model to investigate the effects of model evolution, and to determine whether a low-fidelity “stick” model accurately captures the key dynamics from a higher fidelity model. Since the spacecraft remains identical, the only variable will be the size of the model.

Future work following the SIM disturbance analysis should include:

- Improve upon the discrete wheel speed state-space model to eliminate errors between the final RMS performances computed using the shaping filter, and those computed by the direct PSD tones.
- Run the discrete PSD analysis at every wheel speed and build a waterfall plot of the results. The topology is based on the RWA disturbance plots, so the differences between the disturbance and performance waterfall plots indicates reaction wheel/structure interaction. Use this to identify trends in the performances not apparent in the individual performance PSD plots.
- Use the Teldix wheel model. The performances were driven by the dynamics of the HST wheels; as the comparison with the Ithaco E- and B-wheels showed, the dynamics of the wheel are of critical importance to the final response. In order to predict the actual response of the baseline design, it is important that the true wheel model be used.

- Examine the physical modeshapes. The behavior of OPD #2 and the strong modes around 187 Hz were both noticed, but without the physical modeshapes it is impossible to determine what component on the spacecraft is causing the behavior. A physical parameter sensitivity analysis should be attempted in order to recommend design changes that may improve performance.

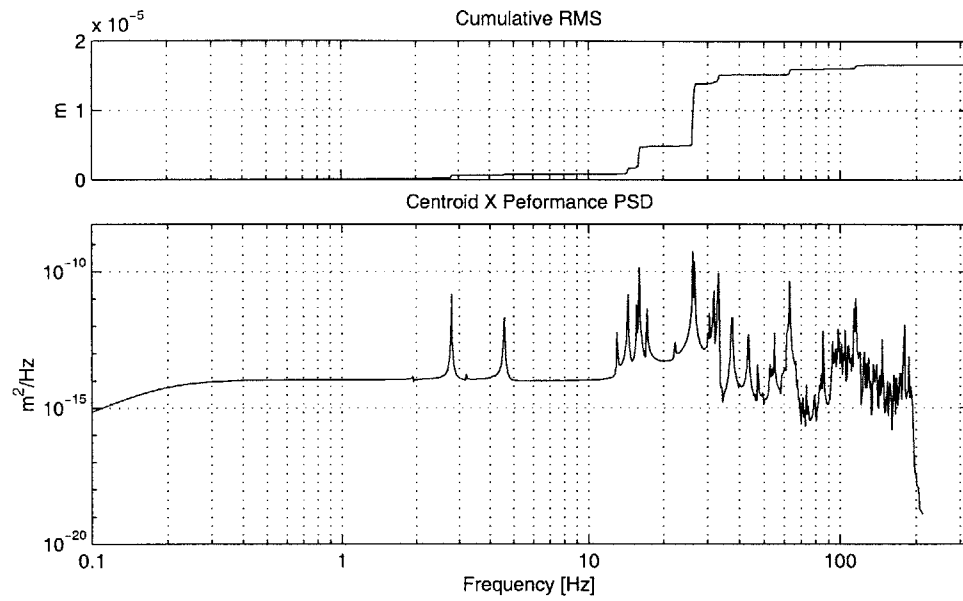


## Appendix A

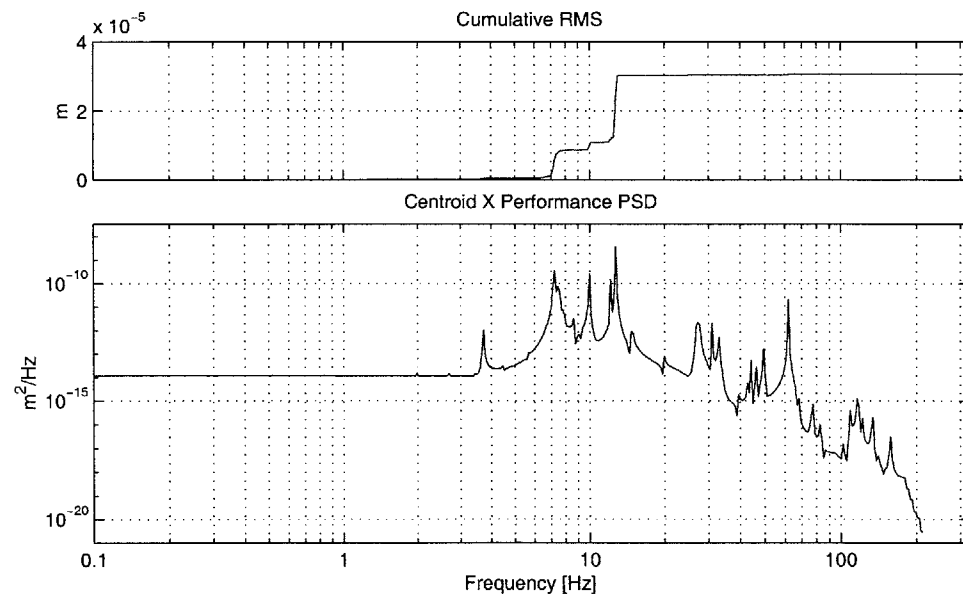
### Nexus/NGST Disturbance

### Analysis Results Comparison

Plots of the Nexus and NGST analyses for centroid X and centroid Y performances are included one on top of the other to allow a comparison of the two spacecraft. See Chapter 7 for the Wave Front Error (WFE) plots.

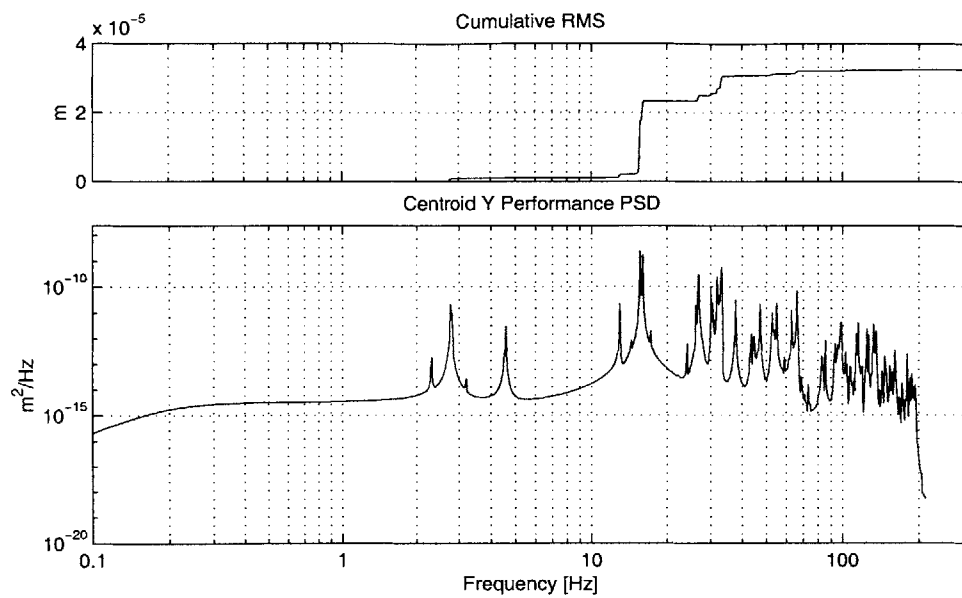


(a) Nexus/Horizon

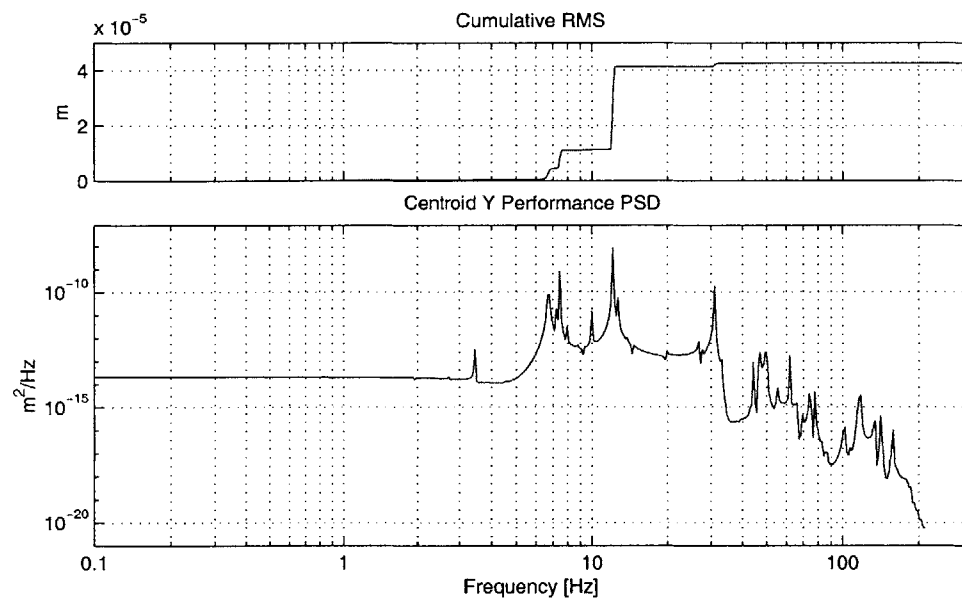


(b) NGST

Figure A-1: Centroid X performance PSD given a broadband wheel speed disturbance.

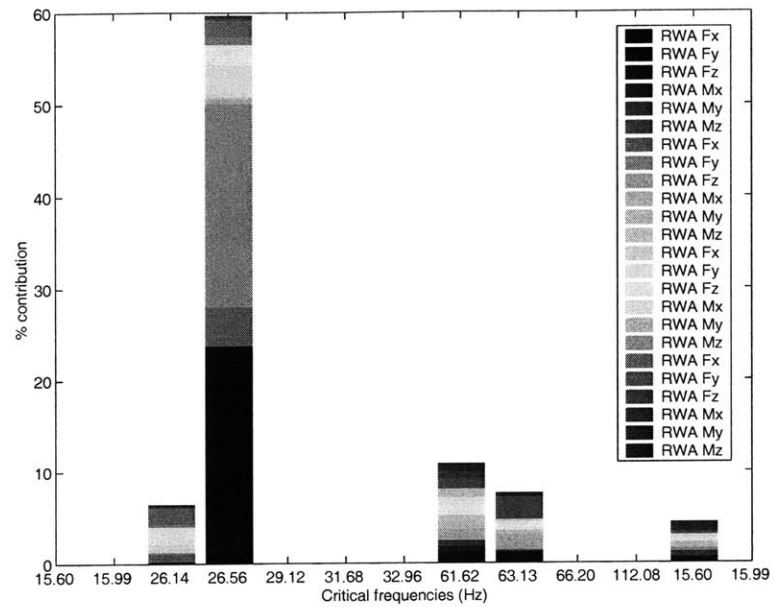


(a) Nexus/Horizon

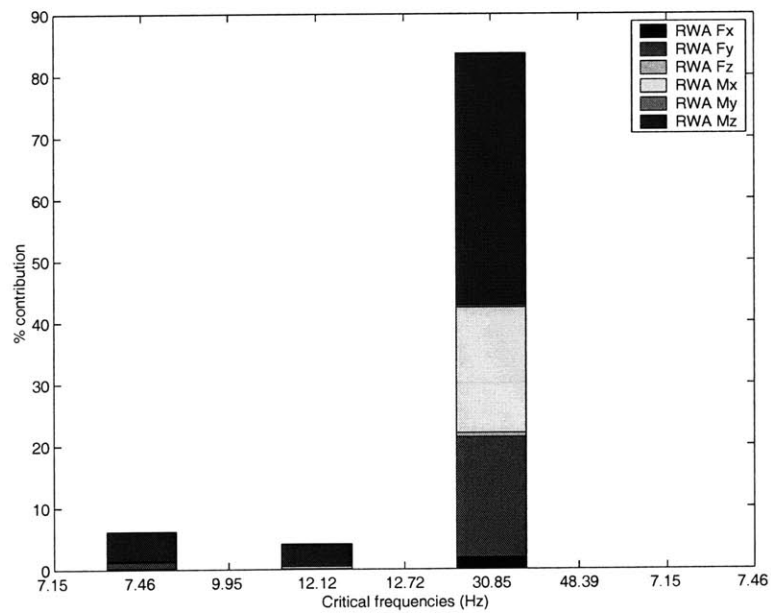


(b) NGST

Figure A-2: Centroid Y performance PSD given a broadband wheel speed disturbance.



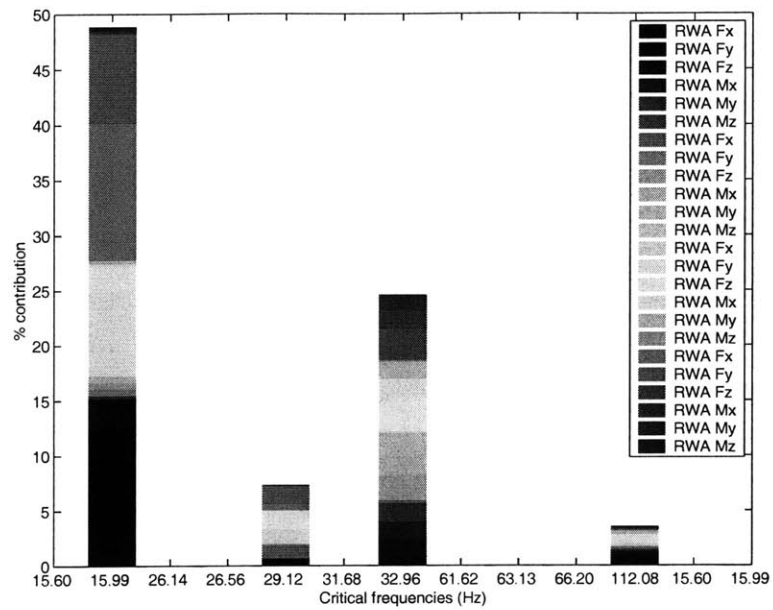
(a) Nexus/Horizon



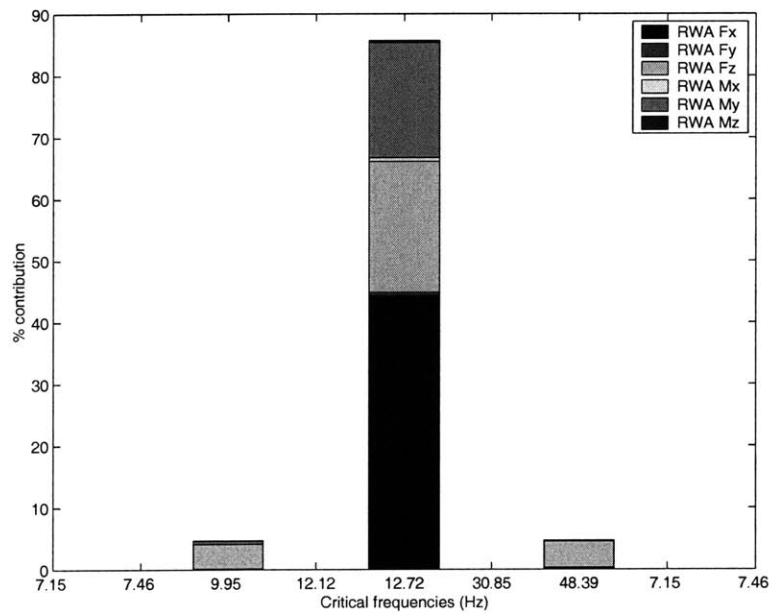
(b) NGST

Figure A-3: Disturbance contribution at the critical frequencies for Centroid X.



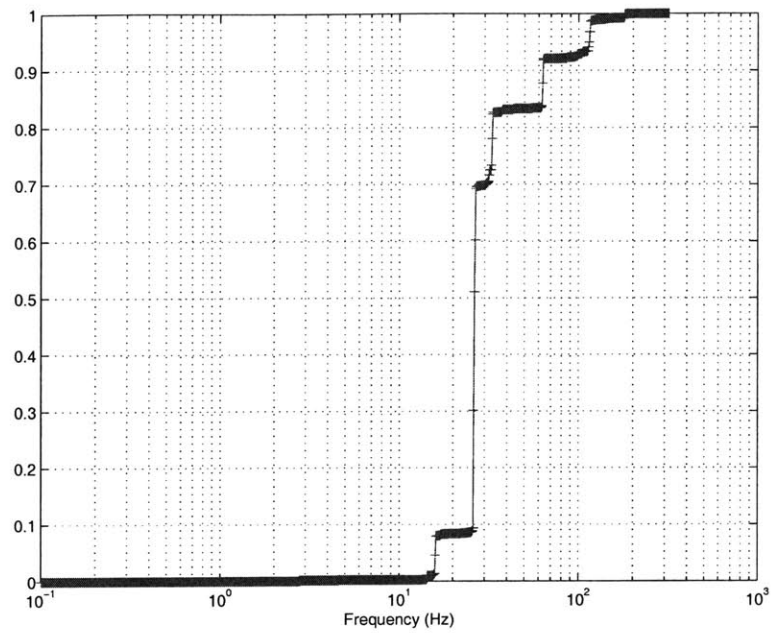


(a) Nexus/Horizon

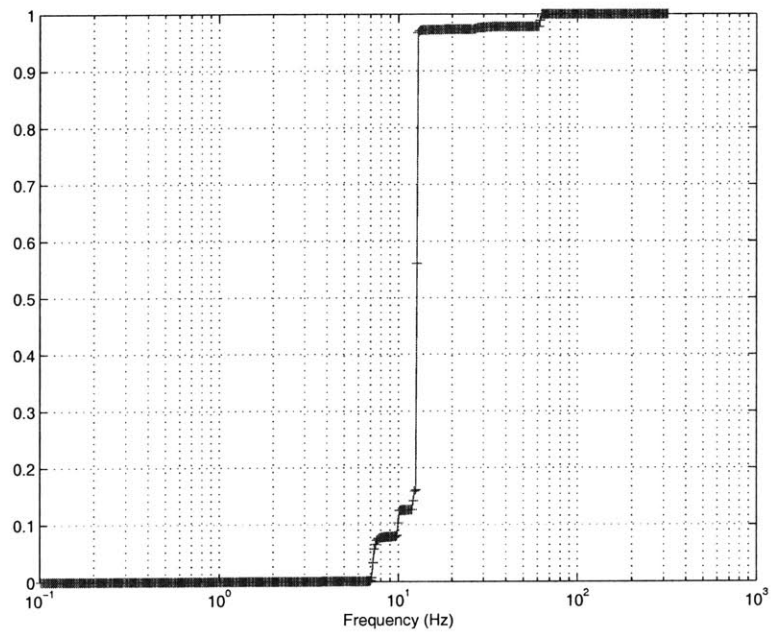


(b) NGST

Figure A-4: Disturbance contribution at the critical frequencies for Centroid Y.

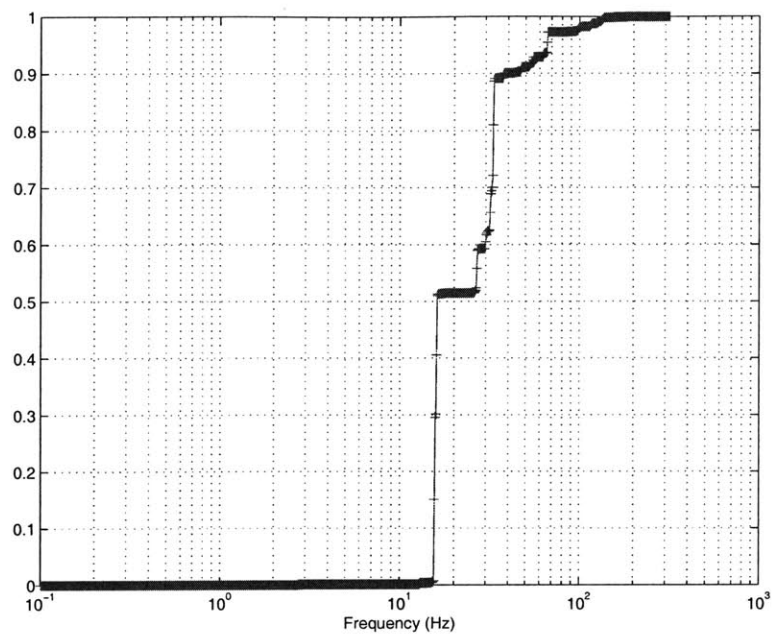


(a) Nexus/Horizon

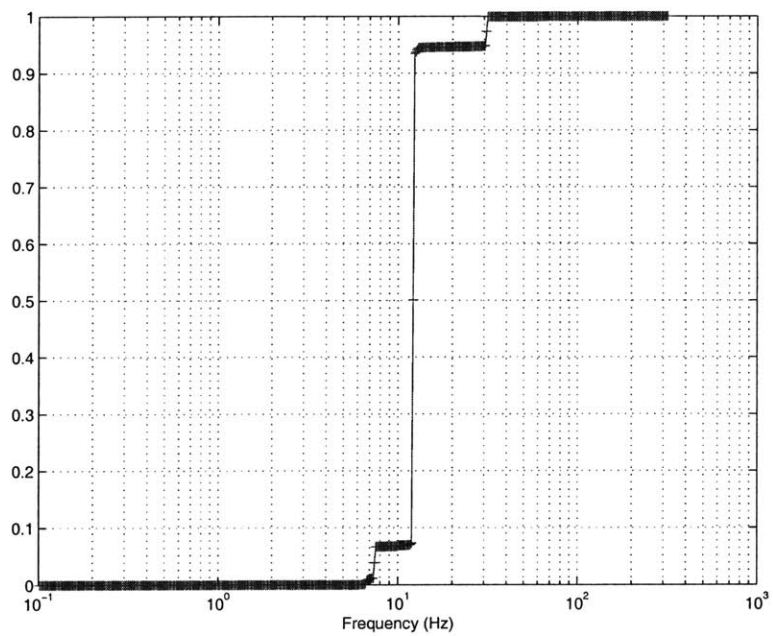


(b) NGST

Figure A-5: Normalized cumulative RMS performance curve for Centroid X

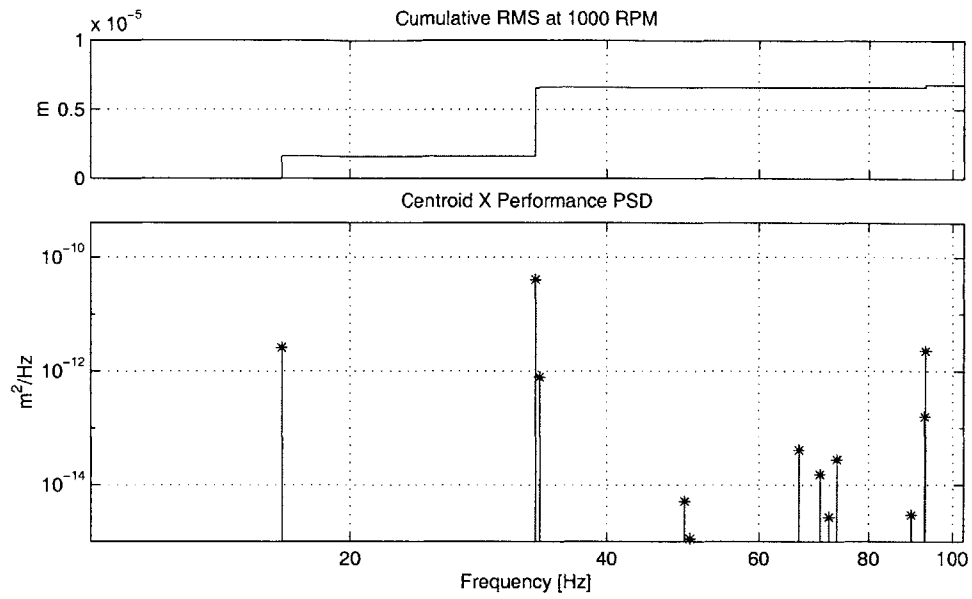


(a) Nexus/Horizon

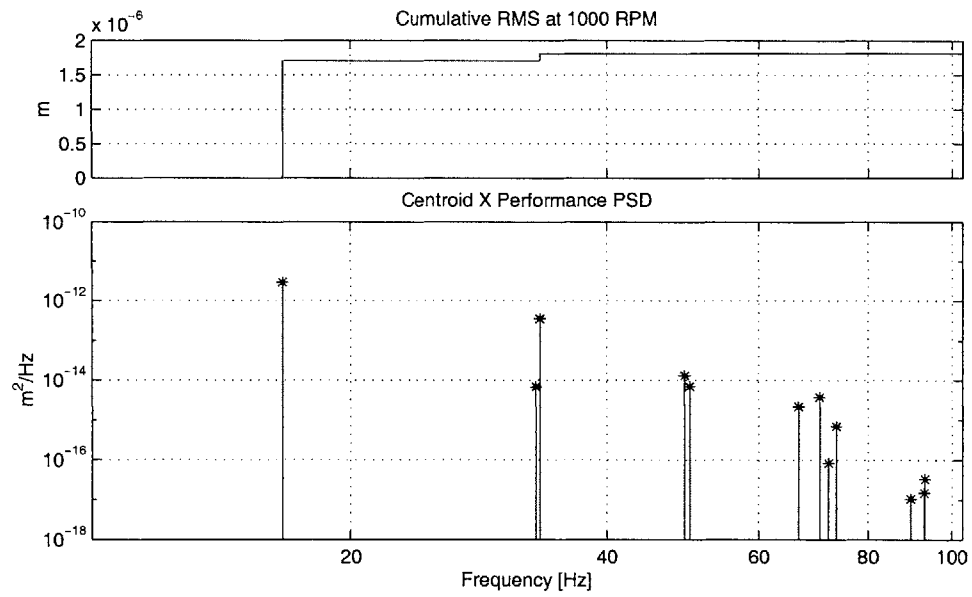


(b) NGST

Figure A-6: Normalized cumulative RMS performance curve for Centroid Y

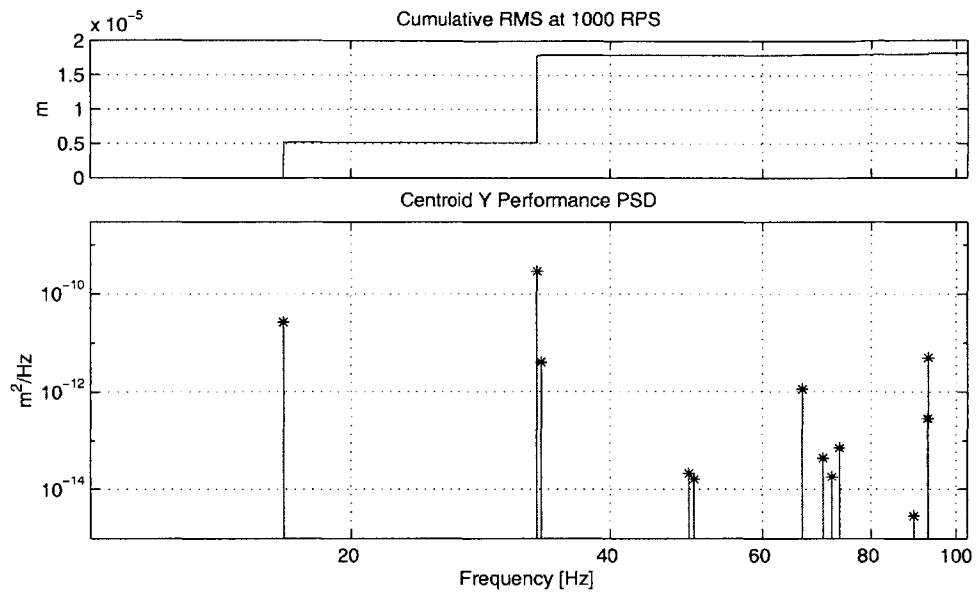


(a) Nexus/Horizon

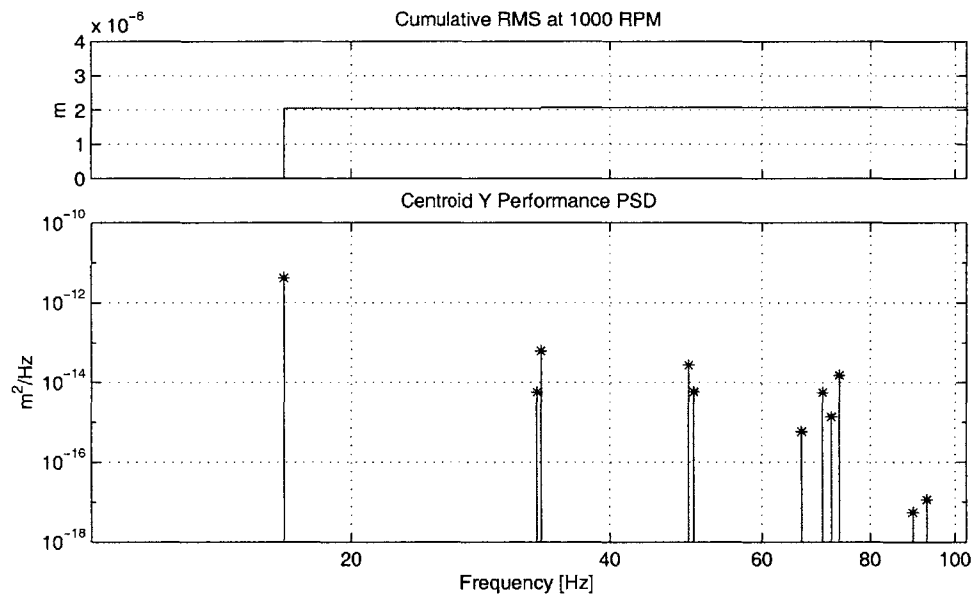


(b) NGST

Figure A-7: Centroid X performance PSD given a discrete wheel speed disturbance at 1000 RPM.

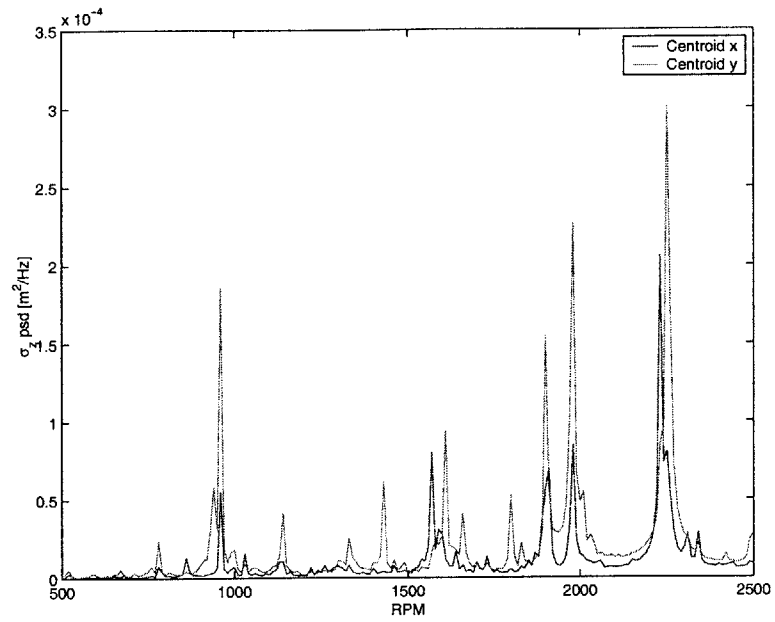


(a) Nexus/Horizon

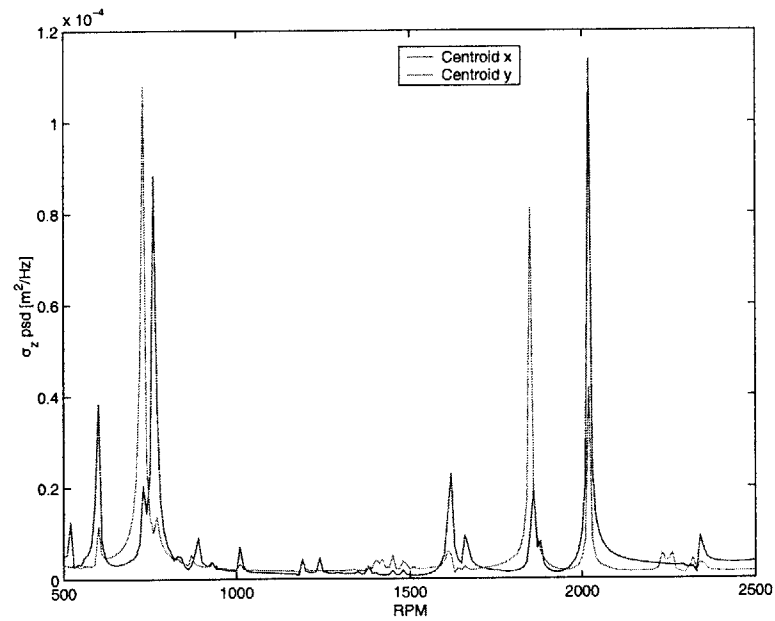


(b) NGST

Figure A-8: Centroid Y performance PSD given a discrete wheel speed disturbance at 1000 RPM.



(a) Nexus/Horizon



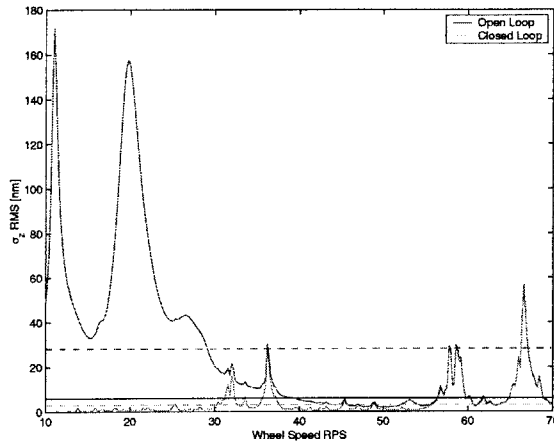
(b) NGST

Figure A-9: Centroid X and Y performance RMS versus Reaction Wheel Speed.

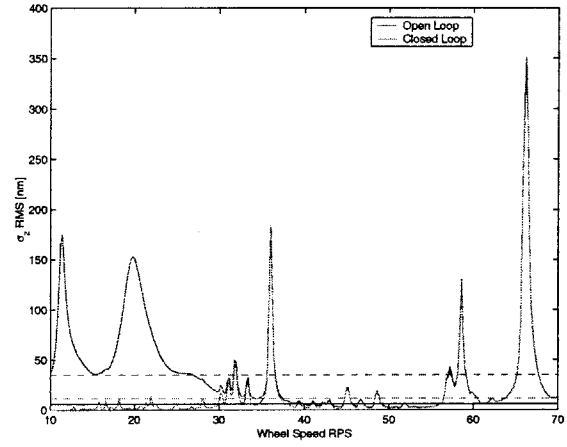
## Appendix B

# SIM Lyapunov Disturbance Analysis Results

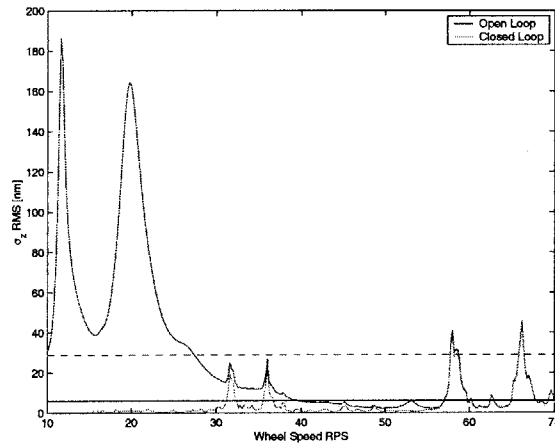
## Star OPD



(a) Star OPD #1



(b) Star OPD #2

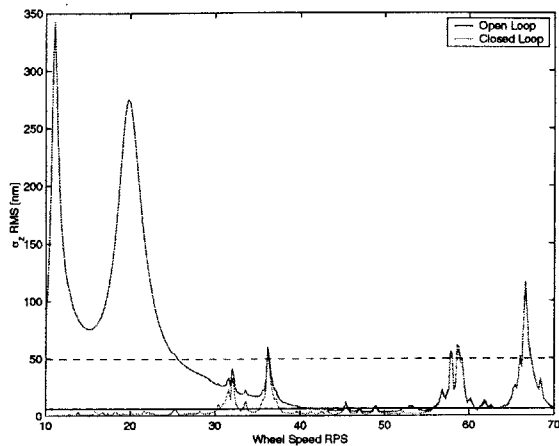


(c) Star OPD #3

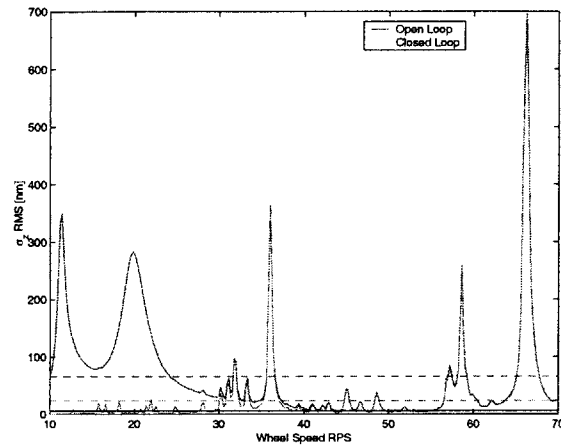
Figure B-1: Star OPD open and closed loop performances. Average values given as dashed horizontal lines, requirements as a solid horizontal line.



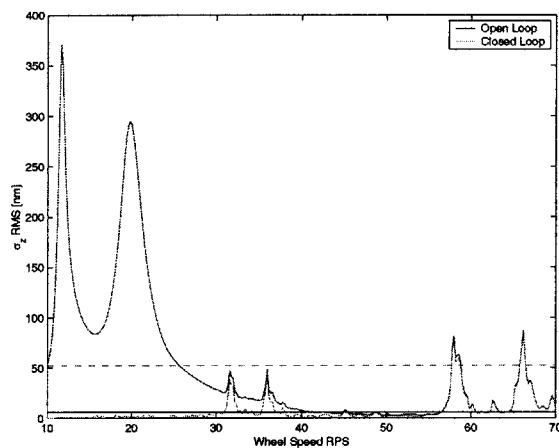
## Internal Metrology OPD



(a) Internal Metrology OPD #1



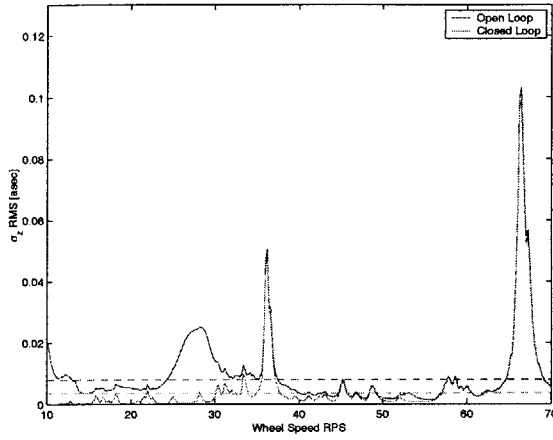
(b) Internal Metrology OPD #2



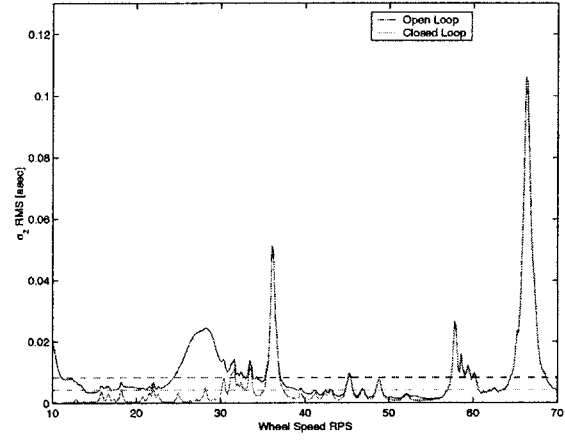
(c) Internal Metrology OPD #3

Figure B-2: Internal Metrology OPD open and closed loop performances. Average values given as dashed horizontal lines, requirements as a solid horizontal line.

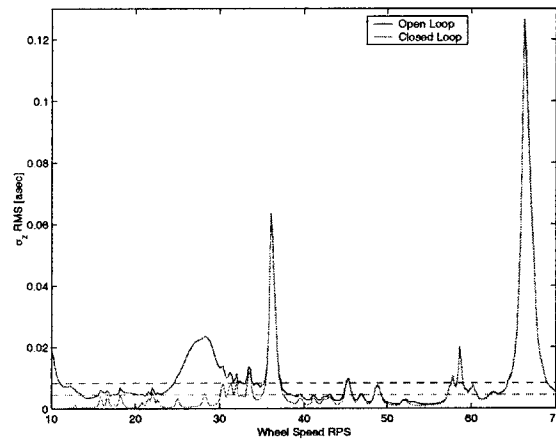
## Wave Front Tilt



(a) Star Wave Front Tilt #1



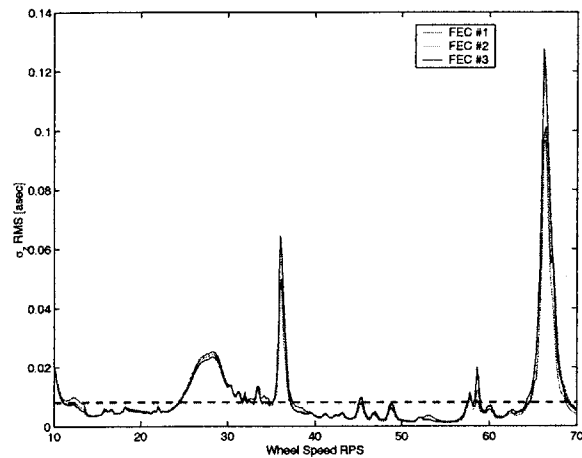
(b) Star Wave Front Tilt #2



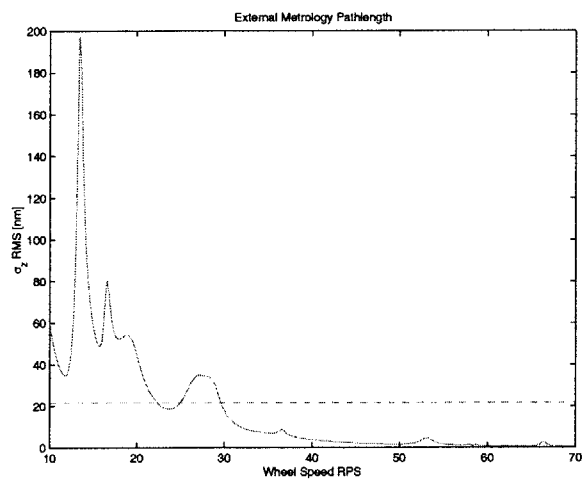
(c) Star Wave Front Tilt #3

Figure B-3: Star WFT open and closed loop performances. Average values given as dashed horizontal lines, requirements are 0.21 asec.

## Front End Camera and External Metrology OPD



(a) Front End Camera Tilt #1  $\rightarrow$  #3



(b) External Metrology Pathlength

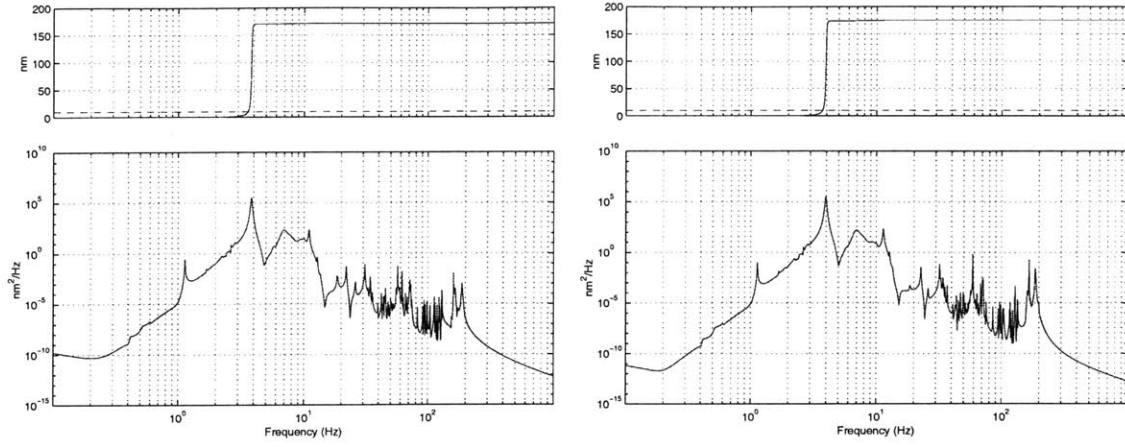
Figure B-4: FEC and External Metrology open loop performances. Average values given as dashed horizontal lines.



## **Appendix C**

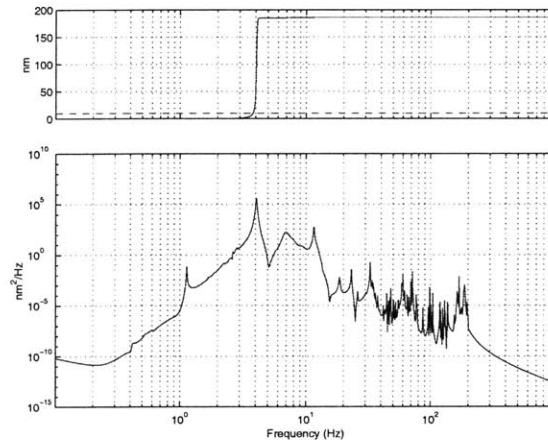
# **SIM PSD Disturbance Analysis Results**

## 11 RPS: Open Loop



(a) Star OPD #1 at 11.0 RPS

(b) Star Opd #2 at 11.4 RPS



(c) Star OPD #3 at 11.6 RPS

Figure C-1: PSD and cumulative RMS plots of Star OPD around 11 RPS

## 19.8 RPS: Open Loop

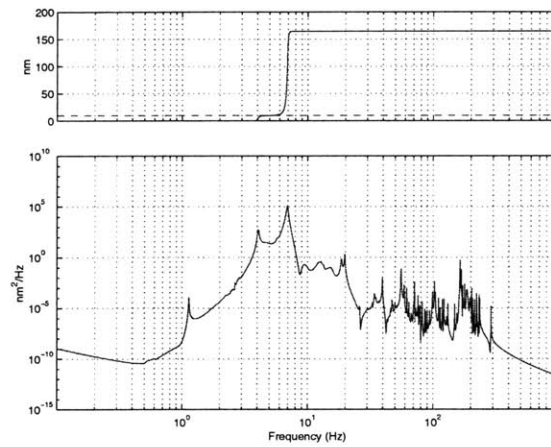
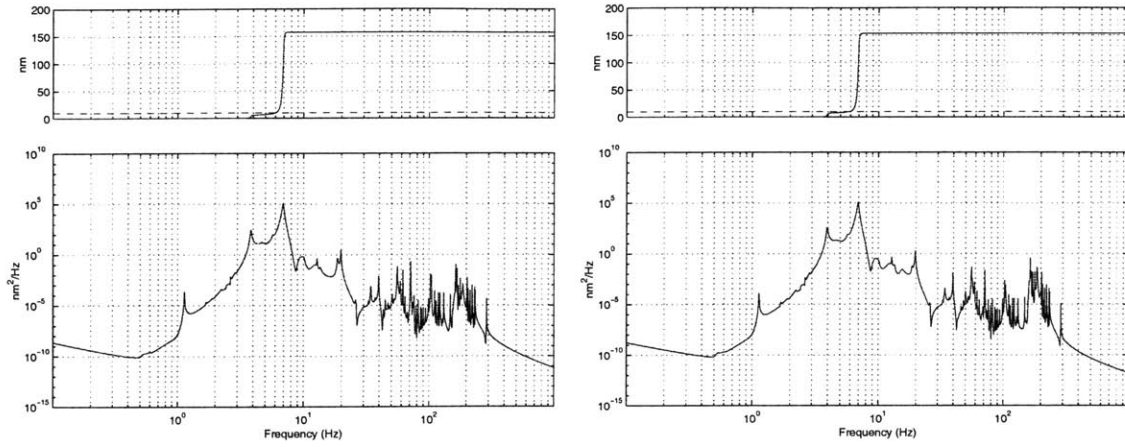
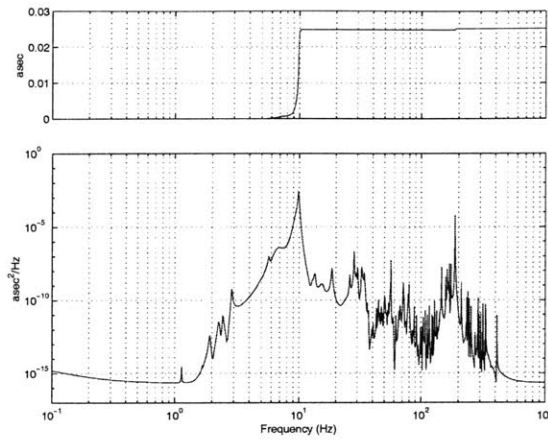
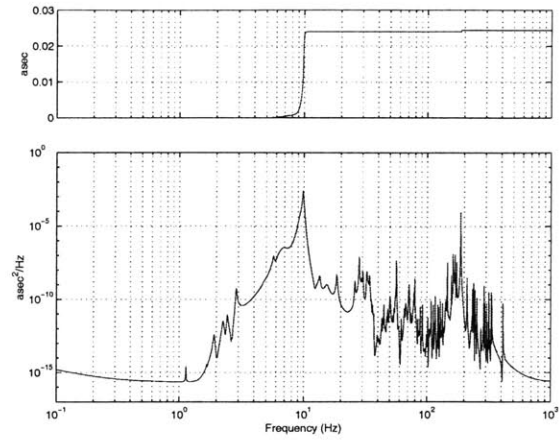


Figure C-2: PSD and cumulative RMS plots of Star OPD at 19.8 RPS

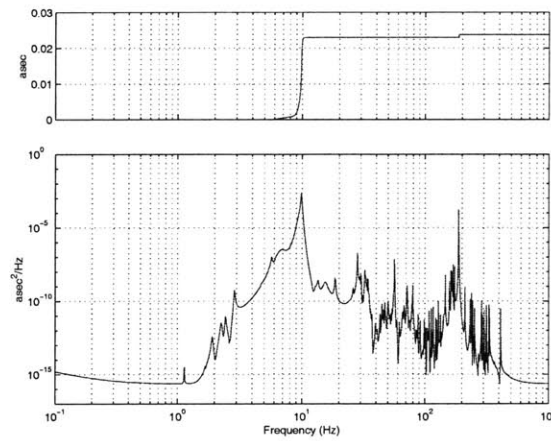
## 28.2 RPS: Open Loop



(a) Star X WFT #1



(b) Star X WFT #2



(c) Star X WFT #3

Figure C-3: PSD and cumulative RMS plots of Star WFT at 28.2 RPS



## 36 RPS: Closed Loop

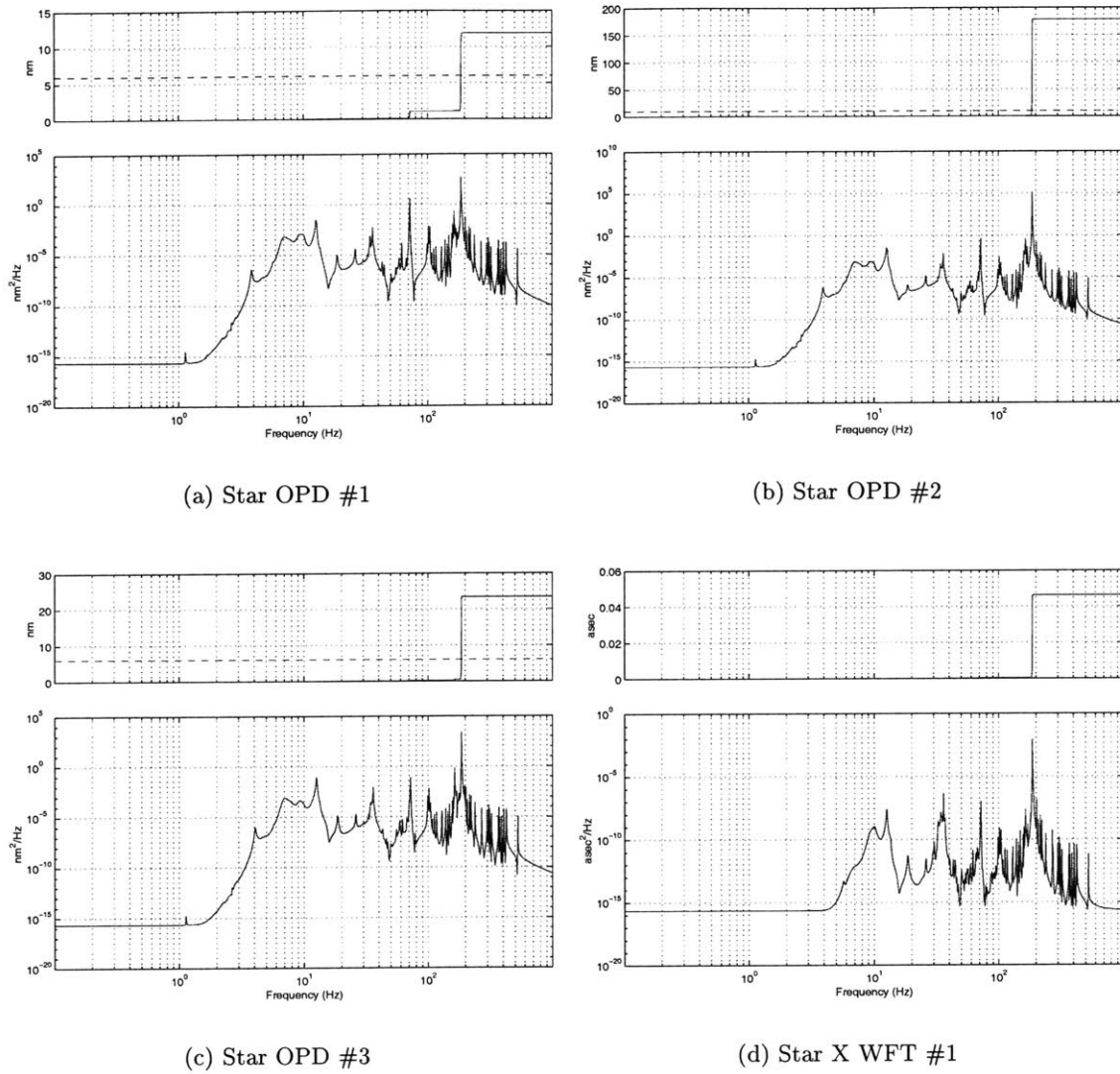
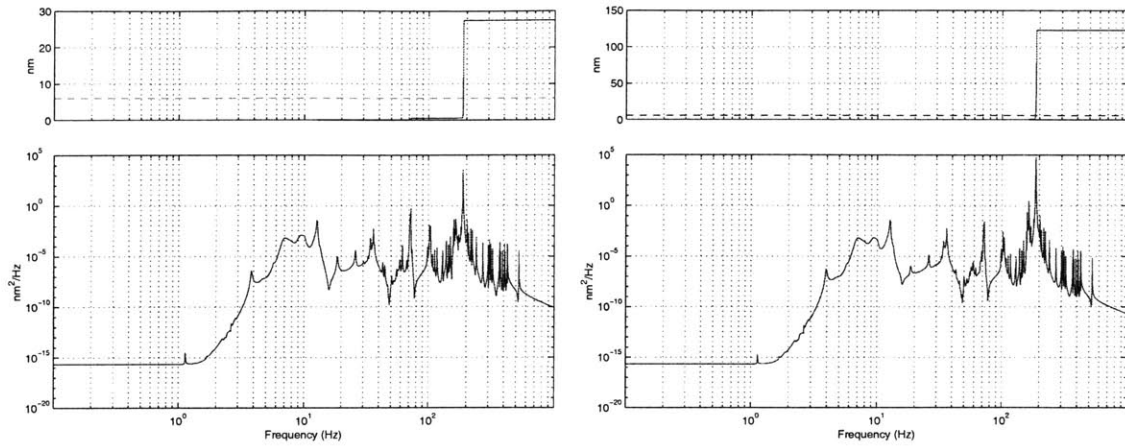


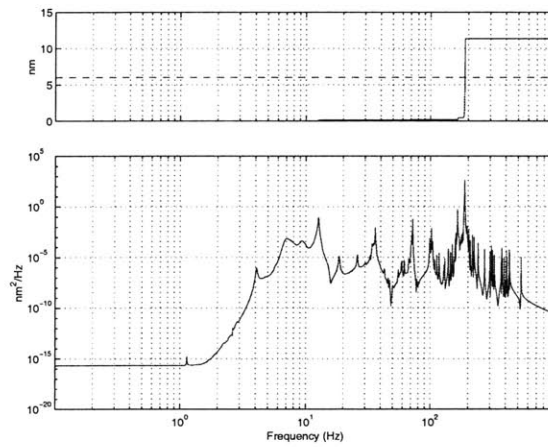
Figure C-4: PSD and cumulative RMS plots of Star OPD and WFT at 36.0 RPS

## 36.2 RPS: Closed Loop



(a) Star OPD #1

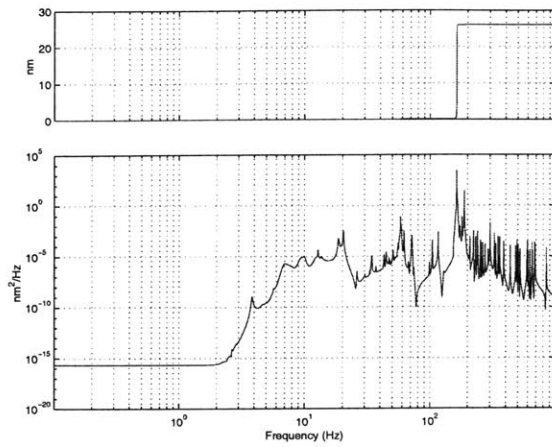
(b) Star OPD #2



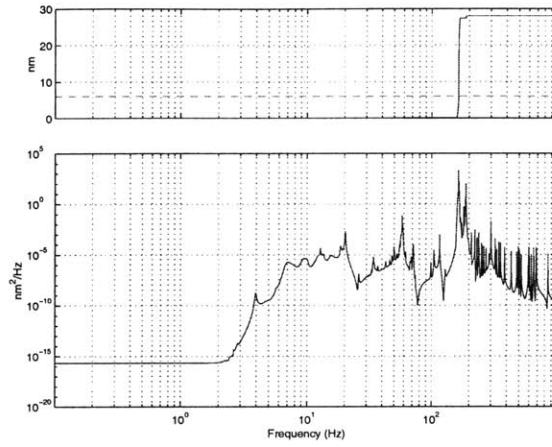
(c) Star OPD #3

Figure C-5: PSD and cumulative RMS plots of Star OPD at 36.2 RPS

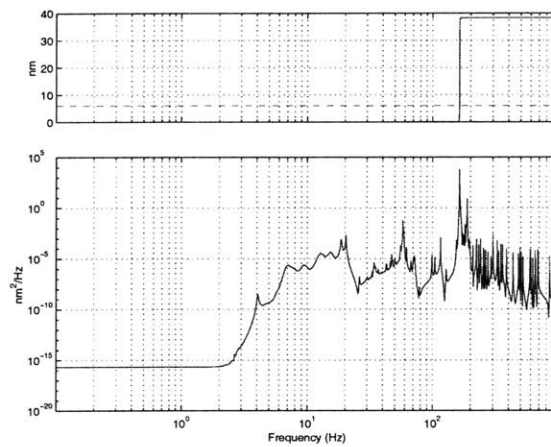
## 58 RPS: Closed Loop



(a) Star OPD #1



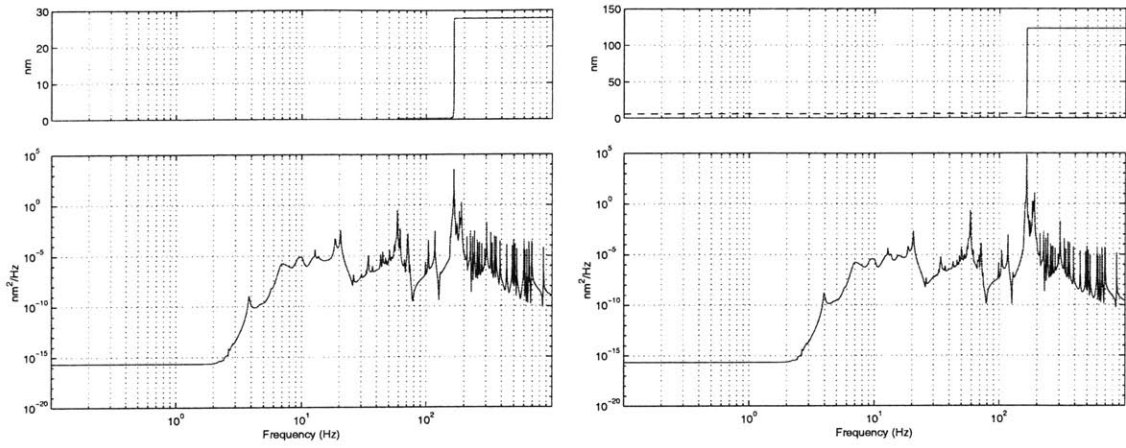
(b) Star OPD #2



(c) Star OPD #3

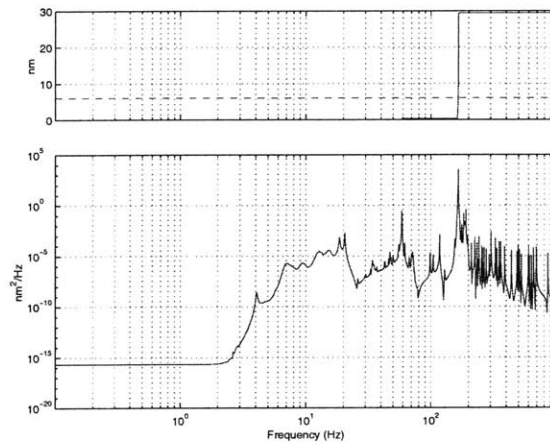
Figure C-6: PSD and cumulative RMS plots of Star OPD at 58.0 RPS

## 58.6 RPS: Closed Loop



(a) Star OPD #1

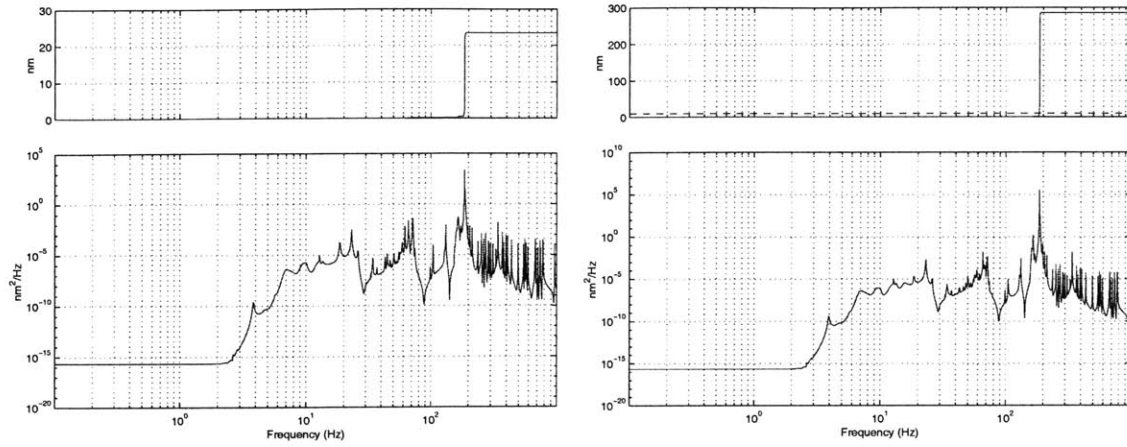
(b) Star OPD #2



(c) Star OPD #3

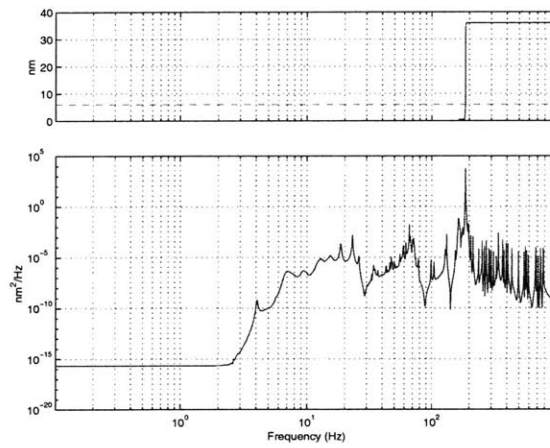
Figure C-7: PSD and cumulative RMS plots of Star OPD at 58.6 RPS

## 66 RPS: Closed Loop



(a) Star OPD #1

(b) Star OPD #2



(c) Star OPD #3

Figure C-8: PSD and cumulative RMS plots of Star OPD at 66.0 RPS



# Bibliography

- [1] Hubble Space Telescope home page. URL: <http://ngst.gsfc.nasa.gov>.
- [2] Ithaco Space Systems. URL: <http://www.ithaco.com/T-Wheel.html>.
- [3] Ball Aerospace and Technologies Corporation  
URL: <http://www.ball.com/aerospace/ptlos.html>.
- [4] NASA Origins home page. URL: <http://origins.jpl.nasa.gov>.
- [5] NGST home page. URL: <http://www.stsci.edu/hst>.
- [6] SIM home page. URL: <http://sim.jpl.nasa.gov>.
- [7] Kim M. Aaron. SIM configuration evolution. In *IEEE Aerospace Conference Proceedings*, volume 3, pages 463–469, March 6-13.
- [8] Mark S. Barlow and Edward F. Crawley. The dynamics of deployable truss structures in zero-gravity: The MODE STA results. Technical Report SERC #1-92, Massachusetts Institute of Technology, Space Engineering Research Center, Cambridge, Massachusetts, January 1992.
- [9] R.H. Bartels and G.W. Stewart. Solution of the matrix equation  $AX+XB=C$ . *Communications of the Association for Computing Machinery*, 15(9):820–826, 1972.
- [10] Breault Research Organization, Tucson, Arizona. *Modeling and Analysis for Controlled Optical Systems User Manual*, v2.4 edition, April 1997.
- [11] Richard Burg. The Nexus flight experiment. Viewgraphs for Nexus Kickoff, June 6, 2000.

- [12] Roy R. Craig Jr. *Structural Dynamics: An Introduction to Computer Methods*. John Wiley & Sons, New York, 1981.
- [13] Olivier de Weck. Singular value decomposition for NGST optics. Memorandum MIT-SSL-NGST-98-3, Massachusetts Institute of Technology, Space Systems Laboratory, December 18, 1998.
- [14] Olivier L. de Weck and David W. Miller. Integrated modeling and dynamics simulation for the Next Generation Space Telescope. Master's thesis, Massachusetts Institute of Technology, Space Systems Laboratory, June 1999.
- [15] Olivier L. de Weck and David W. Miller. Introduction to isoperformance analysis for precision opto-mechanical space systems. Research memorandum, Massachusetts Institute of Technology, Space Systems Laboratory, May 19, 2000.
- [16] Olivier L. de Weck and David W. Miller. Performance and sensitivity analysis for internally balanced and reduced dynamic linear time-invariant (LTI) systems. Research memorandum, Massachusetts Institute of Technology, Space Systems Laboratory, February 18, 2000.
- [17] C.H. Edwards, Jr. and David E. Penney. *Elementary Differential Equations with Boundary Value Problems*. Prentice Hall, Englewood Cliffs, New Jersey, third edition, 1993.
- [18] Christopher E. Eyerman and Joseph F. Shea. A systems engineering approach to disturbance minimization for spacecraft utilizing controlled structures technology. MIT SERC Report #2-90, Massachusetts Institute of Technology, June 1990.
- [19] C.Z. Gregory Jr. Reduction of large flexible spacecraft models using internal balancing theory. *Journal of Guidance*, 7(6):725–732, Nov-Dec 1984.
- [20] Robert Grogan. Personal email correspondence from May 18, 2000.
- [21] Robert L. Grogan, Gary H. Blackwood, and Robert J. Calvet. Optical delay line nanometer level pathlength control law design for space-based interferometry. In *Proceedings of the 1998 SPIE International Symposium of Astronomical Interferometry*, volume 3350, March 1998.



- [22] Homero L. Gutierrez and David W. Miller. *Performance Assessment and Enhancement of Precision Controlled Structures During Conceptual Design*. PhD thesis, Massachusetts Institute of Technology, Space Systems Laboratory, February 1999.
- [23] Jae H. Kim and Robert E. Skelton. Model reduction by weighted component cost analysis. In *AIAA Dynamics Specialists Conference*, pages 153–160.
- [24] Andy Kissil. Documentation of existing NGST FE models. Internal NGST memo, May 6, 1998.
- [25] Alan J. Laub, Michael T. Heath, Chris C. Paige, and Robert C. Ward. Computation of system balancing transformations and other applications of simultaneous diagonalization algorithms. *IEEE Transactions on Automatic Control*, AC-32(2):115–122, February 1987.
- [26] Marie B. Levine. The interferometry program flight experiments: IPEX I&II. In *Proc. SPIE Astronomical Telescopes and Instrumentation Conference, Kona, HI*, number 3350-14, Bellingham, WA, March 1998.
- [27] Gregory J.W. Mallory and David W. Miller. *Development and Experimental Validation of Direct Controller Tuning for Spaceborne Telescopes*. PhD thesis, Massachusetts Institute of Technology, Space Systems Laboratory, April 2000. SERC #1-2000.
- [28] Rebecca A. Masterson. Development and validation of empirical and analytical reaction wheel disturbance models. Master’s thesis, Massachusetts Institute of Technology, Space Systems Laboratory, June 1999.
- [29] J.W. Melody. Discrete-frequency and broadband reaction wheel disturbance models. Interoffice Memorandum 3411-95-200csi, Jet Propulsion Laboratory, June 1, 1995.
- [30] David W. Miller, Edward F. Crawley, Jonathan P. How, et al. The middeck active control experiments (MACE): Summary report. Technical Report SERC #7-96, Massachusetts Institute of Technology, Space Engineering Research Center, Cambridge, Massachusetts, June 1996.
- [31] David W. Miller, Olivier L. de Weck, and Scott A. Uebelhart. SIM nanodynamics integrated model condition, disturbance and modal sensitivity analysis. Technical report, Massachusetts Institute of Technology, Space Systems Laboratory, June 22, 2000.

- [32] David W. Miller, Olivier L. de Weck, Scott A. Uebelhart, and Alissa N. Clawson. SIM integrated nanodynamics model v2.2: MIT SSL analysis. Viewgraphs from SIMTAC #20, October 19, 2000.
- [33] David W. Miller, Olivier L. de Weck, Scott A. Uebelhart, Robert Grogan, and Ipek Basdogan. Integrated dynamics and controls modeling for the space interferometry mission (SIM). Number 51 in IEEE Aerospace Conference 2001, March 10-17, 2001, Big Sky, Montana, March 2001.
- [34] David W. Miller, Scott Uebelhart, and Olivier de Weck. SIM classic version 2.0: Preliminary model reduction, disturbance and sensitivity analysis. Viewgraphs from JPL contract review, April 15, 2000.
- [35] Bruce C. Moore. Principal component analysis in linear systems: Controllability, observability, and model reduction. *IEEE Transactions on Automatic Control*, AC-26(1):17–32, February 1981.
- [36] Gary Mosier, Mike Femiano, Kong Ha, et al. An integrated modeling environment for systems-level performance analysis of the next generation space telescope. In *Proceedings of the Conference, Kona, HI*, volume 3356 of *SPIE Proceedings*, pages 89–97, March 1998.
- [37] Charley Noecker and Steven Kilson. Terrestrial planet finder: the search for life elsewhere. In *IEEE Aerospace Applications Conference Proceedings*, volume 4, pages 49–57, 1999.
- [38] Alan Posey, Drew Jones, and George T. Roach. EO3 Redeye mechanical configuration. Viewgraphs from Integrated Mission Design Center, GSFC, July 15, 1999.
- [39] William H. Press, Saul A. Teukolsky, William T. Vetterling, and Brian P. Flannery. *Numerical Recipes in C: The Art of Scientific Computing*. Cambridge University Press, second edition, 1992.
- [40] David C. Redding and William G. Breckenridge. Optical modeling for dynamics and control analysis. *J. Guidance*, 14(5):1021–1032, Sept-Oct 1991.
- [41] J. Gary Reid. *Linear System Fundamentals: Continuous and Discrete, Classic and Modern*. McGraw-Hill Book Company, New York, 1983.

- [42] Josephine San, Jennifer Bracken, and Dave Olney. EO3 Redeye mechanical configuration. Viewgraphs from Integrated Mission Design Center, GSFC, July 15, 1999.
- [43] Josephine San, Eric Holmes, and Dave Olney. Nexus attitude control subsystem. Viewgraphs from Integrated Mission Design Center, GSFC, May 18, 2000.
- [44] R.E. Skelton and P.C. Hughes. Modal cost analysis for linear matrix-second-order systems. *Journal of Dynamic Systems, Measurement, and Control*, 102:151–158, September 1980.
- [45] R.E. Skelton, R. Singh, and J. Ramakrishnan. Component model reduction by component cost analysis. In *AIAA Guidance Control Conference*, 1988. AIAA-88-4086-CP.
- [46] Robert E. Skelton, Peter C. Hughes, and Hari B. Hablani. Order reduction for models of space structures using modal cost analysis. *Journal of Guidance*, 5(4):351–357, July-August 1982. AIAA 82-4194.
- [47] H. S. Stockman, editor. *Next Generation Space Telescope: Visiting a Time When Galaxies Were Young*. The Association of Universities for Research in Astronomy, Inc., Space Science Telescope Institute, 1998. Second Printing.
- [48] Gilbert Strang. *Introduction to Linear Algebra*. Wellesley-Cambridge Press, Wellesley, Massachusetts, 1993.
- [49] Stephen Unwin. Searching for planets with the Space Interferometry Mission. NASA report, Jet Propulsion Laboratory, 2000. Doc ID 20000056082.
- [50] John Van de Vegte. *Feedback Control Systems*. Prentice Hall, Englewood Cliffs, New Jersey, third edition, 1994.
- [51] Paul H. Wirsching, Thomas L. Paez, and Keith Ortiz. *Random Vibrations: Theory and Practice*. John Wiley & Sons, Inc., New York, 1995.
- [52] Kemin Zhou, John C. Doyle, and Keith Glover. *Robust and Optimal Control*. Prentice Hall, Upper Saddle River, New Jersey, 1996.